2023

The structure and properties of additively manufactured metastable-β Ti-15Mo

Edohamen Awannegbe

UNIVERSITY
OF WOLLONGONG
AUSTRALIA

The structure and properties of additively manufactured metastable-β Ti-15Mo

Edohamen Awannegbe

BSc and MSc

This thesis is submitted in the fulfilment of the requirements for the award of the degree of

Doctor of Philosophy

University of Wollongong

School of Mechanical, Materials, Mechatronics and Biomedical Engineering (MMMB)

Faculty of Engineering and Information Science (EIS)

June 2023

Acknowledgements

I want to specially thank my heavenly father – God Almighty, for granting me divine health and for enabling me intellectually for the pursuit of a doctorate degree at the University of Wollongong (UOW). I would like to express my gratitude to my family members for their words of encouragement and prayers. Specifically, my heartfelt gratitude goes to my father "Patrick Awannegbe" of blessed memories, for investing so much in my education in the USA and Norway and instilling in me a great appreciation for education.

Thanks to the Australian Government for the Australian Research Training Program Scholarship to undertake this study. I am especially grateful to Professor Huijun Li and Professor Buyung Kosasih for their supervision and constructive criticism to bring out the best in me. More thanks to my supervisors for their encouragement in times of despondence in the journey toward achieving this PhD degree.

My thanks go to Professor Elena Pereloma of UOW and Ma Qiang of RMIT for the 3D printing of Ti-15Mo for investigation. I also want to express my appreciation to other staffs of UOW as follows: Mr. Matthew Franklin for providing required training in sample metallographic preparation and x-ray diffraction, Mr. Duncan Best for his expertise in conducting uniaxial tensile tests, Mr. Michael Grantham for Electric Discharge Machining of samples, Dr. Liang Chen for performing thermomechanical processing of samples, Dr. Bach Tran for SEM and EDS training at UOW main campus, Dr. Mitchel Nancarrow for generating high quality SEM images and EDS maps at UOW innovation campus, Dr. Lachlan Smillie for TEM imaging and diffraction pattern acquisition and Dr. Azdiar Gazder for EBSD map acquisitions and training in FEGSEM usage and post-acquisition analysis of EBSD maps.

Finally, I am thankful to all my research colleagues for their kind support and friendship. Specifically, my friends Zhijun Qiu and Hamid Kamali for their guidance in the weeks leading up to my doctoral confirmation.

Abstract

A bidirectional powder deposition strategy was employed to additively manufacture Ti-15Mo wt% using laser metal deposition. Phase identification, elemental analysis and microstructural characterisation were conducted in the As-Built condition and also after uniaxial tensile testing using X-ray diffraction and scanning electron microscopy along the different processing directions. In addition, electron backscattering diffraction and transmission electron microscopy were used to analyse deformation mechanisms. It was found that three distinct zones, namely the fusion, remelted and heat affected zones, evolved in all 25 deposited layers which predominantly comprised coarse columnar grains. These columnar grains were coarser up the build height due to increased distance from the substrate and slower cooling rates determined. Mo segregation was pronounced in the as-built microstructure. The fusion zone was the most solute enriched zone, followed by the remelted zone. The heat affected zone of each deposited layer featured inter-dendritic lamellas of molybdenum rich and lean inter-layers and this zone was the least solute-enriched. Deformation accommodation in β matrix was by a combination of slip, $\{332\}\langle 113\rangle$ and $\{112\}\langle 111\rangle$ twinning, α″ martensite and ω_D formation contrarily to the expected twinning.

The as-built alloy was subsequently subject to post-fabrication heat treatment. Microstructural characterisation was conducted in the heat-treated state and also after uniaxial tensile deformation. X-ray diffraction, energy dispersive spectroscopy and scanning electron microscopy were employed in the heat-treated state. Electron backscatter diffraction was used in investigating the deformed microstructure. Columnar β grain refinement was achieved by fragmentation from a combined contribution from precipitated phases and deformation induced products. The three distinct microstructural zones, namely the fusion, remelted and heat affected zones, observed in each deposited layer of the as-built microstructure were retained after sub-β-solvus heat treatment but completely erased in the super-β-solvus microstructure. Accommodation of plastic deformation in β matrix was by a combination of slip and primary α″ martensite which formed preferentially at grain

boundaries. Elastic modulus decreased from 86.85±0.45 GPa in the as-built alloy to 72.8±0.65 GPa after heat treatment. Ultimate tensile strength of 1168± 1.12 MPa from the heat-treated sample represents only a marginal increase from that of the as-built sample of 1099± 2.3 MPa. This was accompanied by a small decrease in total elongation.

The as-built alloy was also subject to post-fabrication uniaxial thermomechanical processing at strain rates of $0.00055s^{-1}$, $0.0011s^{-1}$, $1s^{-1}$, and $4s^{-1}$ to strains of 20% and 40%. Experiments were conducted at room and elevated temperatures. Phase identification, elemental and microstructural characterisation were conducted using x-ray diffraction, energy dispersive spectroscopy and scanning electron microscopy. The three distinct zones, namely the fusion, remelted and heat affected zones, identified in each deposited layer of the as-built microstructure were retained after thermomechanical processing. After processing, electron backscatter diffraction was used to analyse deformation mechanisms. Deformation accommodation in β matrix was predominantly by a combination of slip and α′′ martensite which formed as a primary product in parent β and at grain boundaries. However, the operation of {332}⟨113⟩ and {112}⟨111⟩ β-twinning was also determined, howbeit with a very small surface fraction. This implies a small surface fraction of secondary α′′ martensite forming within β-twins in the deformed microstructure. Compressive mechanical properties showed a strong dependence on strain rate as higher flow stress and compressive strength were obtained at higher strain rates.

Certification

I Edohamen Awannegbe declare that this thesis submitted in fulfilment of the requirements for the conferral of the Doctor of Philosophy, from the University of Wollongong, is wholly my own work unless otherwise referenced or acknowledged. This document has not been submitted for qualifications at any other academic institution.

_____

Edohamen Awannegbe

25th June 2023

List of Publications

1. **Edohamen Awannegbe**, Huijun Li, Tingting Song, Frank Niessen, Ma Qian, Azdiar Gazder, Mitch Nancarrow and Elena Pereloma, 'Microstructural characterisation and mechanical evaluation of Ti-15Mo manufactured by Laser Metal Deposition', Journal of Alloys and Compounds, **[IF: 5.316]** --- From Chapter 4.
2. G. K. Sujan, Azdiar A. Gazder, **Edohamen Awannegbe**, Huijun Li, Zengxi Pan, Daniel Liang, and Nazmul Alam, 'Hot-deformation behaviour and microstructural evolution of Inconel 718 superalloy fabricated by directed energy deposition', **Metallurgical and Materials Transactions A [IF: 2.556].**

List of Conference papers

1. **Edohamen Awannegbe**, Huijun Li, Tingting Song, Frank Niessen, Ma Qian, Azdiar Gazder, Mitch Nancarrow and Elena Pereloma, 'Deformation mechanisms and mechanical properties of LMDed Ti-15Mo-0.25O', International Conference on the Cooperation and Integration of Industry, Education, research, and Application 2022 – Metal-based New Material and Advanced Manufacturing Technology Sub-forum (ICIERA – 2022).

List of Figures

List of Tables

List of Abbreviations and Symbols

1. Abbreviations

2D	2 Dimension
3D	3 Dimension
AB	As Built
AL	Aluminium
AM	Additive Manufacturing/Additively Manufactured
Ar	Argon
ASTM	American Society for Testing and Materials
at. %	Atomic percentage
BC	Band Contrast
BCC	Body Centered Cubic
BF	Bright Field
BH	Build Height
B_O	Bond order
BMB	Bain strain
BPB	Shape deformation matrix from which the shape strain is derived
BSE	Backscattered Electron
°C	Degree Celsius (unit of temperature)
CAD	Computer Aided Design
CC	Critical Composition
cm	centimetre
Co	Cobalt
CO_2	Carbon Di Oxide
CP	Commercially Pure

Cr	Chromium
CSO	Sample Coordinate System
Cu	Copper
CV	Correspondence Variants
d	Direction of macroscopic shape change
DED	Direct Energy Deposition
DF	Dark Field
DS	Deformed Sample
DSC	Differential Scanning Calorimetry
E	Energy Density having unit of J/mm^3 (Joules per cubic millimetre)
EBSD	Electron Backscattered Diffraction
EBM	Electron Beam Melting
EDM	Electric Discharge Machining
EDS	Energy Dispersive Spectroscopy
E-MOD	Elastic Modulus
Fe	Iron
FEGSEM	Field Emission Gun Scanning Electron Microscope
FWHM	Full Width at Half Maximum
FZ	Fusion Zone
g	grams
GPa	Giga Pascals
h	Hatching distance
HAADF	High Angle Annular Dark Field
HAGB	High Angle Grain Boundary
HAZ	Heat Affected Zone
HCP	Hexagonal Closed Pack

HHT	Homogenisation Heat Treatment
HT	Heat Treatment
H_{U-F}	Height from end of uniform solute zone to interlayer fusion zone
H_V	Vickers Hardness
I	Identity matrix
IPF	Inverse Pole Figure
K	Kelvin (unit of temperature)
KAM	Kernel Average Misorientation
kN	Kilo Newton
kV	Kilo Volts
KW	Kilo Watts
LAGB	Low Angle Grain Boundary
LECO	Laboratory Equipment Corporation
LENS	Laser Engineered Net Shaping
LMD	Laser Metal Deposition
LP	Lattice Parameter
LPBF	Laser Powder Bed Fusion
LSF	Laser Solid Forming
m	Magnitude of macroscopic shape change
Md	Molecular d-orbital energy level
MF	Martensite Finish Temperature
MIM	Metal Injection Molding
µm	Micrometre
mm	Millimetre
Mn	Manganese
Mo	Molybdenum

MO	Misorientation
MoE	Molybdenum Equivalence
MPa	Mega Pascals
MS	Martensite Start Temperature
N	Nitrogen
nA	Nano ampere
Nb	Niobium
ND	Normal Direction
Ni	Nickle
nm	Nanometre
O	Oxygen
ODF	Orientation Distribution Function
OPS	Oxide Polishing Solution
Pa	Pascals
pA	Pico ampere
PDS	Pre-Deformed Sample
PFZ	Precipitate Free Zone
RD	Rolling Direction
RHT	Rapid Heat Treatment
RPM	Revolutions per minute
RT	Room Temperature
RZ	Remelted Zone
s	seconds
SADP	Selected Area Diffraction Pattern
SAED	Selected Area Electron Diffraction
SCCM	Standard cubic centimetre per minute

SE	Secondary Electron
SEM	Scanning Electron Microscopy
SF	Schmid Factor
Si	Silicon
SIMT	Stress Induced Martensite Transformation
SLM	Selective Laser Melting
Sn	Tin
ST	Solution Treatment
STEM	Scanning Transmission Electron Microscopy
STL	Stereolithographic
t	Layer thickness
Ta	Tantalum
TB	Twin Boundary
TD	Transverse Direction
tEL	Total Elongation
TEM	Transmission Electron Microscopy
Ti	Titanium
TiO_2	Titanium Di Oxide
TMCP	Thermomechanical Controlled Processing
tr	trace
TRIP	Transformation Induced Plasticity
TWIP	Twinning Induced Plasticity
UTS	Ultimate Tensile Strength
V	Vanadium
W	Tungsten
W	Watt

WAAM	Wire Arc Additive Manufacturing
Wf	Frictional work
WHR	Work Hardening Rate
WQ	Water Quenched
Wt. %	Weight Percentage
YS	Yield Strength
XRD	X-Ray Diffraction
Zr	Zirconium

2. Symbols

α	HCP alpha phase of titanium alloys
α'	HCP alpha single prime martensite phase
α''_{ath}	Orthorhombic athermal alpha double prime martensite phase
α''_{D}	Orthorhombic deformation induced alpha double prime martensite phase
α_m	Massive alpha
Å	Angstrom
β	BCC beta phase of titanium alloys
m	Friction factor
b	Bulger factor
°	Degree
Δ	Delta (Change)
δ	Delta (Change)
$\emptyset$	Phi (°)
ρ	Rho (density in kg/m^3)

σ_e	Experimental flow Stress (MPa)
σ_c	Corrected flow stress (MPa)
σ_E	Engineering Stress (MPa)
σ_T	True Stress (MPa)
ε_E	Engineering Strain
ε_T	True Strain
Λ	Upper case lambda (Dislocation mean free path)
λ	Lambda
S^{-1}	Per second representing strain rate
ω_{ath}	Hexagonal athermal omega phase
ω_D	Hexagonal deformation induced omega phase
ω_{iso}	Hexagonal isothermal omega phase

Table of Content

1 Introduction

1.1 Background

Additive manufacturing (AM) is used for the prototyping and manufacturing of functional products in the biomedical, aerospace, and automotive industries [1, 2]. When compared to conventional wrought or casting processes, directed energy deposition AM techniques which include Laser Metal Deposition (LMD), Electron Beam Melting (EBM), Wire Arc Additive Manufacturing (WAAM), and Laser Engineered Net Shaping (LENS) among others, present many advantages. Primary benefits include the ease in manufacturing of components with geometrical complexity and the shorter lead times in near-net shape component production [3]. LMD is a multipurpose process, which could be used to repair the damaged components [4], to apply protective coatings and to manufacture new near full density components [5]. Some advantages of LMD over other AM techniques include rapid production of large-scale components, in-situ alloying, and ability to produce functionally graded parts. However, LMD made components experience a higher surface roughness and lower dimensional accuracy compared to selective laser melting (SLM) [5].

LMD studies are focussed on optimisation of parameters for production of both α/β (mainly Ti-6Al-4V alloy) [6-9] and metastable β Ti alloys [10-12], and post-processing heat treatments to modify the microstructure and improve mechanical properties [13, 14]. Typically, the β phase microstructures of additively manufactured Ti alloys using laser as energy source display coarse columnar grains elongated in the building direction with each deposited layer delineated by melt pool boundaries/fusion zone (FZ) [9, 15-17]. The columnar grains elongate over several layers due to their epitaxial growth resulting from the partial remelting of previously consolidated layers [17]. Within the columnar grains, a cellular and cellular-dendritic solidification sub-structure is present, in which the micro-segregation of alloying elements takes place [16-18]. The enrichment of the FZ, for example by Mo, has also been observed in Ref. [17].

Significant effort has been spent on researching wrought Ti-Mo alloys due to their attraction as a biomaterial on account of their nontoxicity, low elastic modulus, and high mechanical strength [19].

Depending on Mo content, the microstructure and mechanical behaviour of Ti-Mo alloys varies significantly [12, 20]. With an increase of Mo from 9 to 15wt.%, β phase stability increases and the operating plastic deformation accommodation mechanisms change from deformation-induced α′′ martensite and ω_D to predominantly $\{332\}\langle 113\rangle$ and $\{112\}\langle 111\rangle$ twinning in addition to slip [21-27].

The columnar microstructure of AM-produced metastable β Ti alloys differs significantly from the typically equiaxed ones in wrought Ti alloys. However, to-date, only limited studies detail the mechanical behaviour of AM-produced metastable β Ti alloys, and in particular Ti-Mo ones [10, 28-32]. Furthermore, the vast majority of research was carried out on SLMed Ti-Mo alloys. Contrarily, this work focuses on LMD-produced Ti-15Mo wt.% alloy and provides insight into the operating deformation mechanisms during uniaxial tensile testing and correlates them to the different zones in the microstructure. These mechanisms were also investigated in the heat treated and thermo mechanically processed samples. Different heat treatment processes in the sub-β-solvus and super-β-solvus phase fields were employed with the aim to achieve solute and grain-structure homogenisation as well as columnar grain refinement in the post-fabrication microstructure.

Metastable β titanium alloys have been subject to several post fabrication heat treatment process paths in the sub-β-solvus and super-β-solvus phase fields with reported grain refinement and solute homogenisation. Grain refinement reported in literature has been primarily achieved by three mechanisms namely recrystallization, formation of sub-structures and grain fragmentation by precipitated α. For instance, it was reported in wrought Ti-15Mo wt.% [33-35] that solute homogenisation and grain refinement were achieved via the stated mechanisms with some enhancement in mechanical properties after conducting heat treatment at 1200°C with a hold time of 6 hours before quenching. Improvements in mechanical properties were convincingly substantiated. However, the claim on solute homogenisation (i.e., microstructure featuring a single β-phase only) was not proven as Energy Dispersive Spectroscopy (EDS) points analysis with associated elemental maps was absent from the cited studies above. In the current study, EDS analysis was conducted to

investigate the prevalent claim on solute homogenisation at 1200°C/6 hour for metastable β titanium alloys. The absence of a single β-phase microstructure after heat treatment invalidated this claim. Rather, an even distribution of super-enriched and super-depleted phases occurred in the emerging microstructure.

Significant grain refinement in comparison to as-built (AB) average grain size was reported in Ti-6V-4Al [36] and β-Ti-5Al-5Mo-5V-3Cr-1Zr [37] produced by LMD with predominantly columnar β-grains in the AB microstructure. In Ref [36], a great degree of grain refinement was reported at higher heating rates for rapid heat treatment when dwell time was kept constant, largely due to less time available for grain growth/coarsening. In β-Ti-5Al-5Mo-5V-3Cr [38-40] a more even distribution of precipitated α within parent β was reported at lower heating rates.

The current work examines grain sizes after heat treatment and analyses zonal dependencies of deformation mechanisms in connection with emerging uniaxial tensile properties of heat-treated Ti-15Mo wt.%. Properties are then compared with those of the AB Ti-15Mo wt.% alloy [41] previously reported by the author of the current work as well as those reported by other authors. Microstructure and micro-texture characterisation were performed using a combination of X-ray diffraction (XRD), EDS, SEM, and electron backscatter diffraction (EBSD).

Thermomechanical uniaxial compression was also conducted on the alloy under investigation with the aim to refine columnar grains and homogenize grain structure. Compression was first conducted at room temperature (RT) and thereafter at an elevated temperature of 650°C. Results from the RT experiments would serve as a reference point in analysing those of the elevated temperature. The temperature, strain rate and strain employed during uniaxial compression of Ti alloys has a direct bearing on surface fraction, distribution density of precipitates, deformation products formed, triggering stress for products and overall flow stress behaviour. Specifically, strain rate can impact a staged/sequential operation of mechanisms by which plastic deformation is accommodated in the deformed microstructure. For instance, it was determined in Ti-10V-2Fe-3Al [42, 43] that during RT compression at a low strain rate of 10^{-4} - 10^{-3} s^{-1}, in addition to slip the alloy displayed a dominant

deformation mechanism with α'' martensite formation. It was also reported that $\{332\}\langle 113\rangle$ β_{twin} and stress-induced ω phase were activated. At an intermediate strain rate of 10^{-1} s^{-1}, there was a competition between stress-induced phase transformations and β_{twin}. When strain rate was increased to 10^{1} s^{-1} or higher, it was found that the dominant deformation mode was β_{twin}.

At elevated temperatures, the strain rate at which a compression test proceeds can have a direct influence on the alloy's β-stability and β-domain size [44, 45]. This is because a TMCP experiment conducted in the α+β phase field such as obtainable in the current study permits the precipitation of hexagonal closed pack (HCP) α-phase which invariably decreases the domain size of β. The extent of decrement is influenced by surface fraction of α precipitated, which is a direction function of strain rate and holding time before straining. Depending on the surface fraction of α during deformation, the occurrence of $\beta \rightarrow \beta_{twin}$ reorientation and/or $\beta \rightarrow \alpha''$martensite transformation could be rendered less likely. In fact, an α-phase precipitate of up to 50% could completely inhibit martensitic transformation from parent β [46, 47]. It was also reported in Ref. [43] that at higher strain rates there is a higher surface fraction and more even distribution of β_{twin}. This was also reported in metastable Ti-10V-2Fe-3Al [48] in connection with strains. The stated correlation with strain is a logical expectation barring multiple switches in operating deformation mechanisms before attainment of near-100% compression. Regardless of temperature of compression, triggering stress for deformation products and ultimate flow stress is higher at higher strain rates [43, 49]. This is corroborated in the current study.

The current work investigates the strain and strain rate dependence of α precipitates and deformation products at room temperature and 650°C compressions. A link is then established between phases/products formed during compression and triggering stress, flow stress behaviour and hardness. Microstructure and micro-texture characterisation were performed using a combination of x-ray diffraction (XRD), scanning electron microscopy (SEM), energy dispersive spectroscopy (EDS) and electron back-scatter diffraction (EBSD).

1.2 Aims and Objectives

This research project is aimed at creating a sound understanding of the chemical composition, microstructure, deformation mechanisms and mechanical properties of as-built (AB), heat treated (HT) and thermo-mechanically processed (TMCP) Ti-15Mo-0.25O, additively manufactured by Laser Metal Deposition (LMD). The associated microstructural imperfections of the AB alloy will be characterised and subsequently observed for changes after subjection to post-fabrication processing. The main targets of the current work are therefore delineated as follows:

1. To characterise the pre-deformation composition and microstructure of AB Ti-15Mo-0.25O and subsequently investigate the deformation mechanisms and mechanical properties of AB Ti-15Mo-0.25O subject to uniaxial tensile deformation to failure at a specified strain rate. Microstructural and nano-structural analysis will be conducted, and results compared to understand the similarities/differences of interaction among deformation features at different scales of microscopy.
2. To analyse the influence of sub-β solvus and super-β solvus heat treatment on evolved composition and grain structure. Average grain sizes will be determined after heat treatment and compared to the AB condition and description of basis for observed changes, will be provided. Comparison between AB and heat-treated samples deformation mechanisms and mechanical properties will be conducted for possible enhancement of properties.
3. To present the composition and microstructure of AB alloy which has been subject to TMCP at a pre-determined temperature to different strains and strain rates. This will provide data and set expectations for possible mechanical performance for future work in uniaxial tensile study on a pre-TMCPed alloy.

1.3 Novelty of research

To the best of my knowledge, Ti-15Mo has never be additively manufactured using the LMD technique. The current study will provide a nano-nuanced understanding of the emerging microstructure and accompanying defects of LMDed Ti-15Mo. An exhaustive/critical literature

review will be conducted to compare the microstructure and mechanical properties of this alloy with those manufactured conventionally and by other AM techniques such as Selective Laser Melting (SLM) and Electron Beam Melting (EBM) among others. The primary areas of novelty of the current study in comparison to the existing knowledge base in metastable Ti-alloys are as follows:

1. Determination of varying grain structure/sizes as well as dominant grain morphology in the different microstructural zones which include the FZ, RZ and HAZ of the pre-deformed AB alloy. This analysis will proceed on a layer-by-layer basis of the AB coupon to investigate for similarities in terms of grain structure/sizes among the distinct zones of each of the 25 deposited layers. Delineation of the growth mechanism of β-grains during LMD process as well as the reason for the existence of the HAZ in the rather heterogeneous microstructure. A comparison of phases in the AB and deformed states to identify the ones which are purely strain induced. A subsequent examination of the preserved but distorted zones and how they uniquely accommodate deformation products in terms of the influence of Mo segregation. An in-depth study will then proceed on the differences in product distribution density and possible association of phases/product morphologies with the different zones. The isolation of columnar grains spanning multiple layers, from the microstructure in EBSD and Schmid Factor analysis of twin variants in the columnar grains, including their identification and colour-patterned labelling.
2. While other metastable Ti-alloys have been additively manufactured by direct energy deposition technique and subsequently post heat-treated, for the first time, metastable Ti-15Mo manufactured by LMD will be post heat treated and analysed. Thus, a novel in-depth investigation of the influence of sub-solvus and super-solvus heat treatment on compositional/microstructural homogenisation of the full microstructure which includes the inter-layer dendritic lamellas of the HAZ is presented. The influence of heat treatment on the nucleation cites preference and growth of strain induced α″ martensite is conducted. Deformation product distribution density is reported in comparison to the AB sample

Mechanism of recrystallisation is reported and connected to the emerging average grain size in comparison with the AB alloy which featured prior β-grains only. Texture analysis is presented and compared to the AB alloy as an evidence to the extent of homogenisation achieved after heat treatment. Feature of fracture surface are compared between AB and HT samples to identify the influence of HT in eliminating AB defects such as pores. Basis for disparity in mechanical properties between AB and HT samples are outlined.

3. The use of TMCP as a grain refinement approach on additively manufactured metastable Ti alloys is rear in literature and its use on Ti-15Mo specifically, is extremely rare. The current work applies a pre-thermal analysis using differential scanning calorimetry (DSC) to determine temperature ranges for possible phase transformation/recrystrallisation. This is conducted on the basis that grain refinement could be achieved by either β-grain fragmentation or dynamic recrystallisation. The influence of TMCP on morphology, size and nucleation cites of α'' martensite is also presented. Texture comparison of TMCPed samples to AB and HT ones is conducted to identify similarities in texture orientations. Texture comparison also indicates the extent to which in-homogeneity in mechanical properties could be abated. Data presented would inform a future uniaxial tensile deformation study on a pre-TMCPed alloy.

1.4 Organisation of thesis

This thesis is organised into 7 main chapters as presented below.

Chapter 1 - An introduction into Ti alloys. This chapter provides a brief background information into the historical applications and advantages of metastable Ti-alloys as well as the merits/demerits of LMD and other AM techniques. The aims and objectives, novel contributions, and an outline of the main chapters of the thesis are also presented in this chapter.

Chapter 2 - A thorough/critical literature review on Ti-alloys of the α and β class is rendered in this chapter with emphasis on the metastable sub-class of the β class. The progress recorded in nuanced-characterisation of the microstructure of conventionally and additively manufactured, and post-

fabrication-processed Ti alloys is well elaborated upon. This review provides the basis for delineating the knowledge gaps which the current work addresses.

Chapter 3 - A description of raw materials, metallographic procedures, micro and nano characterisation techniques, microscopes, mechanical testing equipment and data analysis softwares/methods are presented in this chapter.

Chapter 4 - A characterisation of the microstructure of Ti-15Mo-0.25O additively manufactured by Laser Metal Deposition in the AB and deformed states is presented. In the AB condition, the evolution of predominantly columnar grain structure amid a small fraction of equiaxed grains is elaborated upon, on a layer-by-layer basis. The composition, 3-distinct microstructural zones and phases present in the AB condition is reported. In the deformed state, the mechanism by which deformation products are accommodated in the 3-distinct zones as well as the accommodation of strain by these products and its influence on mechanical properties is well described. Texture analysis is presented as an evidence of the an-isotropic state of mechanical properties in the AB alloy.

Chapter 5 – A literature and DSC informed heat treatment is conducted on Ti-15Mo-0.25O in the sub-β and super-β solvus phase fields. Changes in composition and microstructure in the retained/erased distinct microstructural zones are examined. A comparison of mechanical properties among AB and HT samples of the current study and literature data of metastable β-Ti alloys, is then presented.

Chapter 6 - A DSC informed thermo-mechanically controlled processing of Ti-15Mo-0.25O is presented. The emerging microstructure from elevated temperature compression is compared to those of RT compression. Elaborate microstructural characterisation is then presented to inform a future tensile test on pre-TMCPed Ti-15Mo-0.25O samples.

Chapter 7 - A summary of the main conclusions from this research work is presented. Future research work on variances in LMD fabrication and microstructural characterisation is proffered. Grain refinement strategies and mechanical tests are also recommended.

2 Literature review

The metastable class of β-Titanium (β-Ti) alloys which is the main subject of investigation in this thesis, is one of the 3 sub-classes of β-Ti alloys. Ti alloys are classified based on the molydenum equivalent (MoE) factor which spans the range $10 \leq MoE \leq 30$ for the metastable sub-class [50, 51]. Other sub-classes of bcc β-Ti alloys which include near-β ($5 \leq MoE \leq 10$) and stable-β ($MoE \geq 30$) [50, 51] will not be treated in-depth in this study. The forgoing literature review therefore focuses on the classification/composition, heat-treatment/thermo-mechanical processing of conventionally fabricated and additively manufactured (AM) metastable β-Ti alloys. Alloy microstructures after AM are compared to the microstructures of the conventional alloys. Mechanical properties are subsequently associated with prior microstructure to understand the reason for disparity in performance.

The aforementioned MoE factor is expressed in Eq. 2.1 below [51] and is defined as the critical solute concentration required to retain 100% metastable β-phase upon quenching to Room Temperature (RT) from the single β-phase field [50-53].

$$MoE = 1.0(Wt.\%\ Mo) + 0.67(Wt.\%\ V) + 0.44(Wt.\%\ W) + 0.28(Wt.\%\ Nb) + 0.22(Wt.\%\ Ta) + 2.9(Wt.\%\ Fe) + 1.6(Wt.\%\ Cr) + 1.25(Wt.\%\ Ni) + 1.70(Wt.\%\ Mn) + 1.70(Wt.\%\ Co) - 1.0(Wt.\%\ Al)$$

Equation 2.1

2.1 Classification and Composition of metastable β-Ti Alloys

Ti is an allotropic element existing in more than one crystallographic form [50, 51]. It exihibits a hexagonal close-packed (hcp) crystalline structure at low temperatures with two Ti atoms on planes (0, 0, 0) and (1/3, 2/3, 1/2) known as the α-phase Ti [50, 51, 53]. This α-phase undergoes transformation into a body centered cubic (bcc) crystalline structure upon heating above 883 °C (1621 °F) as shown in Fig 2.1 [51]. Both phases bear an orientation relationship which corresponds to $\{0001\}_\alpha \| \{110\}_\beta$ and $\langle 11\bar{2}0\rangle_\alpha \| \langle 1\bar{1}1\rangle_\beta$ [54, 55]. The bcc structure also shown in Fig 2.1 [51] is

referred to as β-phase Ti with atoms located on (0, 0, 0) and (1/2, 1/2, 1/2) planes. As shown in Table 2.1, alloying elements (primarily functioning as specific phase stabilisers) are introduced to Ti in different combinations/proportions depending on the desired end-properties. Such alloying events lead to α (MoE = 0), near-α (MoE = 1), α+β (MoE $\leq$ 5), near-β (5 $\leq$ MoE $\leq$ 10), metastable-β (10 $\leq$ MoE $\leq$ 30) and stable-β (MoE $\geq$ 30) classifications for Ti alloys. This can be more broadly grouped into α, α+β and β classes. The microstructures of these alloys depend on composition and processing route used in fabrication. As seen in Table 2.1, the β-class in its aged state containing a significant volume fraction of α-phase exhibits superior strength over the other classes [51]. The dual α-β class provides an optimal combination of strength and ductility. The α-class bearing only α-phase and not having many alloying elements evinces the highest ductility measured in terms of percentage of elongation before failure (%EL) [52, 56]. As also listed in Table 2.1 the AM versions of β-Ti alloys exhibit overall inferior YS/UTS when compared to the conventioanlly manufactured alloys.

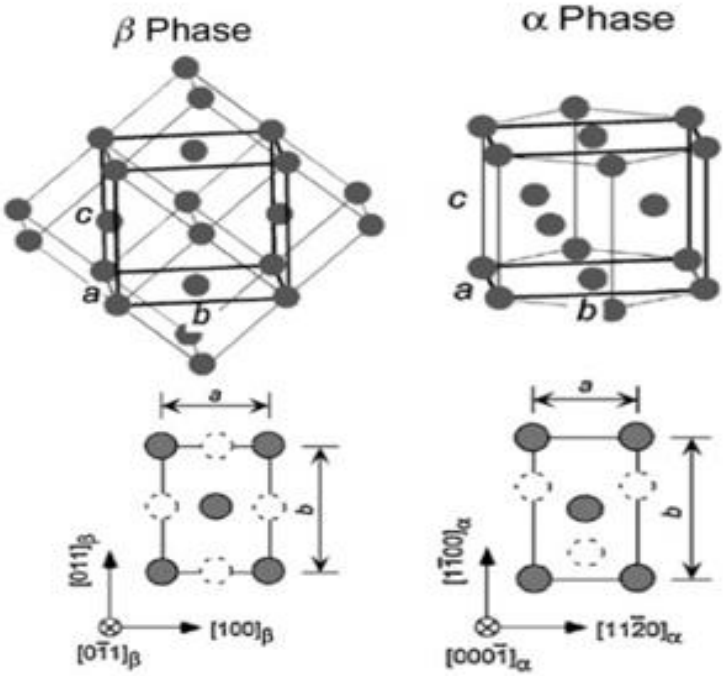

Figure 2.1. Crystal structures of β and α phases and their lattice correspondences [51].

Table 2.1. Composition and RT mechanical properties of α, α+β and β Ti alloys.

Alloys	Al	Sn	Zr	Mo	V	Cr	Nb	Ta	Fe	O	Condition		YS(MPa)	UTS (MPa)	tEl (%)	E-Mod (GPa)	Reference
α Ti-Alloys																	
Grade 1/Ti35A	-	-	-	-	-	-	-	-	≤0.2	≤0.18	Mill-annealed 675°C		170	240	24	-	[51]
Grade 2/Ti50A	-	-	-	-	-	-	-	-	≤0.3	≤0.25	Mill-annealed 675°C		275	344	20	-	[51]
Grade 3/Ti65A	-	-	-	-	-	-	-	-	≤0.3	≤0.35	Mill-annealed 675°C		377	440	18	-	[51]
α+β Ti-Alloys																	
Ti–6–4 (IMI 318)	6	-	-	-	4	-	-	-	-	≤0.2	Mill-annealed ~740°C and		880	950	14	-	[51]
Ti–6–4	6	-	-	-	4	-	-	-	-	≤0.13	Mill-annealed ~740°C		790	860	15	-	[51]
IMI 550	6	2	4	0.5	-	-	-	-	-	-	Solution Treated (ST) (α+β) aged 500°C		1000	1100	14	-	[51]
Conventional β Ti-Alloys																	
Ti–13–11–3	3	-	-	-	13	11	-	-	-	-	ST(β) aged 480°C 36h		1200	1280	8	-	[51]
Ti-12	-	-	-	12	-	-	-	-	-	-	Metal Injection Molding (MIM). Isothermal sintering at 8°C/min to 1100°C – 1450°C for 2h at each temperature and furnace cooled		-	845	4.15	73.2	[57]
Ti15	-	-	-	15	-	-	-	-	-	-	As-cast		745	921	25	84	[58]
AM β Ti-Alloys																	
Ti-24-4-8	-	8	4		-	-	24	-	-	-	SLM	0.5 m/s	563	665	13.8	-	[59]
Ti-15	-	-	-	15	-	-	-	-	-	-	LPBF	0.4-2.8 m/s	-	894	2.82	-	[60]
Ti-34-7-7			7				34	7			LENS^{TM}	-	814	834	19	55	[11]
Ti-15Mo				15							Direct Energy Deposition – Laser Additive Manufacturing	300-500 mm/min	480	815	17.14	73	[61]

Alloying elements bearing an electron to atom ratio of less than 4 are known to be α-stabilisers (e.g. Aluminum (Al), Oxygen (O), Nitrogen (N), Gallium (Ga), Carbon (C) etc.). It should be noted that there exists a limit to the amount of α-stabilising elements (Eq. 2.2) that may be added to Ti alloys due to the overall embrittling effect of these stabilisers [3, 50-55, 62]. This limit is termed the Aluminum Equivalent and alloys begin to show a pronounced brittle behavior when a limit of 9% is exceeded.

$$[Al]_{eq} = [Al] + \frac{[Zr]}{6} + \frac{[Sn]}{6} + 10[O + C + 2N] \qquad \text{Equation 2.2}$$

An electron to atom ratio of 4 translates neither to α nor β stabiliser (i.e. pertaining to neutral elements such as Silicon (Si) and Tin (Sn)). A ratio greater than 4 is associated with β-phase stabilisers which can either be of the β-isomorphous type (Molybdenum (Mo), Vanadium (V), Tungsten (W), Niobium (Nb), Zirconium (Zr) etc.) or the β-eutectoid type (e.g. Copper (Cu), Manganese (Mn), Chromium (Cr), Iron (Fe), Nickle (Ni), Cobalt (Co), Hydrogen (H) (etc.) [50-54, 62]. β is stabilised to RT in both metastable- and stable-alloys. This can be seen in Figure 2.2 where the MS is at RT for composition CC, implying that only β exists at RT for Mo > CC. It was proven that a minimum of 10 Wt. % Mo is required for full metastable β-phase at RT [63, 64].

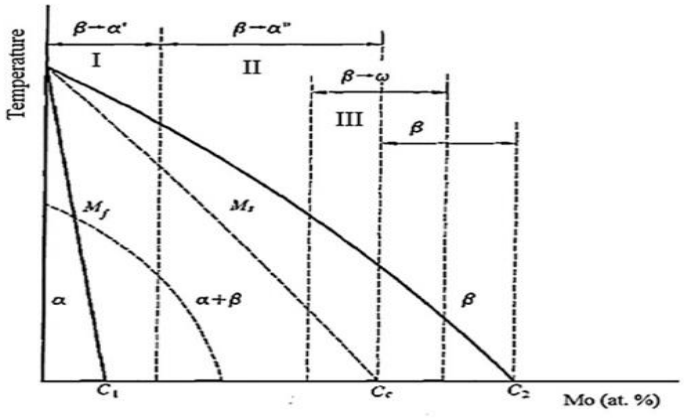

Figure 2.2. Phase transformations in Ti-Mo alloys. α' is the hcp martensite, α'' is the orthorhombic martensite, ω is the hexagonal omega phase, M_s and M_f represent the martensite start and finish lines respectively, C_1 is the Mo concentration required for dual phase α+β, C_c is the minimum Mo concentration required to retain metastable β-phase at RT and C_2 is the minimum Mo concentration required for stable β-phase at RT [65].

Each class of Ti alloys could contain smaller quantities of other phases. Metastable β-Ti predominantly contains the bcc β-phase but can also bear small volume fractions of α-phase, non-equilibrium phases such as the hcp martensitic phase (α′), orthorhombic martensitic phase (α′′), hexagonal athermal omega phase (ω_{ath}) and hexagonal isothermal omega phase (ω_{iso}) [51-53, 66, 67]. Formation of metastable phases is contingent upon composition, processing and β-phase stability. ω_{ath}-phase forms as a result of structural instabilities of the metastable β-phase in a displacive mechanism. This culminates in the full collapse of the $(111)_\beta$ plane in the closed packed direction represented by a body diagonal [68]. It bears an orientation relationship with the parent phase which corresponds to $[11\bar{2}0]_\omega \| [110]_\beta$ and $(0001)_\omega \| (111)_\beta$ [69-71] as shown in Fig2.3a. ω_{iso}-phase evolves from a combined structural and compositional instability of the metastable β-matrix as the new phase bares significant compositional differences from that of the parent phase [68, 72-74]. The formation of α′and α′′ martensites occurs in a diffusionless-shear mechanism [71]. The β → α′′ transformation yields an orientation relationship of $(110)_\beta \| (001)_{\alpha''}$, $(1\bar{1}2)_\beta \| (110)_{\alpha''}$ and $[\bar{1}11]_\beta \| [\bar{1}10]_{\alpha''}$ [51-53, 66] according to the lattice correspondence shown in Fig 2.3b.

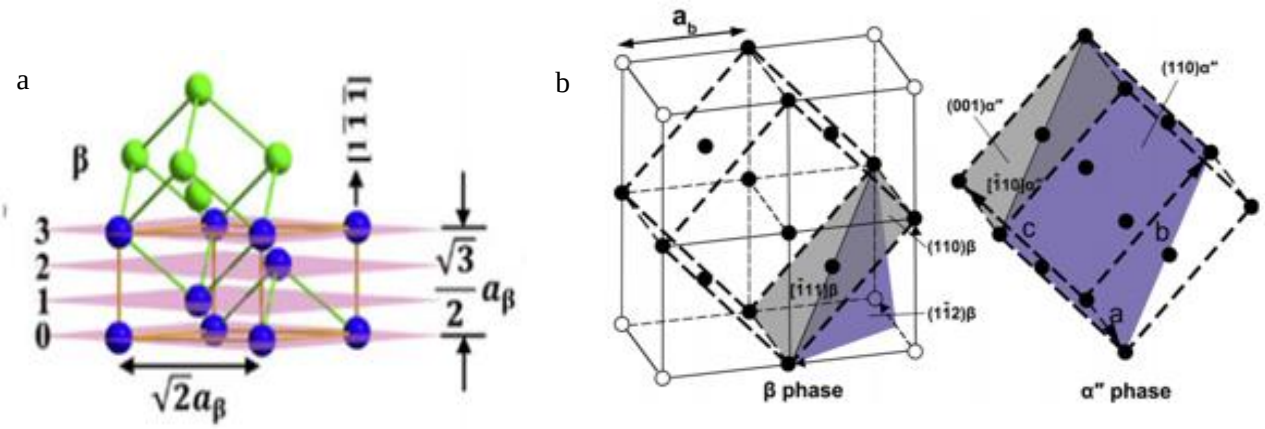

Figure 2.3a. Crystal structures of β and ω and their lattice correspondences [51], (b). Crystal structures of β and α'' and their lattice correspondences [75].

2.2 Effect of molybdenum concentration on phases and lattice parameter in binary Ti-Mo alloys

The effect of varying Mo concentration on phases formed in binary Ti-Mo alloys are presented in Table 2.4 below [76]. LPs are shown in Fig 2.15 in Angstroms for hot isostatically pressed (HIP) Ti-Mo alloy. The data contained in Table 2.4 and Figure 2.4 compare closely to those obtained in Refs. [71, 77-79].

Table 2.2. Phases and crystal structure of commercially pure Ti and Ti-Mo in the As-Cast State [76].

wt% Mo	Phase	Crystal structure
c.p. Ti	α'	Hexagonal
3–5	α'	Hexagonal
6	α'/α''	Hexagonal/orthorhombic
7.5	α''	Orthorhombic
9	α''/β	Orthorhombic/bcc
10–20	β	bcc

From Table 2.4, the atomic concentration of 9 and 15 Wt. % Mo converts to 4.70 and 8.09 at. % respectively. From Figure 2.4, LPs can be traced to be approximately 3.0625 and 3.3250 Å, respectively. Similar LPs were calculated for these alloys in Refs [80, 81]. In the studies of Ti-7.5 Wt. % Mo by Ji et al [82], LPs for α′′-martensite were calculated as a = 3.003, b = 5.035 and c = 4.680 Å. This result had some distortional influence of O in it. LPs for this phase was reported in Ref. [81] in a Ti-(22-24) at. % Nb as 3.140, 4.860 and 4.64 Å without O in the alloy. The different elements contained in the alloys do contribute to differences in LPs. Table 2.4 excludes the hexagonal ω-phase which also forms in Ti-Mo alloys as a metastable phase as stated in Section 2.2.1. Lyasotskaya et al. [71] reported a = 4.60, c = 2.80 Å, and c/a = 0.613 for ω-phase in a Ti-alloy with an isomorphous type β-stabiliser. These LPs were confirmed in Refs. [83-85].

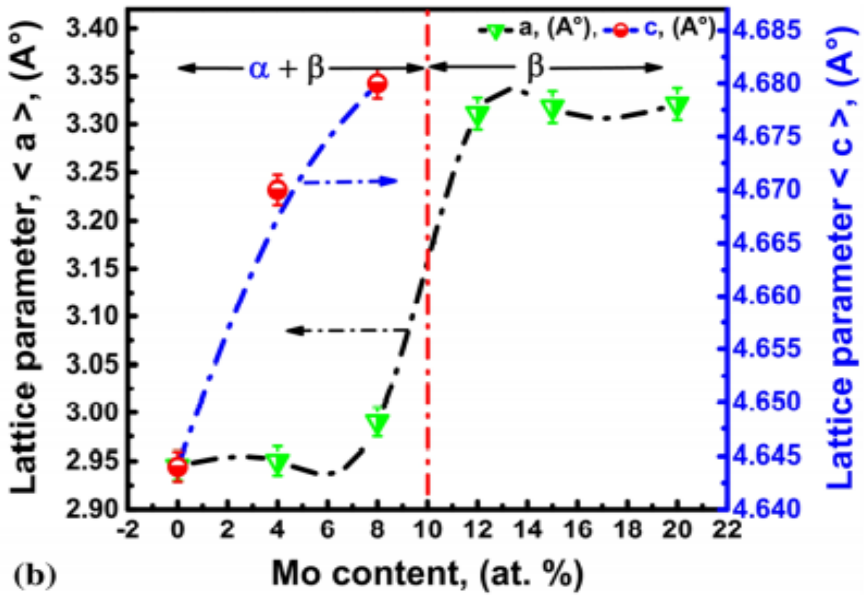

Figure 2.4. Lattice parameters (a and c in Å) of binary Ti-Mo alloys as a function of Mo content (at. %). Error bars indicate the standard deviation (SD) [78].

2.3 Post fabrication processing of β-Ti alloys

Conventionally, metastable bcc β-Ti alloys are thermo-mechanically processed to produce shapes for engineering applications and optimize mechanical properties by controlling the microstructure and phase volume fraction for target service conditions [67, 86, 87]. However, traditional processes such as forging, casting and other common techniques do attract a high cost [88]. This exorbitance is mainly associated with the necessity to use closed dies with inert atmosphere to prevent grain boundary oxidation at high temperatures. Die-coating for insulation which also increases cost significantly is unnegotiable in a hot extrusion process for which the Ti billet temperature is usually in the range 1000-1250°C [51]. More to the limitations of conventional processing is that progressive acidification occurring in the crevice during machining increases alloy's susceptibility to corrosion.

Metastable β-class of Ti alloys have ease of fabrication which implies excellent workability due to their lower β-transus temperature compared to the α+ β dual-phase Ti alloys, thus they are more easily forged, rolled, and extruded [50, 51, 53, 89]. This is due to the dominant bcc crystal structure which has as many as 48 slip systems and as a consequence deforms more easily than the hcp crystal

structure which has only 3 basal slip systems [52, 53]. They are deeply hardenable meaning that their strength can be improved upon significantly by solution treatment (ST) and ageing to attain uniformity in mechanical properties through thick sections of the alloy which is not the case for Ti-6Al-4V [50, 51]. As a result of these attributes, they are processed by hot near net-shape forging methods [50, 51, 53, 89]. In addition, these alloys may also be cold worked, a process which is performed at temperatures significantly below the β-solvus temperature [90]. Generally, the higher the MoE value and the bcc β-phase stability, the lower the β-solvus temperature which in turn reduces the hot deformation temperature used in the thermo-mechanical processing steps.

2.3.1 Heat treatment of β-Ti alloys

Williams R.E.A et al. [91] performed heat treatment on Ti-18Mo alloy according to the processing schedule shown in Fig 2.5. Samples were first homogenised in a vacuum furnace at 1000°C (above β-solvus temperature) for 0.5 hour and then quenched. Samples were subsequently reheated to 475°C which is approximately 50°C below the proposed ω-solvus temperature and isothermally held for 0.5 hour, 48 hours and 330 hours and then water quenched [91]. The as-quenched sample obtained after homogenising contains 3-5nm size ω_{ath}-precipitates [69, 70, 92-95]. Similarly, the formation of ω_{ath} on quenching or accelerated cooling in Ti, Zr and Hafnium (alloyed with V, Mo, Nb, Fe) [70] and Ti-15Mo-5zr [96] alloys has been reported. This phase is also reported in Ref. [35] in ST and quenched Ti-15Mo and Ti-16Mo as sharp reflections (Fig 2.6a) and circular diffused streaks (Fig 2.6b), respectively. Same author described the total disappearance of ω_{ath}-phase in ST-quenched Ti-17Mo (Fig 2.6c) and Ti-18Mo (Fig 2.6d) and attributed this occurrence to increase in β-phase stability.

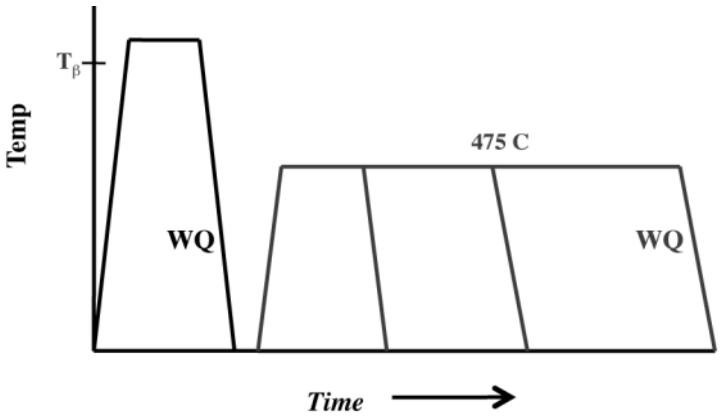

Figure 2.5. Schematic of heat treatment schedule for Ti - 18wt% Mo alloy [91].

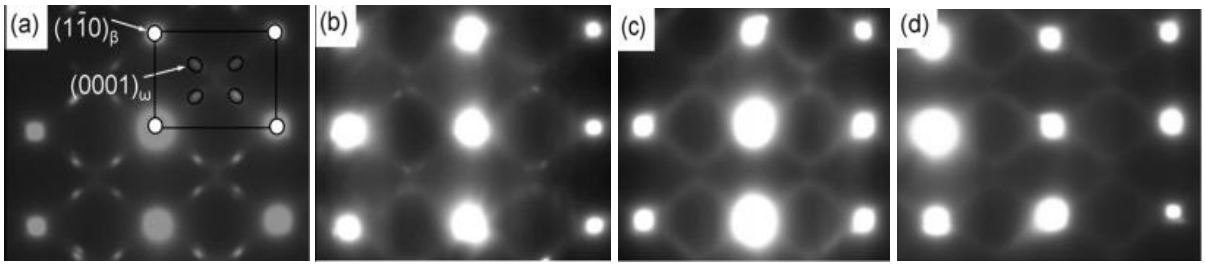

Figure 2.6. Selected Area Electron Diffraction patterns of Ti–Mo alloys subjected to ST and Quenching: (a) Ti–15Mo, (b) Ti–16Mo, (c) Ti–17Mo, (d) Ti-18Mo [35].

ω_{ath} forms by a displacive mechanism in shear. This happens by dislocation movement and has similar to parent phase composition. The same is true when embryonic-ω forms during holding [69, 70, 95]. This displacive mechanism proceeds by a partial collapse of one pair of $(111)_\beta$ planes to the intermediate position. The next $(111)_\beta$ plane is left unaltered within the bcc lattice [93, 97, 98] as illustrated in Fig 2.7 on Ti, Zr and Hf alloys [97]. This partial collapse may appear rumpled as shown in the centre schematic of Fig 2.7. The atomic displacements required are $\pm a_\beta \sqrt{3}/12$, where a_β is the lattice parameter (LP) of the β-lattice [93, 97]. The resulting crystal structure is trigonal [67, 69, 70, 95, 99]. Qazi et al. [100] similarly reported on Ti-35Nb-7Zr-5Ta-(0.06-0.68)O that the collapse of planes results from the interaction of linear defects. These authors stated that these defects are created from the displacement of atoms in the β-phase to 1/3-unit distance toward neighbouring atoms.

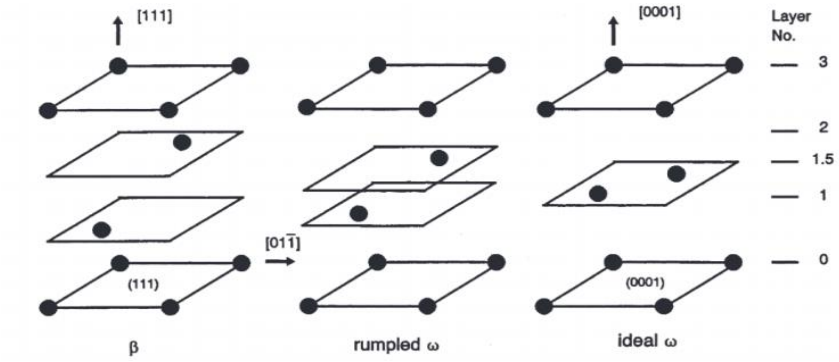

Figure 2.7. Lattice correspondence between β and rumpled ω and ideal ω phases based upon the (111)-plane collapse model. The ω-lattice can be obtained by collapsing one pair of the (111) planes within the β-lattice [97].

Embryonic-ω typically of 1-2nm length with partial collapse forms during cooling/heating or at the start of isothermal holding. As holding progresses or on longer heating, diffusion (e.g. diffusion of Mo in Ti-Mo alloys) takes place and embryonic-ω grows to form ω_{iso}-phase. This phase bears a different composition from that of the parent matrix [54, 101-103]. The full collapse along $\langle 111 \rangle_\beta$ transpires to form the fully developed ω_{iso} structure from embryonic-ω. This complete plane collapse will produce the ideal ω with $a_\omega = \sqrt{2}a_\beta$ and $c_\omega = (\sqrt{3}/2)a_\beta$ shown in the far-right schematic of Fig 2.7 [97], where a_ω and c_ω are the a-axis and c-axis LP of the hexagonal ω-lattice. Similar description has been presented by Samiee et al. [102] on Ti-10V-3Fe-3Al and Barriobero-Vila et al. [54] on Ti-10V-2Fe-3Al.

In isothermally aged at 475°C for 0.5 hour samples reported by Williams et al. [91], three crystallographic variants of ω_{iso} having diameter of 60nm formed. These variants correspond to the primary reflections, intense reflections at $1/3$ and $2/3\,[13]_\beta$ positions. The existence of crystallographic variants in ω_{iso} for Ti-Mo and Ti-V alloys is corroborated in [53, 104, 105]. As ageing time progressed to 330 hours, these precipitates grew and coarsened reaching a diameter of 100 nm. The growth of ω_{iso} took place by lateral motion of growth ledges as shown in Fig 2.8.

Deformation induced omega could form during cold working of as-quenched Ti-Mo alloys with Mo in the range from 1 to 18 Wt. % [27, 106, 107].

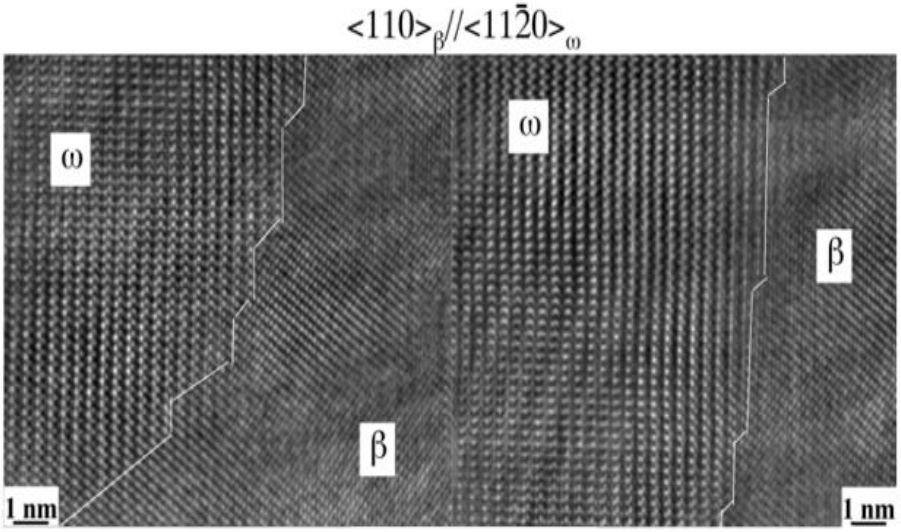

Figure 2.8. High Resolution TEM images of diffusional growth ledges present at the ω/β interface for Ti-18Mo. A gradual shrinkage of the β-phase area fraction is illustrated from left to right during in-situ observations at 475°C past 48 hours [91].

2.3.2 Thermo-mechanical processing of β-Ti alloys

Thermo-mechanical processing is broadly categorised into two steps by Weiss and Semiatin [87]. The first step is performed above the β-solvus temperature to break down ingot structure into a bar, rod or similar mill products [87]. The secondary step is performed just slightly above the β-solvus temperature (super-transus processing) or at the higher end of the α+β dual phase field (sub-transus processing) and involves a combination of heating, cooling and deformation such as isothermal forging to produce a shape that is near the final one to be used in an engineering application [87]. When hot deformation proceeds in the single β-phase field, the emerging alloy possesses high ductility with typically large β-phase grains as shown in Fig 2.9a [50] for Ti-10V-2Fe-3Al. The α-phase which forms along the β-phase grain boundaries may be continuous or short segmented depending on the cooling rate employed [86]. On the other hand when hot deformation is performed in the α+β dual-phase field as shown Fig 2.9b [103] for the same alloy, larger equiaxed globular primary α-phase particles are formed. These pin the β-phase grain boundaries limiting their growth during recrystallization thereby paving way for high strength alloys. The α-phase particles appearing in large volume on the β-grains when forging can be the Widmanstätten α-phase plates and there

exists an almost continuous grain boundary α-phase which indicates that the cooling rate after forging was relatively slow [103].

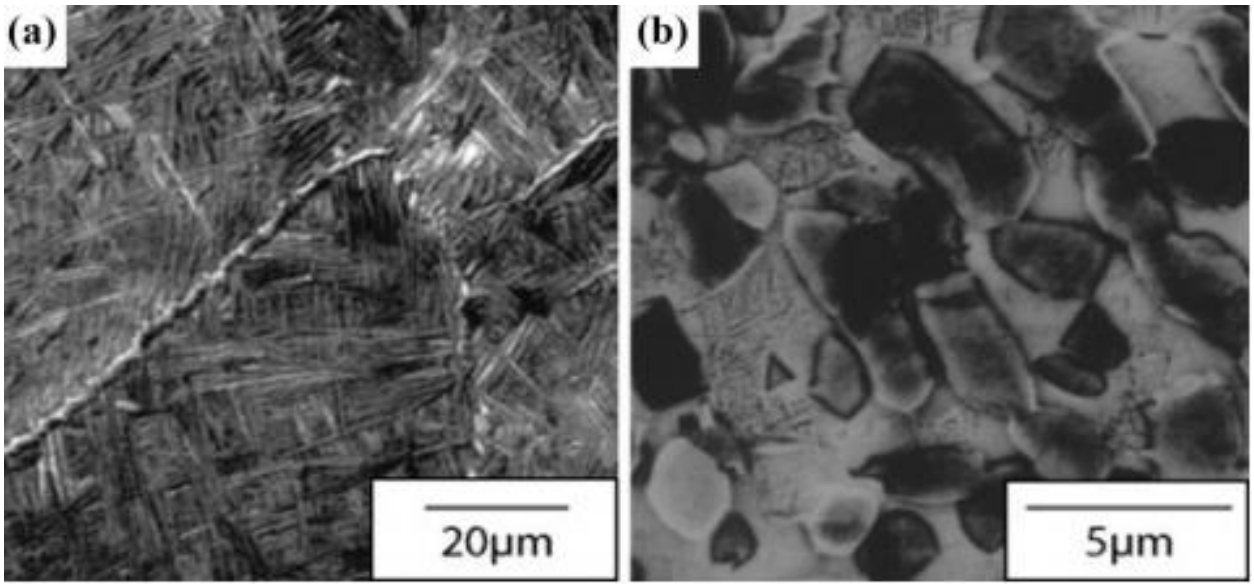

Figure 2.9. The difference in microstructures between hot forgings for Ti-10V-2Fe-3Al in a) the single β-phase field and in b) the α+β-dual phase field. The microstructure in (a) depicts large bcc β-phase grains with almost continuous grain boundary α-phase. The β-grains also contain a high-volume fraction of Widmanstätten α-phase plates. The microstructure in (b) depicts smaller bcc β-phase grains with some martensite and large globular primary α-phase particles [103].

As already stated, α-phase can form during cooling of Ti alloys from high temperature single β-phase field (termed primary-α) and on ageing of metastable β-phase (termed secondary-α). This can occur at any temperature below solvus line in solute-lean and solute-rich Ti alloys alike [51, 67, 108]. Both primary and secondary α-phases could nucleate on dislocations, grain boundaries, at the core of ω-phase and at heterophase interface of ω and β [20, 66, 67, 109-120]. Furuhara et al. [117], suggested that ω-phase assists nucleation of α-phase and this results in refinement by β-grain fragmentation. Ivasishin et al [121], Zheng et al [122] and Ahmed et al. [123] corroborated this claim. Samiee et al. [102] described a co-location of primary-α and ω_{ath} with a suspected nucleation at or near the ω_{ath}/β hetero-interface for a rapidly cooled metastable T-10V-3Fe-3Al as shown in Fig 2.10. Similar findings were reported by Prima et al [124] and Azimzadeh et al [125] for Ti-6.8Mo-4.5Fe-1.5Al

alloy as well as by Nag et al [110] and Ohmori et al [111] for Ti-5Al-5Mo-5V-3cr-0.5Fe and Ti-9.87V-1.78Fe-3.20Al β-Ti alloys, respectively. Tong et al. [112] aged Ti-6Cr-5Mo-5V-4Al at 500°C for 0.17 hours and concluded that nucleation and growth takes place at or near this heterophase interface which further validates the claim of Samiee et al. Ahmed et al. [89] aged Ti–5Al–5V–5Mo–1Cr–1Fe at 650°C for 1-8 hours and inferred nucleation of secondary α-phases at the core of ω_{iso}-phase.

Simply put, if nucleation is not observed in-situ it is not possible to find out whether α-phase is nucleated in β-matrix near ω, at interface or in the core of ω-phase as ex-situ images show only the later stage after nucleation has already materialized.

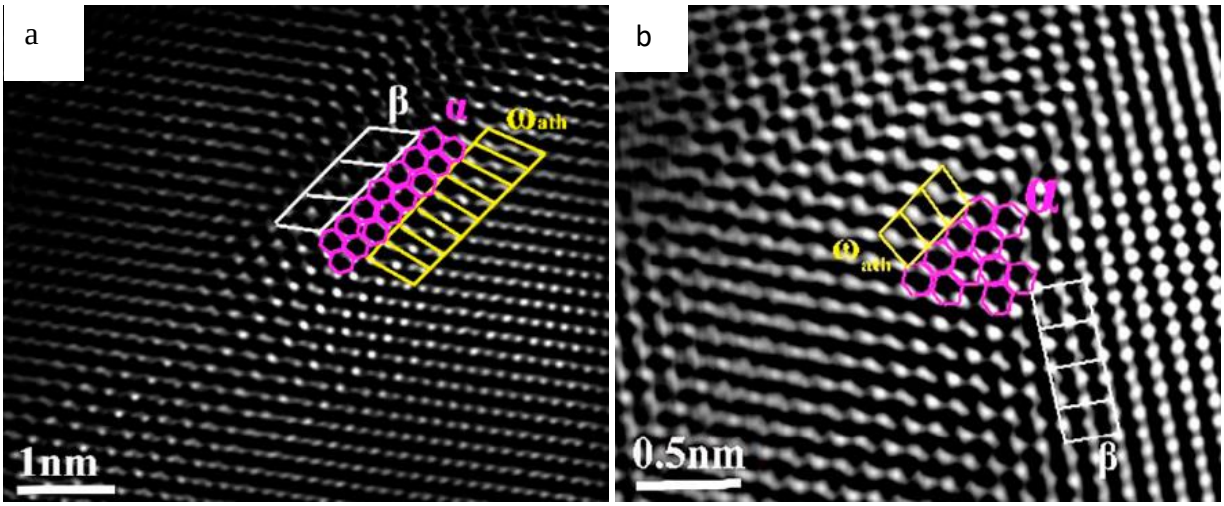

Figure 2.10 (a) and (b). Fourier filtered STEM-HAADF image with $[01\bar{1}]_{\beta}$ zone axis demonstrating co-location of α and ω_{ath} in β-matrix. Nucleation of α-phase is presumed to occur at the interface of ω_{ath}/β with orientation relationship corresponding to $[01\bar{1}]_{\beta}//[0001]_{\alpha}//[2\bar{1}\bar{1}0]_{\omega}$ [102].

Formation of α-phase is deemed to be by displacive-diffusional mechanism. During this process β-stabilisers diffuse out into β-phase and α- stabilisers diffuse into α-phase. This results in a significant variation in composition between α- and β- phases. In general, at temperatures between 420°C and 650°C the stable α-phase forms in metastable β-Ti alloys [51, 54, 67, 126] by one of three pathways: (I) from α''-phase plates which corresponds to Eq. 2.3, (II) from β-phase with assistance for nucleation by both ω_{ath} and ω_{iso} as expressed in Eq. 2.4 and (III) from the decomposition of the metastable β-phase expressed in Eq. 2.5 [54].

$$\alpha''_{lean} \rightarrow \alpha$$ Equation 2.3

$$\beta \rightarrow \beta + \omega_{ath/iso} \rightarrow \beta + \omega_{ath/iso} + \alpha \rightarrow \beta + \alpha$$ Equation 2.4

Alloys with MoE values of 10 or greater, such as Ti-13V-11Cr-3Al (Wt. %) with MoE of 23.3, exhibit the transformation sequence expressed in Eq. 5. The solute lean regions corresponding to β′ serves as nucleation sites for the secondary α-phase [50, 68, 95].

$$\beta \rightarrow \beta + \beta' \rightarrow \beta + \beta' + \alpha \rightarrow \beta + \alpha$$ Equation 2.5

Generally, three morphologies of α-phase can form in Ti alloys. Two of these include allotriomorphic (Grain Boundary-α) and Widmanstätten side-plates-α (shown in Fig 2.11a and b using Ti–24Nb–4Zr–8Sn [59] as an instance). The third is a lamellar morphology and it forms intragranularlly within a single β-grain as shown in Fig 2.11c. This image is for Ti-5Al-4Mo-4Cr-2Sn-2Zr [127] and multiple crystallographic variants of α-phase are denoted by different colours. When allotriomorphic α-phase forms, it is harder than β-phase. However, neighbouring β-regions may become even softer. This depends on the amount of α- and β-stabilizers in the phases. These solutes and vacancies taken into the boundary could cause β-phase to be depleted [20, 116, 117]. This softening effect bears negatively on mechanical properties such as ductility and fatigue crack nucleation. It may be prevented by slow cooling of the alloy from the single β-phase field and isothermally holding in the dual α+β phase field [20, 116, 117]. Widmanstätten α-phase is believed to form stochastically from the allotriomorphic belonging to the same variant or a different variant [20, 116, 117].

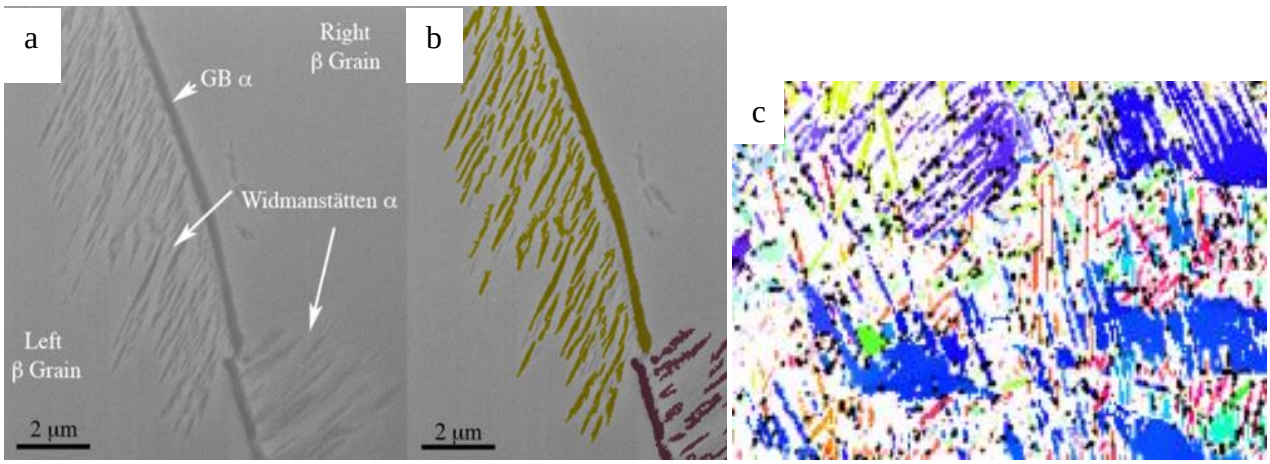

Figure 2.11a. SEM micrograph of allotriomorphic grain boundary α and Widmanstätten α for Ti–24Nb–4Zr–8Sn; (b) Pseudo-colour overlay representing different variants of α-phase [59]; (c) Multiple crystallographic variants of α-phase within a single β-grain [127].

Two types of martensitic phases which form in Ti alloys are the α′- and the α″-phases [3, 50, 51, 56, 128]. The α′-phase formation initiates at a higher martensite start temperature than that required for α″-phase. The start-temperature depends on the composition of the specific Ti alloy [3, 50, 51, 56, 77, 128]. α′-phase forms in α, near-α and α+β classes of Ti alloys where MoE ranges from 0 to 5 [3, 50, 51, 71, 77, 78, 128, 129]. Transition from α′ to α″ occur with increasing β-stabilising content as shown in Figure 2.2. The critical solute content at point of conversion, similar to transformation start-temperature, depends on the composition of the alloy [3, 50, 51, 71, 77, 78, 128]. This critical solute content is believed to be about 3.2 Wt. % for Ti-Mo binary systems [71, 78, 79]. Hence, the emphasis is on α″-martensite since the alloys studied in the current work contain 14.12 ± 0.69 Wt. % Mo.

The α″-martensite may have a lath or plate/lenticular morphology. It forms in Ti alloys by a diffusionless mechanism. Ti alloys composed of isomorphous type β-stabilisers such as (V, Nb, Ta and Mo) and quasi-isomorphous type β-stabilisers which includes (Re, Ru, Os and Rh) favour its formation. In Refs. [51, 62, 71, 128] it was stated that at RT or above, martensite formation is completely suppressed at MoE values in the range from 10 to 30. Figure 2.12c and d clearly show the presence of a single β-phase at RT for Ti-15Mo and Ti-20Mo [75]. α″-martensite could form from the parent β-phase in a shear mechanism following three possible routes:

1. Formation of α′′on quenching of β: β→α″ [51, 67, 71, 77, 109, 128].
2. Decomposition of metastable β-phase by intermediate transformation during isothermal ageing, e.g., through β→β (lean) + β (rich) →α″ + β (rich) pathway. In addition, a short-time holding of the metastable β (e.g., 30 s), at either the ω-formation temperature or at a higher temperature but just before the α-phase forms (through lattice softening), can facilitate the subsequent β→α″ transformation on quenching [51, 56, 67, 71, 87, 118, 130].
3. Stress-induced transformation of metastable β: β→α″ + (twinned) β [44, 51, 52, 71, 128, 131, 132].

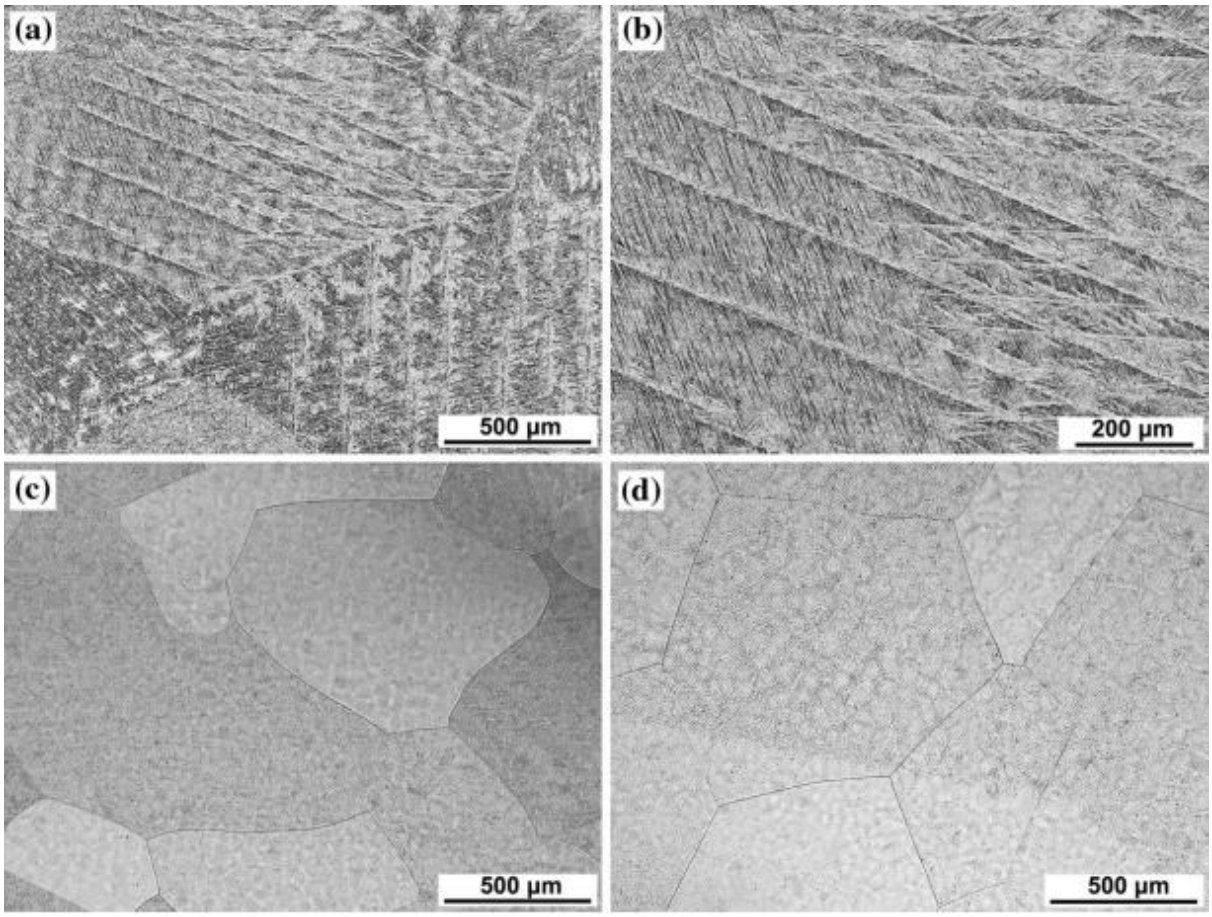

Figure 2.12 (a) and (b). Optical micrographs of Ti-10Mo; (c). Ti-15Mo; (d) Ti-20Mo alloys. Alloys ST to 1000°C for 3.6 x 10-3 s and then quenched [75].

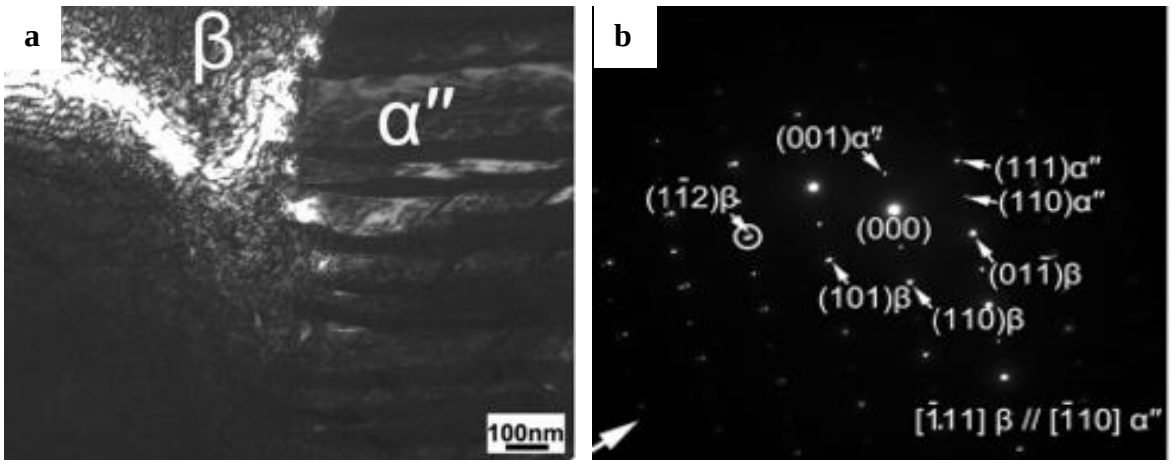

Figure 2.13a. TEM image containing α''-plates and β-matrix; b. Selected Area Electron diffraction (SAED) patterns of α''-plates and β-phase along $[\bar{1}10]$ and $[\bar{1}11]$ zone axes, respectively. This is a representative SAED for martensite shown in Figure 2.12a and b [75].

The β/α″ orientation relationships were presented earlier in this chapter and further illustrated in Figs. 2.3b and 2.13b. Six equivalent crystallographic α″ variants could form on quenching or during deformation and they are listed in Table 2.2. Realisation of three crystallographic variants was reported by Duan, R et al. [133] in Ti-12Mo-6Zr-2Fe (Figure 2.14). In Ref. [134], invariant plane strain theory was used in predicting the corresponding twelve habit plane variants (Table 2.3).

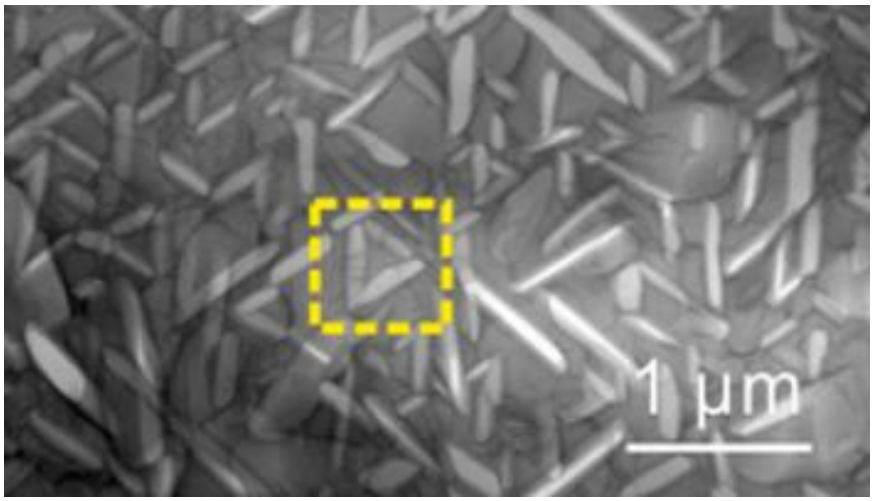

Figure 2.14. 60° rotation of variants of α''-phase along the $[1\bar{1}1]_\beta$ zone axis for Ti-12Mo-6Zr-2Fe [133].

Table 2.3. Six lattice correspondence variants (CV) derived for the β and α''crystals [134].

Variant	$[100]_{\alpha''}$	$[010]_{\alpha''}$	$[001]_{\alpha''}$
V1	$[100]_{\beta}$	$[011]_{\beta}$	$[0\bar{1}1]_{\beta}$
V2	$[100]_{\beta}$	$[0\bar{1}1]_{\beta}$	$[0\bar{1}\bar{1}]_{\beta}$
V3	$[010]_{\beta}$	$[101]_{\beta}$	$[10\bar{1}]_{\beta}$
V4	$[010]_{\beta}$	$[10\bar{1}]_{\beta}$	$[\bar{1}0\bar{1}]_{\beta}$
V5	$[001]_{\beta}$	$[110]_{\beta}$	$[\bar{1}10]_{\beta}$
V6	$[001]_{\beta}$	$[\bar{1}10]_{\beta}$	$[\bar{1}\bar{1}0]_{\beta}$

Table 2.4. The predicted 12 habit plane variants for α'' in a Ti–20 at. % Nb alloy [134].

Variants	Habit plane	
	(+)	(−)
1	$(0.6995, 0.5057, 0.5049)_{\beta}$	$(0.6992, -0.5055, -0.5056)_{\beta}$
2	$(0.6995, -0.5049, 0.5057)_{\beta}$	$(0.6992, 0.5056, -0.5054)_{\beta}$
3	$(0.5049, 0.6995, 0.5057)_{\beta}$	$(-0.5056, 0.6992, -0.5054)_{\beta}$
4	$(0.5057, 0.6995, -0.5049)_{\beta}$	$(-0.5054, 0.6992, 0.5056)_{\beta}$
5	$(0.5057, 0.5049, 0.6995)_{\beta}$	$(-0.5054, -0.5056, 0.6992)_{\beta}$
6	$(-0.5049, 0.5057, 0.6995)_{\beta}$	$(0.5056, -0.5054, 0.6992)_{\beta}$

It is established that in conventionally processed alloys, α″-martensite decreases ductility and strength due to its softening effect [51, 75, 128]. However, when this phase forms in β-phase under mechanical load, it leads to dynamic Hall-Petch phenomenon and increases UTS. This phenomenon describes a decrease in mean free path for dislocation movement in the β-phase caused by α″-martensite which acts as a barrier [51, 75, 128]. This results in grain refinement and a concomitant increase in ductility due to TRIP effect [25, 135]. It has been interestingly observed that Ti alloys with Wt. % Mo of 3.2 and 8 yielded very close stiffness values of 83.8GPa and 82.983GPa, respectively [71, 78, 79]. These studies identified 4.5 Wt. % Mo addition as required one for the martensitic transformation to take place. This thereby makes the presence or disappearance of α″-martensite inconsequential as far as E-Mod is concerned. However there has been an opposing claim by Ho et al. [76], Davis et al. [136], Bania et al. [137] and Bagariatskii et al. [138] regarding martensitic formation only in the range 6-10 Wt. % Mo.

2.4 Additive Manufacturing of metastable β-Ti alloys

AM is also known as free form fabrication and rapid prototyping [139] among other synonyms. It describes a materials processing method in which a three-dimensional (3D) part/compotent is first created in a Computer Aided Design (CAD) application. This is followed by a conversion to a stereolithographic (STL) file and then produced in a 3D-printer in a layer by layer deposition of a specific material until the desired geometry is attained [139]. AM has been used in recent years not just for prototyping purposes but more importantly for manufacturing of functional products in the biomedical, aerospace and automotive industries [1, 2, 139-142]. When compared to coventional wrought or casting processes, AM techniques which include SLM, Electron Beam Melting (EBM) and Laser Engineered Net Shaping (LENS) among others, present many advantages. Some of these benefits are unique to a particular AM technique as listed in Table 2.5. Primary benefits include shorter lead times in near-net shape component production, reduced manufacturing cost due to efficient usage of feedstock materials without the need of tooling [3] and elimination of waste [143, 144]. Other benefits are manufacturing of parts from hard to machine materials such as refractory metals, ceramics and composites (e.g. V, Mo, V, W and etc) [3], greater design flexibility and higher level of compositional control and product customisation [145]. However, in order to expand industrilisation and commercialisation of AM technologies, there are accompanying challenges which have to be overcome. An instance to the said limitations is the lack of mastery over the grain structure which often bears higher average porosity and surface roughness than its conventionally procesed version. This can be directly linked to the solidification process where there also exists a high tendency for texturing as a result of rapid reheating and directionality of the dissipiated heat [1, 2, 139, 142, 146, 147]. This alternating heating and cooling schedule in a typical AM process introduces residual stress to the alloy. Inducement of partial remelting due to high thermal gradient, high cooling rates and complex thermal cycles which can lead to inhomogeneity of morphology of the final product is another example of a limitation [2, 139, 144-148]. On a more generic scale, this limitation is illustrated in the fact that not all commonly used materials may be suitable for

manufactring by AM [141]. Furthermore, the parts being manufactured as a neccesity have to be smaller than the available platform or chamber in AM systems [149]

Table 2.5. Comparison of AM techniques.

AM Technique		Feedstock	Feedstock Delivery	Energy Source	Advantages	Limitations	Ref.
Powder-Bed Fusion	Selective Laser Melting	Metal powder-bed Feed System	Pre-spreading powder	Laser	▪ Low surface roughness ▪ High dimensional accuracy ▪ Good finishing of 8-10 μm ▪ Relatively low maintenance cost ▪ Can be used for a variety of materials including hard polymer, ceramic and metals ▪ Low Substrate plate temperature ($\sim 200\ ℃$) and high cooling rate results in formation of verfy fine β-phase dendrites implying a reduction E-Mod of the structure to ($\sim 0.95 \pm 0.05$ GPa) ▪ Presence of β-phase dendrites yields higher compressive strengths ($\sim 50 \pm 0.9$ MPa) than EBM processed sample	▪ Smaller spot size results in a deeper keyhole caused by radiation reflection thereby leading to deeper melt pool in SLM ▪ Number of defects in SLM samples is ~ 10 times that of EBM samples	[3, 145, 150, 151]
	Electron Beam Melting	Metal powder-bed Feed System		Electron	▪ Since the EBM samples contain less number of defects, they have higher and less variable fatigue life ▪ Good finishing of 15-20 μm	▪ High powder bed temperatures ($\sim 500\ ℃$)and relatively slow cooling rates leads to α+β microstructure and increased E-Mod of porous samples ($\sim 1.34 \pm 0.04$ GPa ▪ Applies only to conductive materials because it is essential for the powder to pull the electron from the gun	[3, 145, 150, 151]
Direct Metal Deposition	Direct metal powder deposition	Metal powder	Powder spray into gas delivery nozzle	Laser, plasmer, or electron beam	▪ High wear resistance and hardness when compared to conventional methods	▪ Significant microstructural inhomogeneity ▪ Fabricated metal parts need more machining than the powder bed or powder feed systems. This is due to higher surface roughness and lower dimensional accurqacy.	[3, 145, 150, 151]
	Direct metal wire deposition	Metal wire	Delivery nozzle		▪ Large build volumes can be rapidly produced in a cost-effective manner ▪ Insitu alloying ▪ Production of functionally graded parts	▪ Fabricated metal parts need more machining than the powder bed or powder feed systems. This is due to higher surface roughness and lower dimensional accurqacy.	[3, 5, 145, 150, 151]

AM technologies can be grouped into two broad categories based on the approach to feedstock delivery. These include Powder Bed Fusion which utilises a pre-spreading powder delivery system and Direct Metal Deposition (DMD) which employs a nozzle spray system [3, 139, 142]. Figure 2.15 shows the different techniques under each AM category.

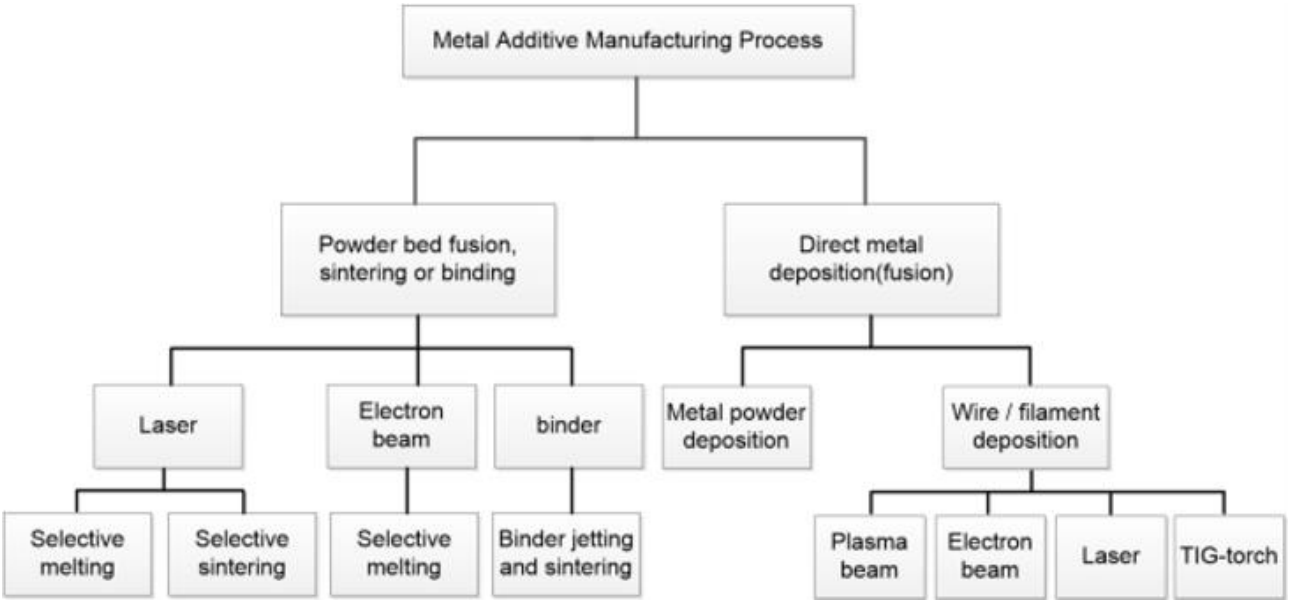

Figure 2.15. Summary of metal additive manufacturing techniques where TIG is an acronym for tungsten-electrode inert gas [3].

The LMD process used in the manufacture of the alloy studied in this work is not as widely used as the SLM and EBM techniques. As stated in Chapter 1 of this thesis, to the best my knowledge there exists extremely limited data on microstructure of LMDed Ti-Mo in literature. SLM and EBM which both utilize powder feed materials are the most popular AM techniques used across multiple industries [1-3, 139-141, 144, 151, 152]. The reason for this is that they yield high dimensional accuracy requiring very minimal post-fabrication machining [1-3, 139-141, 144]. SLM is more widely accepted than EBM for many reasons. These include lower maintenance cost of the manufacturing infrastructure, better surface finishing with roughness of 8-10μm and lower E-Mod of final product [3, 153].

2.4.1 Direct Metal Deposition

DMD which covers the LMD process used in the current study is advantageous in repairing worn components [154]. This technique is also used in producing customised parts such as medical implants and functionally graded materials [155]. The feedstock can either be powder or wire and energy can be supplied from plasma, electron beam, laser or electrick arc. Since powder was used as feedstock in the current work, this will be described in more details in the following section.

2.4.1.1 Direct Metal Powder Deposition

This process is similar to the LENS^{TM} technique developed at the Sandia National Laboratries [156]. The powder is delivered by a powder feeder which sprays powder into a gas delivery system via specialised nozzles. The high energy laser beam is delivered along the z -axis in the center of the nozzle and subsequently focused by a lens very closely to the work piece [157, 158]. A schematic of direct metal powder deposition system is shown in Fig 2.16. In these systems, powder is delivered through a nozzle onto the substrate. A laser is employed to melt the powder. This process is repeated until the desired 3D shape is achieved.

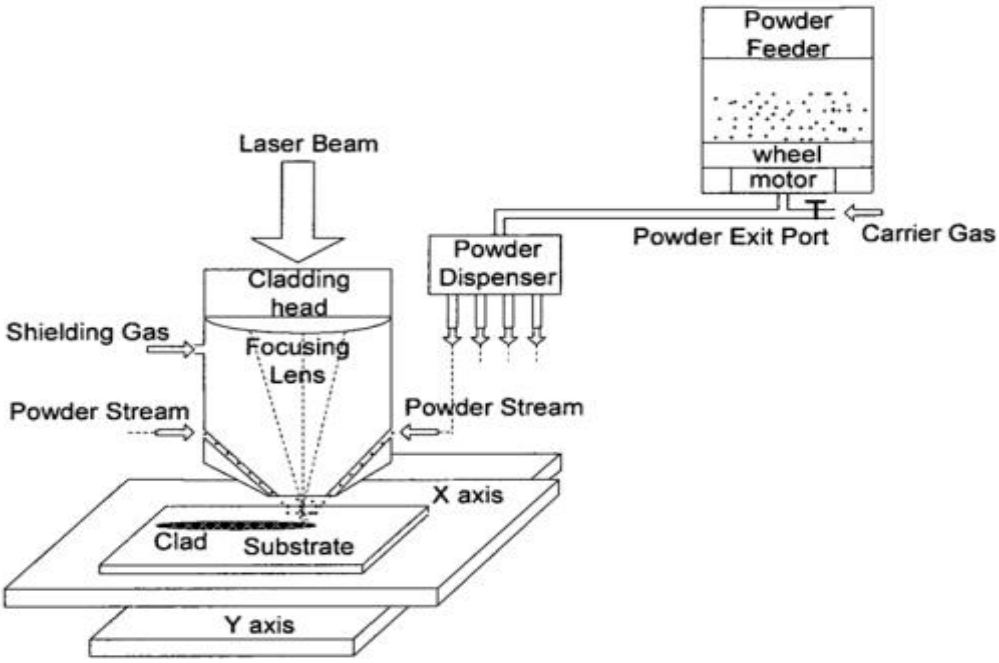

Figure 2.16. Schematic of direct metal powder deposition system [159].

2.4.2 Electron Beam Melting

Karl-Hienz Steigerwald designed and built the first electron beam welding machine in 1958 [2]. An EBM process uses high electron beam to introduce fusion in metal powders in a manner which guarantees great shape control and gives high specific strength property [152, 160, 161]. Fig. 2.17 below shows a typical EBM system which consist of an electron gun with an operating power of 60 KW for generating a focused beam of energy density above 100 KW/cm2 [1]. A powder layer consisting of 100μm is spread over the table for building the part. The electron beam first pre-heats the powder layer with a high scanning speed as a step before powder layer melting occurs based on CAD file geometric specifications [142].

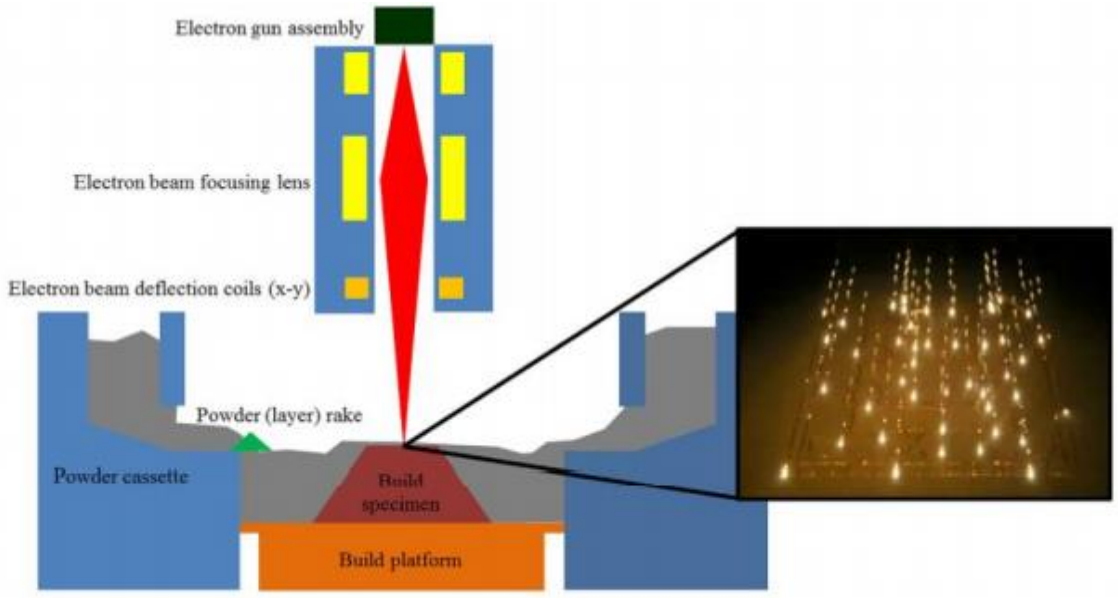

Figure 2.17. EBM system which shows the electron beam scanning the powder [1].

This process is highly susceptible to atmospheric interference and is normally operated under vacuum conditions [1, 2, 152, 162, 163]. The materials used for the cathode tip are normally W or Ti because there so few materials that can meet the requirements [1, 2, 150, 152, 160, 162, 163]. To achieve high power densities the cathode is operated at high temperatures to increase the number of electrons with sufficient kinetic energy to overcome the potential barrier and move into the conduction zone and escape the lattice [1, 2, 150, 152, 162]. While operating at elevated temperatures and under vacuum conditions the cathode material must have a low enough vapor pressure to ensure an acceptable tool

life [1, 2, 162]. Operation under vacuum conditions limits the delivery options of feedstock material and many electron beam systems use pre-alloyed wire feedstock for this reason [1, 2, 162]. The microstructures, defects and mechanical properties of EBM-processed alloys are presented later in this report.

2.4.3 Selective Laser Melting

SLM is a powder bed fusion AM process for complex 3D metal-part fabrication via a layer-wise selective melting system which do not require a vacuum to operate [59, 153, 164-167]. The laser is transmitted from the source to the weld head via fiber, reflective lenses or a combination of the two [139]. Once laser beam reaches the enclosure, it is then directed downward to the weld head and through a final focusing lens [139]. The final focus is done at the weld head to keep the focal point fixed in relation to the component being built as its height increases [139]. This process typically employs a CO_2 laser to create a dense region in one layer from pre-spread powder in the bed and joins the regions in each layer in a layer by layer process [140, 141, 153, 165-169]. A thin layer of loose powder is intitially evenly spread across a processing platform to form a powder bed. As shown in Fig 2.18, an inert gas (e.g. argon) passes over the bed as a protective measure from oxidation and to clear any spatter and metal fumes from melting metal [141, 152, 165, 167, 168, 170]. The laser energy source is programmed to repeatedly deliver energy to the surface of the bed to selectively melt the powder until the desired 3D configuration is attained [152, 165, 168]. This is achieved by isolating selected areas in the powder bed to be melted and consolidated with a line-by-line fashion by scanning laser. As soon as a specific layer is formed the building platform is lowered by the programmed layer thickness [152, 165, 168]. New loose powder is subsequently spread by a powder suppling mechanism and melted on top of the layer below [59, 165, 167, 168].

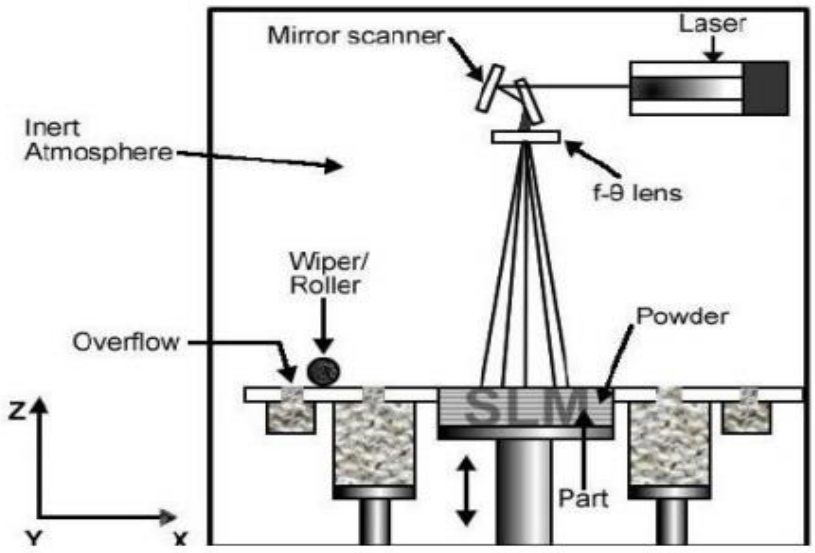

Figure 2.18. Schematic diagram of a generic SLM process [171].

The intricacies involved in metalurgical processing during an SLM process are goverened by 2-levels of factors, firstly the the powder characteristics and secondly the processing parameters [140, 172, 173]. Influencing powder characteristics include chemical components, particle shape, size and its distribution, packing density and flow properties. Processing parameters such as laser power, laser scanning speed, spot size, hatch spacing and layer thicknes have to be carefully selected [140, 172, 173] for superior physical and morphological features. Relationship between these parameters is expressed in Eq. 6 below [142]-

$$E = \frac{P}{v} \times h \times t \qquad \text{Equation 2.6}$$

where E: energy density (J/mm^3), P: laser power (W), v: laser scanning speed (mm/s), h: hatching distance (mm), t: layer thickness (mm). During SLM, alloy deposition is done in layers with pre-determined dimensions. This deposition method leads to the existence of inter-layer fusion lines. The temperature profile generated in a specific layer causes remelting of portions of the previous layer. This determines the emerging grain structure, sizes and boundaries. Remelting and solidification of previously deposited layer leads to the occurrence of intra-layer fusion lines. Solidification rate is therefore a crucial commodity in predicting final mechanical properties of the alloy. Ren et al [174] developed a microstructure selection map (Figure 2.19) for Ti-6Al-4V manufactured by Laser Solid

Forming (LSF). This can be used to predict the microstructure evolution and relative grain size under different thermal gradients and solidification growth rates. It was noted that an increase in scanning velocity of the AM process led to an increase in thermal gradient and solidification growth rate. The crystallographic orientation and the grain size of the substrate greatly affects the microstructure and growth of the deposit during the AM process. Therefore the microstructure of various layers would change the trend of the relationship between the linear input energy density and the width of the prior β-grains. The deposit grows epitaxially from the substrate in the initial stages [175], implying that nuclei will have the same lattice structure and orientation as the grains at the solid-liquid surface of the base metal. At this stage, crystal growth is very slow forming first a planar and then a fine cellular substructure. The intermediate stage of crystal growth is cellular-dendtritic leading to coarse columnar crystal growth in the ⟨100⟩ direction. Final stages is associated with rapid crystal growth and marked segregation. Depending on welding conditions, final dendritic structure can be equiaxed [176]. Thermal dendritic structure is shown in Fig. 2.20.

In layers where there exists a rapid solidification rate and high thermal gradient, columnar grains develop and mechanical properties are anisotropic. Very often, solidification rate will be too rapid to allow substantial diffusion in the solid phase [176]. This creates a solute poor zone underneath the intra-layer fusion line. This solute poor zone is usually in form of an alternating solute sequence occuring as lines having width in the range 1-4 μm. Another consequence of rapid solidification can be that local equilibrium at the solid/liquid interface breaks down [176]. Generally, one or all of three different zones can be distinguished during solidification. These are (i) A zone of equiaxed crystals which results from slow solidification rates, (ii) a columnar zone of elongated or column-like grains and (iii) a transition zone mixed equiaxed and columnar grains. During solidification in alloys with wide freezing range, the interdentritic channels close up and liquid flow is inhibited so that the last pools to solidify leave small voids or pores. Large differences in composition can arise across the denrites due to coring and the formation of non-equilibrium phases in the last solidifying drops of liquid. Four factors can lead to solute segregation during SLM by causing mass flow over large

distances during solidification [176]. These are (i) shrinkage due to solidification and thermal contraction, (ii) density differences in the interdentritic liquid, (iii) density differences between the solid and the liquid and (iv) convection currents driven by temperature-induced density differences in the liquid [176].

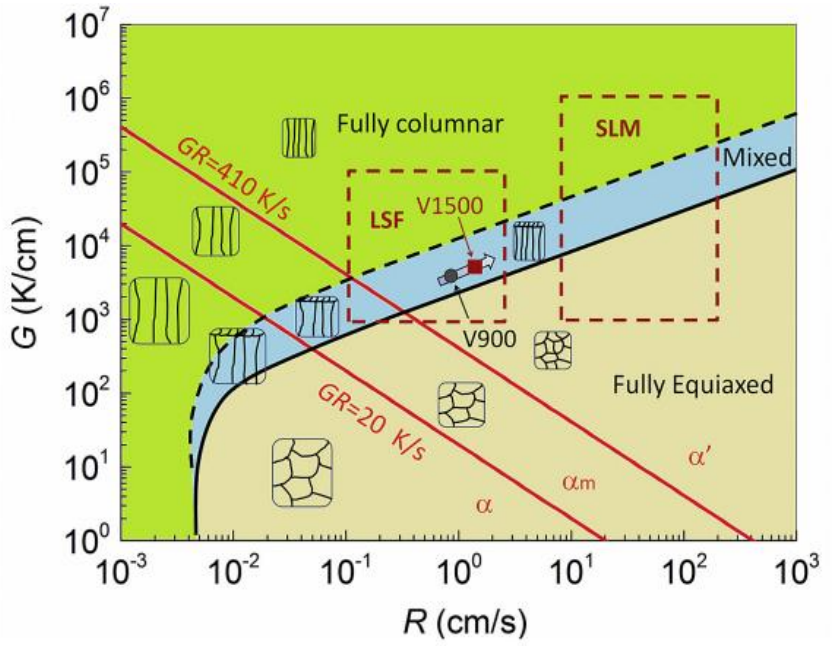

Figure 2.19. A modified microstructure selection map of Ti-6Al-4V alloy by additive manufacturing. GR represents the cooling rate. The critical value of the cooling rates (410 and 20 K/s) derived from ref [177], while the columnar to equiaxed transformation curves cited by reference [178]. The $\alpha', \alpha_m \; and \; \alpha$ denote martensite, massive α and α phase, respectively. The hollow arrow denotes the direction of the scanning velocity increased [174].

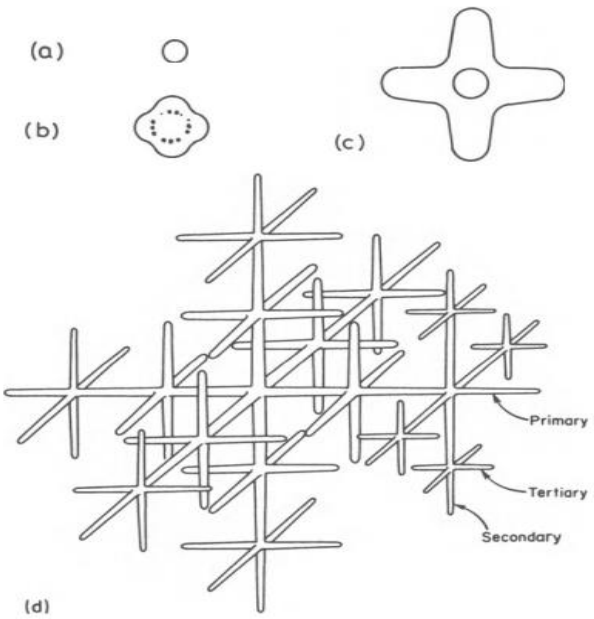

Figure 2.20. The development of thermal dendrites: (a) a spherical nucleus; (b) the interface becomes unstable; (c) primary arms develop in crystallographic directions ⟨100⟩ in cubic crystals); (d) secondary and tertiary arms develop (after R.E. Reed-Hill, Physical Metallurgy Principles, 2nd. edition., Van Nostrand, New York, 1973) [174].

Mebed et al, suggested that a miscibility gap on the high solute side is the reason for segregation which can occur by spinodal decomposition upon quenching [179]. The spinodal mechanism involves homogeneous decomposition of a parent phase by small compositional fluctuations [180]. This leads to either the solute depleted or solute-rich regions transforming to a product phase of a different symmetry. Conditions for spinodal decomposition is illustrated in Figure 2.21 and can be explained on the basis that the nominal composition of the parent phase must lie near the intersection point ($C_0(T)$) of the free energy-composition curves for both parent and product phases. This must occur on the side where the free energy of the parent phase is lower than that of the product phase. Then it becomes feasible that small compositional fluctuations will drive the composition in certain regions of the parent phase to the oposite side of the intersection point [180]. This idea was supported in Refs [181, 182]. In Ref [181] it was also mentioned that the atomic concentration limit of Mo, for spinodal decomposition to occur is 17 at. %.

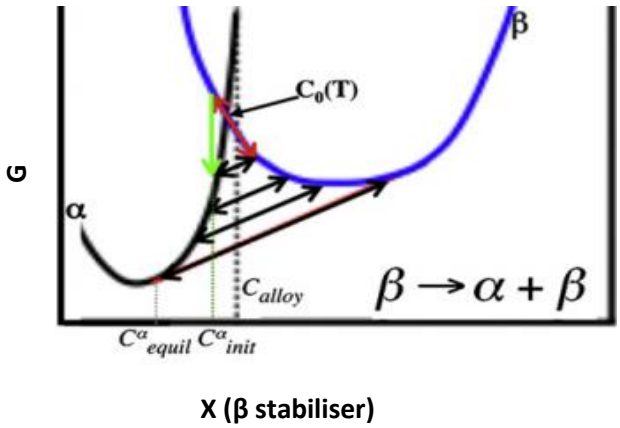

Figure 2.21. Schematic Gibbs free energy vs composition (G-X) plots for the β and α-phases in Ti5553 where at 600°C the C_0 (T) point is close to the nominal alloy composition X_0. The red arrow indicates the range of the possible compositional fluctuations. The green arrow indicates that, for fluctuations that cause the local composition to be less than the C_0 (T) point, transformation from the β-phase directly to the α-phase would be favorable [180].

2.4.4 Defects in additively manufactured Ti- alloys

The lack of acceptable level of adroitness which the user currently has over the evolving microstructure of an AM processed part manifests in forms of dents, keyhole defects and substantial total porosity. Lack of microstructure control is also seen in surface roughness and a quantity termed process-introduced residual stress which is observed in-service where material shows a tendency to fail below its rated mechanical capacity [1, 2, 140, 141, 144, 148, 161]. These surface imperfections are shown in Fig 2.22a-d and it can be observed that the shape of the defects differ between EBM and SLM processed alloys [150]. It is therefore reasonable to state that the manner in which deformation is accommodated must also be different [78]. EBM samples tend to contain spherical defects whilst the SLM sample contains both conical and spherical pores [2, 140, 141, 144, 152, 168]. The shape of voids in EBM samples have been associated to both defects in powder used and metal vaporization [84]. Imperfections found in SLM samples have been connected with intensity of spatter (ejected material) which fluctuates periodically and can interact with the laser radiation resulting in shadowing of the laser and defect formation [85, 86].

From Fig 2.22e it can be seen that the defect count for SLM-processed alloys out-number those for EBM-processed alloys in each size group except for the group between 100 μm and 120 μm [150]. Inspite of this, the strength of the SLM alloy is superior to that of the EBM one. This must point to the fact that defects accrued from the fabrication process has no direct correlation with the strength of the alloy. Contrary to expectation, SLM-alloy exhibits better ductility in the same study. As a general consequence of these defects, mechanical properties such as E-Mod, YS, UTS and impact toughness are significantly lowered in AM-processed alloys compared to conventionally manufactured alloys with the same concentration of Mo [76, 183-185]. The differences in fabricated β-grain size, arrangement pattern and distribution densities of evolving phases do contribute to the disparity in mechanical properties. Nan et al. [185] manufactured Ti-7.5Mo sample using LPBF and the microstructure bore conchoidal two-phase structure made of Mo-poor α-Ti and Mo-rich β-Ti but did not contain α″-martensite. Furthermore, the large-sized Mo particles were only partially melted which led to the values of E-Mod, (UTS) and strain at failure of 70 GPa, 740 MPa and 9.2%, respectively. The fracture mechanism started in the brittle mode for scanning speed of 1000 mm/s and gradually switched to ductile failure at a higher scanning speed of 1700 mm/s [185]. The observed porosity was highly dependent on scanning speed and ranged from 1% to 15% corresponding to 1000 mm/s and 1700 mm/s scanning speeds as shown in Figure 2.23 (a) and (b). This is very much unlike its conventionally processed version reported by Chen et al. [183] in which the presence of α″-martensite was confirmed in the quenched state after ST. α′and β co-existed in the aged state and the E-Mod fell in the range 100-110 GPa (which is undesirably higher than the AM-processed alloy). In the same condition, UTS was 1050 MPa with an elongation of about 29%. Similar results confirming the formation of α″-phase with higher strength and elongation were reported by Ho et al. [76] on the as-cast version of the same alloy and by Chung et al. [184] in the cold rolled alloy. Therefore, lower values of E-Mod are characteristic of AM-processed alloys relative to conventionally processed ones. This is predominantly due to the presence of more pores in the AM-alloys and to a much less degree due to the varying microstructures. This is validated by the absence of α″-martnesite in the reported

AM alloy as the presence of this phase is proven to decrease E-Mod in conventionally processed alloys [58, 186]. Lower ductility reported in the AM-alloys has also been impacted by the total porosity. From a strength and ductility perspective, AM-processed alloys would perform better with post-fabrication heat treatment which could unacceptably increase the E-Mod concomitantly.

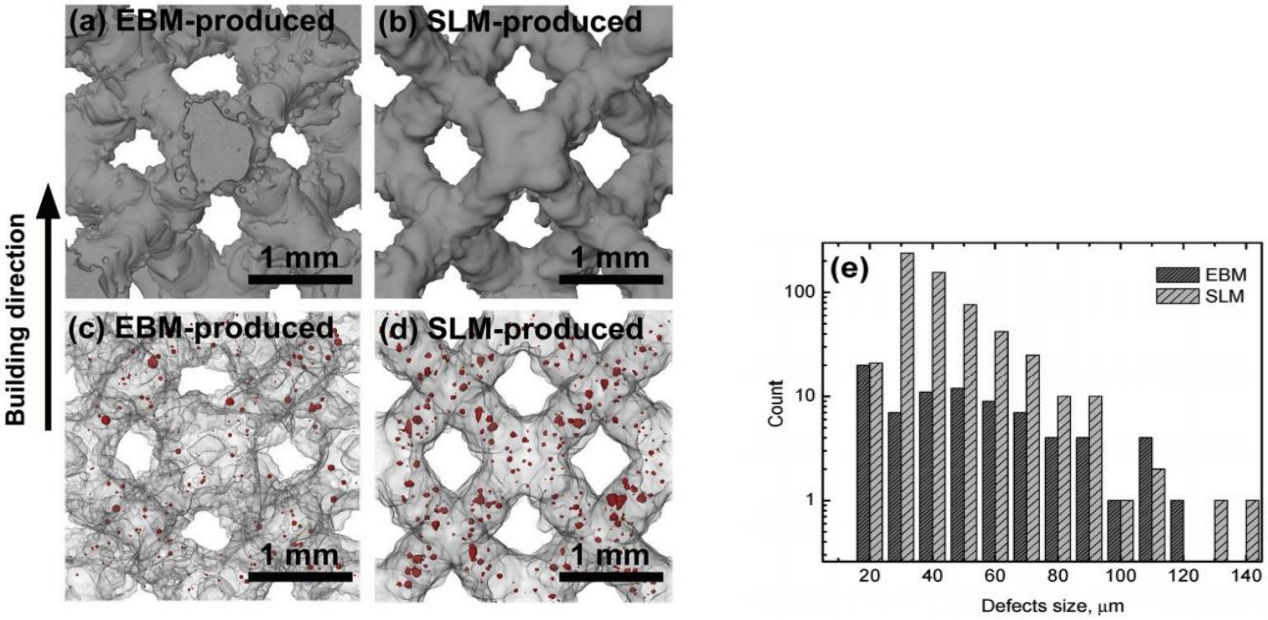

Figure 2.22. The micro-computed tomography reconstructed images showing the strut outside surface of a) Electron Beam Melting (EBM) and b) Selective Laser Melting (SLM) samples. The defects inside of the solid struts of c) EBM and d) SLM samples. e) The size and count distribution of defects inside AM samples as a function of equivalent diameter [150].

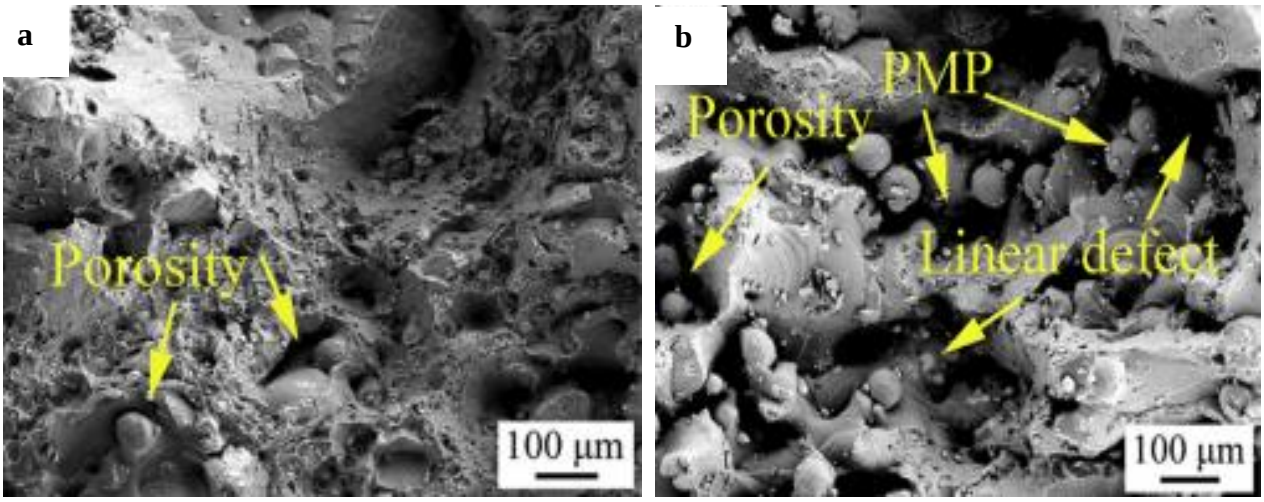

Figure 2.23. Defects in the microstructures of Ti-7.5Mo alloys at scanning speeds of (a) 1000mm/s and (b) 1700mm/s [185].

Yadroitsev et al. [60] produced Ti-15Mo also via LPBF. The microstructure shown in Fig 2.24a and b consisted of regions of α-phase with a lamellar morphology and regions of the bcc β-phase with a cellular dendritic structure which formed during solidification. Both martensite phases (i. e. , α′ and α′′) were reportedly not found in the AB microstructure of the alloy. This alloy exhibited a UTS of 894 MPa and a total elongation of 2.82%, which are respectively higher and lower than the values reported by Nan et al. [185] for Ti-7.5Mo. This is due to the higher concentration of Mo which provides more solid solution strengthening. The smaller β-grains also contribute to the higher UTS in Ti-15Mo alloy. Even though the E-Mod was not given, it can be predicted to be lower than that of Ti-7.5Mo if Ti-15Mo contains smaller volume fractions of α-phase. This prediction is based on the E-Mod values shown in Table 2.6, where the β-phase exhibits a smaller value than the α-phase. The as-cast Ti-15Mo alloy [58] had no α′′-phase present in the β-matrix and displayed superior values of 921MPa for UTS and 25% for elongation.

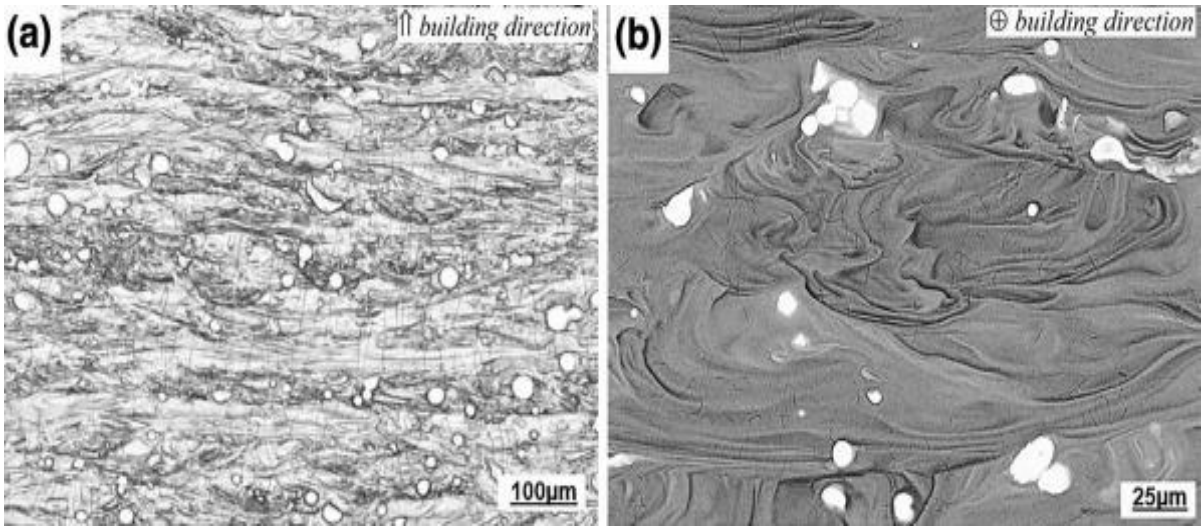

Figure 2.24. Microstructure of LPBFed Ti-15%Mo samples at 150-W laser power, 1.0-m/s scanning speed, and 80-μm hatch distance acquired by (a) optical microscope and (b) SEM in BSE mode [60].

Table 2.6. E-Mod values of phases in Ti-alloys.

Phases	Alloy/Condition (Wt. %)	E-Mod (GPa)	Reference
α	CP-Ti	105	[187]
	CP-TI Grade 1 ASTM 1341	100	[188]
	CP-Ti Grade 1	102.2	[189]
	CP-Ti Grade 3	103.4	[189]
β	Ti–35Nb–7Zr–5Ta (TNZT)	55	[188]
	Ti–29Nb–13Ta–4.6Zr	65	[188]
	Ti–15Mo–5Zr–3Al	82	[188]
	Ti-15Mo	84	[58]
α''	Ti-7.5 Wt. % Mo	70	[58]
	Ti-7.5 Wt. % Mo	55.4	[82]

2.5 Deformation mechanisms in β-Ti-Mo alloys

Three deformation mechanisms are possible in β-Ti alloys and they include Stress Induced Martensite (α''_D) Transformation (SIMT), Twinning and Dislocation slip [25, 26, 190]. Activation of a deformation mechanism is mainly dependent on the stability of the β-phase. This stability can be a function of the MoE, electron to atom (e/a) ratio, bond order (Bo), molecular d-orbital energy level (Md) and shear modulus [191, 192]. Wt. % of Mo represents the MoE in binary Ti-Mo alloys. This parameter is illustrated by the yellow highlight of Fig. 2.25.

It has been proven that a separate or simultaneous activation of SIMT and twinning can increase work hardening rate (WHR) [25]. These mechanisms result in Transformation Induced Plasticity (TRIP) and Twinning Induced Plasticity (TWIP), respectively. These promote high strength and improved ductility. In alloys which deform solely by dislocation glide (i.e. stable β-Ti alloys), there's an accompanying low WHR with strength and ductility bearing an inverse relationship [193]. Twins have played an insignificant role in WHR in binary Ti-Mo alloys with high β-stability and in homogeneous ternary Ti-Mo-X alloys [35, 194].

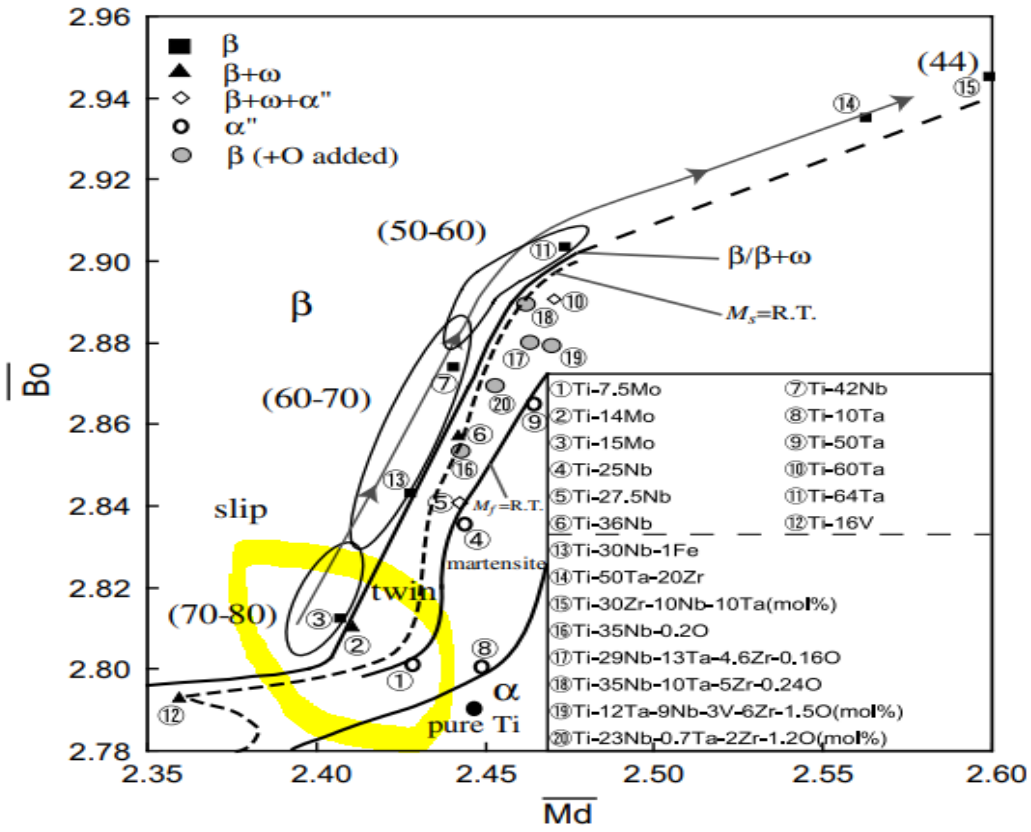

Figure 2.25. Extended $\overline{Bo}$ and $\overline{Md}$ diagram in which the β/β+ω phase boundary is shown together with the boundaries for Ms=RT and for Mf=RT. Bo is the bond order that is a measure of the covalent bond strength between Ti and an alloying element. Md is the metal d-orbital energy level of alloying transition-metal. M correlates with the electronegativity and the metallic radius of elements. The value of E-Mod (GPa) is given in parentheses for typical alloys [190].

Other factors determining deformation mechanism may include β-grain size, phase distribution relative to GB, grain orientation and homogeneous/heterogeneous elemental distribution [35, 194]. Heterogeneity causes compositional partitioning which implies non-uniform distribution of elements in phases and twins. This can result in anisotropy of mechanical properties in the alloy.

As an estimate, Fig. 2.25 puts Ti-7.5Mo in the SIMT domain, Ti-14Mo and Ti-15Mo in the twin and slip domains, respectively. Nevertheless, slip does occur in all regions. Schmid factor (SF) (expressed in Eq. 7 can be an indicator of which slip or twin system will be operational and this is usually the system with the highest SF. SF therefore shows the orientation dependency of slip and twinning systems under a given stress [195].

$$\tau = F/A\ cos\ \emptyset\ cos\ \lambda$$ Equation 2.7

Where τ is the shear stress on system, F is the applied force, A is the area of the slip plane, ∅ is the angle between the applied force direction and the normal to the slip plane and λ is the angle between the applied force and the trace of the slip plane.

2.5.1.1 Ti-xMo alloys

Hanada et al. [107] reported that when the ratio of reciprocal distance of $d^*_{0002\omega}$ to $d^*_{222\beta}$ is larger than 0.660, twinning occurs in Ti-15Mo. When this ratio is less, dislocation slip occurs. It was stated in Refs. [47, 196] that Ti-10V-2Fe-3Al, Ti-10V-1Fe-3Al and Ti-10V-2Cr-3Al deformed only by slip when the α-phase fraction reaches 0.5, corresponding to MoE of ∼16. In Ti-10V-3Fe-3Al [44, 102] change from martensite to twinning to slip takes place with decrease in β-domain and increase in β-phase stability due to more α-phase formed.

Zhao et al. [35] performed ST on Ti-15Mo (Wt. %) at 850°C for 3.6 ks under vacuum conditions and water quenched. A microstructure comprising of equiaxed β-grains and a small amount of fine ω_{ath}-phase (Fig. 2.26a) was reported. The same phases were reported in the alloy by IM et al. [33]. These authors did not provide TEM images showing ω_D. Fig. 2.26b shows TEM image of a plate-like ω_D in Ti-16V [197] which clearly differs in morphology from ω_{ath}. Elongated β-grains and straight bands of $\{332\}_\beta\langle 113\rangle_\beta$ mechanical twinning (Fig. 2.26c) were identified in the microstructure after CR. $\{332\}_\beta\langle 113\rangle_\beta$ twinning was verified by Electron Back Scattered Diffraction (EBSD) in Ti-17Mo (Fig 2.27a and b) in the same study [198, 199] as the twins had a 50.5° tilt from the $\langle 111\rangle$ axis of the β-matrix. Min et al. [200] reported that a $\{332\}\langle 113\rangle$ twin is formed by successive slip of zonal dislocations with a small Burgers vector of $a/22\ \langle 113\rangle$ in pairs of neighbouring $\{332\}$ planes. This mechanism is confirmed by Rusakov et al. [201] and Kawabata et al. [202]. Crocker [203] proposed that this type of twin is formed by shear-shuffling mode. Tobe et al. [204] described lattice modulation as a key player in formation of this twin, in terms of shear magnitude and shuffle complexity. These authors agree that $\{332\}\langle 113\rangle$ twinning occurs at a certain triggering stress level. This triggering

stress depends on phases present, previous processing including β-grain size, deformation type (tension, compression or torsion) and strain rate. The other type of twin found in metastable β-alloys is the $\{112\}\langle 111\rangle$ type which is less commonly reported. It usually forms in more stable β at higher triggering stress [45]. This relatively higher triggering stress is connected to the larger Burgers vector of partial dislocations participating in $\{112\}\langle 111\rangle$ twinning. This results in an increase in the shear modulus reflecting the resistance to shear of $\{0\bar{1}1\}_\beta$ planes along $\langle 111\rangle_\beta$ directions. The increase in shear modulus suggests that the lattice instability of β-phase activates the $\{332\}\langle 113\rangle$ twinning preferentially over the $\{112\}\langle 111\rangle$ type [204]. The $\{112\}\langle 111\rangle$ twin type however, is most favourable in bcc metals and alloys. This is because unlike the $\{332\}\langle 113\rangle$ type, it does not require an additional shuffling of one-half of the atoms after the twinning shear to form [203]. Bertrand et al [205] reported in Ti-25Ta-24Nb that for $\{332\}\langle 113\rangle$ twinning systems, the highest SF value of 0.41 found on $(\bar{3}32)[\bar{1}1\bar{3}]$ is obtained for a tensile direction close to $\langle 111\rangle$. It was also reported that for $\{112\}\langle 111\rangle$ twinning systems, the highest SF value of 0.43 corresponding to $(121)[\bar{1}1\bar{1}]$ was obtained when the tensile direction is close to the $\langle 100\rangle$ direction of the parent crystal.

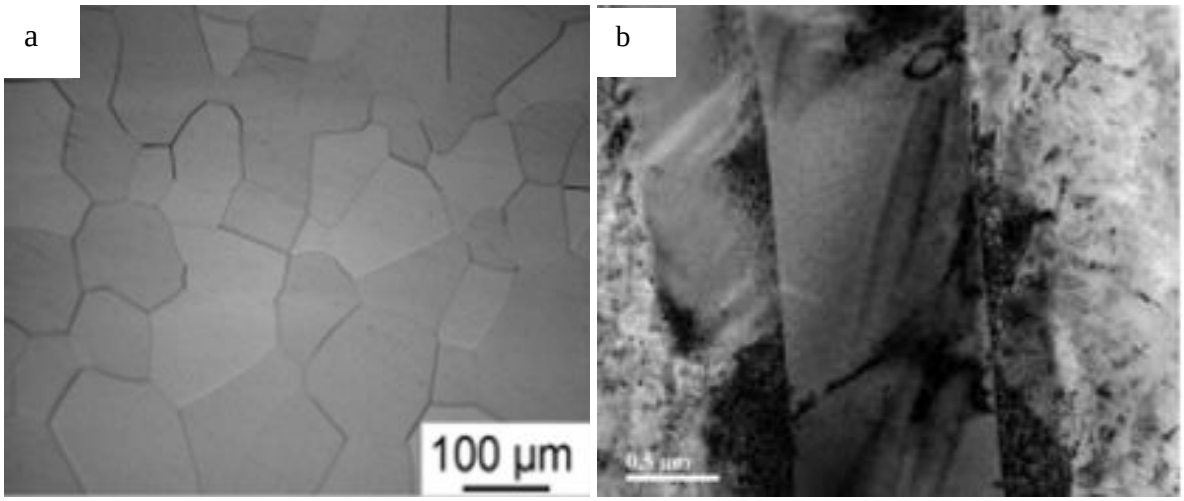

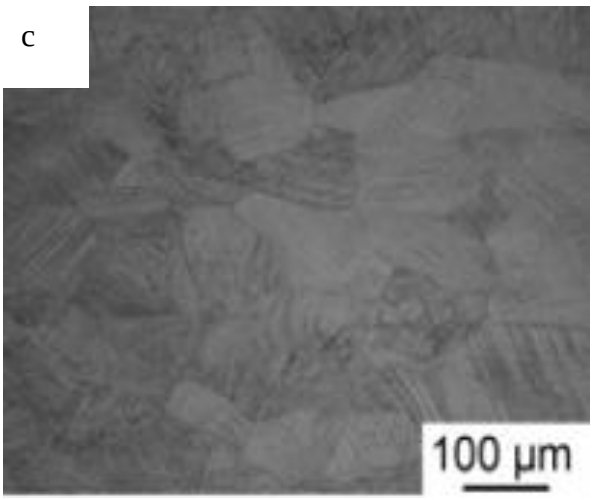

Figure 2.26a. OM image of ST Ti-15Mo showing ω_{ath} [35], (b) TEM image showing ω_D in Ti-15V [197] and (c) CR Ti-15Mo [35].

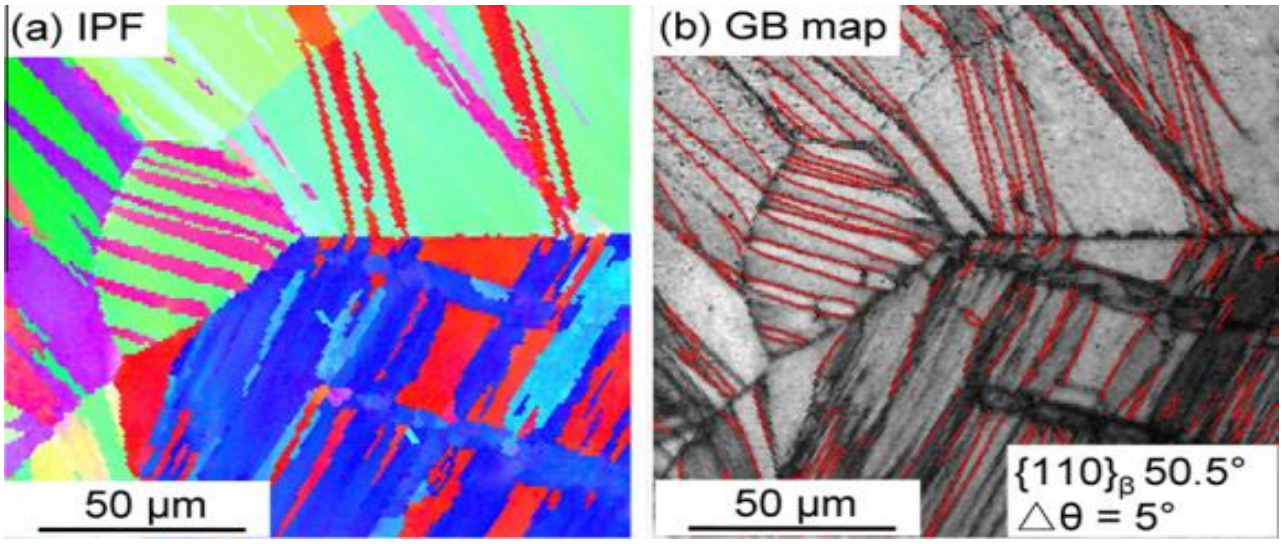

Figure 2.27. EBSD maps of Ti-17Mo alloy subject to CR: (a) Inverse Pole Figure (IPF) mapping, (b) boundaries with misorientation angle of 50.5° along $\langle 110 \rangle_\beta$ direction corresponding to $\{332\}_\beta\langle 113 \rangle_\beta$ twins [35].

Fig. 2.28a which is a Selected Area Electron Diffraction (SAED) pattern of the $[110]_\beta$ zone confirms the presence of ω_{ath}-phase shown in Fig. 2.26a. Reflections of ω-phase after CR shown in Fig. 2.28b were much sharper, indicating an increase in this phase fraction. This is possibly due to the formation of deformation-induced omega (ω_D). During tensile deformation, ω_D accompanied with the

$\{332\}\langle 113\rangle$ twinning was observed. TEM micrographs during and after deformation were not provided in this study.

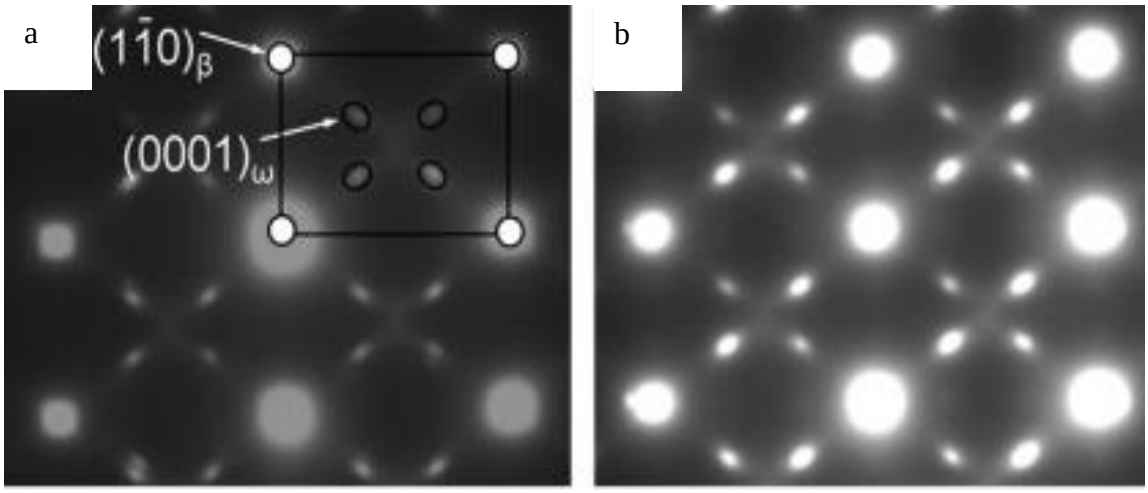

Figure 2.28 TEM selected area electron diffraction (SAED) patterns of (a) ST Ti-15Mo and (b) CR Ti-15Mo [57].

Lai et al [94] reported that an energy barrier has to be overcome in order for the stress induced $\beta \rightarrow \omega_D$ transformation to take place in Ti-36Nb-1.4Ta-2.8Zr-0.3O. This transformation causes an enlargement in $a_{\langle 110\rangle\beta}$ $\left(\sqrt{2a_\beta}\right)$ and a decrease in $a_{\langle 1\bar{1}1\rangle\beta}$ $\left(\sqrt{3a_\beta}/2\right)$. There is also an accompanying change in spacing between adjacent $\{111\}_\beta$ planes due to a homogeneous isotropic strain in the $\{111\}_\beta$ planes. The difference in lattice parameter results in a lattice mismatch between ω and the surrounding β. This introduces an elastic misfit strain into the system. Intermediate transition states $(0 < Z_w < 1/6)$ were identified during the transformation process. If there is a local stress moving a pair of adjacent $\{211\}_\beta$ atomic planes along the $\langle 1\bar{1}\bar{1}\rangle_\beta$ direction by a displacement of $Z_w = \pm 3/48$, the energy barrier will be overcome and transformation will take place spontaneously. The atomic shear along $\{211\}_\beta\langle 1\bar{1}\bar{1}\rangle_\beta$ direction can be an assisting factor. This explains why the $\{211\}_\beta\langle 1\bar{1}\bar{1}\rangle_\beta$ twinning or $\beta \rightarrow \alpha''$ transformation induces a plate-like ω_D-phase in the Ti-Nb-based alloys with an e/a range of 4.22-4.24. Crystallographically, the $\{211\}_\beta\langle 1\bar{1}\bar{1}\rangle_\beta$ twinning can be referred to as a consecutive shearing of $\{211\}_\beta$ planes along the $\langle 1\bar{1}\bar{1}\rangle_\beta$ direction [93]. This process imposes a $\{211\}_\beta\langle 1\bar{1}\bar{1}\rangle_\beta$ shear stress on the surrounding β matrix which assist in overcoming the

energy barrier on the $\beta \rightarrow \omega_D$ transition pathway. This induces the formation of a sequence of plate-like ω_D-phases aligned along the $\{211\}_\beta\langle 1\bar{1}\bar{1}\rangle_\beta$ twin/β interface as shown in Fig. 2.29a for Ta-2.5 and 10W (Wt. %) alloys [93]. Furuhara et al [206] studied Ti-15V-3Cr-3Sn-3Al and found arrangements of parallel ω_D plates inside the $\{332\}\langle 113\rangle$ twin – along its width (Fig. 2.29c and d). ω_D of same morphology was reported at the $\{332\}\langle 113\rangle$ twin/β interface in Ti-27Nb (at. %) [207] without an indexed micrograph. Indexing was done for same occurrence in Ti-15Mo [33] as shown in Fig. 2.29e-i. ω_D has also been reported at the interface between α'' martensite and the β-matrix in Ti-10V-3Fe-3Al and Ti12Mo [44, 132].

a

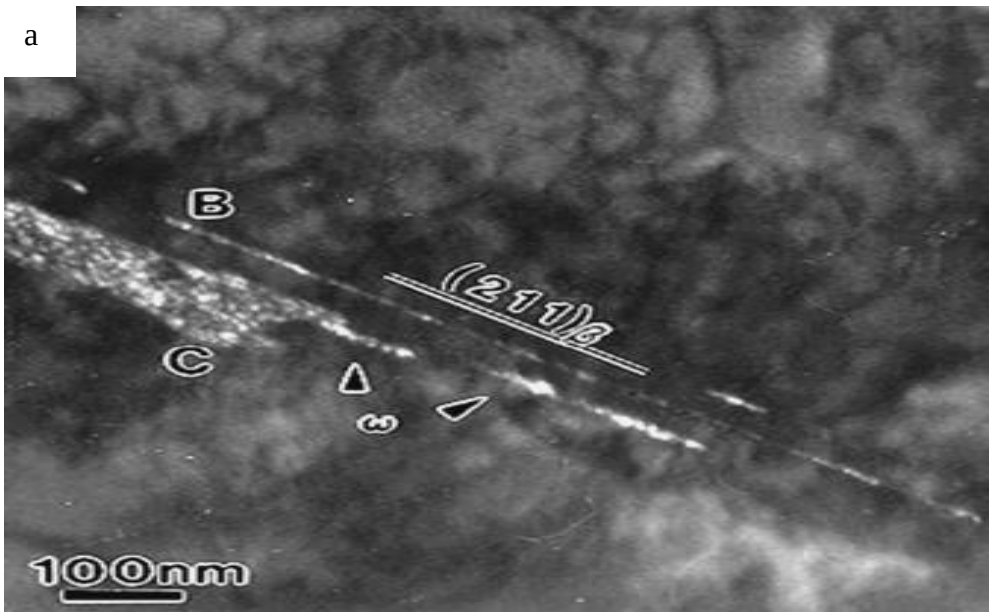
B
(211)α
C
3
100nm

b

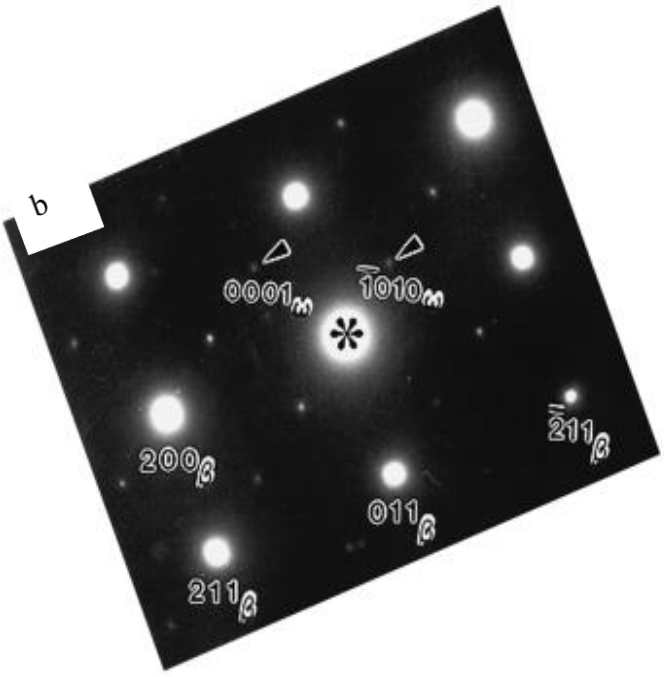
0001m
1010m
200α
011α
211α
211α

c

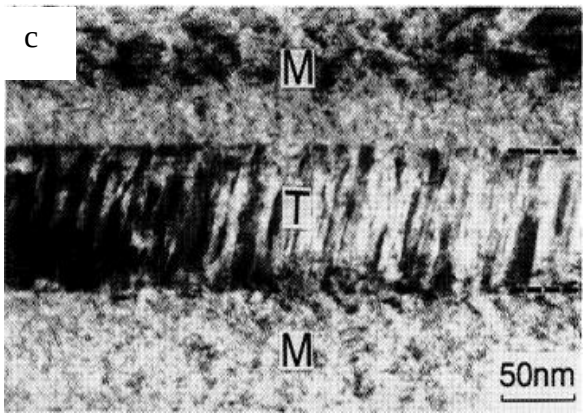
M
T
M
50nm

d

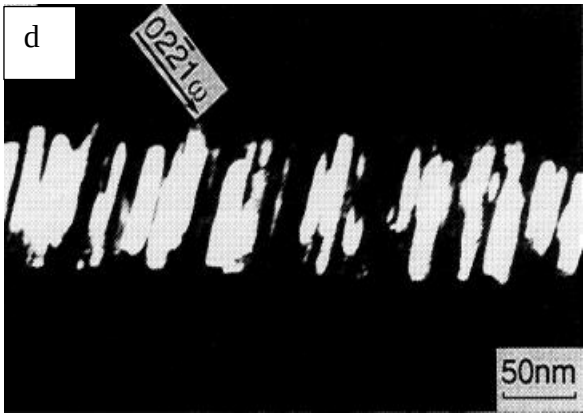
0221ω
50nm

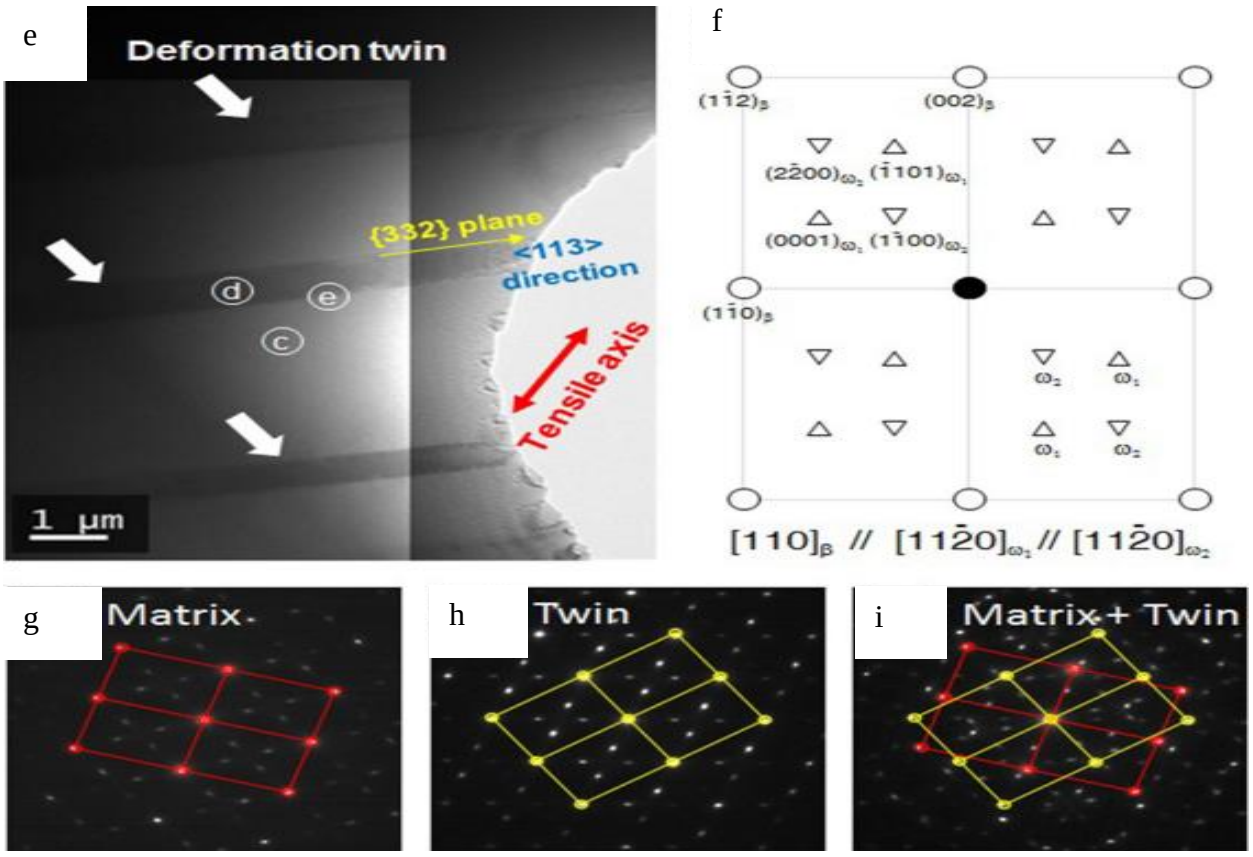

Figure 2.29 (a) A dark-field TEM image of Ta-2.5 and 10W (Wt. %); (b) the corresponding SAD pattern generated from the area in (a) revealing that the microbands at sites B and C in Fig. 2.29(a) are domains of ω_D, $OR \approx [1\bar{2}\bar{1}0]_{\omega_D} \parallel [0\bar{1}\bar{1}]_\beta$ [93]; (c) bright-field image showing ω_D plates which formed inside the $\{332\}\langle 113\rangle$ twin of Ti-15V-3Cr-3Sn-Al. M and T represent matrix and twin respectively. $OR \approx [1\bar{1}0]_M \| [\bar{1}10]_T \| [11\bar{2}0]_{\omega_D}$; (d) dark-field micrograph of (c) [206]; (e) Bright-field image of the 5% tensile-strained specimen of Ti-15Mo; (f) Index of the SAD patterns shown in the matrix (g), deformation twin (h), and the interface between matrix and twin (i) [33].

Zhao et al. [35] performed tensile test on Ti-15Mo at a strain rate of 0.01 S-1 starting at a strain of 0.01 up to 0.1. The E-Mod for the ST sample was 79 GPa. This value increased in the CR sample due to forming of ω_D. The ST sample showed low 0.2% proof stress but high WHR resulting in excellent ductility. After CR, the 0.2% proof stress and UTS increased drastically (Fig. 2.30) but the ductility decreased. Reduction in ductility is because after CR, many twins formed and capacity to accommodate deformation was significantly reduced compared to the ST sample.

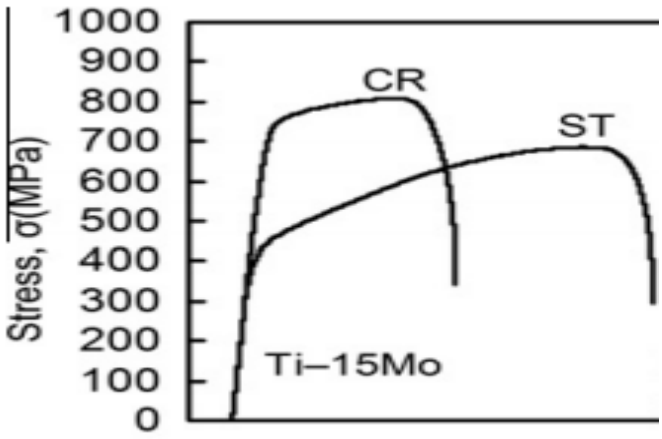

Figure 2.30. Stress Strain Curve of Ti-15Mo [35].

Min et al. [26] reported a similar fully β microstructure in ST Ti-15Mo. Tensile test was conducted at a strain rate of 2.78 × 10-4 s-1. The same type of twins found in Ref. [35] induced microstructural refinement and was primarily responsible for strain hardening at strains up to 0.12 (Fig. 2.31a). This effect has been confirmed in respect to the dynamic Hall-Petch effect in TWIP steels [208, 209]. Slip and twinning could either occur simultaneously or successionally. Slip participates in the nucleation and growth of twins in this alloy. Twins are known to cut across the grains to form boundaries which act as barriers to dislocation motion (slip). This results in a decrease in the dislocation mean free path. The twins became denser and thicker with increasing strain up to 0.12. No increase in twin density was observed up to a strain of 0.17. Further strain hardening at strains up to 0.24 was brought about by rapid increase in dislocation density. Dislocation density is indirectly indicated by the Full Width at Half Maximum (FWHM) values from XRD [210]. There was a steady increase in FWHM values at strains up to 0.12 and sharper increase at strains from 0.12 to 0.17. It was also mentioned that sessile dislocation impeded the motion of other dislocations. They do so independently and beyond grain and twin boundaries to contribute to strain hardening at higher strains (i.e. between 0.12 and 0.24).

WHR was grouped into 4 stages based on the true strain (Fig. 2.31a): (i) a sharply decreasing stage up to 0.05; (ii) a constant stage at strains from 0.05 to 0.12; (iii) a gradually decreasing stage, at strains up to 0.24 (i.e. uniform elongation) and (iv) a necking stage, with further straining beyond that point.

This non-monotonic WHR behaviour was further explained in terms of evolving deformation microstructure. Total contribution of a given deformation mechanism to true stress ($\sigma_{(\varepsilon)}$) is expressed in Eq. 2.8.

$$\sigma_{(\varepsilon)} = \sigma_0 + \frac{K_1}{\sqrt{\Lambda_{(\varepsilon)}}} + K_2\sqrt{\rho_{(\varepsilon)}} \qquad \text{Equation 2.8}$$

Where σ_0 is taken to be close to the YS of a single crystal, Λ is the dislocation mean free path, ρ represents density, K_1 and K_2 are constants. In stage (i) the ease of primary twinning combined with rapid decease in dislocation mean free path leads to significant strain hardening. From here a slowdown in the primary twinning rate brings about a steady decrease in the WHR. Stage (ii) sees a further decrease in the primary twinning rate. Secondary twinning and twin-twin intersections increases in frequency, thereby decreasing the dislocation mean free path further. Hence, a constant WHR was maintained at this stage. In both stages (i) and (ii) WHR is dominated by the dynamic Hall-Petch effect which is the second term on the right hand side of Eq. 8. In stage (iii), the volume fraction, thickness and inter-twin spacing do not significantly change. This indicates an end of twinning activities. The dislocation density increases sharply implying that twin-dislocation and dislocation-dislocation interactions are operational. In this stage, WHR is dominated by the third term on the right hand side of Eq. 8. Stage (iv) sees the initiation of necking which is preceded by a continuous yielding of twins by dislocations as well as an increase of dislocation density. This is evidenced by a gradual decrease in WHR.

YS, UTS and total elongation were reported as 504 MPa, 765 MPa and 40% respectively as can be read from Fig. 2.31b.

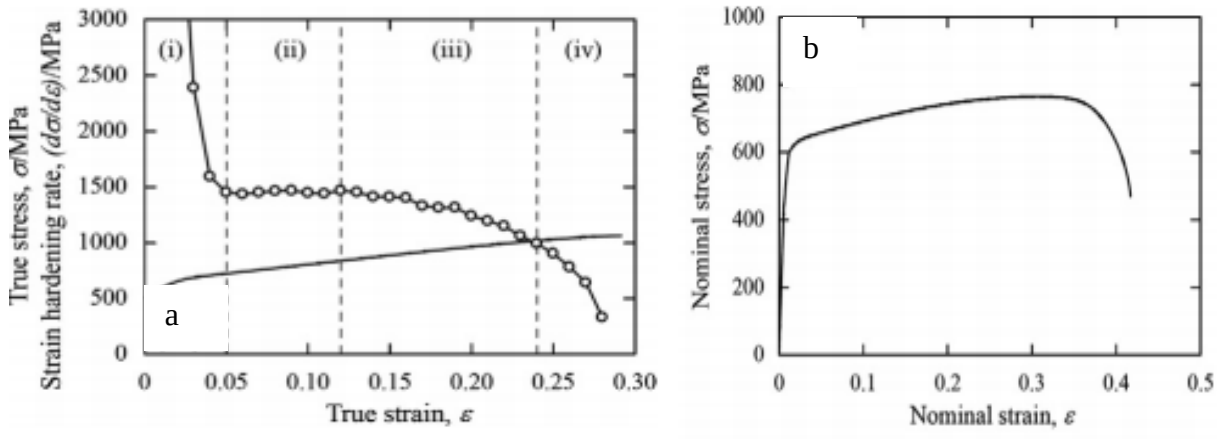

Figure 2.31. True stress–strain curve and corresponding strain hardening rate and (b) Nominal stress–strain curve [26].

In a separate study on the same alloy, Min et al. [34] reported on the grain orientation dependence of twinning and dislocation slip during tensile deformation. Twinning was observed in plastic deformation region and depending on grain orientation, the operating twinning systems either obeyed or contravened Schmid's Law. For example in the $[\bar{1}22]$ grain, operation of only $(233)[\bar{3}11]$ twinning system with the highest SF of 0.497 was identified, whereas in the $[001]$ grain three twinning systems were observed after strain reached 0.01 (Fig. 2.32a). These include $(233)[\bar{3}11]$, $(3\bar{2}3)[131]$ and $(\bar{3}\bar{2}3)[\bar{1}31]$ with SF's of 0.212, 0.214 and 0.214, respectively. 0.214 was the highest SF of all 12-twinning systems in this grain implying that the $(233)[\bar{3}11]$ twinning system violates Schmid's law. This violation was attributed to the geometric constrains between neighbouring grains and/or local stress concentration. Observations of $\{332\}\langle113\rangle$ twin systems with SF energies below 0.1 has been reported in Ti-15Mo-5Zr [211] subject to 0.04 tensile strain and in Ti-10V-3Fe-3Al [212]. In the study by Min et al. [34], the smallest SF for twin was recorded as 0.407. $(1\bar{1}2)[\bar{1}11]$ dislocation slip system (Fig 2.32b) with a maximum SF of 0.481 mainly contributed to plastic deformation in the elasto-plastic region after yielding. The 12-slip systems in the $[001]$ grain had a lowest SF of 0.212 implying the lowest SF for slip to occur. This is a possible hint at the transition SF between fully-twin and fully-slip in Ti-15Mo for this grain orientation. In the nearly $[\bar{1}22]$ grain, strain hardening was dominated by $(233)[\bar{3}11]$ twinning at strains up to 0.15. The

smallest SF for twins in this grain was reported as 0.279. Secondary twins were also observed inside the primary twins as strain reached 0.05. These twins led to increased strain hardening by microstructure refinement. Upon further deformation, the dominance was by $(\bar{2}11)[111]$ dislocation slip having the maximum SF of 0.465. The smallest SF for slip was reported as 0.252. The active interactions of twin-dislocation and dislocation-dislocation at larger strains describes the strain hardening mechanism in this grain.

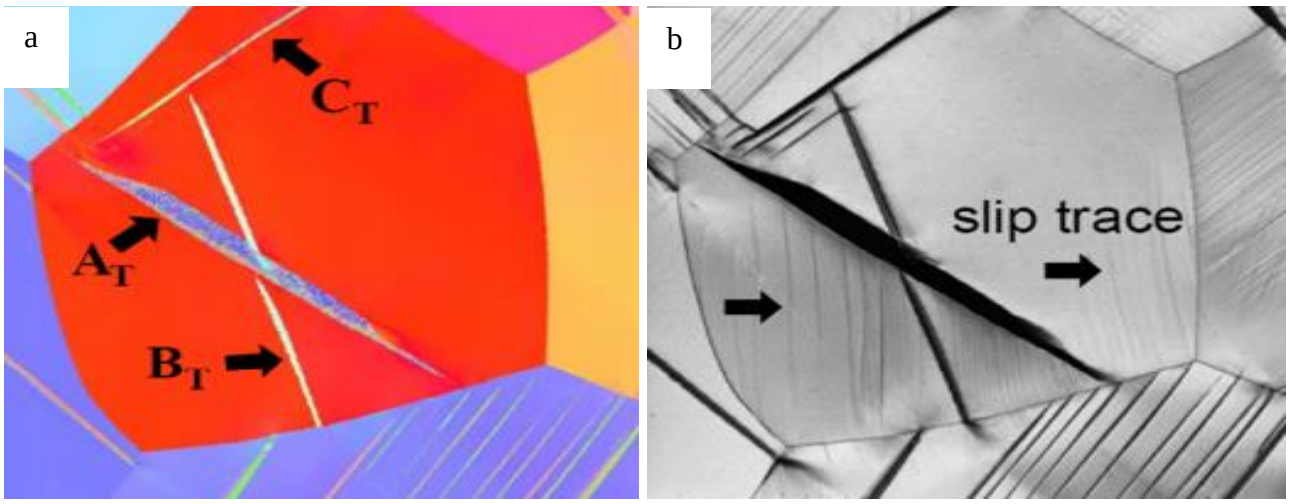

Figure 2.32a. IPF map in the nearly $[001]$ oriented grain at a strain of 0.01 where AT, BT and CT correspond to twin systems $(233)[\bar{3}11]$, $(3\bar{2}3)[131]$ and $(\bar{3}\bar{2}3)[\bar{1}31]$, respectively; (b) Image quality map in the same grain and strain value [34].

Marteleur et al. [25] manufactured Ti-12Mo (Wt. %) by cold crucible levitation melting under Ar atmosphere. Sample was then ST at 870°C and water quenched. Upon quenching, microstructure comprised majorly of β-phase with some ω_{ath}-phase as revealed by XRD. This is similar to the microstructure obtained by Min et al [26] and Zhao et al [35] for Ti-15Mo.

During tensile test, a microstructure comprising of $\{332\}_\beta\langle 113\rangle_\beta$ mechanical twinning at a strain of 0.05 as shown in Fig. 2.33a was reported. α_D'' at the nanoscale was also revealed at a strain of 0.10. It appeared as a dense network of nanoscale needles as shown in Fig 2.33b. Power spectra taken on both sides of twins exhibit diffracting signature of ω_D-phase. This phase accommodates the deformation induced by twin formation and intensifies the twins [35, 194]. Prior to tensile test, the measured

oxygen content was 0.0115 Wt. % and its effect on deformation was not mentioned. Tensile deformation was performed and a combined TRIP and TWIP effect evolved at different stages. The derived maximum WHR was not mentioned but a true stress of 1000 MPa at a necking strain of 0.37 was reported.

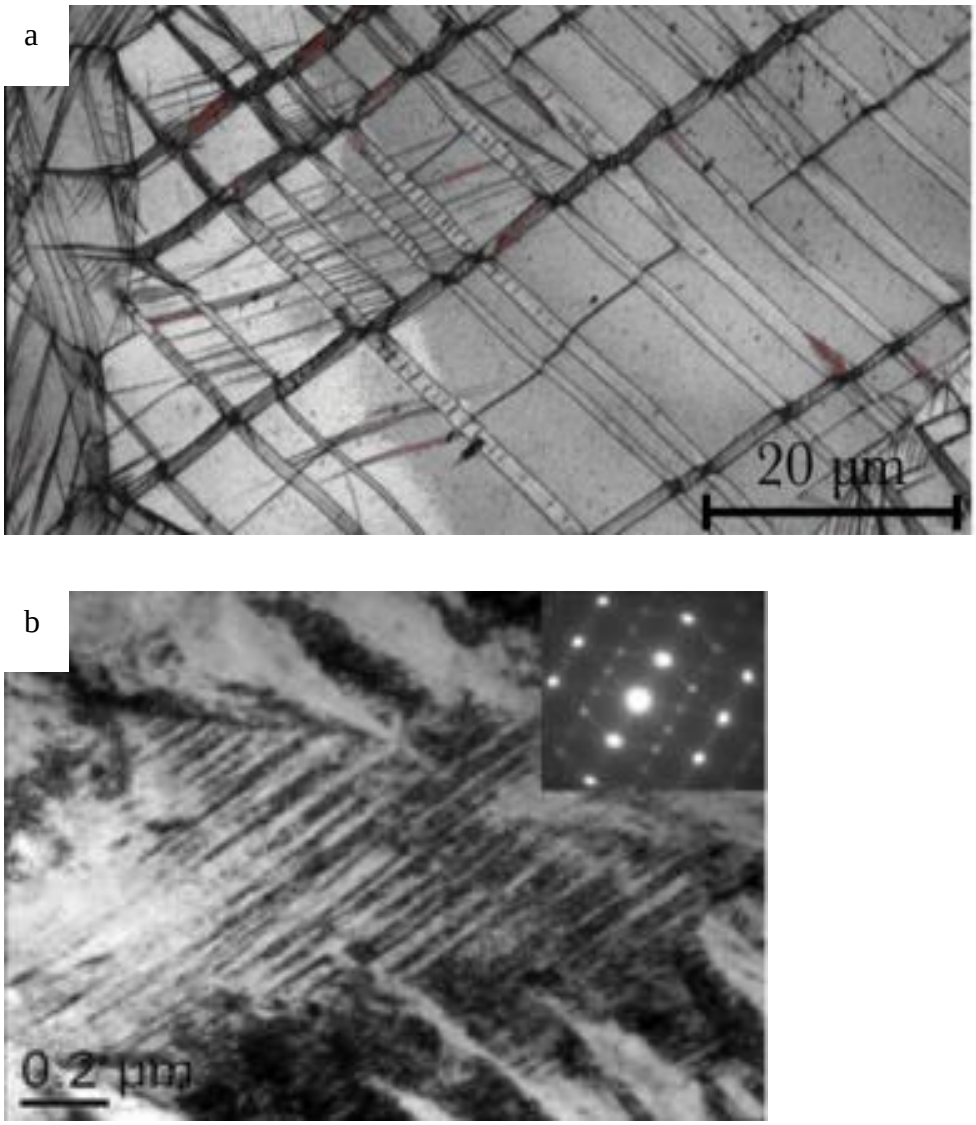

Figure 2.33a. EBSD map of Ti-12Mo deformed to a tensile strain of 0.05 showing twin bands and α'-phase in red and (b) TEM micrograph of Ti-12Mo deformed to 0.38 – Bright Field micrograph along the $\langle 113 \rangle_\beta$ zone axis illustrating the formation of α_D'' [25].

Mantri et al. [132] performed tensile deformation on the same alloy and confirmed all the phases reported by Marteleur et al. [25]. However, a hierarchical twinning system at multiple length scales was noted. $\{332\}_\beta\langle 113\rangle_\beta$ primary twins contained different variants of secondary and tertiary twins.

Secondary twins are believed to be either another variant of the $\{332\}_\beta\langle 113\rangle_\beta$ type or the more common $\{112\}_\beta\langle 111\rangle_\beta$ type in bcc metals [213].

The formation of α''_D- and ω_D-phases took place within the primary and tertiary twins respectively. α''_D-phase was observed to transform back to another β-band with a different orientation from β-matrix and primary twin. This happened after deformation to failure.

Crystallographically The $\beta \rightarrow \alpha''$ transformation involves (i) shearing of atoms in the $\langle 1\bar{1}\bar{1}\rangle_\beta$ direction within the $\{211\}_\beta$ plane and (ii) shuffling of atoms in every other $\{01\bar{1}\}$ atomic plane [214, 215].

Process described above imposes a $\{211\}_\beta\langle 1\bar{1}\bar{1}\rangle_\beta$ shear stress on the surrounding β matrix which assist in overcoming the energy barrier on the $\beta \rightarrow \omega_D$ transition pathway. This induces the formation of a sequence of plate-like ω_D-phases aligned along the α''/β interface. ω_D forms due to a glide of the $1/3\ [111]$, $1/6\ [111]$ and $1/12\ [111]$ partial dislocations. These dislocations dissociates from the perfect $1/2\ [111]$ dislocation in the bcc structure [93].

Due to slip, there existed ω_{ath} free zones. ω_{ath} was destroyed during the formation of primary twins with dislocations shearing through the ω_{ath}-phase. This action transforms it back into the structure of the β-matrix (i.e. the primary twin).

Niessen et al. [216] predicted the available work for α''-martensite transformation using the matrix expression in Eq. 9.

$$U = tr\big((B\boldsymbol{P}B - \boldsymbol{I})\boldsymbol{\sigma}\big) = \boldsymbol{h}\boldsymbol{\sigma}m\boldsymbol{d} \qquad \text{Equation 2.9}$$

Where tr represents a trace of the expression in the bracket, B**P**B is the shape deformation matrix from which the shape strain is derived, **I** is an identity matrix, $\boldsymbol{\sigma}$ is the external stress matrix on the system, **h** is the vector normal to the habit plane, m and **d** are the magnitude and direction of macroscopic shape change respectively.

It was reported that the available work is a function of the β-crystal orientation and in-plane stress state. It is however independent on alloy composition. The shape strain of an alloy is a requirement for this prediction and can be obtained experimentally. In the absence of this property, Bain strain (BMB) has be proven to provide insignificant errors in Ti-12Mo [216].

The work required for martensitic transformation in Ti-12Mo was derived from the third principal strain λ_3 as 0.2. This falls in the range of strain values for initiation of α''-martensite as reported by Marteleur et al. [25]. λ_3 approximately corresponds to the dilatation associated with the martensitic transformation. Since λ_3 of 0.2 is small, the orientation relationship is close to Burgers orientation relationship: $(100)_{\alpha''} \| (100)_{\beta}$; $(010)_{\alpha''} \| (01\bar{1})_{\beta}$; $(001)_{\alpha''} \| (011)_{\beta}$. λ_1 is almost equal to $-\lambda_2$ (first and second principal strains).

2.6 Effect of oxygen on microstructure and mechanical properties of Ti-Mo alloys.

The effect of oxygen on phases/microstructure, deformation mechanisms and mechanical properties of Ti-Mo alloys have been studied by Ji et al [82], Min et al [101, 200, 217] and Martins et al [218-221] among other authors. The methods of introducing oxygen into this alloy in these groups were different ones and this could have effect on the reported findings.

2.6.1 Ti-xMo-yO alloys

Martins et al [218-221] reported on Ti-15Mo that the main phase was bcc-β which contained precipitates of acicular α'-phase (Fig. 2.34 and 2.35). This martensite phase reportedly varied from 2.3 to 27.1% (Table 7) and followed no apparent order of relationship with the oxygen content (0.137 – 0.251 wt. %). The α'-phase fraction was determined with Rietveld analysis on XRD patterns. It is puzzling that the martensite formed is not α''-phase since this was the predominant phase reported by Ji et al [82] on Ti-7.5Mo which represents a lower MoE factor than that for Ti-15Mo. More so, Min et al [101, 200] equally studied the effect of oxygen on Ti-15Mo and did not report the presence of α'-phase in the microstructure. The variation of Nitrogen from 0.001 to 0.020 wt. % also showed no

logical trend with martensite phase fraction (Table 2.7). It is pertinent that Nitrogen is controlled as it may have effects on the alloy independent of oxygen effects.

The authors in Ref. [221] arc-melted (y = 0.137) and hot-swagged (y = 0.177) Ti-15Mo between 780°C and 860°C, followed by rapid cooling in air. In a separate investigation [218] they equally arc-melted the alloy (y = 0.137) but swagged it at RT (y = 0.177) and subsequently performed homogenisation heat treatment at a rate of 263.15°C/min up to 1000°C over 24 hours (y = 0.223). These processes were followed by slow cooling and 3 successive oxygen doping processes entailing heating to 700°C at 263.15°C /min followed by 2 hrs holding. This yielded oxygen nominal weight contents of y = 0.251, 0.229 and 0.204 respectively. It was unequivocally stated in this study that there is no direct correlation between oxygen concentration levels and precipitated α'-phase fraction. An increase in martensite fraction from 2.1% to 27.1% was recorded during the 3-successive doping process which saw a gradual decrease in oxygen levels from 0.251 to 0.204 w. %. In view of the fact that these two quantities are relationally sporadic, the authors ascribed the observed martensitic fluctuations solely to the sequential melting, swagging, homogenisation, heating and rapid cooling processes rather than to the content of oxygen. This is a rational deduction since there was a decrease in oxygen content at every single stage of the doping process as shown in Table 2.7.

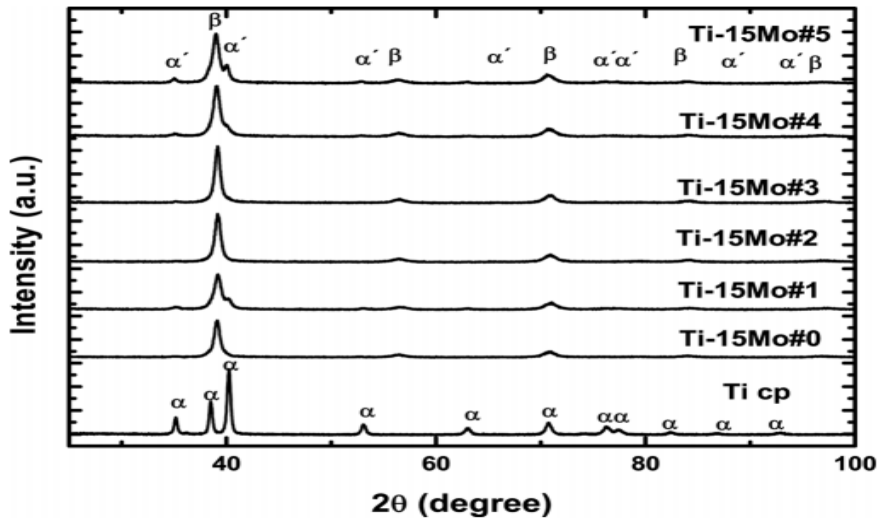

Figure 2.34. X-ray diffractograms for the Ti-15Mo alloy samples with varying oxygen content [220].

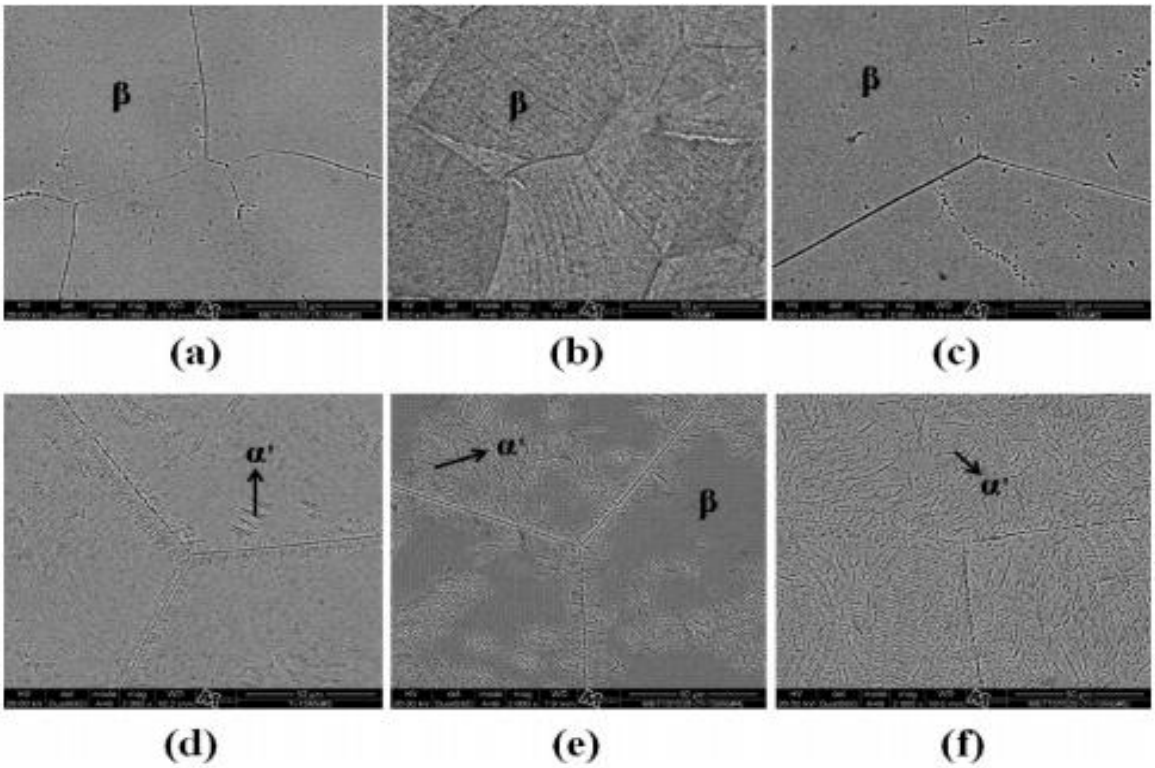

Figure 2.35. Micrographs of Ti-15Mo with oxygen Wt. % of (a) 0.137, (b) 0.177, (c) 0.223, (d) 0.251, (e) 0.229 and (f) 0.204 [220].

Table 2.7. Density and fraction of α′ phase for Ti–15Mo samples [218].

Sample	Oxygen (wt%)	Nitrogen (wt%)	ρ (g/cm^3)	α′ phase (%)
Ti–15Mo#0	0.137 ±0.005	0.006 ±0.001	4.96 ±0.01	2.3
Ti–15Mo#1	0.177 ±0.004	0.007 ±0.002	5.02 ±0.01	24.5
Ti–15Mo#2	0.223 ±0.002	0.001 ±0.002	4.99 ±0.01	2.1
Ti–15Mo#3	0.251 ±0.008	0.020 ±0.002	4.98 ±0.01	4.3
Ti–15Mo#4	0.229 ±0.005	0.018 ±0.003	5.03 ±0.02	18.2
Ti–15Mo#5	0.204 ±0.008	0.015 ±0.003	5.00 ±0.01	27.1
Ti–15Mo [22]	–	–	4.97	–
cp–Ti	–	–	4.50 ±0.01	–

Martins et al. [218-221], in their multiple investigations only reported E-Mod and Hardness values. E-Mod was measured by mechanical spectroscopy using the torsion pendulum technique at frequency range of 4-30 Hertz. They noted the smallest E-Mod value of about 75GPa associated with Ti-15Mo-0.204O which represents the alloy with the lowest oxygen content after doping as shown in Fig. 2.36a. This value is higher than the 60GPa obtained for Ti-7.5Mo-0.2O [82]. A succinct explanation for this can be tied to the higher molybdenum content in the alloy studied by Martins et al. Ti-15Mo-0.251O

which is the alloy with the highest oxygen content also was the hardest one with ~500 Vickers Hardness (Hv) (Fig. 2.36b). The reason why this value is greater than the approximately 240 Hv derived for Ti-7.5Mo-0.25O studied by Ji et al [82] is also attributable to the higher Mo content.

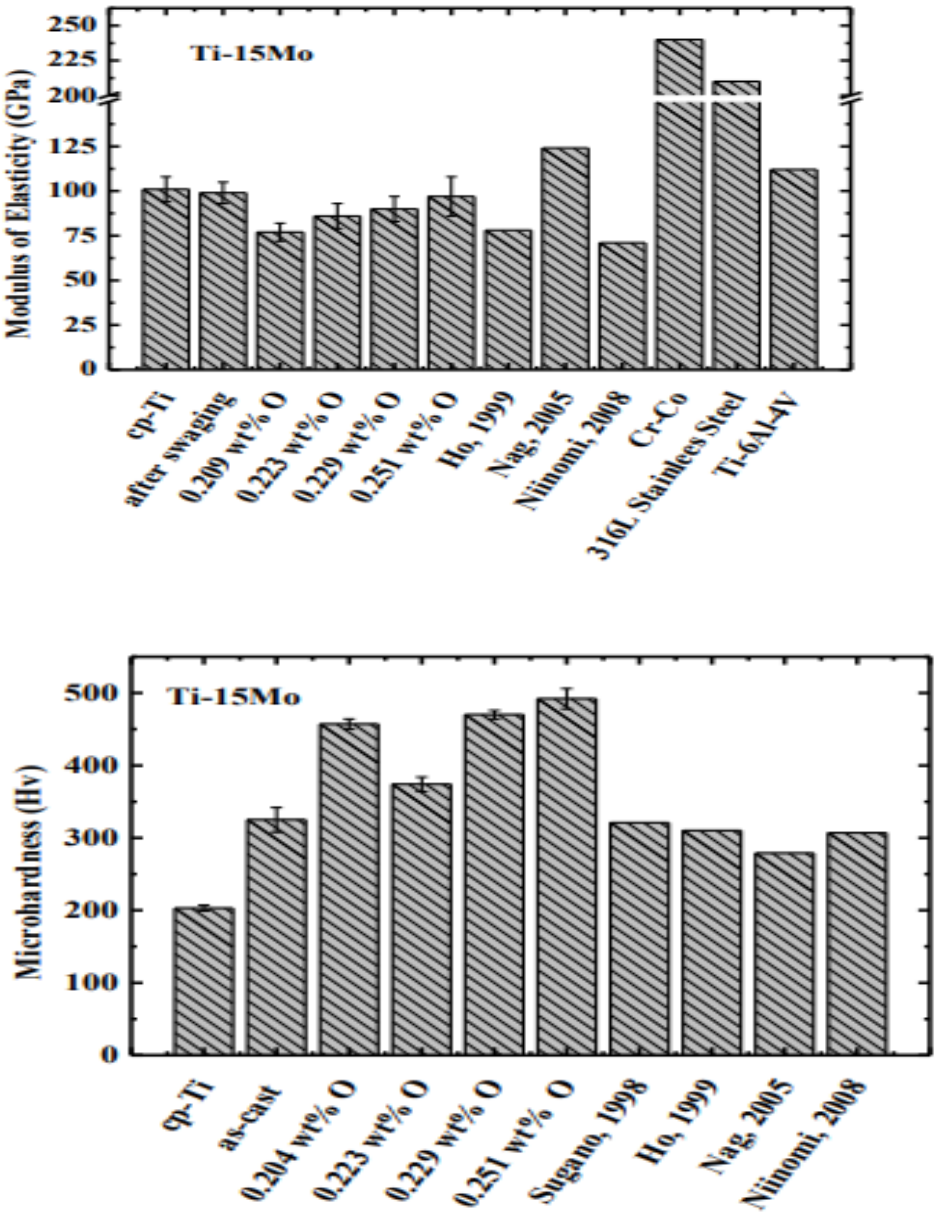

Figure 2.36a. E-Mod (GPa) of Ti-15Mo with different Wt. % of oxygen, (b) Microhardness (Hv) of Ti-15Mo with different Wt. % of oxygen [218].

Min et al. [200] conducted tensile deformation studies on Ti-15Mo with varying oxygen content from 0.1 to 0.5 Wt. %. Only parent β-phase was clearly detected by XRD patterns in all alloys. As oxygen content increased, decreasing reflections of ω_{ath} were detected by TEM with similarity in

fleetingness as reported by Zhao et al. [35] in section 2.3.1. Hence, $\beta \rightarrow \omega_{ath}$ transformation was suppressed by oxygen in the ST state of the alloy. Williams et al. [222] suggested that solute oxygen atoms interact with the stress field of the linear defects. This interaction pins the atomic displacement of the $\langle 111 \rangle$ direction thereby hindering the collapse of $\{111\}$ planes of β-phase. Liu et al. [223] reported that oxygen atoms occupy octahedral sites randomly in Ti-Cr and introduce lattice distortion in the β-phase. This increases the resistance to the atomic displacement in the $\langle 111 \rangle$ direction. Niu et al. [224] reported that solute oxygen atoms in Ti-Nb-Ta-Zr gum metal make the ω-phase thermodynamically less favourable relative to β-phase. These authors reported an increase in energy barrier in the $\beta \rightarrow \omega$ transformation caused by oxygen based on first principles calculations.

Dominant deformation mechanism switched from $\{332\}\langle 113 \rangle$ twinning which appeared as plate-like features to dislocation slip at an oxygen content of above 0.3 Wt. %. Oxygen atoms interfere with the lattice shear-shuffling or partial dislocation movement resulting in the total absence of twins in Ti-15Mo-(04-0.5) O.

LP of β-phase gradually increased from 0.3259 to 0.3263 nm with increasing oxygen content. Vickers hardness increased from 232 Hv to 350 Hv indicating a strong solid solution strengthening caused by oxygen atoms. 0.2% proof stress also increased with higher oxygen content. Ti-15Mo-0.1O exhibited low YS of 420 MPa, large uEl of 47% and E-Mod of 73 GPa. Ti-15Mo-0.5O showed high YS of 1180 MPa, negligible uEl with a tEl of 10% only and E-Mod of 87 GPa. This low tEl was due to a decreased WHR from a reduction in twin density resulting from increase in O content. The small increase in E-Mod is caused by the O content which decrease the interatomic distance in the crystal lattice [225]. Ti-15Mo-0.3O displayed a balance between YS (940 MPa) and tEl (22%) due to the activation of twinning and slip deformation mechanisms

In a study by Min et al. [217] on Ti-10Mo, the alloy was ST at 900°C for 3.6 ks and water quenched. Oxygen was introduced by using the mixtures of Ti, Mo and TiO2. OM revealed only equiaxed β-grains in Ti-10Mo-0.1O and Ti-10Mo-0.2O alloys. In the Ti-10Mo-0.3O and Ti-10Mo-0.4O some

slight acicular features were observed as seen in Fig. 2.37 in addition to the β-grains. These acicular features had a larger area fraction in the Ti-10Mo-0.4O alloy. XRD confirmed these features to be thermally induced martensitic α′′-phase and substantiated the presence of parent β and ω_{ath} in all the alloys. Oxygen content of 0.3 Wt. % and above can be described as responsible for this martensitic transformation during quenching to RT. This is on the basis that it was proven that 10 Wt. % of Mo is required for full β-phase [63, 64]. Since XRD did not detect ω-phase in Ti-15Mo [200], it can be said that the volume fraction of this phase is larger in the less β-stabilised Ti-10Mo.

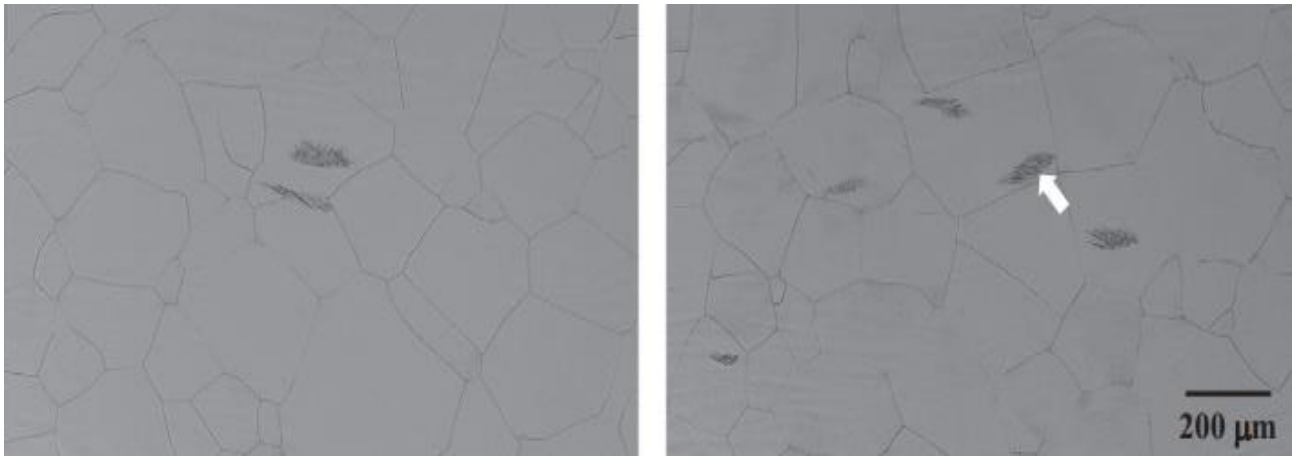

Figure 2.37. Optical micrographs of (a) Ti-10Mo-0.3O and (b) Ti-10Mo-0.4O. Alloys are in the ST condition. The observed plane is the rolling plane, and the horizontal direction is parallel to the rolling direction [217].

The alloys were then plastically strained to 4% in tension. Dominant deformation mode changed from α''_D martensitic transformation to $\{332\}\langle113\rangle$ mechanical twinning and further to dislocation slip with increasing O content. α''_D appearing as slight acicular features were observed in OM for Ti-10Mo-0.4O. This phase as reported by XRD peaks on deformation microstructure had its highest volume fraction in Ti-10Mo-0.1O. This once again confirms the suppressing effect of oxygen on $\beta \rightarrow \alpha''$ transformation. Kim et al. [226] reported for Ti–22Nb–(0.5–2.0)O(at%) that 1 at.% increase of oxygen content decreases martensite start temperature (Ms) by 113°C. The decreased Ms due to oxygen addition was evidenced by shape recovery of Ti-23Nb-1O upon unloading in studies performed by Tahara et al. [227]. Nii et al. [228] confirmed this claim on Ti-23Nb by describing the formation of nanosized modulated domains in the β-matrix at 0.3 at.% oxygen. It was suggested that

these domains could suppress long-range martensitic transformation upon cooling after ST. Duan et al. [229] reported a similar finding on martensite suppressing effect by oxygen on Ti-23Nb-0.7Ta-2Zr during cooling. Based on these findings it is accurate to say that with sufficient content of oxygen in a given Ti-alloy, Ms can be suppressed below RT. In the work by Min et al. [217] on Ti-10Mo the corresponding habit planes of α″-martensite were determined as (334) and $(\bar{4}\bar{3}3)$. The (334) habit plane was confirmed in [230, 231] for β-Ti alloys. Martensitic transformation is accompanied by an introduction of lattice defects, such as stacking faults and dislocations. This accommodates the transformation misfit [135, 232].

Twins appeared as plate-like features in all alloys and their area fraction decreased with increasing oxygen content (Fig. 2.38). Specifically, the twinning systems activated were the $(233)[\bar{3}11]$ and $(\bar{3}\bar{2}3)[\bar{1}31]$. Both systems have a SF of 0.446 which is the maximum SF implying that twinning obeyed the Schmid law.

EBSD revealed that most of α″ martensite and twins coexisted in the same plates (Fig. 2.39d, e and f). With increasing oxygen content, line-like features (indicated by white arrow in Fig. 2.40) formed in the Ti-10Mo-0.4O alloy. These features were identified as slip traces [233, 234]. The slip systems were either $(\bar{2}11)[111]$ or $(\bar{1}21)[\bar{1}\bar{1}1]$ with a SF of 0.343.

The presence of ω_D was not verified as the XRD peaks did not really differ in intensity and shape from the undeformed samples and ω_D is too fine to be resolved by EBSD.

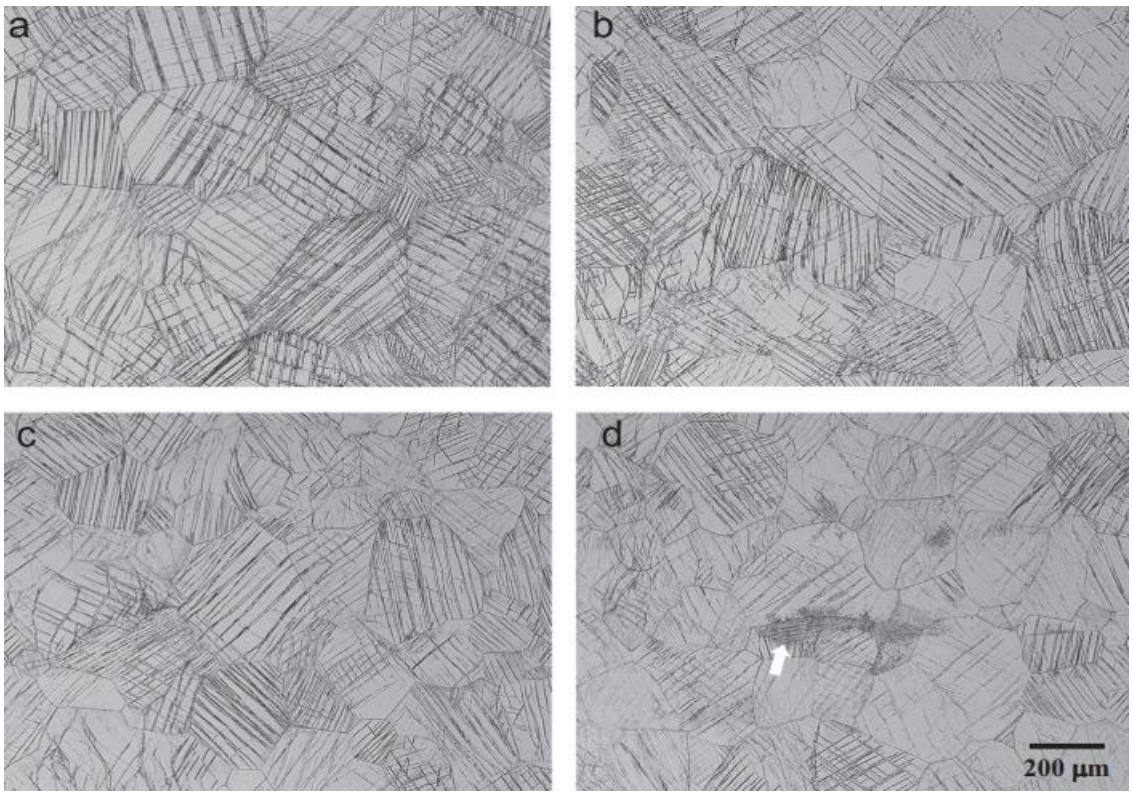

Figure 2.38. Optical micrographs of (a) Ti–10Mo–0.1O alloy, (b) Ti–10Mo–0.2O alloy, (c) Ti–10Mo–0.3O alloy and (d) Ti–10Mo–0.4O alloy. All have been strained to 4%. The observed plane is the rolling plane, and the horizontal direction is parallel to the RD (tensile axis) [217].

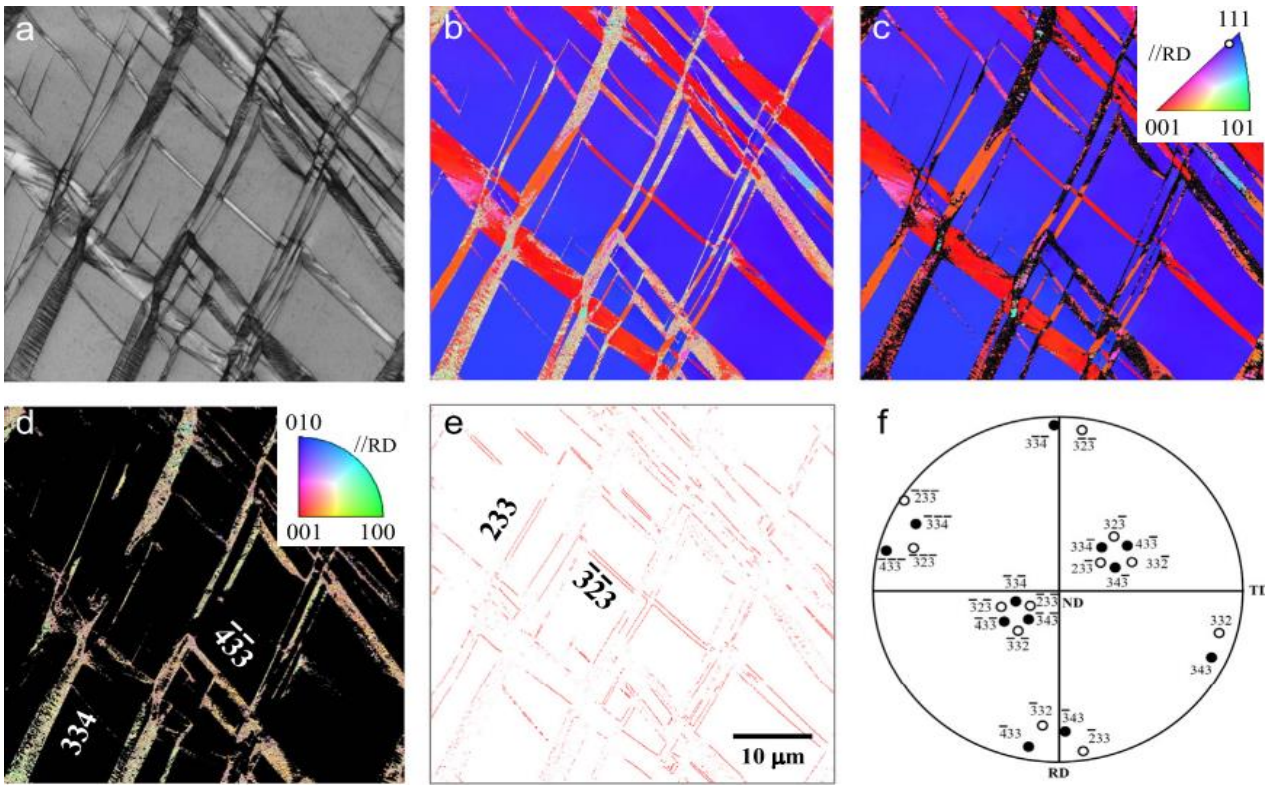

Figure 2.39. EBSD maps for RD of Ti–10Mo–0.2O alloy after strained to 4%: (a) image quality map, (b) inverse pole figure map, (c) β phase map, (d) α″ phase map, (e) twin boundary map and (f) corresponding stereogram (open circles for twins, solid circles for α″ phase). The observed plane is the rolling plane, and the vertical direction is parallel to the RD (tensile axis) [217].

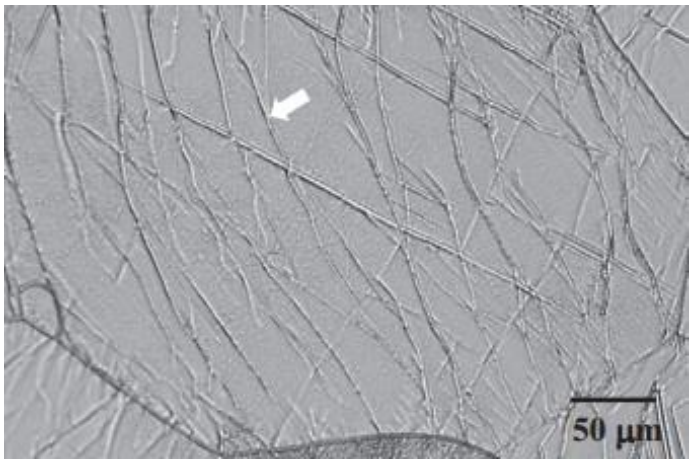

Figure 2.40. Ti–10Mo–0.4O alloy strained to 4%. The observed plane is the rolling plane, and the horizontal direction is parallel to the RD (tensile axis) [217].

Strength increased but ductility decreased with increasing O content. This primarily reflects a transition of deformation mode from α_D'' martensitic transformation to $\{332\}\langle 113\rangle$ mechanical twinning and further to dislocation slip. It is also an indication of solid solution strengthening. The

YS and tEl of Ti-10Mo-0.1O of 615 MPa and 46% were respectively higher and lower than that of Ti-15Mo-0.1O [200] of 420 MPa and 61%. However, in Ti-15Mo-(0.3 and 0.4)O, the YS's of 940 and 1144 MPa were higher than values reported in Ti-10Mo-(0.3 and 0.4)O of 895 and 1035 MPa. This implies that with an oxygen content of 0.3 Wt. % or higher, the effect of solid solution strengthening is more pronounced in an alloy with higher Mo content. This further elucidates the fact that Ti-XMo-0.3O represents a balance between YS and tEl.

Ji et al. [82] produced Ti-7.5Mo-xO by cold crucible levitation melting under argon gas atmosphere and introduced oxygen (x = 0, 0.2, 0.3, 0.4 and 0.5 (Wt. %), nominal composition) into the alloy during this process. After this, it was hot forged and hot rolled at 1000 °C and 900 °C respectively and finally air cooled. Samples were then ST at 900 °C for 1 hr followed by water quenching. It was reported that the α''-phase bearing a fine acicular plate morphology with a lamella substructure formed as shown in Fig. 2.41. These α''-martensite laths contained internal Type I $\{111\}_{\alpha''}$-twins and Type II twins which shared $\langle 211 \rangle$ direction in martensite. This observation agrees with reports of as-quenched α'' in Ti-Mo [235-237], Ti-Nb [238, 239] and Ti-Ta [240] all of which are β-Ti alloys. Volume fraction of α''-phase gradually decreased with increasing content of oxygen as shown in the XRD pattern of Fig. 2.42. At a weight percentage of 0.4, hcp α-phase bearing a lenticular morphology was detected on the $(11\bar{2}0)$ plane. This suggests an initial α-phase stabilising effect of oxygen. Interestingly at a weight percentage of 0.5, oxygen functioned as a dual α-phase and β-phase stabiliser. This is a plausible claim because there was an increase in α-phase volume fraction with a concomitant increase in XRD peak corresponding to $(110)_{\beta}$ and $(200)_{\beta}$. The latter occurrence denotes a sufficient level of oxygen content which triggered a suppressing effect on the $\beta \rightarrow \alpha''$ transformation.

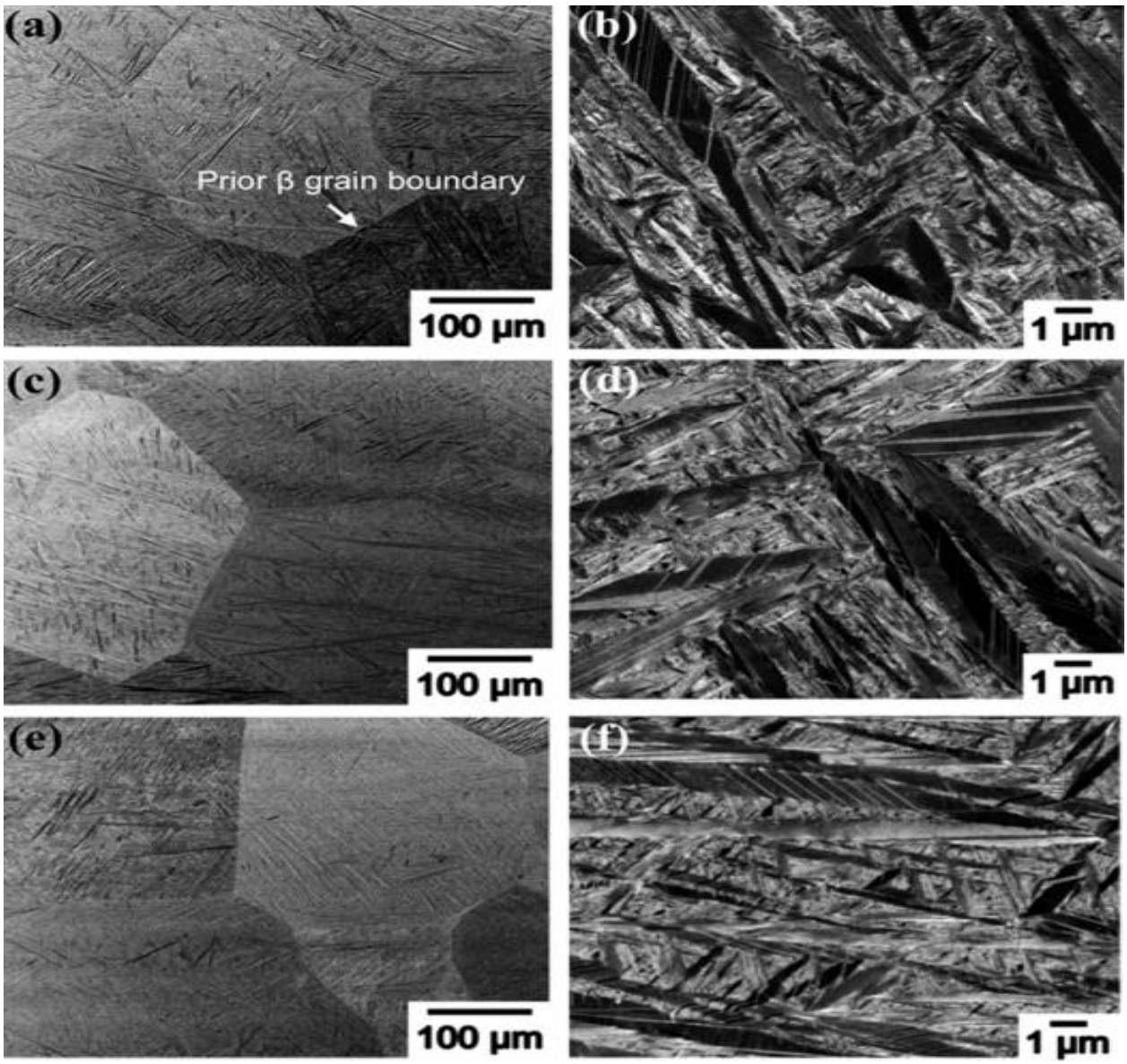

Figure 2.41. Low-magnification and high-magnification backscattered electron (BSE) images of the as-quenched microstructures taken from Ti-7.5Mo alloys with different levels of oxygen: (a)-(b) 0O, (c)-(d) 0.2O, (e)-(f) 0.3O [82].

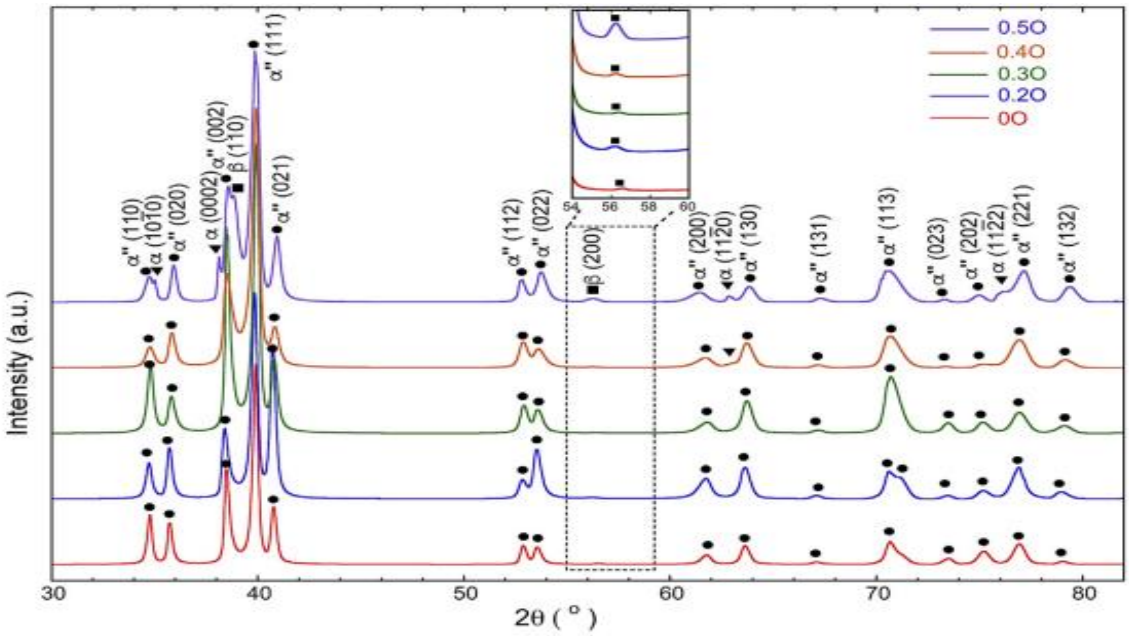

Figure 2.42. X-ray diffraction (XRD) profiles of the as-quenched Ti-7.5Mo-xO (x = 0, 0.2, 0.3, 0.4 and 0.5 (Wt. %)) alloys [82].

According to the theory of martensitic nucleation proposed by Ghosh and Olson [241, 242], interstitial elements such as oxygen may induce large local strain fields. These fields act as obstacles to dislocation motion and thus enhance the frictional work (Wf) against the motion of martensite interface [242, 243]. Wf is dependent on atomic fractions of alloying elements and it lowers MS temperature. The critical condition for martensite to nucleate is given by Eq. 11 [241]. For martensite in solid solutions Wf comes solely from solution hardening. The claim on oxygen induced strain fields is corroborated in Ref. [244]. These strain fields induce a domain structure (lattice modulation) and suppress long-range martensitic transformation. 1 at. %O produced nanosized modulated domains in β-matrix. Due to shuffling process, the nanodomains may grow as the temperature decreases. The growth of a particular nanodomain variant is suppressed by the local barriers presented by other nanodomains variants. This thereby inhibits long-range martensitic formation. Similar suppression of long range martensitic transformation by nanodomains impurity has been reported in Ti-Ni-based alloys [245, 246]. Obbard et al. [247] reported that oxygen raises the critical stress required to induce martensitic transformation and reduce the transformation strain in Ti–24Nb–4Zr–8Sn–(0.08–0.40)O (Wt.%). This report was confirmed by Kim et al. [226].

$$\Delta G_{ch} + \Delta G_{\sigma} = -\left(W_f + G_0\right)$$ Equation 2.10

Where ΔG_{ch} represents chemical thermodynamics, ΔG_{σ} is the applied stress and G_0 stands for nucleant potency.

Oxygen content did bear directly upon mechanical properties but was discerned to produce an overall combined effect with the martensite phase and other phases formed. Mechanical properties can be directly linked to the emerging martensite LP after an oxygen doping process. These parameters have been confirmed to generally disproportionately increase with higher oxygen content [82]. However the "b" dimension in an orthorhombic geometry is an exception to this finding as it increases slightly but begins to decrease above an oxygen content of 0.2 Wt. % as shown in Fig. 2.43b. LP ratio ($b_{\alpha''}/a_{\alpha''}$) decreases with increasing oxygen content as shown in Fig. 2.43d. Composition affects LP which in turn affects rhombicity ($R,\sqrt{3a_{\alpha''}}/b_{\alpha''}$). Rhombicity affects how the α″- martensite accommodates strain and deformation [47, 214, 230, 248]. Unit cell volume for α″ gets larger with higher oxygen content.

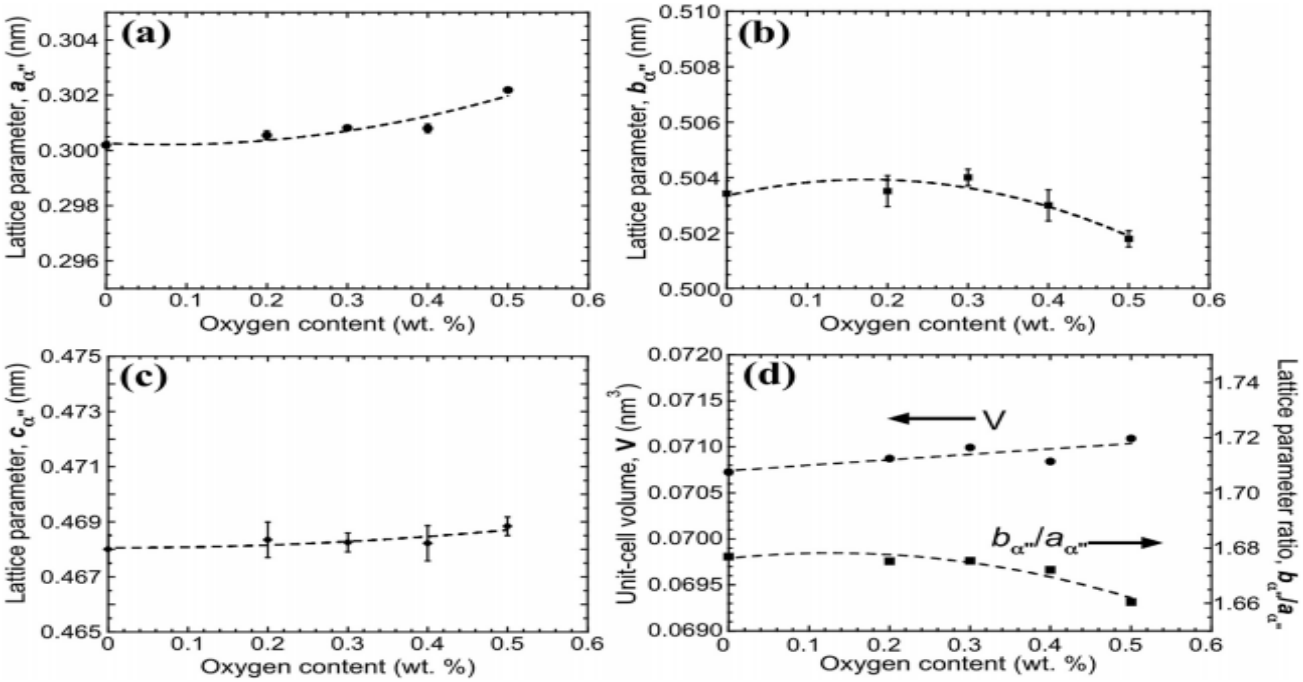

Figure 2.43. The dependence of LP on oxygen contents: (a) $a_{\alpha''}$ -axis, (b) $b_{\alpha''}$ -axis, (c) $c_{\alpha''}$- axis and (d) the unit cell volume and the axis ratio $b_{\alpha''}/a_{\alpha''}$ [82].

The YS, UTS, E-Mod and Hardness all showed an increasing trend with increasing oxygen content as shown in Fig. 2.44a and b. This is owing to the decreasing volume fraction of the α″-phase which is a softening phase and exhibits low strength upon fast cooling from the ST state [75, 236, 249, 250]. The solid solution strengthening effect of oxygen has also contributed to the observed trend in mechanical properties [241, 242, 251]. Samples with oxygen content of 0.4 and 0.5 Wt. % showed very little ductility due to the presence of the embrittling α-phase. The samples with lower oxygen content having zero to little volume fraction of α-phase were more ductile during uniaxial tensile test and alloy with 0.2-0.3 Wt. % of oxygen showed the best combination of strength and ductility [82]. 0 Wt. % O and especially 0.2 Wt. % O sample indicate possible TRIP effect is present in initial condition β-phase. There is also $\{111\}_{\alpha''}$ twinning plane in the α″ martensite.

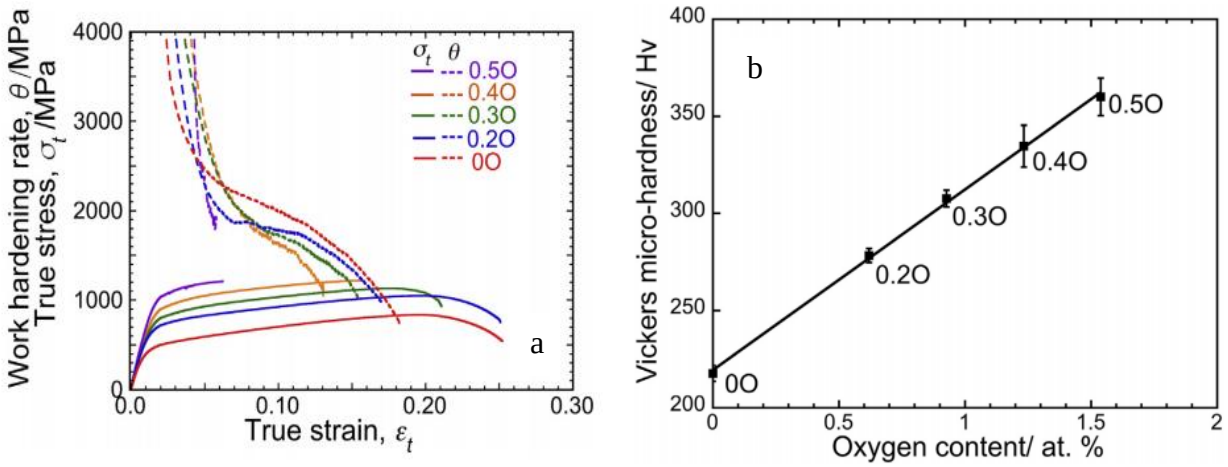

Figure 2.44a. True stress-strain and corresponding work-hardening rate curves of the as quenched Ti-7.5Mo-xO (x = 0, 0.2, 0.3, 0.4 and 0.5 (Wt. %)) alloys, (b). the dependence of Vickers micro-hardness on the oxygen contents [82].

2.8 Conclusion

An exhaustive literature review has revealed microstructural similarities between conventionally and additively manufactured metastable Ti alloys with β-twins and α″ martensite being the primary deformation mechanisms during uniaxial tensile and compressive tests. The simultaneous activation of both mechanisms has reportedly enhanced the alloy's plasticity but had very minimal impact on mechanical strength. α″ martensite has formed at very low surface fraction when the MoE factor of the alloy exceeded 20. However, it was ascertained that the conventional alloys exhibit more ductility at fracture, largely owing to the surface defects (i.e., pores, cracks and etc) present in the 3D printed alloys which occurs very sparsely in the conventional ones. Nevertheless, these defects do not have a significant impact on ultimate tensile strength as this property varies negligibly between the conventionally and additively manufactured alloys when the MoE factor are the same.

2.8.1 Knowledge gaps

Inspite of the in-depth studies of metastable Ti-alloys currently available in literature, there still exists inadequate knowledge in the following areas which this thesis would be addressing:

1. There has been microstructural characterisation and mechanical evaluation conducted by other authors on metastable Ti alloys additively manufactured by other Direct Energy Deposition methods, however not on alloys produced by the Laser Metal Deposition technique which employs a unique bidirectional deposition strategy. This will outline the benefits of the bi-directional deposition strategy in the experimentally determined yield strength, ultimate tensile strength, total elongation, and elastic modulus.
2. Data on the variation of deformation product morphology and density among the distinct microstructural zones in all deposited layers is absent in literature but addressed substantially in relation to parent β-stability, in this PhD thesis. Understanding of disparity in deformation mechanisms/accommodation of deformation products is key to understanding anisotropy in

mechanical properties. This understanding forms a basis for determining the required fabrication modifications and post-fabrication processing to achieve homogeneity.

3. Data on in-depth Schmid factor analysis for additively not conventionally manufactured metastable titanium alloys, for β-twins including twin variant identification/distribution is limited in literature but sufficiently addressed in the current study. This analysis allows the determination of not just the dominant β-twin system but also the prevalent twin variant within a given twin system and if there be a preferential nucleation site and growth mechanism for these variants. An understanding of this, has a direct connection with the mechanical properties.
    a. Analytical study of specific columnar grains which span the FZ, RZ and HAZ and drawing correlation between columnar grain size / β-stability / orientation with deformation product morphology and density is addressed in the current work but absent from literature data.
4. The use of differential scanning calorimetry to determine temperature ranges for phase transformation and potential recrystallisation, as a basis for heat treatment and thermomechanical processing schedule is presented in the current work but absent in literature. The aim of post-fabrication heat treatment is chemical homogenisation and a refined grain structure which replaces predominant columnar grain structure with fragmented ones or equiaxed grains. The ultimate advantage would be the attainment of isotropic mechanical properties
5. Thorough quantitative and qualitative elemental analysis of post-heat treatment microstructure is absent from literature. The current study fills this gap by investigating extent of homogenisation in comparison to AB microstructure, on a microstructural zonal basis at sub-β-solvus temperature. Same analysis is conducted on samples subject to super-β-solvus temperature where prevalent data in literature lays claim to homogenisation of metastable

titanium microstructure at 1200°C after 6 hours of holding, without a convincing substantiation of this claim by EDS point, line, or area analysis.

6. Fractograph comparison of deformed AB and HT alloys and the effect of heat treatment on average porosity has been delineated in the current work as it is absent from literature even though it is key to understanding plastic behaviour during uniaxial tensile test.

3 Experimental equipment and methodology

In this chapter, a description of the bi-directional LMD process used in the manufacture of metastable β Ti-15Mo-0.25O is presented. Metallographic preparation methods with associated pattern acquisition/imaging techniques are also delineated.

3.1 Composition of material

Alloy studied in this project have composition listed in Table 3.1. Nominal concentrations of Ti and Mo which are considered heavy elements were determined by EDS area analysis. concentration of light elements including O and N were measured with Instrumental Gas Analysis (IGA) on a LECO TC500 (Laboratory Equipment Corporation) analyzer with the inert gas fusion method [252]. The sample is placed in a graphite crucible and inserted into a furnace, where it is held between the electrodes. After purging with an inert gas (He or Ar), a high current is passed through the crucible, creating a temperature increase (above 2500ºC). Any gases generated in the furnace (CO, CO_2, N2 and H2) are released into a flowing inert gas stream, which is directed to the appropriate detectors: infrared for O measured as CO and CO_2, or thermal conductivity for N. Instrument calibration is performed using known reference materials to bracket the concentration range of materials to be tested. The reported values are the average of at least three measurements. The density of AB sample was determined to be $36.5 \pm 0.05\ \mathrm{mg/mm^3}$.

Table 3.1. Ti-15Mo-xO alloy composition

	Powder composition		AB composition			
Element	Nominal	Analysed	Ti	Mo	O	N
Wt. %	Ti-15Mo-0.15O	Ti-15Mo-0.18O	85.88±0.69	14.12±0.69	0.25±0.05	0.028±0.003

3.2 Laser Metal Deposition Process

Powder deposition was conducted using a TRUMPF TruLaser Cell 7020 (Fig. 3.1a) on a CP Ti substrate (Fig. 3.1b) of dimensions $100\mathrm{mm} \times 200\mathrm{mm} \times 10\mathrm{mm}$. Water atomized Ti-15Mo pre-alloyed powder in the diameter range of 50–100 μm was used for bi-directional laser metal deposition (LMD) of this alloy as illustrated in Fig. 3.2. A total of 25 layers were deposited at the layer thickness

of 0.2mm (Z-axis). Fabricated coupon dimensions (Fig. 3.3 and 3.4) were 41mm × 12.5mm × 5mm (l x w x h). Alloy was fabricated by ball milling of Ti-15Mo and TiO_2 powders together. Powder sizes for Ti-15Mo and TiO_2 were 50-100μm and <5μm, respectively. Ball milling process was performed using SFM-1 (QM-3SP2) high speed shimmy ball mill. A 250g stainless steel ball was used with a ball to powder ratio of 1:1. Rotation of the ball mill was at a speed of 500rpm with total process duration of 15 minutes. Process parameters are listed in Table 3.2 (for more details please refer to Ref. [9]). Argon (Ar) was used as protective atmosphere.

Cooling rate and stabilization temperature listed in Table 4.1 was taken from Table 3 in Ref. [9]. It was determined from simulations using the DED module in Simufact Welding for Ti6V-4Al alloy. The thermal and physical properties vary significantly with temperature from RT to the molten state. No such temperature-dependent data exists for Ti-15Mo and most other Ti alloys. The predictions based on Ti-6Al-4V for Ti-15Mo provide a useful guideline or general trend. The data is for the central points of layers, which was now amended in the note to Table 3: "Note that cooling rate and stabilized temperature were determined from simulations for central points of layers 1, 8, 13 and 18 using the DED module in Simufact Welding for Ti-6V-4Al alloy and used here in order to illustrate the trend".

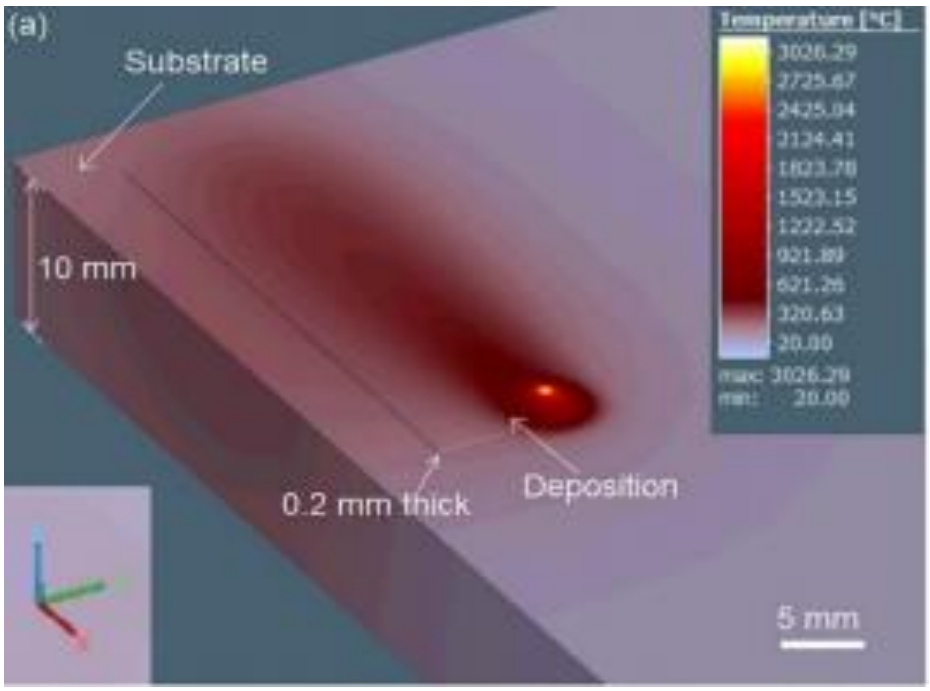

Figure 3.1. TruLaser Cell 7020; (b). LMD process of a rectangular coupon on a 10 mm-thick CP Ti substrate [9].

A bidirectional scanning strategy (illustrated in Figure 3.2 and 3.3), i.e., alternate unidirectional scan along the length (X-axis) and width (Y-axis) directions from one layer to the next was used. Odd numbered layers were scanned in the length direction while even numbered layers were scanned in the width direction [9]. This bidirectional scanning strategy is expected to minimize the residual stress in the as as-built rectangular base Ti-15Mo coupons shown in Figure 3.4 [9]. LMD processing parameters are listed in Table 3.2.

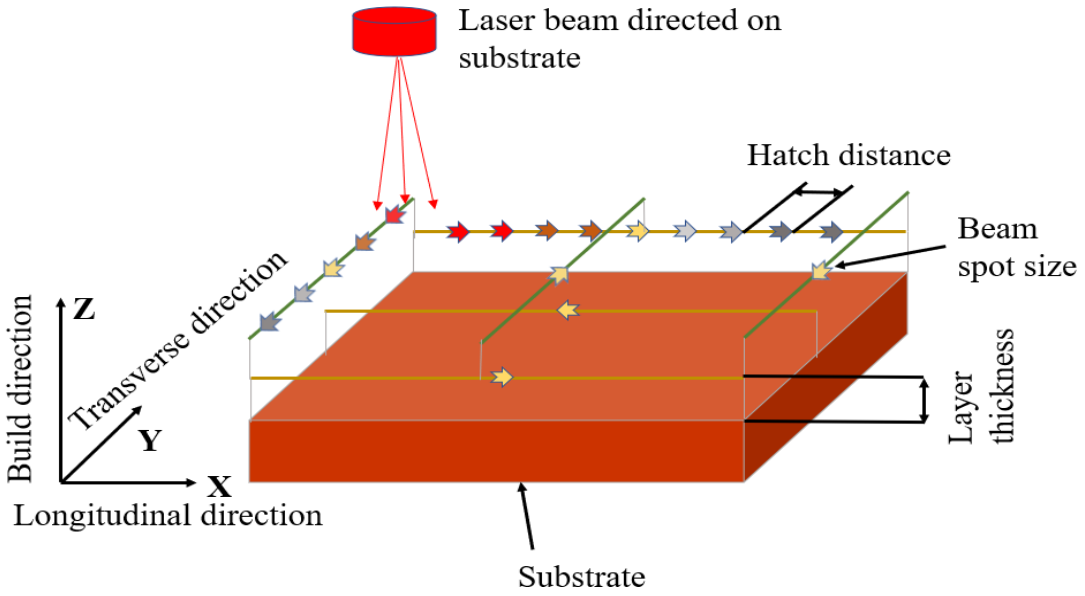

Figure 3.2. Schematic diagram of laser metal deposition.

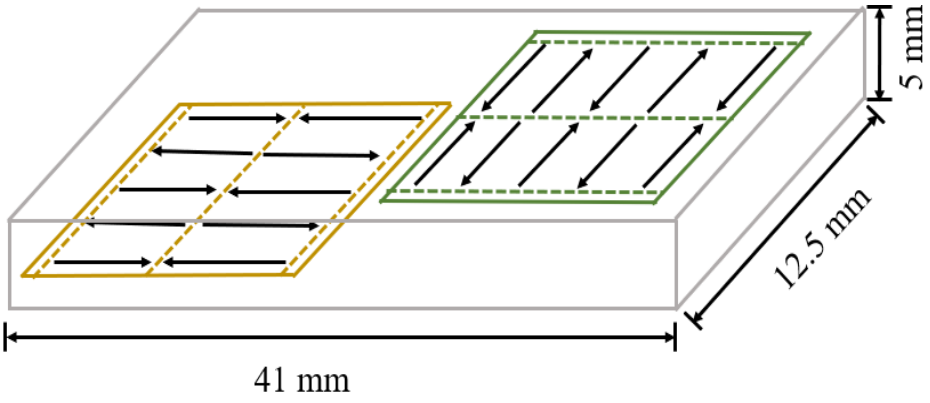

Figure 3.3. Schematic showing build sequence with odd numbered layers and even numbered layers scanned in the length and width directions, respectively.

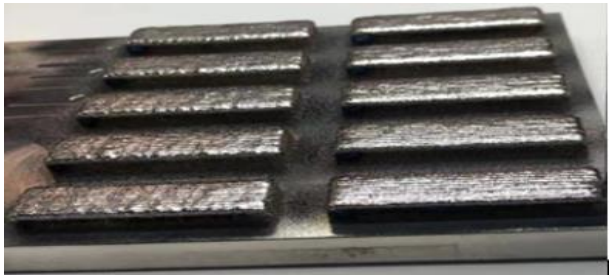

Figure 3.4. As-Built 10 coupons built via LMD process on one plate [9].

Table 3.2. Detailed LMD processing parameters [9].

Laser wavelength (nm)	Laser spot size (nm)	Laser Power (W)	Laser Transverse speed (mm/min)	Laser energy density (J/mm^2)	Powder flow rate (g/min)	Step-over width (mm)	Carrier gas (Ar) flow rate (l/min)	Shielding gas (He) flow rate (l/min)
1030	1.5	500	800	25	1.2	1.05	10	16

3.3 Sample machining

All samples were cut using a computer-controlled wire-cut Electric Discharge Machining (EDM) process from coupons shown in Fig. 3.4. Fig. 3.5 represents a schematic of the directions in which samples were extracted. X-Ray Diffraction (XRD) and Scanning Electron Microscopy (SEM)/Energy Dispersive X-Ray Spectroscopy (EDS)/Electron Backscatter Diffraction (EBSD) samples were $6\ mm \times 12.5\ mm \times 5\ mm$ in dimension. Surface area for XRD and SEM samples spanned from layer 1 to 25. 6 samples for LECO instrumental gas analysis measured $5\ mm \times 6.25\ mm \times 5\ mm$ each. LECO samples thickness had a span of half the total number of layers in the Z-direction.

TMCP samples were cut to dimension, $6mm \times 4mm$ ($L \times \Phi$) with the cylinder length along the longitudinal axis and the flat surface of the cylinder on the Y-Z plane of the AB coupon. This is illustrated by the red and black schematics of Fig. 3.5.

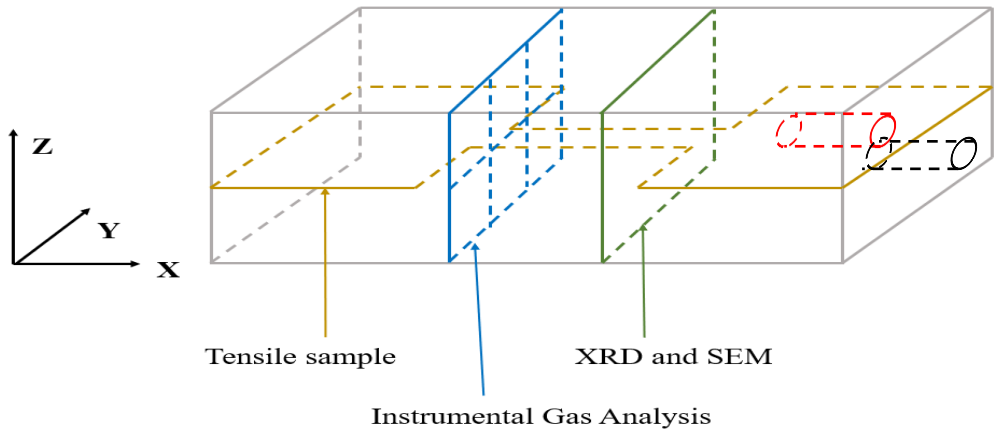

Figure 3.5. Schematic showing orientations of the machined samples.

Dog-bone-like tensile specimens shown in Figure 3.6 were machined to gauge dimensions of $10.26 \pm 0.1mm \times 2.56 \pm 0.2mm \times 1mm$ (l x w x t) in conformance to proportionally scaled

down ASTM E8/E8M standards [253]. The standard specifications for 12.5mm wide specimen provided the closest match to LMDed coupon of this study which is also 12.5mm wide in the AB state. This standard requires a total length (200mm) to gauge length (50mm) ratio of 4:1. As seen in Fig 3.6, the total and gauge length of specimen used in this study are 41mm and 10.26mm, receptively which also yields a ratio of 4:1. According to the same standard, gauge length (50mm) and gauge width (12.5mm) should have a ratio of 4:1 and the ratio of 10.26mm: 2.56mm obtained in this work conforms to this requirement. The standard does not stipulate a specific requirement on gauge thickness as it allows flexibility based on material thickness which is machined to 1mm in this study. Two test samples were machined with width spanning from layer 8 through 12 and from 13 through 17 along the Z-axis. This was a measure taken to confirm accuracy/repeatability of test results.

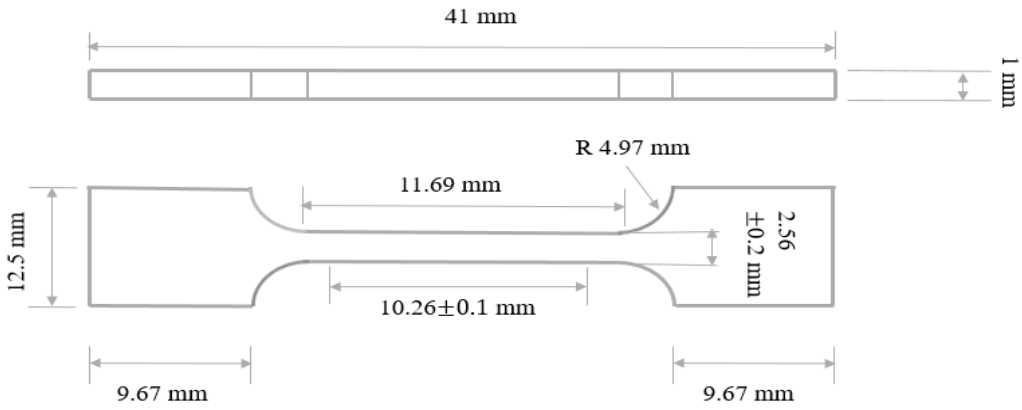

Figure 3.6. Dog-bone like specimen machined using EDM for tensile test.

3.4 Sample metallographic preparation

3.4.1 X-Ray Diffraction

Samples were ground manually with 500 grit-pad with flowing tap water for about 5 minutes before commencing XRD process.

3.4.2 Scanning Electron Microscopy, Energy Dispersive Spectroscopy, Electron Backscatter Diffraction and Tensile Samples

Each SEM/EDS/EBSD sample was hot mounted on polyfaster material of 30 mm diameter using Struers Citopress-20 [254] (Fig. 3.7). The polyfaster is a thermosetting polymer-based resin of black

Bakelite containing carbon filler which serves as good electrical conductor for SEM. Metallographic preparation steps were customized in-house at the Electron Microscopy Center of UOW according to the general ASTM standards [255]. Sample was polished using Struers Tegramin-21 [256] (Fig 3.8). Sample was ground with 500 and 1200 grit for about 5-10 minutes each. It was then ground with 2000 grit Silicon Carbide (SiC) foil for 5 minutes. Polishing followed with 3 and 1 μm diamond for 30 minutes each on a nap pad. Nap pad was in new condition, cleaned thoroughly with soap between polishes. Polishing continued with oxide polishing suspensions (OPS) for 5 minutes. OPS was 1/5 diluted to 500 mL with water, 2 mL of peroxide solution and 2 mL of ammonia solution. This was done in counter-rotation and 10 Newton (N) of force on a Chem pad which was pre-wetted and in a very good condition. Sample was then rinsed with tap water and soap and then sonicated in a solution of ethanol and water immediately after the OPS step was finished and finally dried in air blower before microscopic characterisation.

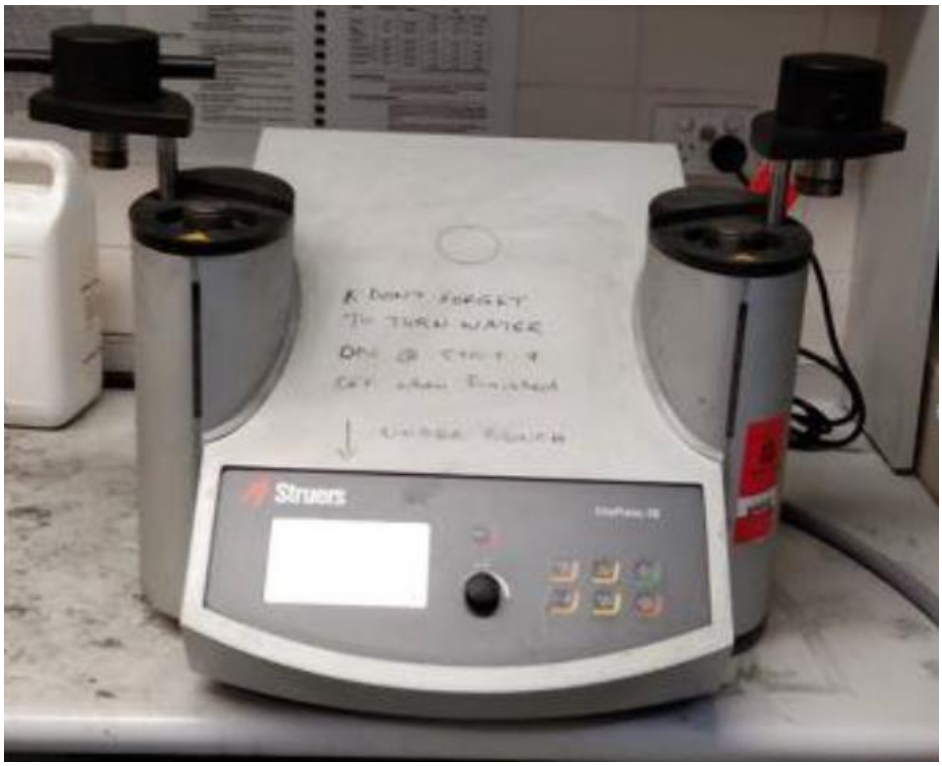

Figure 3.7. Struers® CitoPress-20 hot mounting press.

Figure 3.8. Struers® TegraPol-21 Grinder polisher.

3.4.3 Transmission Electron Microscopy

Focused Ion Beam FEGSEM (i.e. FEI Helios NanoLab G3 CX) [257] (Fig. 3.9) was used for preparing site- and orientation specific lift-outs with [113] and [110] plane normal for TEM investigation. The ideal lift-out orientation was computed using EBSD map data and the Crystal Aligner code [258]. A multi-step process was used for the lift-outs. The specimen was ion milled on the Leica EM TIC020 (triple ion cutter) system. This uses 3 broad Ar ion beams to gently remove material leaving a smooth clean surface. A 25x1x1µm protecting layer of carbon was deposited using the ion beam at 30kV and 0.23nA. Initial trenching was conducted at 30kV and ~21nA followed by rough polishing at reduced current of 9.3nA (±2°) to yield a lamella ~20µm long and 1.5µm thick. The nano-manipulator needle was welded with the I-beam at 18pA with platinum and the lamella lifted for in-situ thinning. Coarse thinning and ion polishing was undertaken at 30kV, 2.5nA-0.23nA with ±1.8° tilt (which was maintained for all thinning stages) and 8µm thickness (equivalent Si) per pass. With each step per side the width of the thinning window was reduced by ~1µm to prevent over-thinning at the window extremities. Final polish was conducted at 5kV and 68pA (±5°), single pass

removing 100nm (equivalent Si) and again at 2kV and 72pA. The final polish was performed in 4µm wide windows rather than across the whole lamella to maintain structural rigidity.

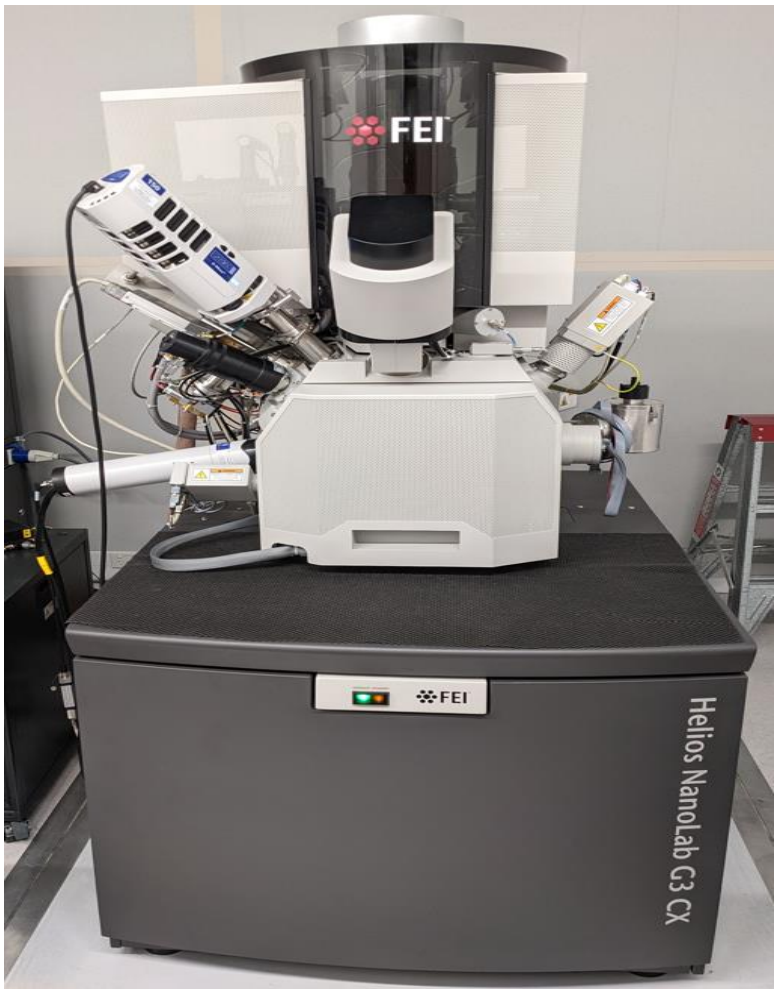

Figure 3.9. FEI Helios NanoLab G3 CX

3.5 Techniques for analysis

Prior to commencement of pattern acquisition and microscopic imaging, polished samples were iteratively inspected to ensure absence of metallographic defects.

3.5.1 Patterns and Imaging

3.5.1.1 X-Ray Diffraction

XRD was carried out using GBC MMA X-ray diffractometer [259] (Fig 3.10) fitted with a Cu-K_α tube at a wave length of 0.15406nm. Operating Cu tube current and voltage were 28.4mA and 35kV, respectively with a 1000W power supply. 2θ ranged from 20° to 105°-120° depending on expected phases in the different results chapters. A scanning step size of 0.02° and a scan rate of 1°/minute were employed in pattern generation.

Data analysis was carried out in Traces® and Match-3® software's. XRD data was first processed by performing a $K\alpha_2$ strip. Peak threshold was set to a factor of 3. Powder diffraction File (PDF) cards for α-, β-, ω-, α′- and α″- phases in Ti-Mo and Ti-Nb alloys were obtained from PDF4 database. Peak intensity given in counts provides information on the multiplicity and texture of a specific plane. From Bragg's law (Eq. 3.1) [260], a shift in peak to the right which implies an increase in 2θ angle is an indication of an increase in d-planar spacing. This also indicates a decrease in crystallite size of a plane. In this equation n represents the order of reflection, which is an integer, λ is the wavelength of X-ray beam, d is the inter-planar spacing and θ is the incident angle on the specimen. Peak width/shape gives an indication of the stored energy in form of microstrain and dislocation density. Full Width at Half Maximum (FWHM) gives an indication of variation in dislocation density.

$$n\lambda = 2d\ sin\ \theta \text{ [260]} \qquad \text{Equation 3.1}$$

Figure 3.10. GBC MMA X-Ray diffractometer.

X-ray diffraction (XRD) uses X-rays to investigate and quantify the crystalline nature of materials by measuring the diffraction of X-rays from the planes of atoms within the material. It is sensitive to both the type of and relative position of atoms in the material as well as the length scale over which the crystalline order persists. It can, therefore, be used to measure the crystalline content of materials; identify the crystalline phases present (including the quantification of mixtures in favorable cases); determine the spacing between lattice planes and the length scales over which they persist; and to study preferential ordering and epitaxial growth of crystallites. In essence it probes length scales from approximately sub angstroms to a few nm and is sensitive to ordering over tens of nanometers. In materials science to be specific, XRD can be used to examine crystal size, quantify microstrain, determine the dislocation density, measure crystallographic preferred orientation, quantify the volume fraction of phases within a specimen and also to determine the crystal structure of unknown samples such as corrosion products and new materials [261].

3.5.1.2 Field Emission Gun-Scanning Electron Microscopy/Energy Dispersive Spectroscopy

SEM Imaging was performed using the JEOL JSM-7001F instrument [262] (Fig 3.11) in the Secondary Electron Imaging mode. This is a 30kV analytical thermal field emission gun SEM capable of 3 nm spatial resolution. This microscope is equipped with EDS and EBSD detectors. SEM imaging was conducted at 10 kV (to yield slightly higher spatial resolution than 15kV while permitting Ti analysis) and 11nA. These parameters were selected to obtain both high spatial resolution and sufficient energy to see the Ti peaks. Dwell time was 100 μs.

ImageJ freeware [263] was used to determine grain sizes and other microstructural features listed in Table 4.1. 15 grains on 20 lines were used in determining grain sizes for columnar grains calculated using the line intercept method according to ISO 643:2012 [264]. The equivalent grain diameter method on 20 grains yielded sizes of equiaxed grains [264].

SEM uses a focused beam of electrons to create a magnified image of a sample. The electron beam is scanned in a regular pattern across the surface of the sample and the electrons that come out of the sample are used to create the image. The SEM is a tool for creating images of the otherwise invisible worlds of microspace (1 micrometer = 10^{-6}m) and nanospace (1 nanometer = 10^{-9}m). SEMs can magnify an object from about 10 times up to 300,000 times. A scale bar is usually provided on an SEM image. The scale bar is used to calculate the sizes of features in the image.

SEM images have no colour (but may be artificially colored), they may look quite three dimensional (due to depth of field) and they show only the surface of the sample (due to minimal penetration of the electron beam into the sample).

Detectors on SEMs can routinely capture two different types of SEM image: a secondary electron image or a backscattered electron image. The shades of grey in a secondary electron image are created by the topography of the sample. The shades of grey in a backscattered electron image stem from the atomic weight of the constituent elements in the sample [265].

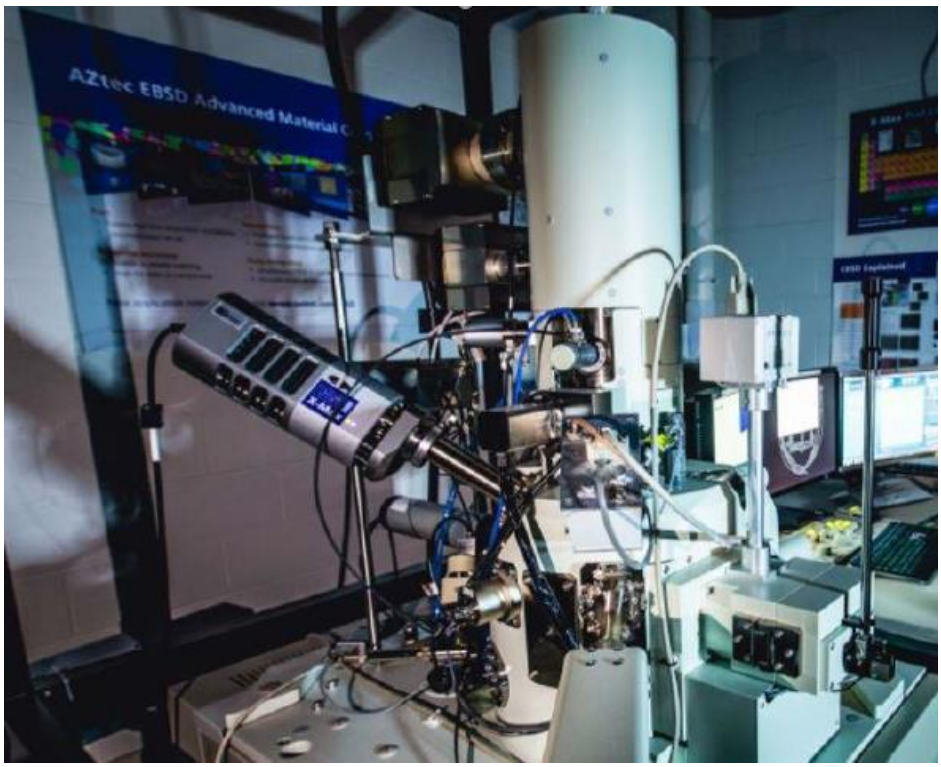

Figure 3.11. Field emission gun JEOL JSM-7001F SEM system equipped with EDS and EBSD detectors.

In the current study, the high-count rate advanced EDS detector of Figure 3.11 was operated at 10 kV. Area scan, line-scan and point analysis modes were used for data acquisition. The standardless method was used for data analysis in Aztec® software.

EDS is one technique within the grouping known as microanalysis. Microanalysis the identification of the chemical elements present either within or on the surface of an object, and additionally, how the atoms of the elements are arranged with respect to each other. Identification of the elements present may be qualitative or quantitative. Different isotopes of the elements, or their ratios, can also be measured. Microanalysis can also require working out the spatial relationships between the atoms in the object, i.e., its structure, particularly if it is crystalline. Some micro-analytical techniques can provide information about crystal defects, chemical bonding or redox state. In microanalysis, the analytical spot size ranges from about 100μm to 100nm, although many techniques are capable of generating maps of larger areas millimeters or centimeters across. The depth of the analysis is also important, and some techniques will analyse only the top few nanometers of the sample (surface

techniques) while others will penetrate to depths of several microns. Smaller length-scales (<100 nm) that allow analysis at molecular or atomic resolution are part of nanotechnology or nano-analysis.

An electron beam is focused on the sample in either a scanning electron microscope (SEM) or a transmission electron microscope (TEM). The electrons from the primary beam penetrate the sample and interact with the atoms from which it is made. Two types of X-rays result from these interactions: Bremsstrahlung X-rays, which means 'braking radiation' and are also referred to as Continuum or background X-rays, and Characteristic X-rays [266].

The X-rays are detected by an Energy Dispersive detector which displays the signal as a spectrum, or histogram, of intensity (number of X-rays or X-ray count rate) versus Energy. The energies of the Characteristic X-rays allow the elements making up the sample to be identified, while the intensities of the Characteristic X-ray peaks allow the concentrations of the elements to be quantified.

The detection limit of EDS analysis in the SEM depends on the composition of the sample being analysed but is in the range 0.1-0.5 wt%. It is an effective technique for major and minor element analysis but lacks the sensitivity for light elements such as O and N. EDS data may not be accurate in the presence of sub-surface inhomogeneity such as shallow boundaries, buried phases, channeling contrasts and cavities. In this case the observer should be mindful of detector shadowing and align features accordingly and accept that any quantitative data will have large errors.

EDS is considered a non-destructive analytical technique, that is, the sample can be re-analysed many times. Most materials will experience some damage under an electron beam, and some samples are particularly susceptible, e.g., clay minerals and glasses. No special sample preparation, other than that required to image the sample in the SEM or TEM, is required for qualitative analysis, but for quantitative analysis in the SEM the sample must be bulk, flat and polished.

As in SEM and STEM imaging, the electron beam can be rastered over an area of the sample to produce X-ray element distribution maps [266].

3.5.1.3 Electron Backscatter Diffraction

EBSD is an SEM-based method that provides crystallographic data regarding the microstructure of a sample. This method involves interaction between an electron beam and a slanted crystalline sample, and the diffracted electrons create a pattern that can be identified with a fluorescent screen [267].

JEOL JSM-7001F shown in Fig. 3.11 was used to conduct EBSD map acquisition with spatial resolution of 3 nm. The 7001F SEM comprised of a high-resolution Nordlys II(S) EBSD detector. Map was acquired using Oxford Instrument's Aztec software at an accelerating voltage of 15kV, a probe current of 6.5nA, a working distance of 20 mm and a step size of 0.2μm for high resolution maps and 2μm for low resolution maps. A 4×4 binning was used, with up to 11 Kikuchi bands indexed using the refined accuracy algorithm. During EBSD map acquisition, the matrix was indexed as body centered cubic Ti-Mo (space group = $Im\bar{3}m$) with a LP of 0.325 nm, whereas the orthorhombic stress-induced α'' martensite (space group = CmCm) was indexed using LPs of a = 0.306 nm, b = 0.491 nm and c = 0.462 nm. All LPs were obtained from XRD.

Prior to data analysis, The sample coordinate system (CS0) was defined as follows: The longitudinal X-axis was parallel to the rolling direction (RD), the Y-axis was parallel to the transverse direction (TD) and the Z-axis which is the build direction was parallel to the normal direction (ND) according to the standard ISO/ASTM 52900-15 [268] for AM technology. Analysis was performed in the HKL-Channel 5® [269] and ATEX® [270] softwares. This involved the removal of orientation spikes followed by cyclic extrapolation of zero solutions down to five neighbours followed by thresholding the band contrast to exclude regions where no indexing was possible. A minimum area of 3 pixels and 2° of critical misorientation angle were used for grain detection. Boundary misorientations (θ) between $2° \leq \theta < 15°$ were defined as low angle grain boundaries (LAGBs), whereas boundary misorientations $\theta \geq 15°$ were classified as high angle grain boundaries (HAGBs). The misorientation angle distributions of the β-phase were used to identify twin boundaries: 50.58° misorientation angle around the $\langle 101 \rangle_\beta$ axis corresponds to $\{332\}\langle 113 \rangle$ twin boundaries and 60° misorientation around

the $\langle 111 \rangle_{\beta}$ axis represents $\{112\}\langle 111 \rangle$ twin boundaries [24, 132, 206]. ATEX freeware was used for analysis of twinning systems.

Prior to ODF analysis both low- and high-resolution maps acquired from a given plane (i.e. X-Y or X-Z planes) were stitched together. In order to ensure that both planes match, the CSO was rotated by 90° aroung the X-axis for the X-Z sample before generating ODFs.

3.5.1.4 Fractography

Sample was mounted in the "as deformed" state onto the SEM stub and the fractured surface was observed. This was done on JEOL JSM-6490 LA [262] (Fig. 3.12) which is a 30 kV conventional tungsten filament, variable pressure SEM. The Secondary Electron Imaging (SEI) mode of SEM was used to generate images. Images were taken at a voltage of 15kV, 10 mm working distance (WD) and 40 mm beam spot size.

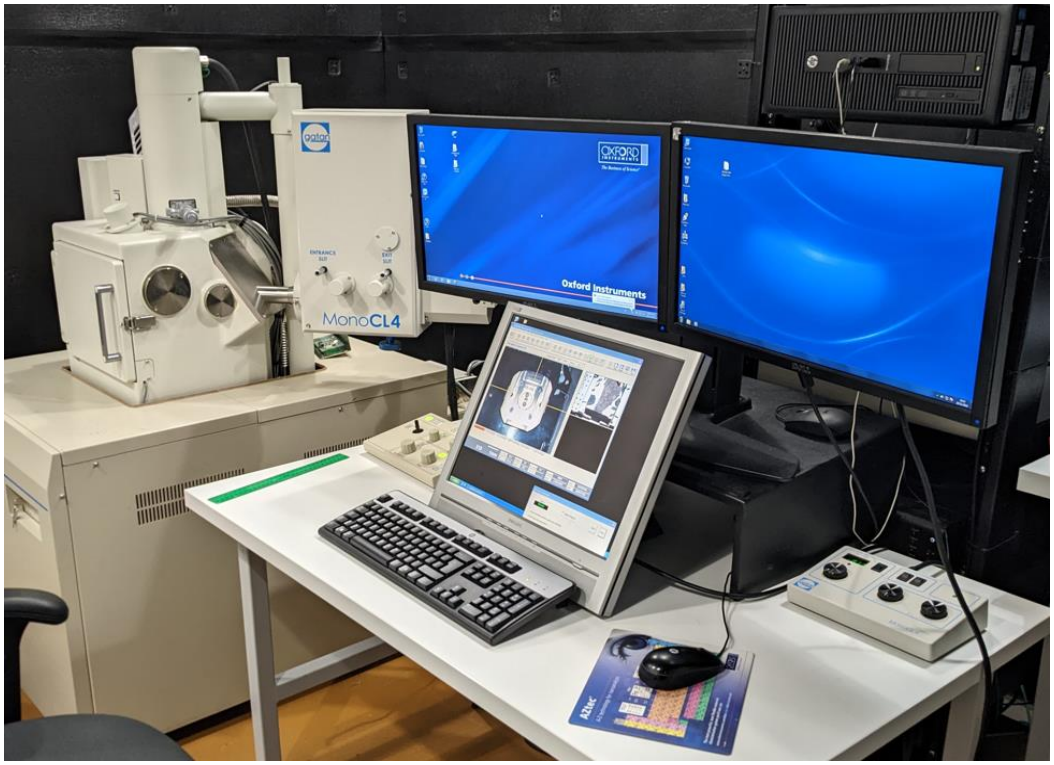

Figure 3.12. JEOL JSM-6490 LA for generating fractographs.

3.5.1.5 Transmission Electron Microscopy

Bright field (BF) images, selected area electron diffraction (SAED) patterns and dark field (DF) images were generated using JEOL JEM-F200 [262] (Fig 3.13) operating at 200kV with a resolution of 0.23nm. The F200 has 100µm, 50µm, 20µm and 10µm selected area apertures for creating selected area diffraction patterns. Note that this is the physical size of the aperture, not the effective size on the specimen. Here a picture was either taken with the aperture inserted, or a circle was placed indicating the area from which a pattern is formed. All images were collected on a 'Gatan RIO' CMOS® camera. This consists of a scintillator to convert the electrons to visible light. The light runs down optical fibers which are coupled to the CMOS detector. Note that older TEM cameras use CCD sensors rather than CMOS sensors. Some of the new fancy ones directly detect the electrons.

Data was subsequently analysed in Gatan Microscopy Suite® (GMS).

Figure 3.13. JEOL JEM-F200 equipped with Segmented Annular All Field Detector (SAAF) which is suitable for STEM imaging, Conventional STEM BF and ADF/HAADF detectors and a Gatan RIO CMOS TEM camera with 4k-by-4k resolution.

In conventional TEM specimen is illuminated with a broad, parallel beam of electrons. As illustrated in Fig 3.14, the specimen causes these electrons to scatter in a variety of ways. We have the direct beam which is principally composed of un-scattered electrons and in-elastically scattered electron at extremely shallow scattering angles such that they basically overlap. At intermediate angles we have diffracted electrons (coherent elastically scattered), and at higher angles we have incoherent, elastically scattered electrons which are basically like back scattered electrons in an SEM, except that they are still going forward.

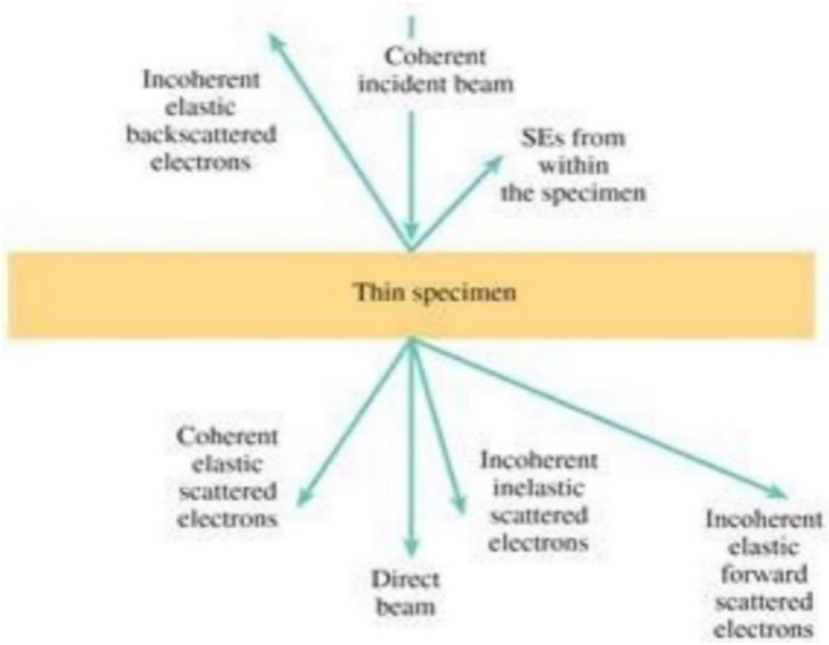

Figure 3.14. A schematic illustrating electron scattering after a specimen is illuminated with coherent incident beam [271].

As shown in Fig. 3.15, the objective lens brings these scattered electrons to focus, first as a diffraction pattern at the back focal plane (bfp), then as an intermediate image. By changing its strength, the intermediate lens in the projector lens system can select either the diffraction pattern or the image to project down onto the camera to be recorded.

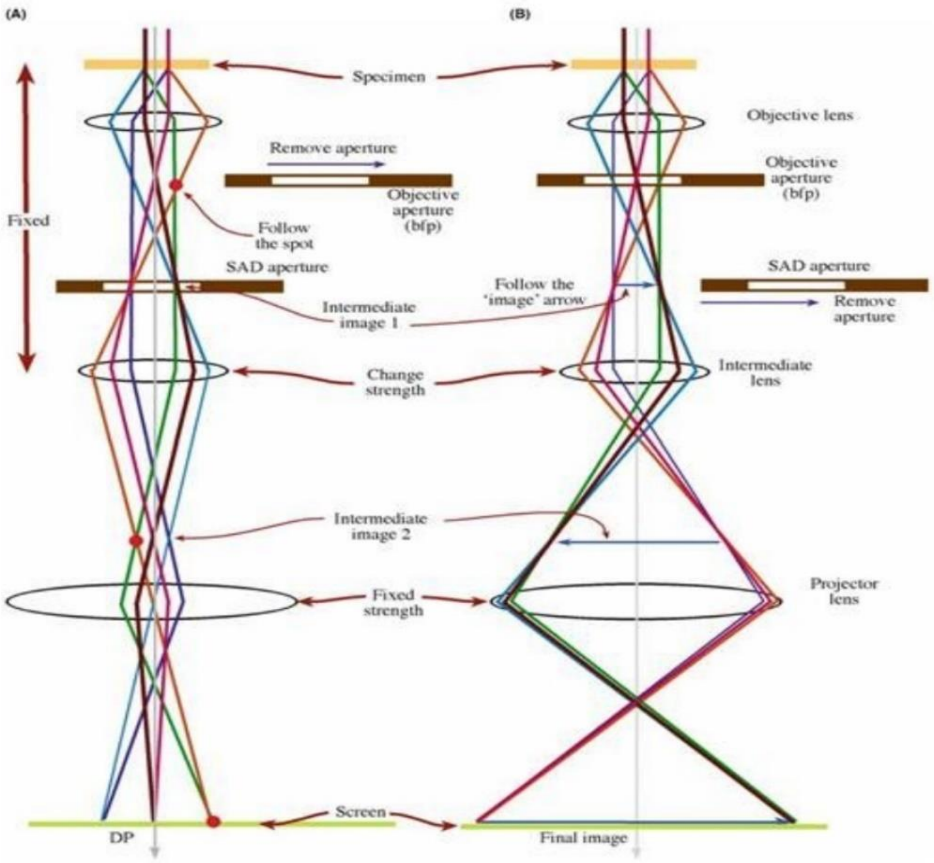

Figure 3.15. Diagram illustrating the function of the objective lens in bringing scattered electrons to focus [271].

These are the same electrons at both the back focal plane and the image plane, so apertures can be used to select which electrons can contribute to either the diffraction pattern, or the image. For example, we can use an objective aperture to admit the direct beam, but block the diffracted electrons, thus forming an image which will be darker in the strongly diffracting regions. This is known as a BF image and this is how most imaging are done in a TEM. However, while it creates plenty of contrast, it isn't always easy to understand why we have that contrast. Alternatively, the objective aperture can be used to only allow specific diffracted electrons, so the resulting dark field image is bright only where the crystal is strongly diffracting in that specific condition. For example, one might have a diffraction pattern which has unexpected diffraction spots, by creating a dark field image from the spots, one can find out which part of the material is responsible for it. This is a great way to highlight a precipitate for example. Alternatively, if 2 phases exist in a material, both will create diffraction contrast so it might not be possible to determine which is which from a bright field image, but they

should have distinct diffraction patterns from which they can be identified. Then, we can use a diffraction spot that is unique to each of those phases to form dark field images, thus making images that are bright only where those specific phases are. Similarly, we can often pick specific diffraction spots to highlight defects such as dislocations.

Diffraction patterns may also be collected from specific areas. While imaging the specimen a selected area diffraction aperture can be inserted at the image plane. With this only the electrons that come to that area will then contribute from the diffraction pattern, allowing us to form selected area diffraction patterns from either large, or very small areas depending upon the size of the aperture.

A major complication is that diffraction patterns change depending on the orientation of the crystal. Generally, the crystal is tilted to allow the observer to look down low index crystal directions, <100> or <110> for example, where the diffraction patterns are easy to index. In practice there exists a limited tilt range, and the process of tilting onto zone axis can be very difficult. Furthermore, some defects are only visible when viewed along specific orientations, which one needs to know from literature.

There also exists a mass-thickness contrast, i.e., the image will be darker in areas that are heavy or thick, and from phase contrast, where interference between electrons creates alternating dark and light bands. Thus, it is important that the observer understands what is contributing to the contrast and trying to emphasise the information of interest and deemphasise trivial information.

An inherent limitation of TEM is that only thin slices of a small amount of material can be analysed. Thus, it is pertinent that a microstructure is first understood on a larger scale before TEM analysis is conducted.

3.5.2 Differential Scanning Calorimetry

The STA 449 F5 Jupiter® equipment (Fig. 3.16) manufactured by NETZSCH Geratebau GmbH was used for Differential Scanning Calorimetry (DSC) experiments. It has a 124W capacity, a nominal current and voltage of 0.54A and 230V, respectively. Proteus® software version 6.1.x was used for data visualisation and analysis.

Figure 3.16. STA 449 F5 Jupiter® DSC equipment.

DSC is a simple and rapid method for determining the heat capacities of small samples (typically 1x1x1mm) over a wide range of temperature. The performance of most currently available DSCs is such that an accuracy of ± 1 to 2% should be routine but this can be undermined by unsuitable samples, incorrect calibration, or by inadequate data treatment. In any DSC experiment (Fig. 3.17) the response of the sample (subscript s) relative to that of an inert reference (subscript r) is monitored as the two are heated, or cooled, at a constant rate. In heat-flux DSC, there is a common heat source,

and the signal is the differential temperature between sample and reference cells; specific arrangements of thermocouples or thermopiles characterize the many heat-flux systems that are currently available. The reference cells usually contain only an empty pan and the signal ΔX ($X = P$ or T) is of opposite sign for the two forms of DSC because in the heating mode, for example, a loaded sample cell can only be maintained in the $\Delta T = 0$ condition of power-compensation DSC when $P_s > P_r$; conversely, with a common heat source the sample cell temperature invariably lags behind that of the reference cell and $T_s < T_r$ for heat-flux DSC. Conditions are reversed in cooling experiments. The abscissa is time in both forms of DSC, but it is usual to transform this to temperature using the known linear heating or cooling rate [272].

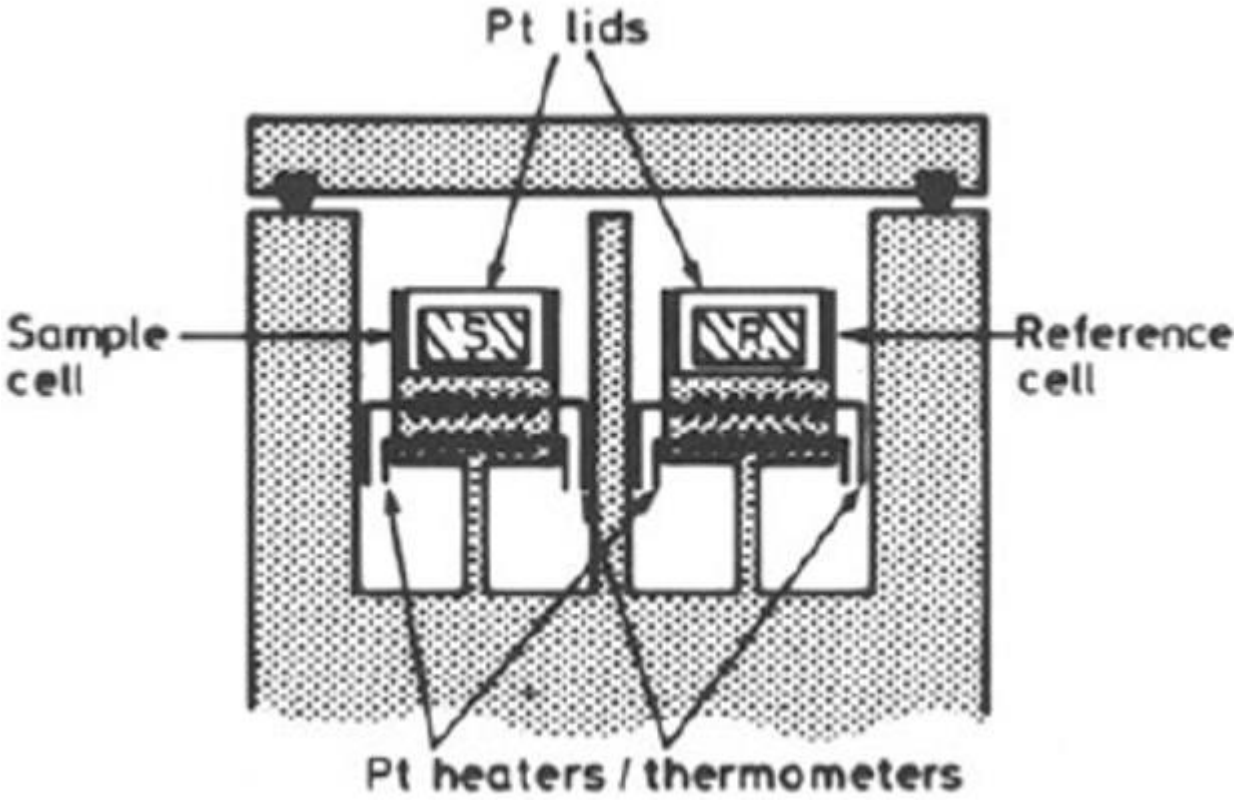

Figure 3.17. Sample and reference cell arrangement for DSC experiments [272].

3.5.3 Heat treatment

The heat treatment experiments were carried out in an in-house built 3-zone tube furnace (Fig 3.18) with atmosphere control. The quartz tube has a diameter of 60mm and sealed by high temperature rubber O-rings with stainless steel end-caps. High purity argon (99.995%) was used to purge the quartz tube and constant flow rate of 40SCCM was maintained throughout the duration of experiments to prevent oxidation of samples. A water bubbler contained in a jar was used to prevent oxygen back-flow and monitor the argon flow rate. For the sub-1200°C experiments, heating proceeded at a rate of 20°C/s to the target temperatures and was held for 600s for soaking and then quenched in tap water. The 1200°C experiment proceeded at the same heating rate and was held for 21,600s before quenching. More detailed description of HT parameters can be found in Chapter 5.

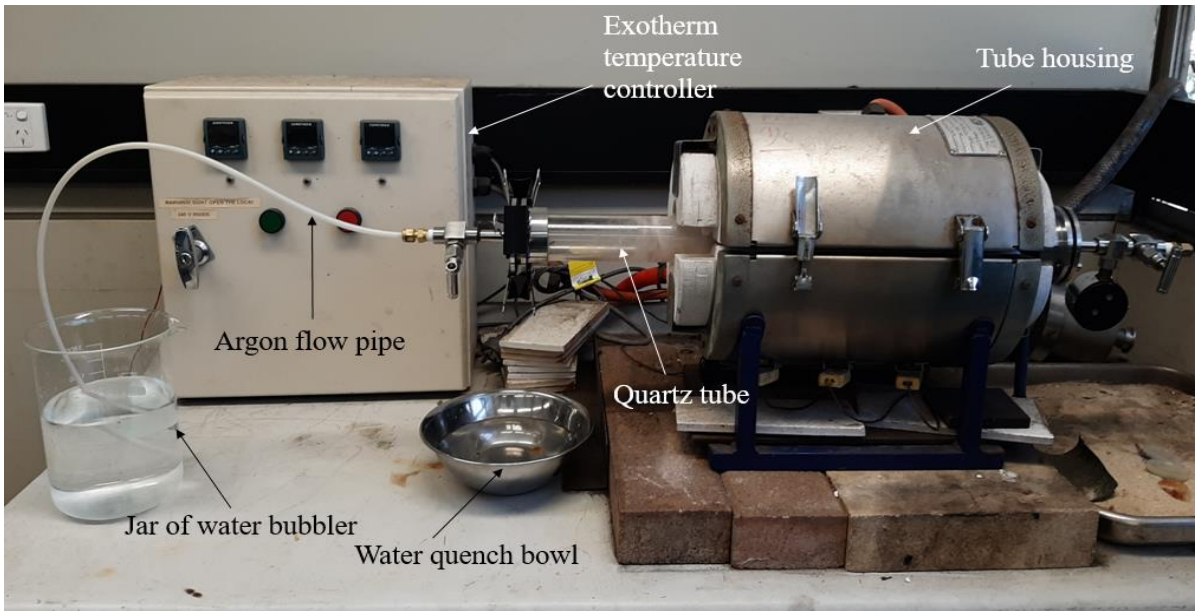

Figure 3.18. 3-zone tube furnace set-up.

3.5.4 Mechanical tests

3.5.4.1 Tensile test

Instron 3367 [273] (Fig 3.19) rated at 30 KN was used for RT tests reported in Chapter 4 and 5. A white paint pattern was made on the sample before test to follow it with video. The equipment used for measuring strain is a contactless Mercury®RT video extensometer developed by Sobriety [274]. This non-contact extensometer has a resolution of 1280 × 720 pixels and consists of a state-of-the-

art optical measuring system controlled by the Mercury RT® software. Measurement was conducted based on the digital image correlation technique. Because it is a contactless equipment, it presents the advantage of having no direct effect on the specimen. At a video recording speed of ~ 5 frames per second, 2-tensile tests were performed to failure at room temperature (RT) with an initial strain rate of $1.1 \times 10^{-3}\ s^{-1}$. Load-displacement data were recorded and true stress, true strain and work hardening rate (WHR) were calculated using Eqs. 1.4, 1.5 and 1.6, respectively [275].

$$\sigma_E = \frac{F}{A} \qquad \text{Equation 3.2}$$

$$\varepsilon_E = \frac{\Delta L}{L_o} = \frac{L - L_o}{L_o} \qquad \text{Equation 3.3}$$

$$\sigma_T = \sigma_E \times (1 + \varepsilon_E) \qquad \text{Equation 3.4}$$

$$\varepsilon_T = ln(1 + \varepsilon_E) \qquad \text{Equation 3.5}$$

$$WHR = \frac{\delta\sigma_T}{\delta\varepsilon_T} \qquad \text{Equation 3.6}$$

Where σ_E = engineering stress, F = applied force, A = cross sectional area on sample where force is applied, ε_E = engineering strain, L_o = original length, L = new length, σ_T = true stress, ε_T = true strain, $\delta\sigma_T$ = change in true stress and $\delta\varepsilon_T$ = change in true strain.

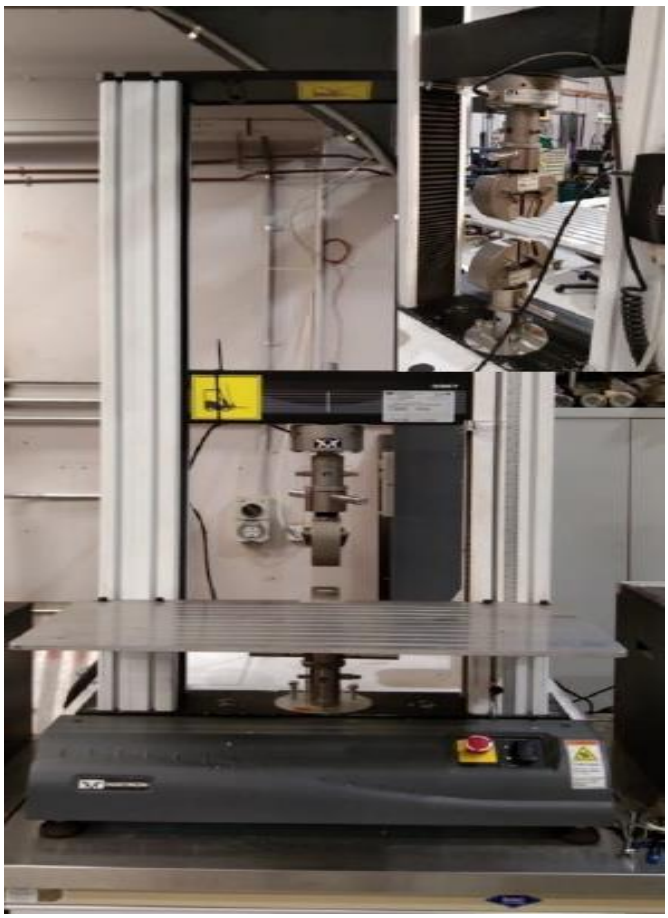

Figure 3.19. The Instron® 3367 tensile testing equipment.

3.5.4.2 Hardness test

The Vickers hardness (H_V) values were obtained using an automatic microhardness tester shown in Figure 3.20 [276]. The tests were performed on the X-Y plane for all alloy conditions (i.e., AB, HT and TMCP samples). Under all testing conditions, a 300g indentation load was applied for 10s on the mirror-polished surface and results from a 3-point test on each sample was averaged and presented in Chapter 4, 5 and 6.

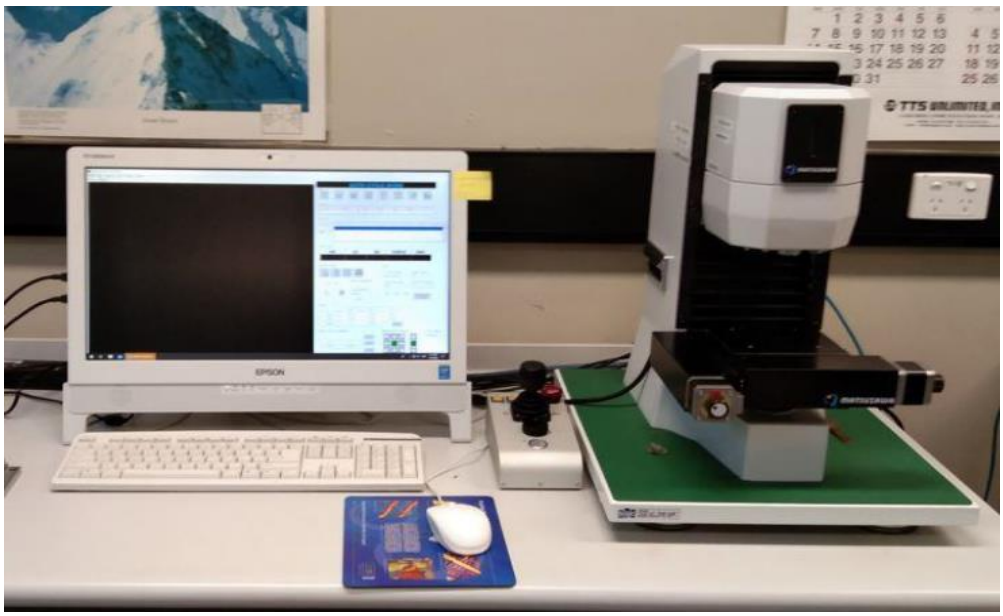

Figure 3.20. The Matsuzawa automatic hardness testing machine.

3.5.4.3 Thermomechanical processing

A Gleeble® 3500-GTC thermo-mechanical apparatus [277] shown in Fig 3.21 was used to conduct RT and high-temperature compression tests, aimed at refining the large columnar grains of LMD fabricated Ti-15Mo-0.25O. The entire hot-deformation process was computer-controlled to precisely monitor the thermal and mechanical parameters. A total of 7 tests were conducted and details of parameters are provided in Chapter 6. The cylindrical samples measured 6mm x 4mm (L x ϕ) to yield an L/ϕ ratio of 1.5 in conformance to Dynamic Systems Inc (DSI) requirements. The length of samples is parallel to the longitudinal X-axis and the flat circular end of cylinder is parallel to the Y-Z plane. Prior to the deformation tests, the cylindrical samples were inspected to ensure absence of surface roughness. R-type thermocouples were spot welded-on to the mid-point of long axis of cylindrical samples for the in-situ measurement of the temperature. A thin layer of tantalum sheet was attached to the circular ends of the samples, and a layer of graphite was glued on to the interface between sample and platens to minimise frictional effect. The samples were resistively heated to the target deformation temperature of 650°C at a heating rate of $20°CS^{-1}$ and held for 600s for soaking. Mechanical compression followed as specified for different samples in Chapter 6. Samples were

immediately water-quenched after test. The compressed samples were then cut in the longitudinal direction and polished for XRD and SEM analysis.

Figure 3.21. Gleeble® 3500-GTC thermomechanical testing equipment.

4 Microstructure, deformation mechanisms and mechanical properties of as-LMDed Ti-15Mo-0.25O

In this chapter, the microstructure of the AB alloy was studied to determine its dominant grain morphology/size, solute compositional variations and phases. Dog-bone samples were then machined and subject to uni-axial tensile deformation to failure. Subsequently, ex-situ fracture modes, deformation mechanisms and mechanical properties were determined and compared to those of other AM metastable Ti-alloys available in Literature.

4.1 XRD Pattern analysis

In Fig. 4.1, the two planar observations in the AB state revealed a single β-phase in the microstructure with a strong $(110)_\beta$ texture observed on the Y-Z plane. However, a splitting of the peaks occurs and there is the presence of main and shoulder $(110)_\beta$ and $(211)_\beta$ peaks. LPs which matched the main and shoulder peaks are 0.326nm and 0.325nm, respectively. In comparison to database lines of the Commercially Pure-Ti (CP-Ti) β PDF card used, a shift in peaks to the right was observed in Trace. Since Mo atomic radius of 0.139nm is smaller than that of Ti of 0.147nm, peaks should have shifted to the left to accurately depict a reduction in LP. Thus, the presence of residual stress and dislocations in the AB state of the alloy is the primary reason for the shift rather than a compositional change from the CP-Ti alloy. This residual stress arises from rapid solidification which permits limited grain growth. A high thermal gradient existing within a layer and between 2 neighbouring layers can be another cause for residual stress.

The FWHM of $(110)_\beta$ plane for AB state of Alloy 1 (Y-Z) and (X-Y) are 0.176° and 0.614°, respectively. The DS has a the highest FWHM of 0.766° on the same plane as expected since the dislocation density in the deformed state should be higher than the AB states of the alloy. The crystallite size of AB (Y-Z) and AB (X-Y) are very similar, and they are 83.363 μm and 83.335 μm, respectively. This shows that crystallite size is probably a feature of printed/solidified samples, showing negligible planar dependence. The peak intensity observed on $(110)_\beta$ plane for AB (Y-Z)

plane is much higher than the X-Y plane. The reason for this is the multiple appearance of β-textures up the build (Y-Z) plane which represents the width of 25 layers. This is on the basis that the direction of columnar grain growth is aligned on the Y-Z plane. In comparison, the X-Y plane has a lower β-texture because it only contains texture from a single center layer. It should be noted that while XRD analysis cannot be used for a comprehensive texture analysis, its peaks can serve as a first indication of the formation of a texture orientation. Texture analysis is presented in Section 4.3.4. Based on planar multiplicity only, intensities from the $(310)_\beta$ and $(211)_\beta$ planes should be higher since they have a multiplicity factor of 24 compared to a factor of 12 for $(110)_\beta$. However, this is not the case due to the much higher combined effect of multiplicity and 2θ angle on $(110)_\beta$ peak intensity.

The pattern for DS sample (blue pattern of Fig. 4.1) shows appearance of a distinct single $(041)_{\alpha''}$ peak indicating martensite formation during deformation. Depending on the β texture and in-plane stress states, martensite formation could be hindered or promoted by realisation of specific martensite lattice variants out of the six variants which have specific ORs with β [278]. This in turn leads to the development of different texture components [216].

ω_D is formed in the same 2θ positions after deformation as also reported in Refs. [93, 132, 213].

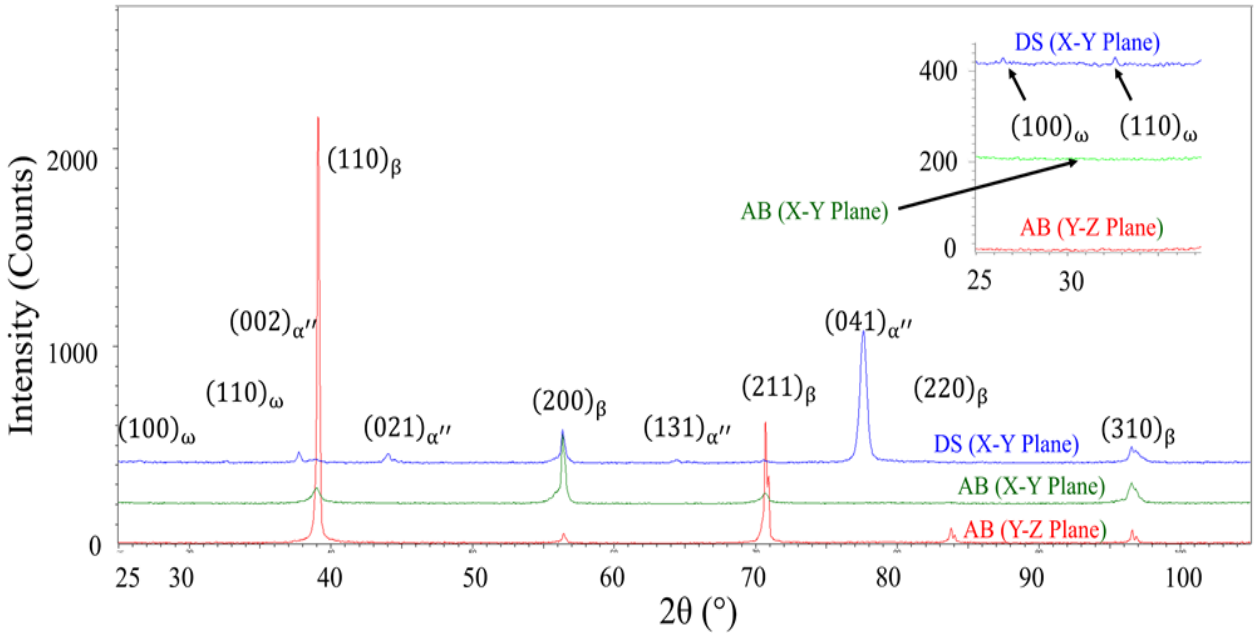

Figure 4.1 XRD patterns observed in the as-built (AB) and deformed (DS) states.

4.2 Microstructural Characterisation of As-Built samples

4.2.1 SEM analysis

The overall microstructure of Y-Z cross-section is shown in Fig. 4.2a, whereas more details for the first three layers and for central layers are shown in Fig. 4.2b and 4.2c, correspondingly. The microstructure of the first two layers consists predominantly of coarse equiaxed grains (Fig. 4.2b), which is associated with the effect of faster cooling due to proximity to the substrate plate. In all other layers, the microstructure is typical of AM- made Ti alloys [14, 16, 17] consisting of coarse columnar grains elongated along the building direction. The melt pool/FZ lines clearly delineate each deposited layer. The interlayer FZ has a thickness of 14.5 ± 4.9μm. Triple junctions in FZ are formed because of bidirectional deposition. Within each layer, the bottom region of heat-affected zone (HAZ) exhibits cellular-dendritic microstructure, whereas the top region re-melted by a subsequent pass has a uniform microstructure. In some areas, like at the top of lower FZ of layer C+1 in Fig. 4.2c (yellow dash lines), a thin layer before the start of cellular-dendritic microstructure is visible. Its appearance is related to the change from a planar solidification front to a cellular one as reported by Vrancken et al. [17] for SLMed Ti-6V-4Al-10Mo alloy.

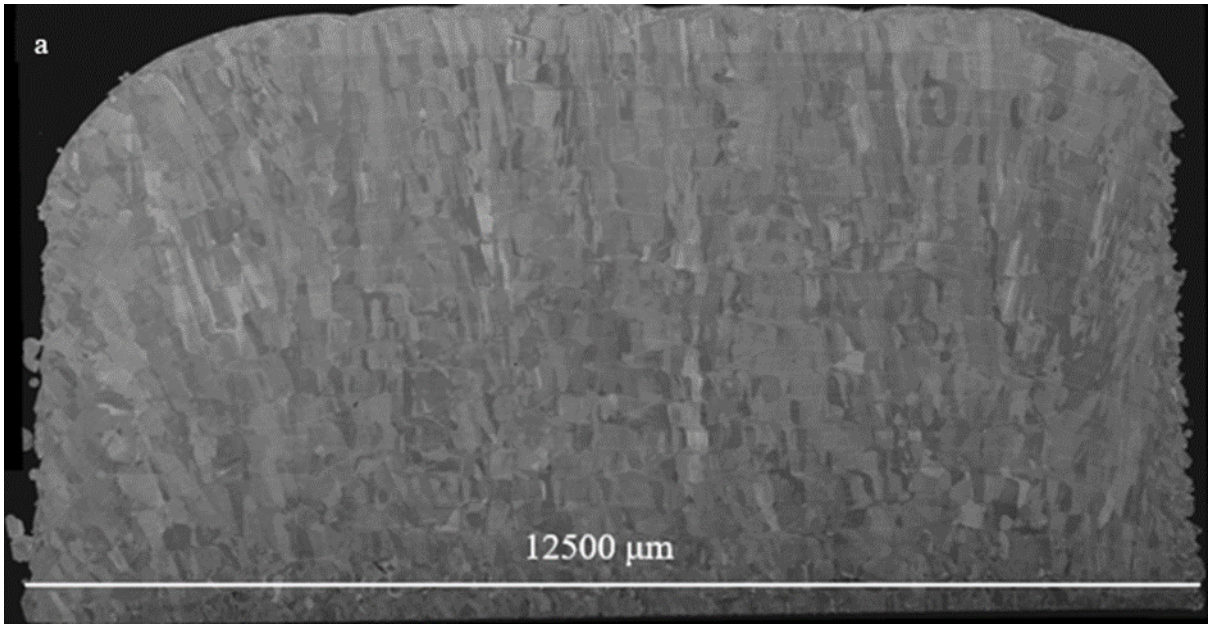

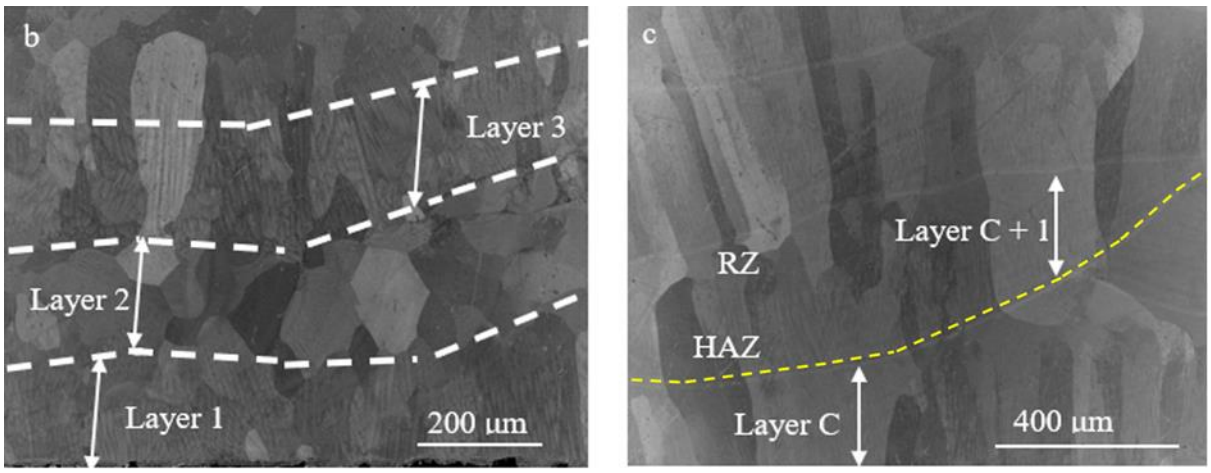

Figure 4.2 (a) Backscattered electron (BSE) image showing Y-Z cross section of a coupon (b) BSE image taken from layers 1, 2 and 3; (c) Centre layers C and C+1 consisting predominantly of columnar grains. RZ is re-melted zone. HAZ is heat-affected zone. Dashed line in (c) shows the end of planar solidification region.

Table 4.1 shows a summary of grain sizes where build height (BH) groupings were selected based on closeness in stabilisation temperature and solidification rate [9]. In general, it was observed that stabilisation temperature, solidification rate and grain size became higher, slower, and coarser, respectively, in the build direction (Table 4.1). The parameter designated $H_{U\text{-}F}$ represents the height measured between intra-layer (between HAZ and RZ) and inter-layer FZ. It also increases with an increase in the number of deposited layers

Table 4.1. Microstructure parameters in relation to cooling rate and stabilised temperature during production. $H_{U\text{-}F}$ represents height of uniform Mo zone to interlayer fusion line.

Build Height	Layers	Cooling Rate (°C/s) from β_{solvus} to M_S [9]		Stabilised temp (°C) [9]	Mean width (µm)		Mean $H_{U\text{-}F}$ (µm)
		Length scan	Width scan		Equiaxed	Columnar	
A	1-7	791 ± 330	171 ± 73	~ 580	68±16	43±40	108±13
B	8-12	582 ± 30	98 ± 16	~ 600	N/A	54±51	113±12
C	13-17	538 ± 110	77 ± 9	~ 620	N/A	76±45	119±15
D	18-25	427 ± 27	70 ± 9	~ 640	N/A	88±44	123±12

*Note that cooling rate and stabilised temperature were determined from simulations for central points of layers 1, 8, 13 and 18 using the DED module in Simufact Welding for Ti-6V-4Al alloy and used here in order to illustrate the trend.

4.2.2 EDS area analysis

An EDS area analysis represents the most accurate estimation of solute concentration as it considers the average of a representative area where solute concentration may fluctuate. A high concentration of Mo (15.1±0.2 wt. %) in FZ and in Mo-rich regions of HAZ (15.3±0.8 wt. %) was clearly visible in the map (Fig. 4.3). Contrarily, low-Mo layers in HAZ contain only 13.1±0.4 wt.% Mo, whereas the distribution of Mo in RZ was relatively uniform with the average content of 14.1±0.2 wt. %Mo. The observed segregation of Mo arises from the partitioning of the solute into a liquid of the solidification front (FZ) and micro-segregation in cellular-dendritic structure (HAZ) [17]. However, the ~6.8 ± 1.7 μm intercellular spacing is much coarser than the 1 μm reported by Vrancken et al [17].

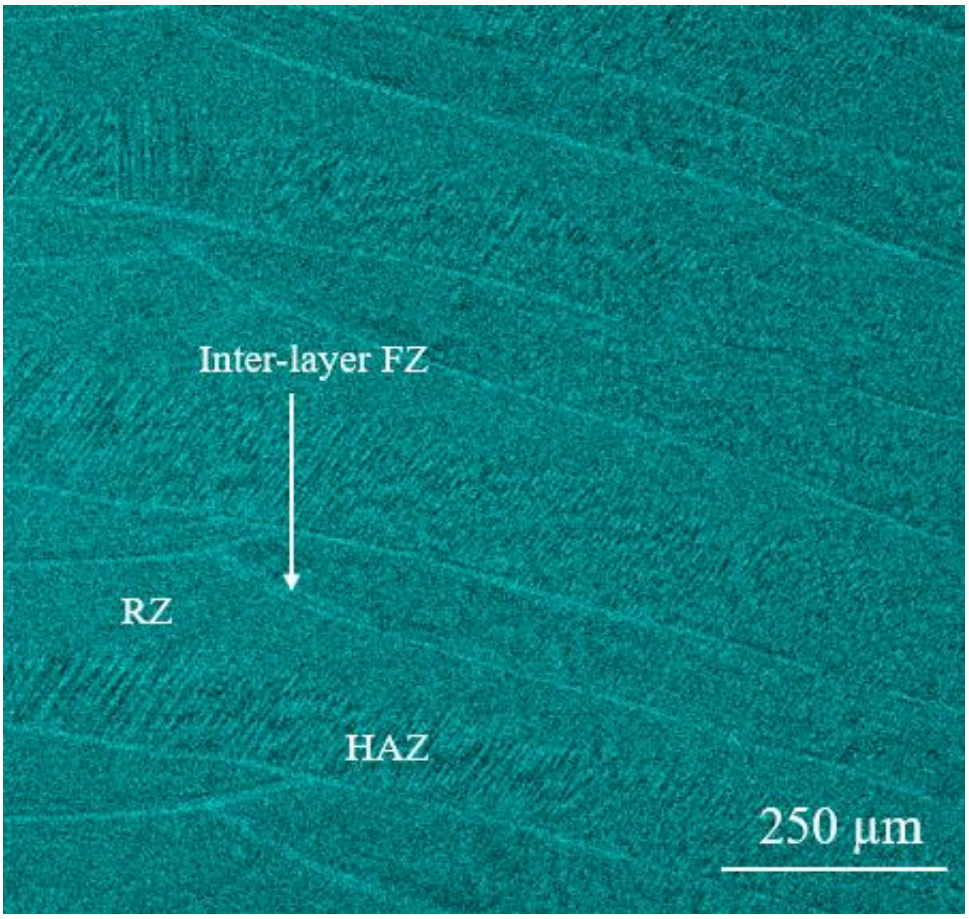

Figure 4.3. Mo EDS map of multiple layers in the centre showing fusion zone (FZ), re-melted zone (RZ) and interlayers of heat-affected zone (HAZ).

4.2.3 EDS point analysis

A compositional analysis conducted on a point-by-point basis (Fig. 4.4) can provide useful information on the variation in Mo between adjacent points in the alloy. These results can form a background for understanding the link between prior concentration distribution and emerging variations in zonal deformation mechanisms.

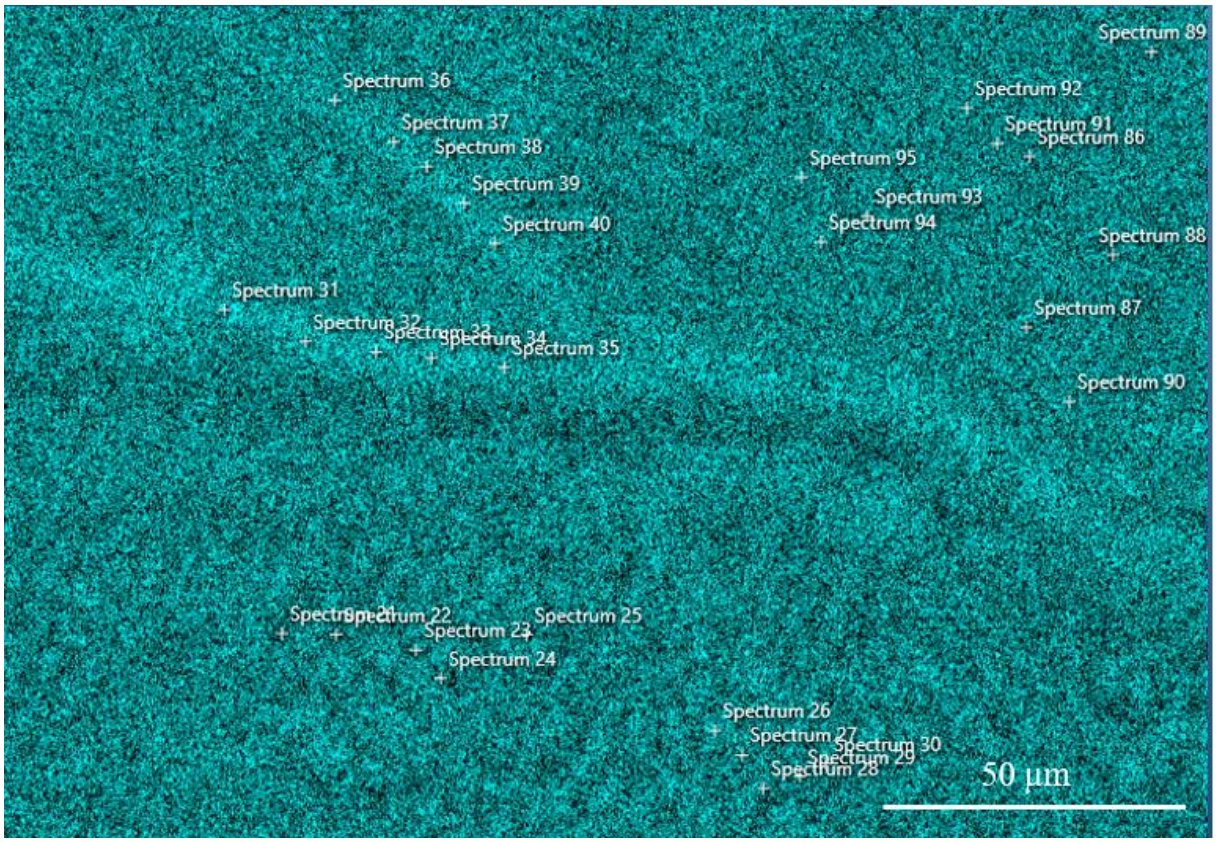

Figure 4.4. EDS map with 30 points from where Ti and Mo spectrums were generated.

Table 4.2. Mo concentrations (wt. %) generated from point spectrums of Figure 4.4.

HAZ, Mo-Lean Interlayers					HAZ, Mo-Rich Interlayers				
Spec 21	Spec 22	Spec 23	Spec 24	Spec 25	Spec 26	Spec 27	Spec 28	Spec 29	Spec 30
12.2	12.0	13.1	12.6	12.8	14.8	13.0	12.9	12.8	14.0
FZ									
Spec 31	Spec 32	Spec 33	Spec 34	Spec 35	Spec 36	Spec 37	Spec 38	Spec 39	Spec 40
14.6	14.9	15.1	14.6	14.6	14.5	14.8	14.7	15.0	14.6
RZ									
Spec 86	Spec 87	Spec 88	Spec 89	Spec 90	Spec 91	Spec 92	Spec 93	Spec 94	Spec 95
10.0	1.0	0.7	9.8	11.8	24.6	20.2	14.5	15.5	9.1

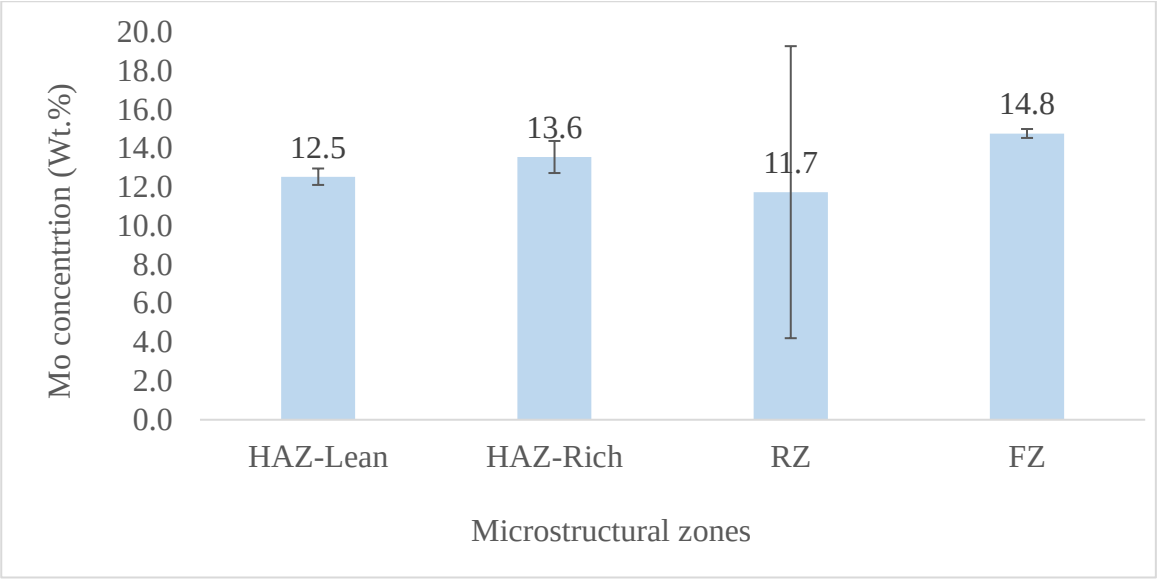

Figure 4.5. Zonal Mo concentration averages from EDS points analysis.

As previously alluded to, each layer has 2 distinct zones namely the RZ and the HAZ which are bound by an upper and lower FZ. As shown in Fig. 4.4, EDS point spectrum analysis was conducted on 5 points each from HAZ, Mo-lean and Mo-rich lamellas, 10 RZ points, and 10 FZ points. Statistical analysis of Table 4.2 data is presented in Fig. 4.5. In the FZ, Mo concentration averaged to 14.8$\pm$0.2 Wt. %. Averages from RZ, Mo-rich and Mo-lean inter-layers of HAZ were 11.7$\pm$7.5 Wt. %, 13.6$\pm$0.8 Wt. % and 12.5$\pm$0.4 Wt. %, respectively. The expected differences in zonal/inter-layer solute concentration arising from Mo depletion from matrix is observed in all zones with the exception of the RZ. This is because the segregated points/particles not lamellas of the RZ contain some super depleted points as well as super enriched points indicated by the red fonts of Table 4.2. This occurrence is reflected in the rather large standard deviation of 7.5 Wt. % and resulted from exit of β-stabilising solute from precipitated phases into adjacent β-grains [279] during SLM - second laser path. These super depleted particles represent α-titanium, and the super enriched grains are of higher β-stability than the HAZ and FZ. The RZ therefore represents a more inhomogeneous state of solute distribution, implying a greater extent of Mo segregation than the HAZ howbeit with the absence of visible thin-long lamellas.

The HAZ interlayers have a thin long lamella-like structure which forms by spinodal decomposition during the second laser pass on the next layer which sees the remelting of approximately 30% of the

height of previous layer. This happens by a diffusional mechanism where the final β-phases differ individually in composition from initial β-phase [280]. The remelting process creates a heat affected zone (HAZ) on the already solidified volume under the remelted thickness purely by heat effects leading to a solid-state splitting into β-lean and β-rich sequence of inter-layers. Two factors can lead to Mo segregation in the HAZ during SLM [176]. These are (i) non-equilibrium solute distribution during solidification and (ii) density differences between the solid in the HAZ and the liquid in the remelted zone. Mebed et al [179], suggested that a miscibility gap on the high solute side is the reason for segregation.

The laser beam spot size in the even-number layers which were scanned in the width-direction creates a non-linear thermal gradient in the HAZ of previous layer. This kind of thermal gradient results in a non-uniform thickness of the layers. Non-parallelism is due to the laser temperature being highest at source (i.e., spot location), causing a non-even distribution of heat over the regions farther away from the beam source. There also exists triple junctions in the lower and center layers where overlapping occurs in narrow regions coming under right angle Mo-rich lines. These triple junctions also form during the second laser pass.

4.3 Characterisation of deformed microstructure

4.3.1 SEM analysis

Fig. 4.6 shows the microstructure within the uniform elongation zone of gauge length of fractured dog-bone samples after uniaxial tension test. An abundance of deformation products formed in a vast majority of grains. The products form complex arrangements of grids (examples are indicated by white arrows in Fig. 4.6a), packets (blue arrows in Fig. 4.6a) of assumed primary (thicker, more developed ones of solid blue arrow of Fig. 4.6b) and secondary products (dash blue arrow of Fig. 4.6b). As could be seen in Fig. 4.d, the deformation products are continuously spread over FZ, RZ and HAZ regions, confined within individual columnar grains. For a more detailed characterisation of the nature, morphology, and crystallography of the deformation products, EBSD and TEM were carried out.

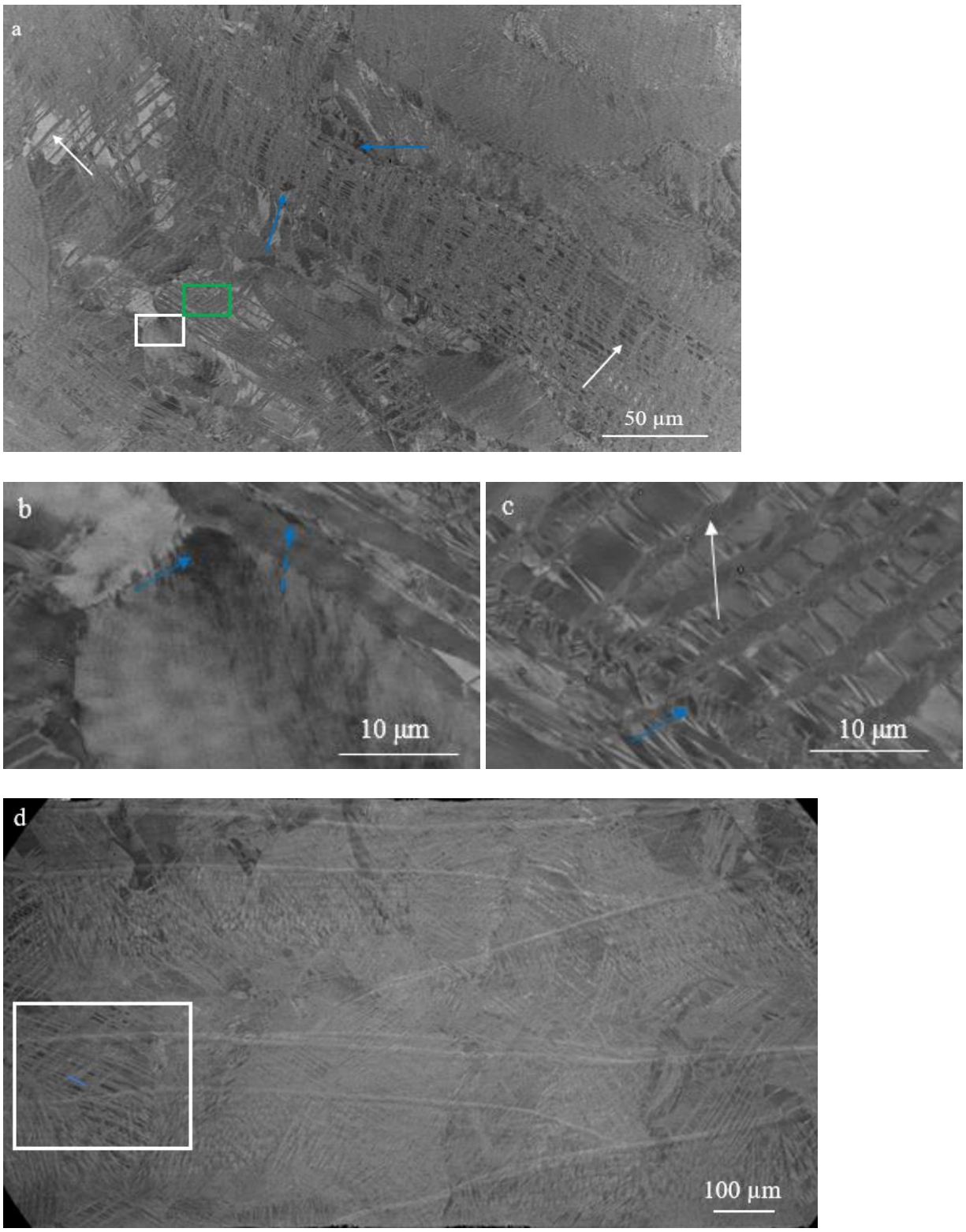

Figure 4.6. SEM image of (a) X-Y plane of sample's gauge length after tensile deformation; (b) magnified view of white rectangle of Fig. 4.6a; (c) magnified view of green rectangle of Fig. 4.6a. White and blue arrows in (a-c) show the examples of grid and packet formations, respectively, of deformation products; (d) X-Z plane of sample's gauge length after tensile deformation. White box shows, as example, position of EBSD map of Fig. 4.7c, whereas blue line defines position of lift-out for TEM. X direction is horizontal.

4.3.2 EBSD analysis

Fig. 4.7 shows inverse pole figure (IPF) maps with side-by-side band contrast maps of representative regions of X-Y and X-Z planes. Although phase maps are overlaid on the band contrast maps (Figs. 4.7b and d), due to the low magnification of these maps, fine α′′ martensite is not visible well and the reader is referred to Figs. 4.8a and b for α′′ martensite observations. Fig. 4.7c corresponds to the white box region in Fig. 4.6d. IPFs were generated with respect to the X-axis of LMD sample which is the tensile direction and axis of most relevance. Smaller grains (G1 and G10 in Fig. 4.7a, and G3 in Fig. 4.7c) demonstrate a very limited presence of deformation products. The grain orientation is not the determining factor in these cases. For example, grains G8, G9 and G11 with high density of deformation products have the same orientation as G10 (Fig. 4.7a). It could be that the stress state of smaller grains are affected by the one in the surrounding grains and that smaller grains yield at a later stage than coarser ones, thus displaying a less advanced stage of deformation products development. However, in coarser grains, the orientation affects the density of deformation products. For example, in similar-sized grains G3, G5 and G12 (Fig. 4.7a), the G5 grain of {110} orientation contains less deformation products compared to G12 whose orientation is close to {111} and G3 with an orientation close to {112}. The deformation products in each grain were analysed with representative examples shown in Fig. 4.8. Phase analysis revealed that in addition to the β phase, α′′ martensite formed (Figs. 4.7b, 4.7d, 4.8a and 4.8b), consistent with the XRD result in Fig. 4.1. However, the area fraction of α′′ martensite was very small (~0.007-0.02). The major deformation products were identified as {332}⟨113⟩ twins (Figs. 4.8g and 4.8h, 0.06-0.14 fraction), which is the primary deformation product forming first in the matrix. α′′ martensite was formed preferentially within the twins and at their intersections (Figs 4.8a and 4.8b). Additionally, {112}⟨111⟩ twins (~0.006-0.013 fraction) formed (Figures 4.8g and 4.8h). The kernel average misorientation (KAM) maps (Figs. 4.8c and 4.8d) show a non-uniform distribution of strain in the deformed matrix. Relatively higher strain areas (yellow and red in maps) are mostly related to interfaces between the products. Relatively lower strain areas denoted in blue are at twin intersections and within twins in martensite free areas. There is

predominantly lowstrain and seldom high strain accumulation in martensite which formed as a secondary product within β-twins. Relatively intermediate strains are located in untransformed β grains.

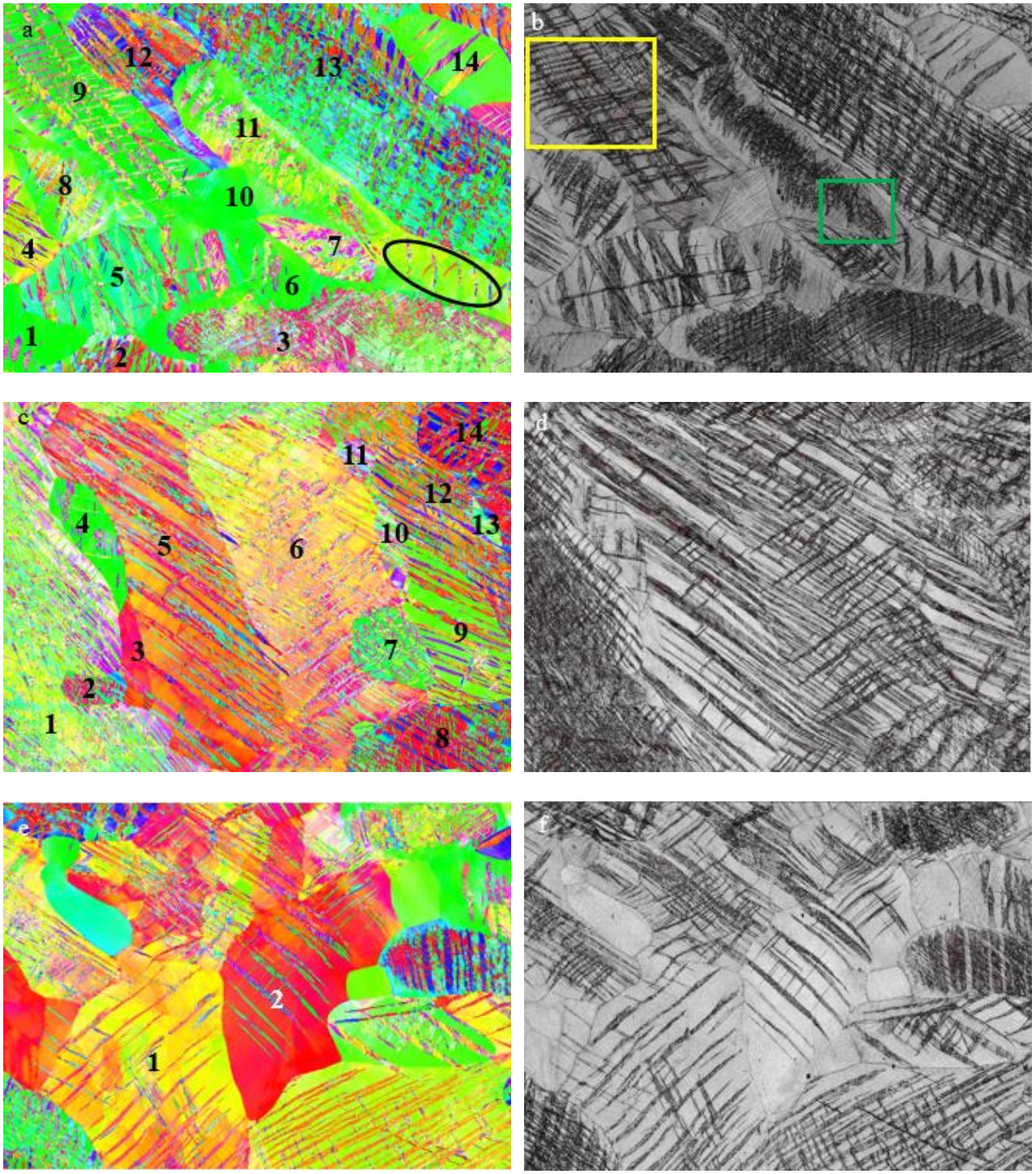

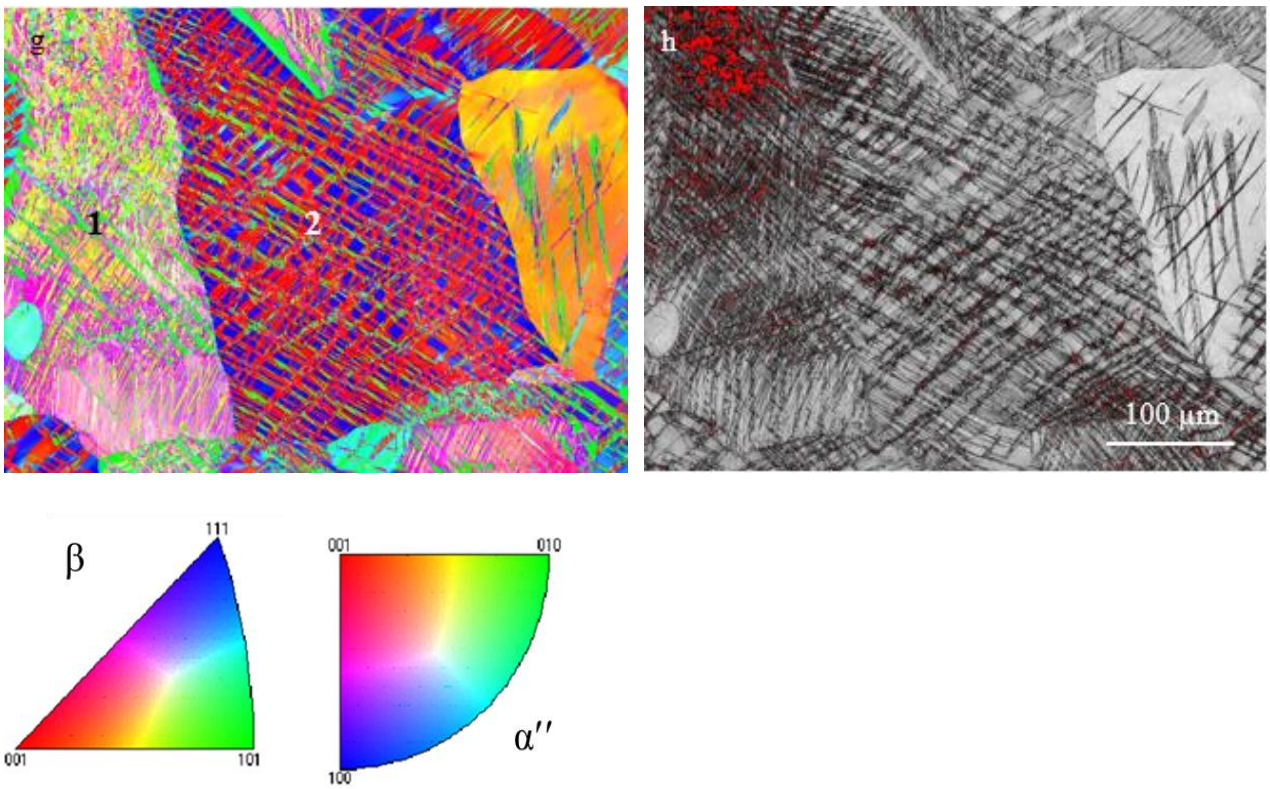

Figure 4.7. Representative (a, c, e and g) IPF and (b, d, f and h) Band Contrast (BC) maps of (a, b, e and f) X-Y and (c, d, g and h) X-Z planes. (Z is vertical). Red in BC maps is overlay for α′′martensite. The horizontal axis corresponds to X, which is the tensile loading direction.

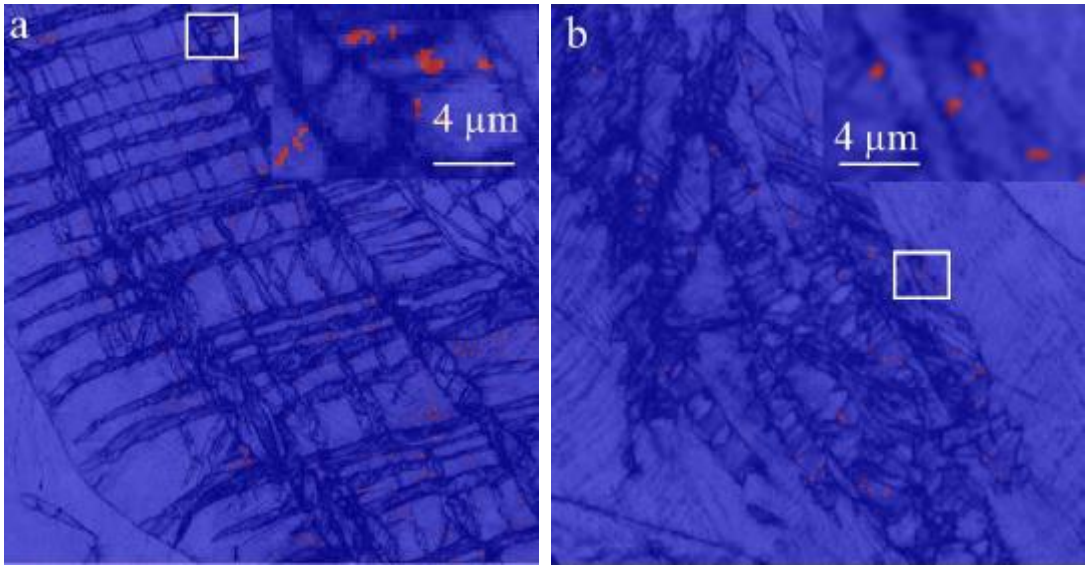

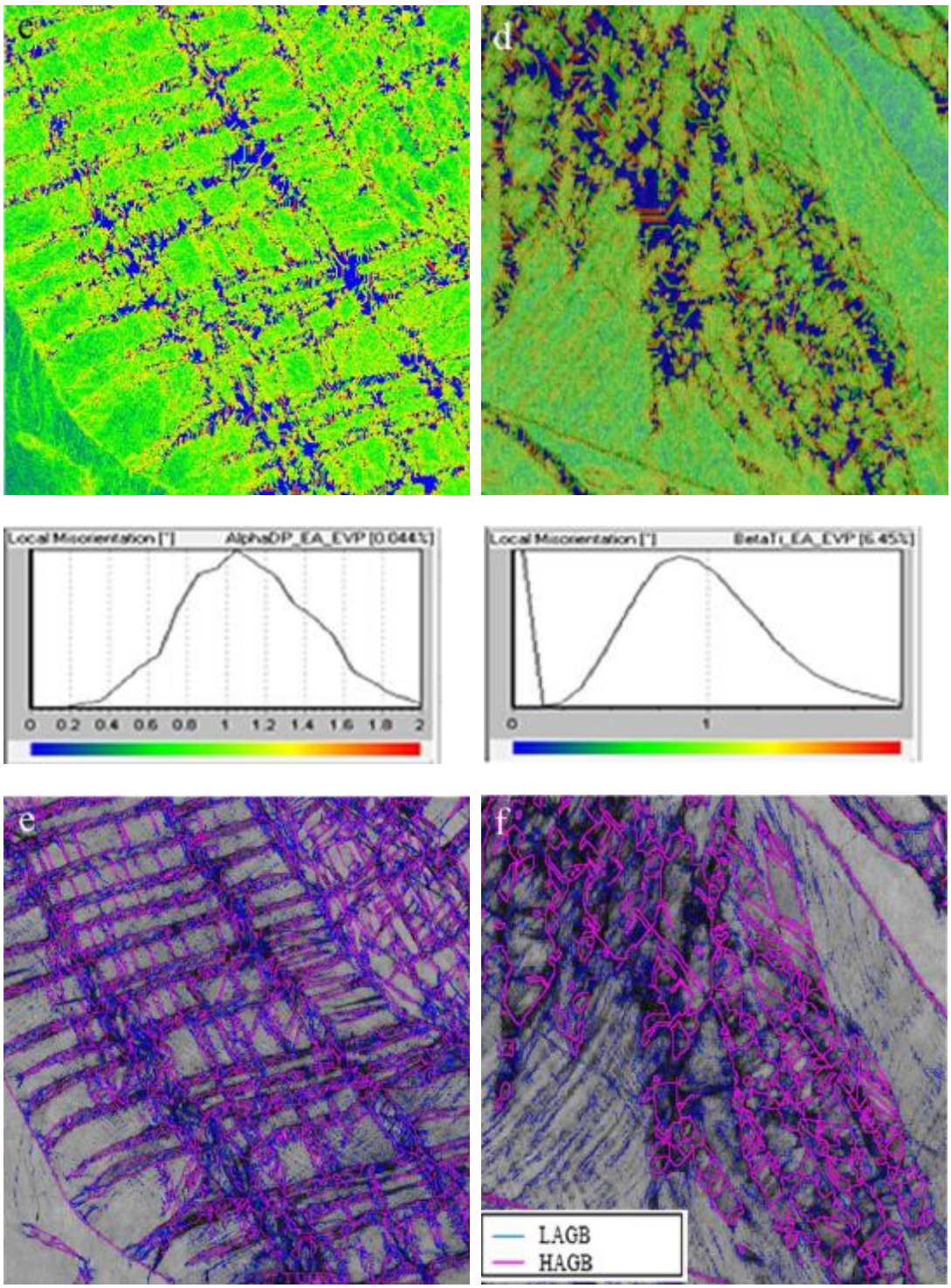
c
d
Local Misorientation [°]
AlphaDP_EA_EVP [0.044%]
0 0.2 0.4 0.6 0.8 1 1.2 1.4 1.6 1.8 2
Local Misorientation [°]
BetaT_EA_EVP [6.45%]
0 1
e
f
LAGB
HAGB

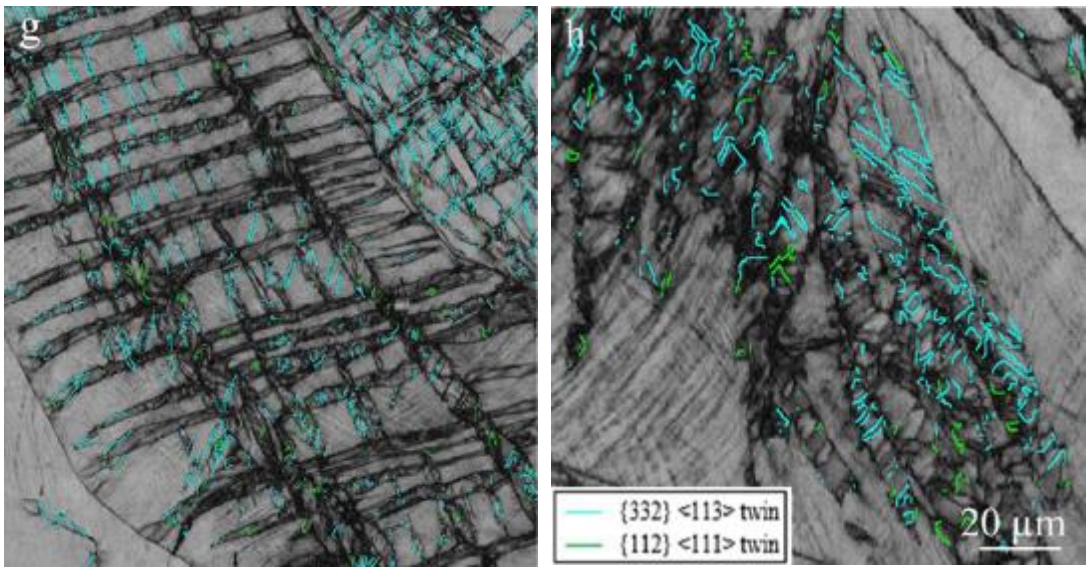

Figure 4.8. (a, b) Phase map with blue and red colours representing β and α′′ martensite, respectively, (c, d) kernel average misorientation map, (e, f) grain boundary map and (g, h) twin boundary map for the regions outlined by yellow rectangle (a, c, e, g) and green rectangle (b, d, f, h) in Fig 4.7b. Insets in (a) and (b) are enlarged area of corresponding white rectangles. The horizontal is X axis (tensile loading direction) and vertical is Y axis.

4.3.2.1 Twin analysis

Analysis of the operative twin system and calculations of their Schmid factors (SF) was performed for each grain (see the examples in Tables 4.3a and 4.3b). The summary for the EBSD maps in Fig. 4.7 is provided in Tables 4.3a and 4.3b. Examples of magnified band contrast maps with operative $\{332\}\langle 113\rangle$ and $\{112\}\langle 111\rangle$ twin systems are shown in Fig. 4.9, where the red-font variants have the highest surface fraction of the three activated twin variants within each twin system. This is followed by the green font variants. Three variants of each twin system operate in each grain, with SF values ranging from 0.31 to 0.49. In most grains, the twin system with the highest SF comprised the largest area fraction. Although the SF analysis was also applied to $\{112\}\langle 111\rangle$ twins using the original β phase stress state and resulted in SFs ranging from 0.33 to 0.38, the analysis needs to be conducted with caution, as these twins form as secondary products within $\{332\}\langle 113\rangle$ twins with different stress states from the β matrix. Comparison of deformation products within the RZ and HAZ in columnar grains was also undertaken. The analysis revealed a higher density of twins and a corresponding

slightly higher fraction of martensite in the HAZ than in the RZ. This could be linked to the lower overall concentration of Mo in HAZ compared to the RZ, and thus easier twinning in the less stable β phase. The twins in the HAZ appear to be thinner than those in the RZ. Similarly, Ruzic et al. [281] also reported the formation of a higher density of primary deformation-induced products in Mo-lean interlayers and zones than Mo-rich ones in Ti-12Mo alloy.

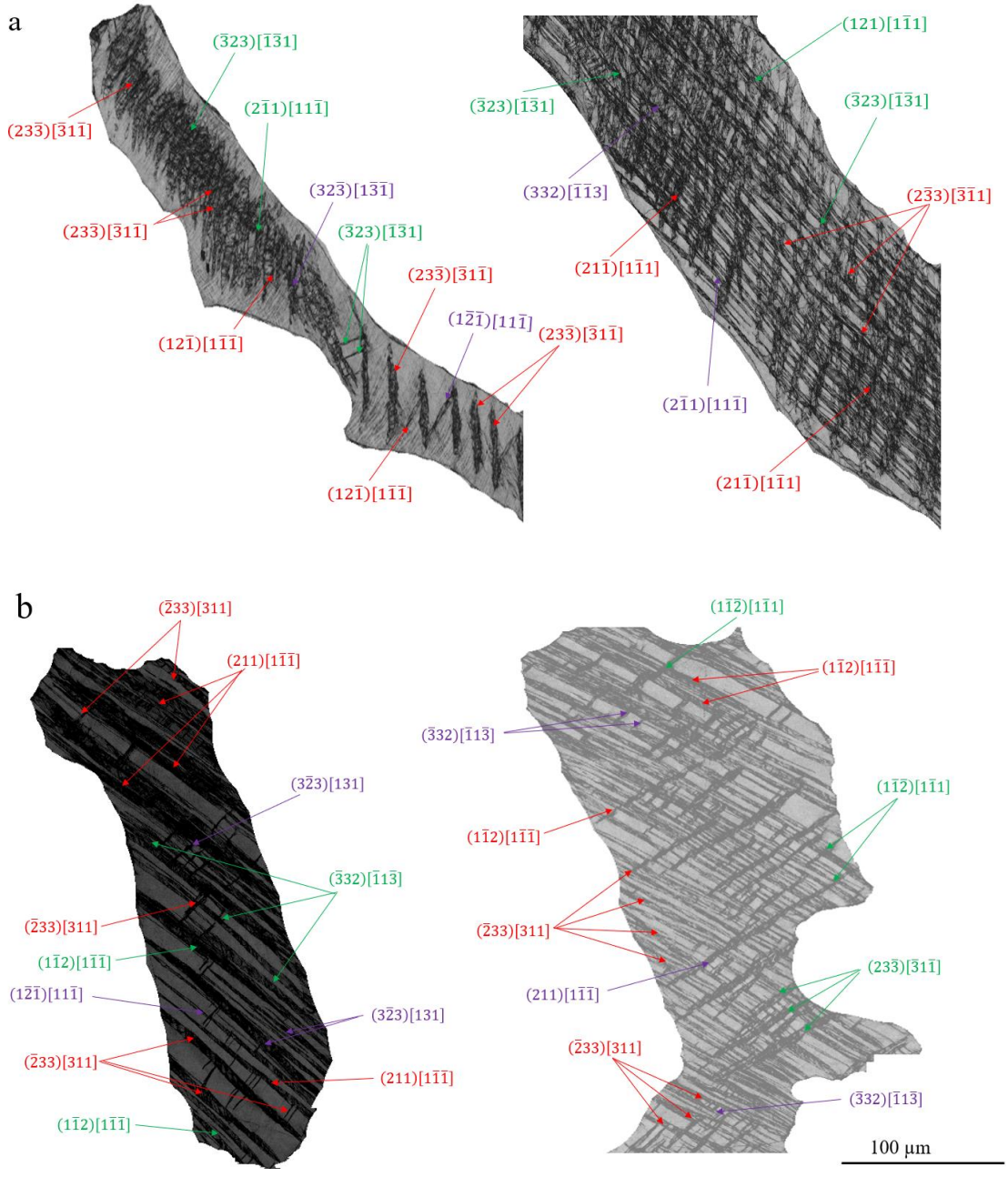

Figure 4.9. Examples of twin systems analysis (a) grains G11 and G13 in Fig. 4.7a; (b) grains G5 and G6 in Fig. 4.7c.

Table 4.3. Schmid Factors for all grains in (a) Fig. 4.7a and (b) Fig. 4.7c. Twin variants of the columnar grains shown in Fig. 4.9 are listed in red, green, and purple fonts in a descending order of surface fractions.

(a)	Twin Variant	SF	Twin Variant	SF
G1	$(23\bar{3})[\bar{3}1\bar{1}]$	0.43	$(211)[1\bar{1}\bar{1}]$	0.33
	$(2\bar{3}3)[\bar{3}\bar{1}1]$	0.41	$(1\bar{2}\bar{1})[11\bar{1}]$	0.31
	$(332)[\bar{1}\bar{1}3]$	0.47	$(21\bar{1})[1\bar{1}1]$	0.30
G2	$(2\bar{3}3)[\bar{3}\bar{1}1]$	0.38	$(11\bar{2})[111]$	0.30
	$(332)[\bar{1}\bar{1}3]$	0.47	$(1\bar{1}2)[1\bar{1}\bar{1}]$	0.30
	$(\bar{3}23)[\bar{1}\bar{3}1]$	0.44	$(1\bar{1}\bar{2})[1\bar{1}1]$	0.30
G3	$(23\bar{3})[\bar{3}1\bar{1}]$	0.45	$(211)[1\bar{1}\bar{1}]$	0.38
	$(32\bar{3})[1\bar{3}\bar{1}]$	0.48	$(1\bar{1}2)[1\bar{1}\bar{1}]$	0.34
	$(\bar{3}23)[\bar{1}\bar{3}1]$	0.44	$(1\bar{2}\bar{1})[11\bar{1}]$	0.31
G4	$(23\bar{3})[\bar{3}1\bar{1}]$	0.39	$(1\bar{1}\bar{2})[1\bar{1}1]$	0.31
	$(2\bar{3}3)[\bar{3}\bar{1}1]$	0.35	$(211)[1\bar{1}\bar{1}]$	0.31
	$(332)[\bar{1}\bar{1}3]$	0.33	$(1\bar{1}2)[1\bar{1}\bar{1}]$	0.30
G5	$(23\bar{3})[\bar{3}1\bar{1}]$	0.45	$(1\bar{1}\bar{2})[1\bar{1}1]$	0.35
	$(2\bar{3}3)[\bar{3}\bar{1}1]$	0.47	$(1\bar{1}2)[1\bar{1}\bar{1}]$	0.34
	$(332)[\bar{1}\bar{1}3]$	0.48	$(1\bar{2}\bar{1})[11\bar{1}]$	0.33
G6	$(23\bar{3})[\bar{3}1\bar{1}]$	0.47	$(1\bar{1}\bar{2})[1\bar{1}1]$	0.32
	$(2\bar{3}3)[\bar{3}\bar{1}1]$	0.49	$(1\bar{1}2)[1\bar{1}\bar{1}]$	0.31
	$(332)[\bar{1}\bar{1}3]$	0.47	$(1\bar{2}\bar{1})[11\bar{1}]$	0.30
G7	$(23\bar{3})[\bar{3}1\bar{1}]$	0.44	$(1\bar{1}\bar{2})[1\bar{1}1]$	0.30
	$(32\bar{3})[1\bar{3}\bar{1}]$	0.35	$(1\bar{1}2)[1\bar{1}\bar{1}]$	0.30
	$(\bar{3}23)[\bar{1}\bar{3}1]$	0.33	$(1\bar{2}\bar{1})[11\bar{1}]$	0.30
G8	$(3\bar{2}3)[131]$	0.45	$(21\bar{1})[1\bar{1}1]$	0.33
	$(32\bar{3})[1\bar{3}\bar{1}]$	0.48	$(1\bar{2}\bar{1})[11\bar{1}]$	0.33
	$(2\bar{3}3)[\bar{3}\bar{1}1]$	0.49	$(2\bar{1}1)[11\bar{1}]$	0.30
G9	$(23\bar{3})[\bar{3}1\bar{1}]$	0.44	$(12\bar{1})[1\bar{1}\bar{1}]$	0.36
	$(2\bar{3}3)[\bar{3}\bar{1}1]$	0.43	$(2\bar{1}1)[11\bar{1}]$	0.34
	$(332)[\bar{1}\bar{1}3]$	0.46	$(121)[1\bar{1}1]$	0.31
G10	-	-		
	-	-		
	-	-		
G11	$(23\bar{3})[\bar{3}1\bar{1}]$	0.44	$(12\bar{1})[1\bar{1}\bar{1}]$	0.33

	$(\bar{3}23)[\bar{1}\bar{3}1]$	0.43	$(2\bar{1}1)[11\bar{1}]$	0.33
	$(32\bar{3})[1\bar{3}\bar{1}]$	0.41	$(1\bar{2}\bar{1})[11\bar{1}]$	0.31
G12	$(2\bar{3}3)[\bar{3}\bar{1}1]$	0.45	$(1\bar{2}\bar{1})[11\bar{1}]$	0.31
	$(332)[\bar{1}\bar{1}3]$	0.47	$(21\bar{1})[1\bar{1}1]$	0.31
	$(\bar{3}23)[\bar{1}\bar{3}1]$	0.48	$(121)[1\bar{1}1]$	0.31
G13	$(2\bar{3}3)[\bar{3}\bar{1}1]$	0.47	$(21\bar{1})[1\bar{1}1]$	0.36
	$(\bar{3}23)[\bar{1}\bar{3}1]$	0.42	$(121)[1\bar{1}1]$	0.33
	$(332)[\bar{1}\bar{1}3]$	0.41	$(2\bar{1}1)[11\bar{1}]$	0.32
G14	$(23\bar{3})[\bar{3}1\bar{1}]$	0.41	$(12\bar{1})[1\bar{1}\bar{1}]$	0.33
	$(2\bar{3}3)[\bar{3}\bar{1}1]$	0.48	$(2\bar{1}1)[11\bar{1}]$	0.30
	$(332)[\bar{1}\bar{1}3]$	0.45	$(1\bar{2}\bar{1})[11\bar{1}]$	0.30

(b)	Twin Variant	SF	Twin Variant	SF
G1	$(23\bar{3})[\bar{3}1\bar{1}]$	0.47	$(211)[1\bar{1}\bar{1}]$	0.34
	$(32\bar{3})[1\bar{3}\bar{1}]$	0.44	$(1\bar{1}2)[1\bar{1}\bar{1}]$	0.32
	$(\bar{3}23)[\bar{1}\bar{3}1]$	0.45	$(1\bar{2}\bar{1})[11\bar{1}]$	0.31
G2	$(2\bar{3}3)[\bar{3}\bar{1}1]$	0.38	$(1\bar{1}2)[1\bar{1}\bar{1}]$	0.33
	$(332)[\bar{1}\bar{1}3]$	0.45	$(1\bar{1}\bar{2})[1\bar{1}1]$	0.31
	$(\bar{3}23)[\bar{1}\bar{3}1]$	0.32	$(12\bar{1})[1\bar{1}\bar{1}]$	0.31
G3	$(3\bar{3}2)[1\bar{1}\bar{3}]$	0.44	$(2\bar{1}1)[11\bar{1}]$	0.34
	$(\bar{2}33)[311]$	0.48	$(121)[1\bar{1}1]$	0.33
	$(\bar{3}32)[\bar{1}1\bar{3}]$	0.49	$(12\bar{1})[1\bar{1}\bar{1}]$	0.30
G4	$(23\bar{3})[\bar{3}1\bar{1}]$	0.44	$(1\bar{1}\bar{2})[1\bar{1}1]$	0.35
	$(2\bar{3}3)[\bar{3}\bar{1}1]$	0.47	$(1\bar{1}2)[1\bar{1}\bar{1}]$	0.31
	$(332)[\bar{1}\bar{1}3]$	0.42	$(1\bar{2}\bar{1})[11\bar{1}]$	0.31
G5	$(\bar{2}33)[311]$	0.46	$(211)[1\bar{1}\bar{1}]$	0.35
	$(\bar{3}32)[\bar{1}1\bar{3}]$	0.41	$(1\bar{1}2)[1\bar{1}\bar{1}]$	0.34
	$(32\bar{3})[131]$	0.44	$(1\bar{2}\bar{1})[11\bar{1}]$	0.31
G6	$(\bar{2}33)[311]$	0.48	$(1\bar{1}2)[1\bar{1}\bar{1}]$	0.32
	$(23\bar{3})[\bar{3}1\bar{1}]$	0.44	$(1\bar{1}\bar{2})[1\bar{1}1]$	0.33
	$(\bar{3}32)[\bar{1}1\bar{3}]$	0.40	$(211)[1\bar{1}\bar{1}]$	0.33
G7	$(\bar{3}23)[\bar{1}\bar{3}1]$	0.31	$(211)[1\bar{1}\bar{1}]$	0.30
	$(2\bar{3}3)[\bar{3}\bar{1}1]$	0.38	$(1\bar{2}\bar{1})[11\bar{1}]$	0.30
	$(332)[\bar{1}\bar{1}3]$	0.43	$(21\bar{1})[1\bar{1}1]$	0.30
G8	$(2\bar{3}3)[\bar{3}\bar{1}1]$	0.47	$(11\bar{2})[111]$	0.33

	$(332)[\bar{1}\bar{1}3]$	0.35	$(1\bar{1}2)[1\bar{1}\bar{1}]$	0.31
	$(\bar{3}23)[\bar{1}\bar{3}1]$	0.44	$(1\bar{1}\bar{2})[1\bar{1}1]$	0.30
G9	$(2\bar{3}3)[\bar{3}\bar{1}1]$	0.41	$(1\bar{1}\bar{2})[1\bar{1}1]$	0.33
	$(332)[\bar{1}\bar{1}3]$	0.38	$(211)[1\bar{1}\bar{1}]$	0.33
	$(23\bar{3})[\bar{3}1\bar{1}]$	0.39	$(1\bar{1}2)[1\bar{1}\bar{1}]$	0.32
G10	$(23\bar{3})[\bar{3}1\bar{1}]$	0.48	$(211)[1\bar{1}\bar{1}]$	0.30
	$(2\bar{3}3)[\bar{3}\bar{1}1]$	0.45	$(1\bar{1}2)[1\bar{1}\bar{1}]$	0.30
	$(\bar{3}32)[\bar{1}1\bar{3}]$	0.47	$(1\bar{2}\bar{1})[11\bar{1}]$	0.30
G11	$(23\bar{3})[\bar{3}1\bar{1}]$	0.44	$(211)[1\bar{1}\bar{1}]$	0.31
	$(2\bar{3}3)[\bar{3}\bar{1}1]$	0.33	$(1\bar{1}2)[1\bar{1}\bar{1}]$	0.30
	$(\bar{3}32)[\bar{1}1\bar{3}]$	0.37	$(1\bar{2}\bar{1})[11\bar{1}]$	0.30
G12	$(23\bar{3})[\bar{3}1\bar{1}]$	0.38	$(1\bar{1}2)[1\bar{1}\bar{1}]$	0.34
	$(2\bar{3}3)[\bar{3}\bar{1}1]$	0.45	$(211)[1\bar{1}\bar{1}]$	0.33
	$(332)[\bar{1}\bar{1}3]$	0.47	$(1\bar{1}\bar{2})[1\bar{1}1]$	0.30
G13	$(23\bar{3})[\bar{3}1\bar{1}]$	0.36	$(1\bar{1}\bar{2})[1\bar{1}1]$	0.30
	$(2\bar{3}3)[\bar{3}\bar{1}1]$	0.45	$(1\bar{1}2)[1\bar{1}\bar{1}]$	0.30
	$(\bar{3}32)[\bar{1}1\bar{3}]$	0.44	$(1\bar{2}\bar{1})[11\bar{1}]$	0.30
G14	$(2\bar{3}3)[\bar{3}\bar{1}1]$	0.46	$(11\bar{2})[111]$	0.33
	$(332)[\bar{1}\bar{1}3]$	0.42	$(1\bar{1}2)[1\bar{1}\bar{1}]$	0.32
	$(\bar{3}23)[\bar{1}\bar{3}1]$	0.45	$(1\bar{1}\bar{2})[1\bar{1}1]$	0.31

4.3.2.1.1 Twin systems validation

In Fig. 4.10a, measurements on phase/twin map were taken in ImageJ and compared with misorientation profiles. Along the white line, the 36.5μm mark reads to about 61° MO about the $[111]_{\beta}$ axis which corresponds to the $\{112\}\langle 111\rangle$ twin system as denoted by the green color on the map. Angle-axis relationship is satisfied. The 57.5μm mark reads to a misorientation of about 1.3° verifying the claim that α″martensite primarily accommodates very low strains, as primary products as well as secondary products within β-twins. The 70.8μm mark reads to a misorientation of about 49.5°, verifying the $\{332\}\langle 113\rangle$ twin system about the $[101]_{\beta}$ axis. Along the yellow line, the 89μm mark reads to an MO of about 58.1°, verifying the $\{112\}\langle 111\rangle$ twin system with a tolerant deviation of $\pm 5°$ as defined in Channel 5 software [269]. The 72.3μm mark on the yellow line reads to a

misorientation of about 1.3°, once again verifying the claim that martensite accommodates low strains during uniaxial tensile deformation of this alloy. The 35.2μm mark reads to a misorientation of about 53.1°, verifying the {332}⟨113⟩ twin system with a deviation of up to ±5° about the $[101]_{\beta}$ axis.

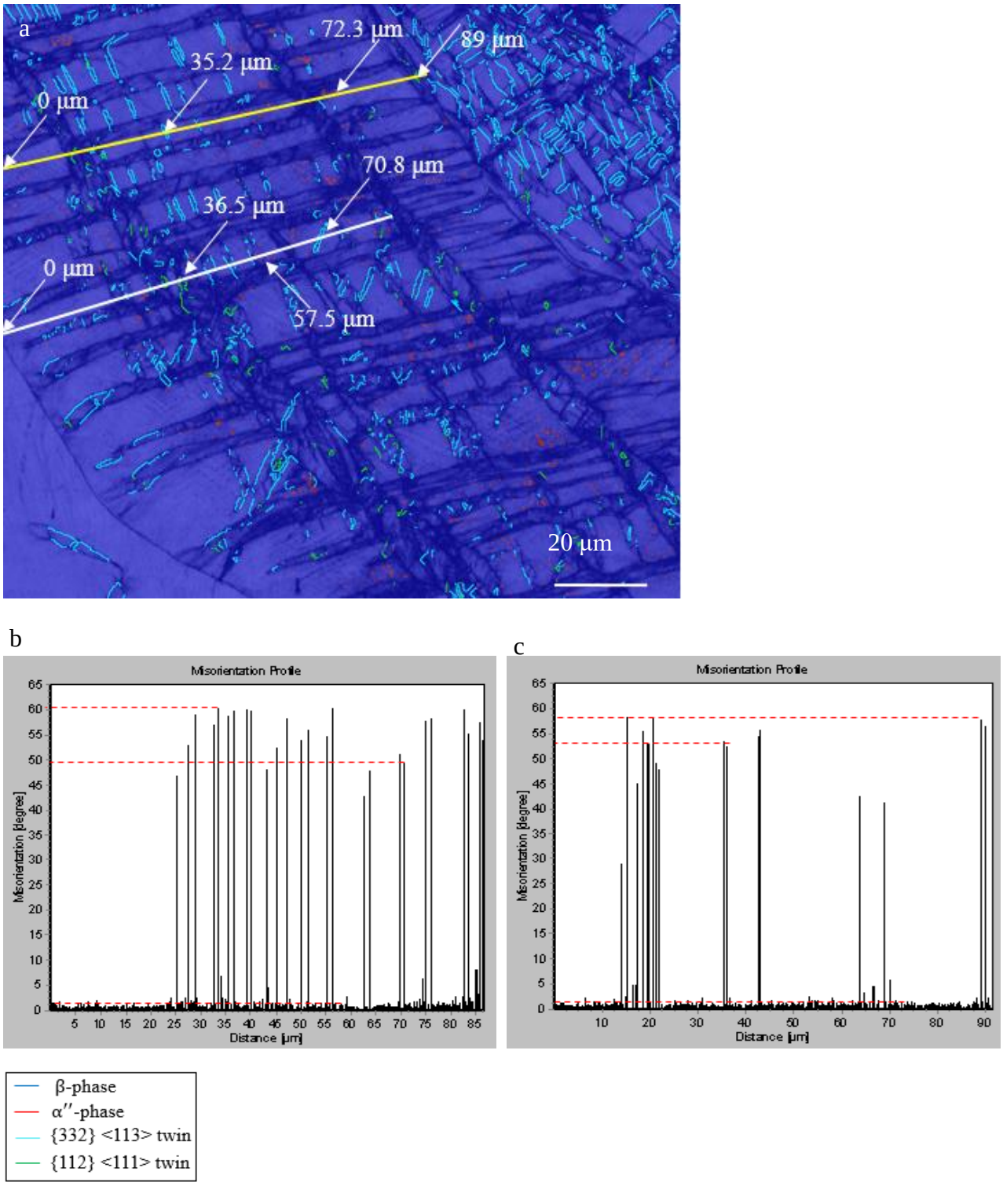

Figure 4.10a. Combined phase and twin boundary maps of area within yellow rectangle of Fig 4.7b; misorientation profile along (b) white line and (c) yellow line of Fig 4.10a.

4.3.2.2 Deformation products in RZ and HAZ

Fig 4.11 shows the separated RZ of G5 of Fig. 4.7c from the HAZ. This allows the investigation of possibilities of zonal influence on deformation product configuration and surface fraction. This grain was selected because it is one of the top two largest in this map and martensite formed are coarser and twins appear longer than the other grains in this map. The RZ and HAZ have phase fractions of 99.1% / 0.9% and 98.1% / 1.9% for β / α″ martensite. The twin system fractions were calculated relative to the entire zonal area. For the RZ, 7% and 0.8% were obtained for the {332}⟨113⟩ and {112}⟨111⟩ twin systems, respectively. Those for the HAZ were 9.8% and 1.1% in favor of the {332}⟨113⟩ twin system. The HAZ has an area of very dense twinning indicated by the black ellipse of Fig. 4.11d.

Twin orientation in both regions is aligned along a mixture of $[111]_\beta$, $[113]_\beta$, $[101]_\beta$ and $[233]_\beta$ directions. The configuration of twins appears similar in both RZ and HAZ of this grain as they are predominantly diagonally parallel to each other – hence not affected by difference in β-stability. Thus, configuration of twins must be a direct consequence of the orientation of a particular columnar grain with respect to the direction of applied load. Twins formed in the HAZ are generally, slightly thinner and denser than those of the RZ as seen in the area within the black ellipse of Fig. 4.11d in comparison to the twins of Fig. 4.11a. This is because the HAZ total area is leaner in average solute concentration than the RZ which is close to the FZ. As such unstable β grains allow for formation of more twins compared to the more stable β grains in RZ which has twins that are on the average thicker. The same β-stability argument put forward above can be made in favour of primary α″ martensite in the HAZ. Also, secondary martensite would contribute to the higher surface fraction in the HAZ since it forms within twins which are more densely distributed in this zone.

As a general observation from all columnar grains of Fig. 4.7 (a, c, e and g), Mo concentration effect on product formation is more pronounced in β reorientation into twins than a complete structural transformation into α″ martensite. The findings in the comparison of RZ and HAZ in G5 of Fig. 4.7c holds true in the other columnar grains which span both zones in the other 3 maps of Figure 4.7. A

statistical analysis of G11 and G13 of Fig. 4.7a, G5 and G6 of Fig. 4.7c, G1 and G2 of Fig. 4.7e and G1 and G2 of Fig. 4.7g yielded a α'' martensite phase fraction of 1.3 ± 1.2 / 1.6 ± 1.0 for the RZ and HAZ, respectively. Statistical analysis also yielded $\{332\}\langle 113\rangle$ and $\{112\}\langle 111\rangle$ surface fractions of 8.5 ± 4.2 / 11.2 ± 3.5 and 1.1 ± 0.7 / 1.6 ± 0.4 for the RZ and HAZ, respectively. Thus, Mo segregation results in a small difference in the volume of product formed between RZ and HAZ with the HAZ being slightly more uniform as indicated by the consistently smaller standard deviation. Ref. [281] also reported in Ti-12Mo, the formation of higher density of deformation induced products in Mo-lean interlayers and zones than Mo-rich ones for primary products which form on parent β.

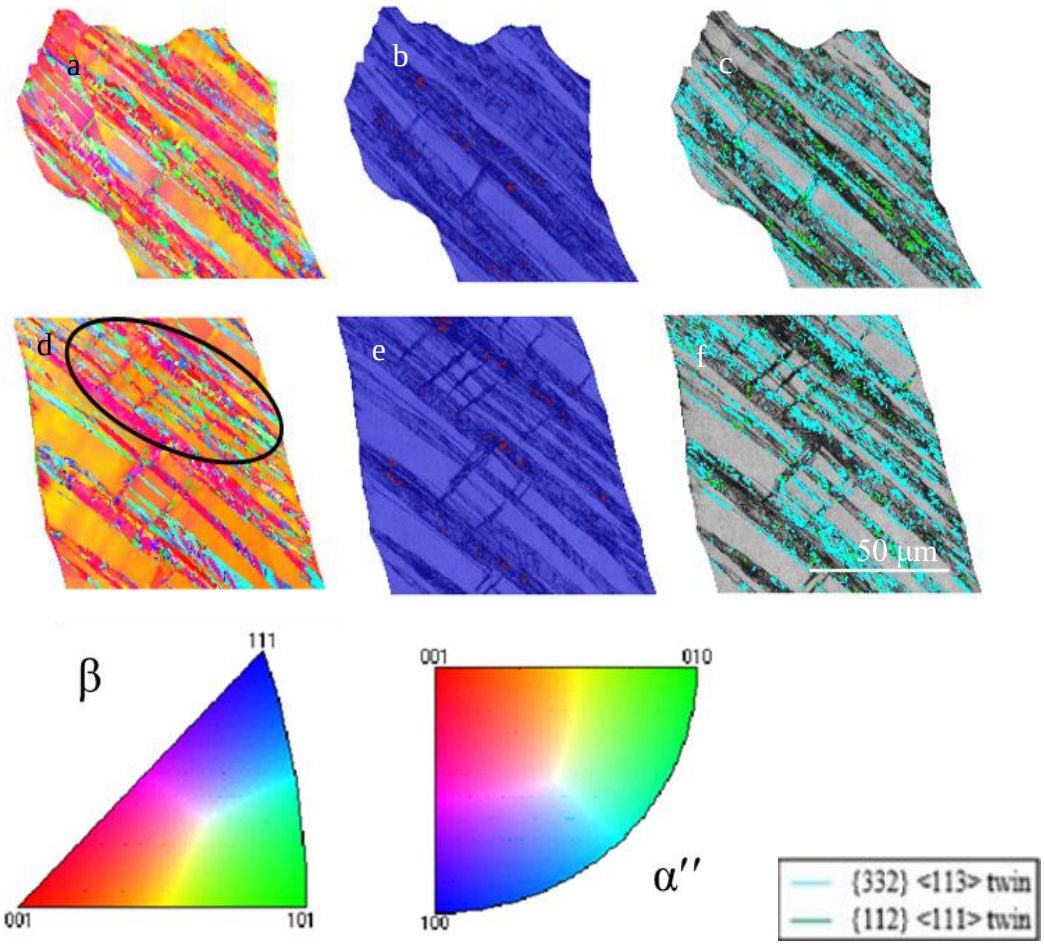

Figure 4.11. IPF maps (a and d); phase maps (b and e); blue and red colours represent β and α'' martensite, respectively; band contrast map with overlayed twin boundaries (c and f) of remelted zone (a-c) and heat affected zone (d-f) of G5 of Fig. 4.7c.

4.3.3 TEM analysis

The details of the microstructure after tension are shown in Figs 4.12 and 4.13. It comprises a complex and hierarchical structure of relatively coarse (300-600 nm thick) primary $\{332\}\langle113\rangle$ twins (Fig. 4.12a), martensite plates of two variants (Fig. 4.12c) or a single variant (Fig. 4.13d) located within the twin or the β matrix, correspondingly, and ~70-110 nm thick deformation-induced ω_D (Fig. 4.13e). Athermal ω (Fig. 4.13c) was also detected within the β phase, which was formed during LMD. Two variants of athermal ω were present, as commonly reported in the literature [24, 27, 45]. The orientation relationship (OR) between athermal ω and β phase as well as between ω_D and β phase was the standard Burgers OR: $[\bar{1}\bar{1}0]_\beta \parallel [2\bar{1}\bar{1}0]_{\omega,}$ $[111]_\beta \parallel [0001]_\omega$. The OR for α′′ martensite was determined as $[0\bar{1}1]_\beta \parallel [001]_{\alpha''}, (01\bar{1})_\beta \parallel (0\bar{1}0)_{\alpha''}$, similar to the ones reported in Refs. [282, 283].

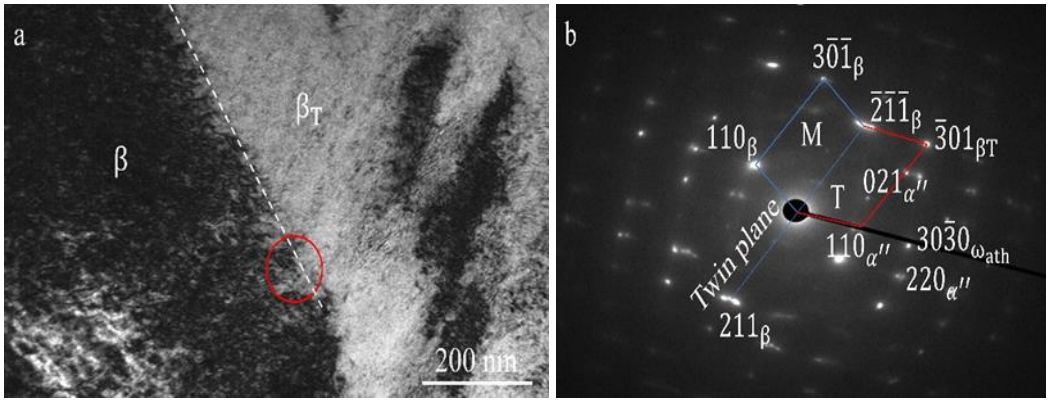

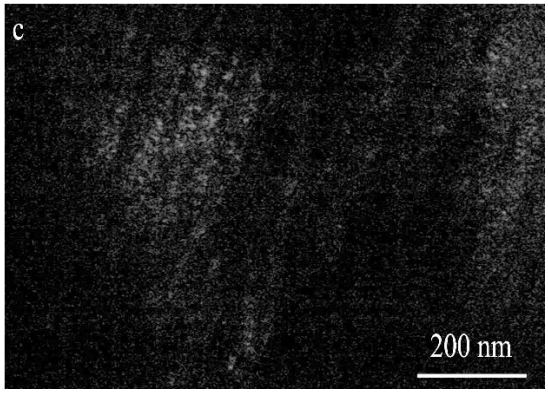

Figure 4.12a. Bright field image showing β-products interface (white dashed line), (b) SAED pattern taken from the red circle area of (a). Zone axis is $[113]_\beta \| [001]_{\alpha''}$; (c) Dark field image taken from reflection $(220)_{\alpha''}$ shows martensite plates within twin.

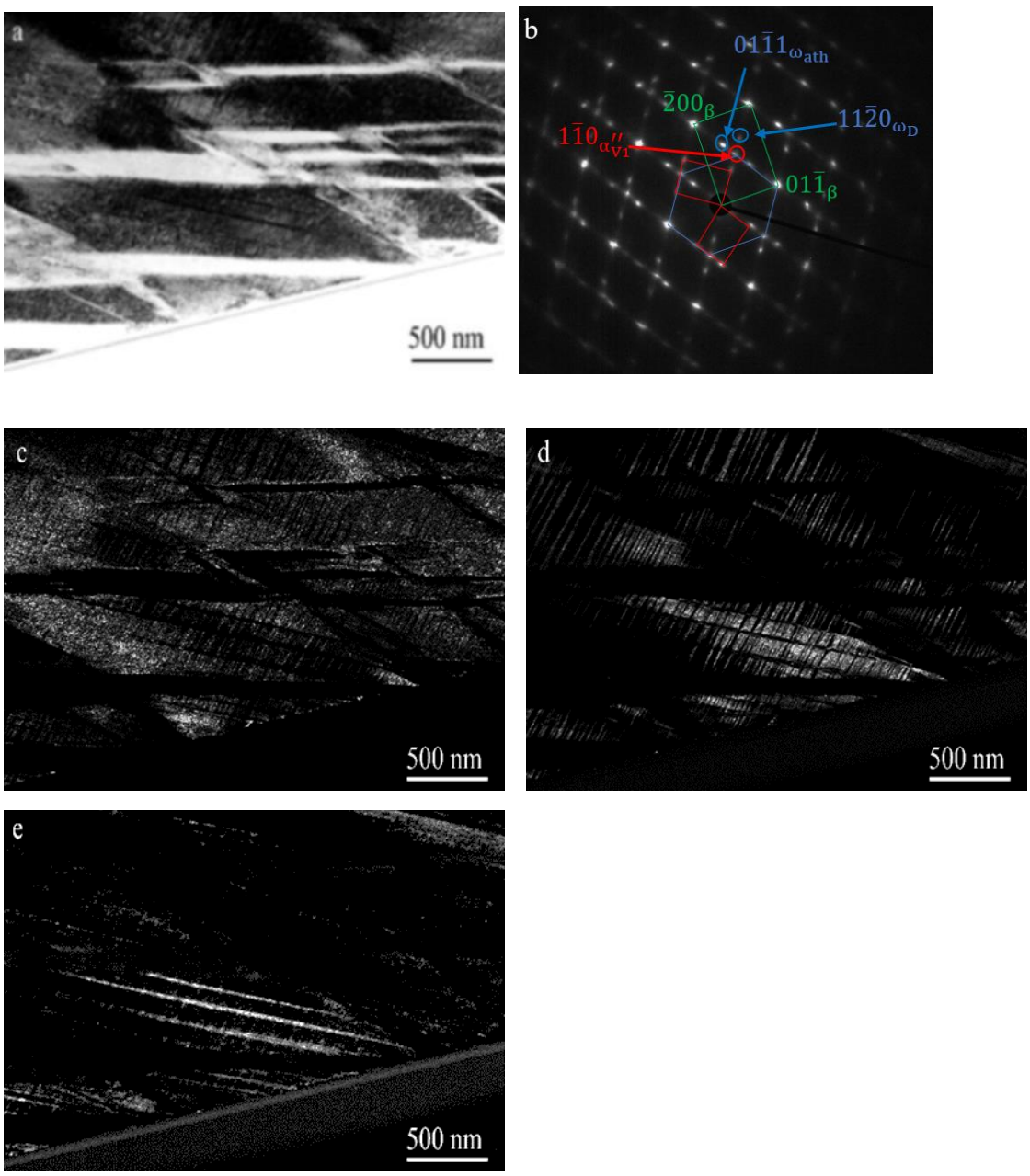

Figure 4.13. (a) Bright filed image and (b) corresponding SAED with zone axis $[0\bar{1}1]_{\beta}//[2\bar{1}\bar{1}0]_{\omega}//[001]_{\alpha''}$. (c) Dark field (DF) image showing athermal ω using reflection $(01\bar{1}1)_{\omega_{ath}}$, (d) DF of α″martensite taken using $(1\bar{1}0)_{\alpha''}$ spot; (e) DF of deformation-induced ωD taken with $(11\bar{2}0)_{\omega_D}$ reflection.

4.3.4 Texture analysis

The overall micro-texture from X-Y plane of the AB and DS samples are presented in Fig. 4.14a-b and Fig. 4.14c-d, respectively. Tensile sample Orientation Distribution Function (ODF) (i.e., Fig. 4.14c-d) were obtained from the uniform elongation part of the gauge length (i.e., area not including the visibly necked region where shape change occurred before fracture of tensile sample). As shown

in Fig. 4.14c, Orientation Distribution Function sections for β phase display relatively stronger $(001)[1\bar{1}0]$, $(010)[101]$, $(001)[1\bar{1}0]$, and $(021)[0\bar{1}2]$, $(012)[0\bar{2}1]$ orientations, and weaker $(001)[0\bar{1}0]$ and $(113)[0\bar{3}1]$ orientations. A comparison between the AB β ODFs (i.e., Fig. 4.14a) and the DS β ones (i.e., Fig. 4.14c) confirms that while the $(001)[1\bar{1}0]$, $(051)[2\bar{1}5]$ and $(114)[1\bar{7}2]$ orientations formed during the LMD fabrication process, the $(021)[0\bar{1}2]$ and $(113)[0\bar{3}1]$ orientations initiated only during uniaxial plastic deformation.

Fig. 4.14b shows no significant martensite orientation textures and confirms the absence of α''_{ath} in the AB microstructure after the LMD process. This therefore corroborates XRD patterns (i.e., Fig. 4.1) and EBSD phase maps (i.e., Fig. 4.8a-b), that martensite forms only as a result of a stress induced structural transformation from BCC to orthorhombic. Fig. 4.14d shows ODFs for α″ martensite in the sample which underwent uniaxial tensile deformation to fracture. A high intensity occurs in orientations of $(010)[001]$ and $(011)[3\bar{2}2]$. The limited number of crystallographic orientations present in α″ is a direct consequence of parent β phase texture and variant selection during stress-induced β→α″ martensite transformation, as discussed in Section 4.5.

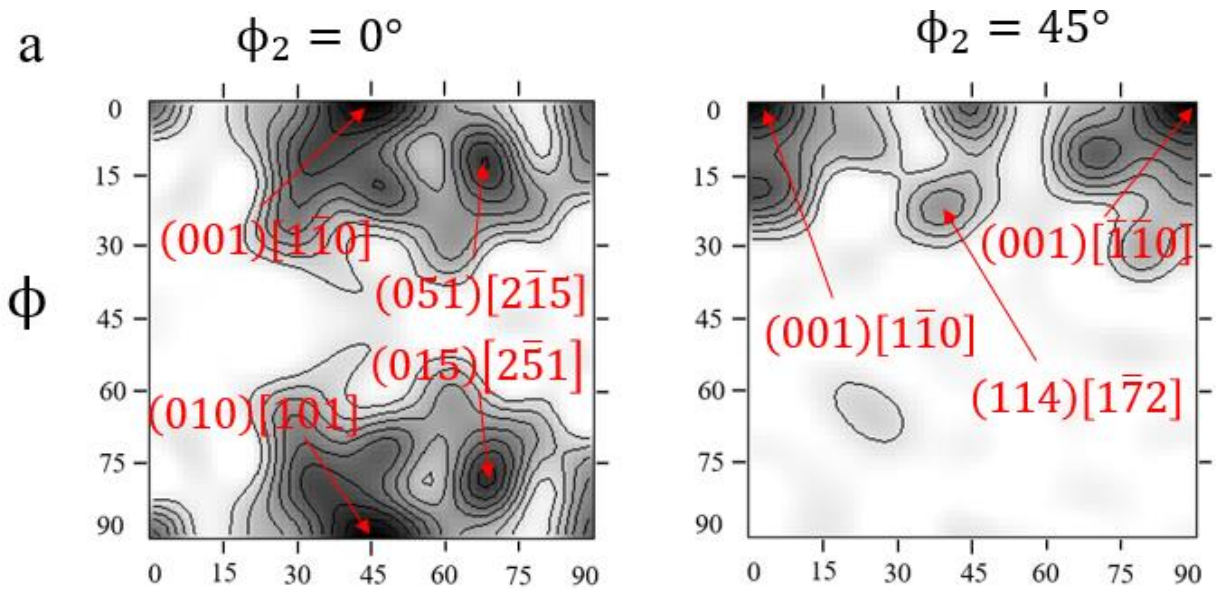

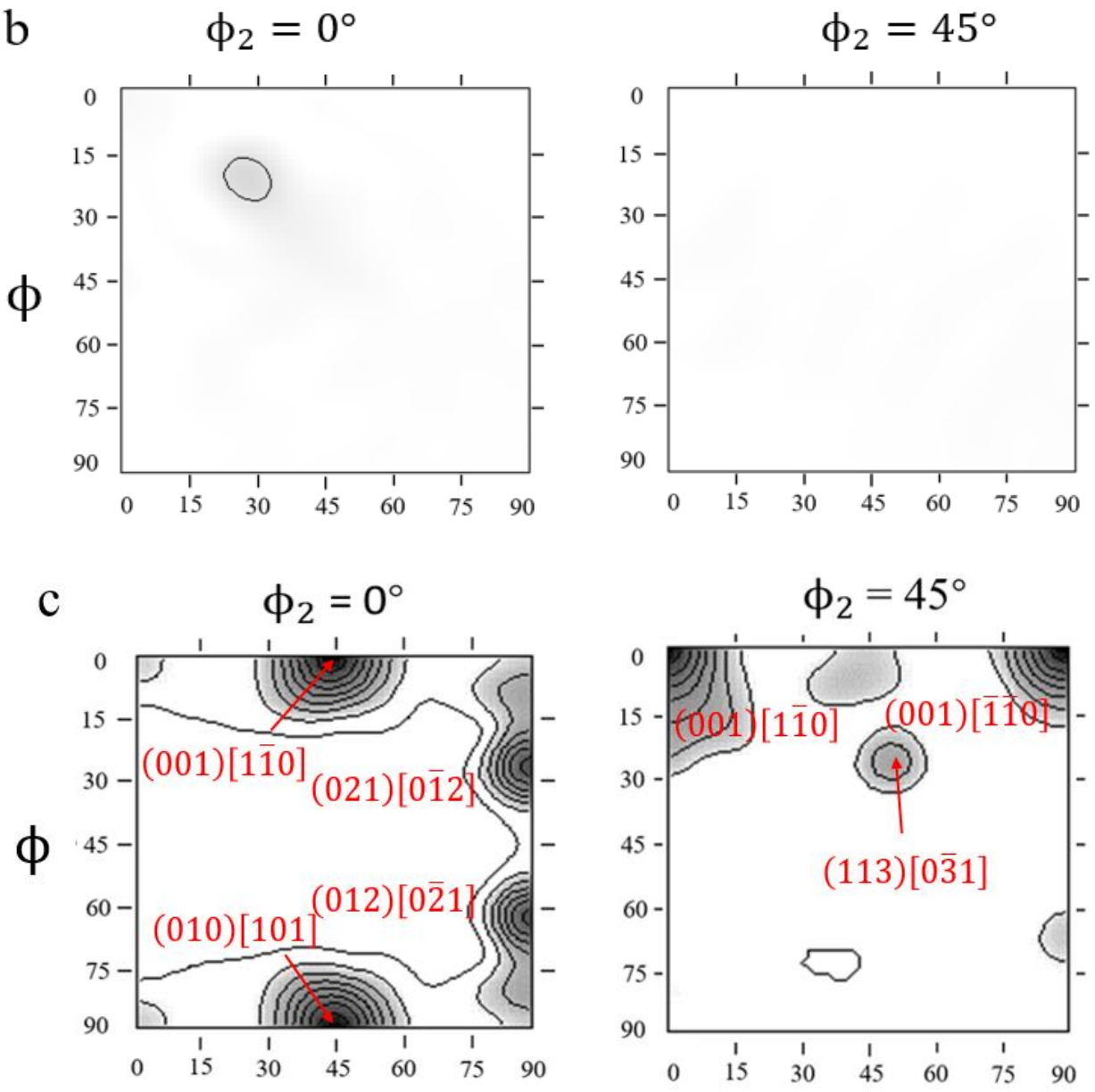
b
$\phi_2 = 0°$
$\phi_2 = 45°$
ϕ
0
15
30
45
60
75
90
c
$\phi_2 = 0°$
$\phi_2 = 45°$
ϕ
$(001)[1\bar{1}0]$
$(021)[0\bar{1}2]$
$(012)[0\bar{2}1]$
$(010)[101]$
$(001)[1\bar{1}0]$
$(001)[\bar{1}\bar{1}0]$
$(113)[0\bar{3}1]$

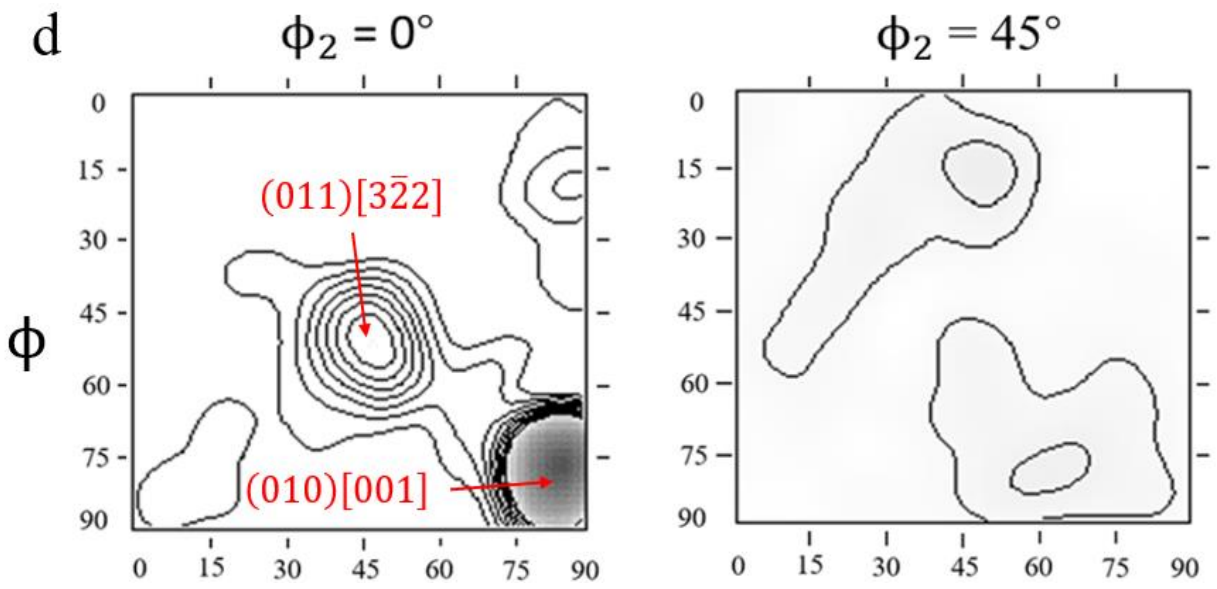

Figure 4.14. AB ODF ϕ_2 sections for (a) β-phase and (b) α′′ martensite taken from X-Y plane. Intensity levels are x0.67 and x9.82 for β and α′′ martensite, respectively; DS ODF ϕ_2 sections for (c) β-phase and (d) α′′ martensite taken from X-Y plane of tensile specimen. Intensity levels are x0.74 and x4.03 for β and α′′ martensite, respectively.

4.4 Tensile properties

Figs. 4.15a and 4.15b show a representative stress-strain curve and work-hardening rate (WHR) behaviour, respectively. The stress-strain curve shows a smooth transition from the linear elastic region to elasto-plastic region and then gradual increase in plastic region. The plateau or slowly rising stress region on stress-strain curves typical of deformation-induced phase transformation and twinning [24, 284], is absent. A similarly shaped stress-strain curve was reported for the wrought Ti-15Mo alloy with intense twinning [26]. Young modulus was calculated as 86.85±0.45 GPa. The yield strength (YS) was 850 ± 1.4 MPa, the ultimate tensile strength (UTS) was 1098.9±2.3 MPa and a total elongation of 0.0915±0.004. Although the WHR curve shown in Fig. 4.15b is a non-monotonic one, based on the variations in gradient, initially only two stages could be clearly defined: a rapid decline in WHR in stage I and a nearly plateaued WHR in Stage II. Transition from Stage I to Stage II occurs at WHR of ~3.47 GPa and true strain of ~0.017. However, after zooming-in (Fig. 4.15c), there are clear variations in gradient in Stage I: rapid linear decline (Stage IA, ends at WHR of ~85

GPa and true strain of 0.0088), followed by slower gradient decline with intermixed regions of increase and decrease in WHR (Stage IB, finishes at ~18.3 GPa and true strain of 0.013) and Stage IC with even lower gradient. These non-monotonic changes in WHR gradient and values are attributes of deformation-induced phase transformation and twinning [24, 285], which are also evidenced by the microstructure observations (Figs. 4.6-4.8 and Figs. 4.12-4.13).

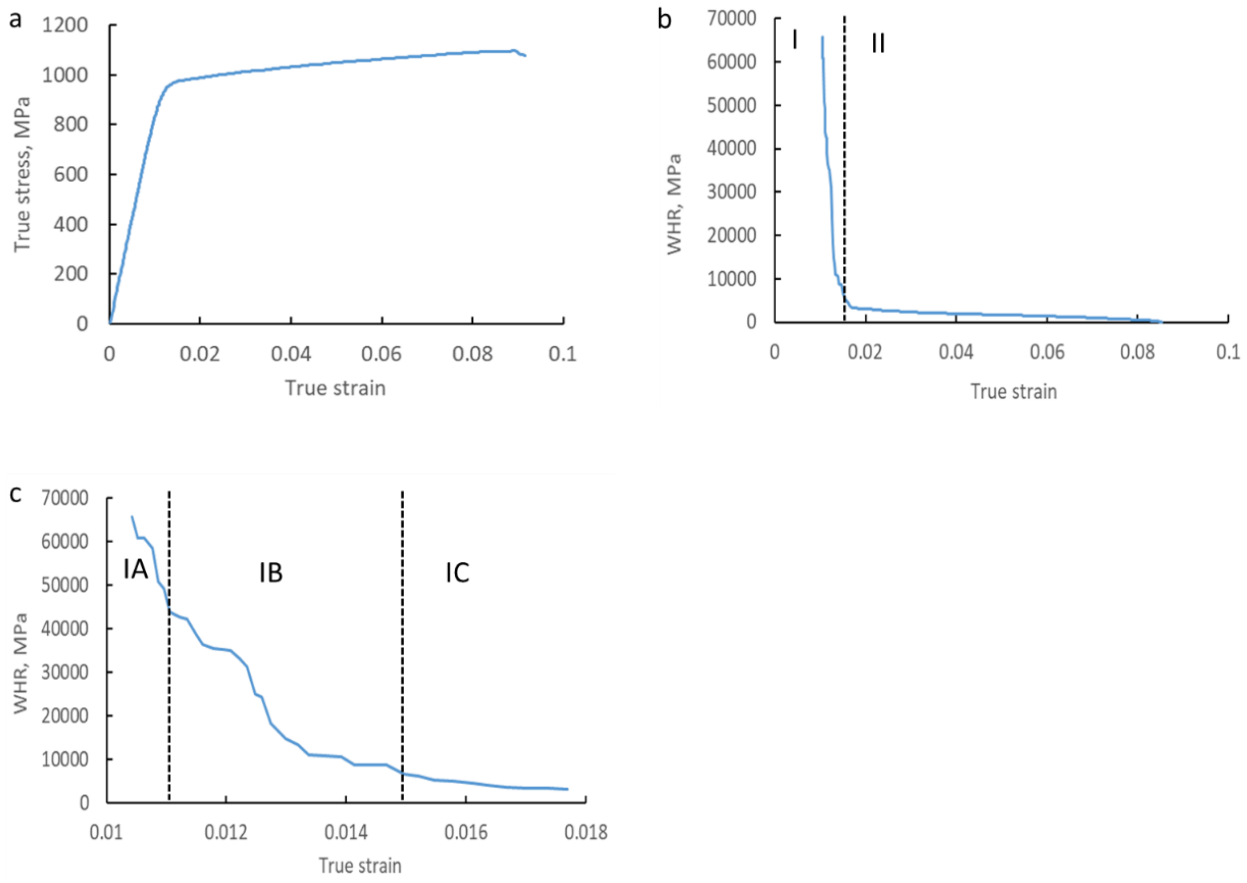

Figure 4.15(a). True stress versus True strain plot, (b) work hardening rate versus true strain plot, (c) magnified view of sub-stages within stage I of Fig. 4.15b. Dashed lines separate stages and sub-stages.

4.4.1 Fracture analysis

Fracture surfaces shown in Fig. 4.16 indicate a mixture of operating failure mechanisms: both trans-granular ductile fracture and brittle fracture modes. Micro-dimples (Fig. 4.16b) with a mean diameter of 9.4±3.1 μm were observed in many regions. In addition, finer dimples in the size range of 1-4μm were present within the micro-dimples. The pores are sparsely distributed over the fracture surface with an inter-pore spacing of 209±107 μm and an average diameter of 13.7±5.2 μm. The tear ridges

(yellow arrow of Fig. 4.16c) which surround LMD defects and pores mainly occur on flat cleavage facets and indicate the initiation of cracks at voids which formed during LMD. This and the observed characteristics of fracture surfaces are consistent with the finding for other additively manufactured Ti alloys [32, 286, 287].

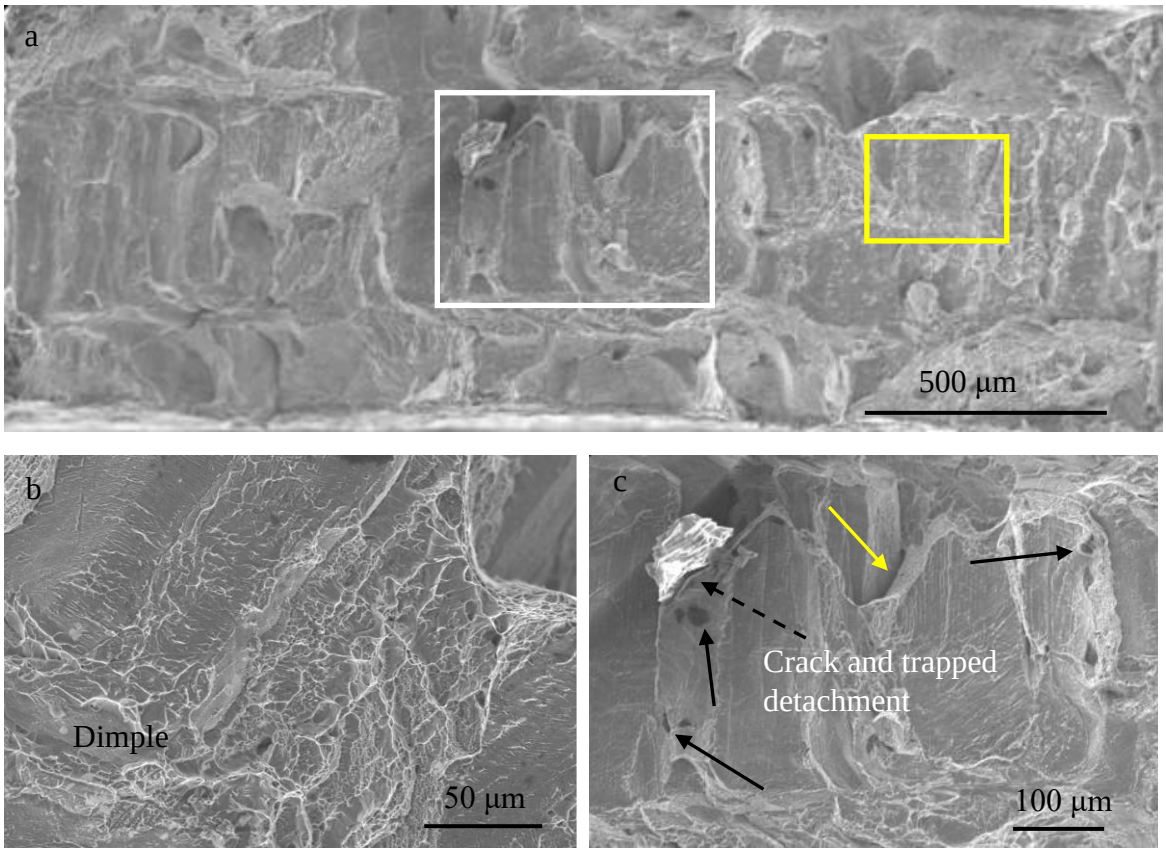

Figure 4.16 (a). Large area image of fracture surfaces of tensile sample (Vertical- build direction Z, horizontal-Y); (b) magnified view of yellow rectangle showing region with predominantly ductile fracture and (c) magnified view of white rectangle showing region with predominantly brittle fracture (cleavage facets). Black solid arrows indicate examples of pores with tear ridges around some of them.

4.5 Discussion

The microstructure after LMD was a typical one for bcc materials with predominantly coarse columnar grains and cellular-dendritic sub-structure within the grains. The heat is extracted during deposition of the layers from the liquid melt pool to the previous solidified layer and the substrate plate resulting in epitaxially-grown columnar grains oriented along the building direction. It was previously reported that the crystallographic growth direction of dendrites in the bcc lattice is along

the six equivalent <100> directions, which are the directions of the axis of the pyramid formed by four equivalent closed packed planes [288]. However, Lee et al. [289] have shown that the minimum elastic modulus and maximum heat conductivity directions also influence the direction of the dendrite growth during solidification. Due to preferential grain growth, the developed columnar grain structure exhibits a preferential orientation with dominant (110) X-ray diffraction peak in the Y-Z plane and a (100) peak in the X-Y plane (Fig. 4.1). A preference for <100> orientations along the building direction was also noted in Ref. [290], and a strong [100] texture in the build direction was noted in Ti-12%Mo alloy [291]. Depending on SLM parameters, the preferred grain orientation in X-Y plane being (100) or (110) was reported for metastable β Ti-Nb-Sn alloy [286]. The observed elemental distribution of Mo is also closely related to the conditions and processes taking place during LMD (initial solidification and subsequent partial re-melting of previously deposited layers). Although some elemental segregation of other alloying elements, such as V, Al and Sn was observed in SLM microstructure of Ti alloys, the segregation of Mo is much more pronounced [14, 290]. This is linked to a large partitioning gradient of Mo and its low diffusion coefficient in Ti, which increases the critical temperature gradient, reduces the stability of the planar solidification front and thus, stimulates cellular-dendritic solidification [290]. The interdendritic layers are enriched in Mo. Due to the change of solidification conditions in RZ, the micro-segregation of Mo resulted from cellular-dendritic solidification is removed leading to relatively uniform distribution of Mo in RZ.

The AB microstructure had a pronounced effect on tensile behaviour and properties. The YS (~850 MPa) and UTS (~1099 MPa) (Fig. 4.15) values in this study somewhat exceed those recorded in other additively manufactured metastable β Ti alloys (for example, YS 728 ± 34 MPa in Ti-15Mo [292], UTS 800 MPa in Ti-5553 [16], YS 730-790 MPa and UTS 870-890 MPa in Ti–37Nb–6Sn [286], UTS 830MPa in Ti-1023 [285]). However, except for the above Ti-1023 alloy, other alloys exhibited much better total elongation of 0.12-0.37 compared to the ~0.09 in this study. This and the higher YS/UTS ratio could be related to the operation of not only twinning as in wrought Ti-15Mo alloy with YS of only 504 MPa, UTS of 765 MPa and ~0.4 elongation, but deformation-induced

α′′martensite and ω_D. Poor ductility in AM Ti-1023 alloy was also linked to residual stresses resulting from AM. Furthermore, the presence of pores and the formation of tear ridges also impacts the ductility. The tensile samples were aligned perpendicular to the build direction and due to the strong anisotropy of the LMD microstructure this may also lead to a lower strain to failure. In addition, the alloy contained 0.25%O. In the case of a Ti-7.5Mo alloy it was reported that an increase in oxygen content >0.2% results in a decrease in ductility [82].

The masked stress plateau in stress-strain curve, which is a feature for wrought Ti alloys exhibiting twinning and phase transformation during deformation, could be linked to the coarse columnar β structure in the studied SLM material and the dominance of twinning at the early stage of plastic deformation. During continued sub-division of coarse columnar grains by twins and α′′martensite plates, the free mean path for dislocation movement did not reach the same small values (it remained > 1-5 μm) as in the wrought alloys with smaller β grain sizes (or β domains) resulting in lower work hardening rates. Although the generation of new, geometrically necessary dislocations and back-stresses arising from the formed transformation products contributed to some increases in WHR (Fig. 4.15c), the dynamic Hall-Petch effect was not so pronounced due to the coarseness of the formed deformation products (twin, martensite and ω_D width/thickness) and large areas of the matrix remained untransformed (Figs. 4.7 and 4.8). This is also why the characteristic increase in WHR towards the hump in Stage II was absent. Similar WHR behaviour was observed in the annealed additively manufactured β Ti-1023 alloy, in which α′′ martensite formation was pronounced [285].

Generally speaking, the stability of β phase Ti-15Mo alloy is reasonably high such that only {332}⟨113⟩ twinning is usually activated [26]. However, the observed operative deformation mechanisms in this alloy are more in accordance with the behaviour of Ti-12Mo alloy [24, 293].

Xu et al. [292] also reported the formation of {332}⟨113⟩ twins only in SLM-made Ti-15Mo alloy. This conclusion was based solely on EBSD data and no Mo segregation was noted. Contrarily, from the EDS area analysis in this study, the FZ was enriched in Mo. Thus, its concentration was reduced

in the RZ and HAZ regions to ~13-14 wt.%, making the β matrix less stable. This, in combination with a coarser grain structure led to the ease of formation of deformation-induced α′′ martensite and ω_D. Although some researchers have reported for Ti-Nb alloys [207, 294] that the origin of $\{332\}\langle 113\rangle_\beta$ twins is within α′′ martensite and the reversion of $\{130\}\langle 3\bar{1}0\rangle_{\alpha''}$ on load removal, others either observed in-situ, remained untransformed α′′ martensite on unloading in Ti-10V-3Al-2fe alloy [295] or just its detwinning in Ti-12Mo alloy [23]. Here, we detected variants of α′′ martensite within $\{332\}\langle 113\rangle_\beta$ twins.

The developed texture in deformed samples is also the manifestation of the operating mechanisms of the accommodation of plastic deformation. Strong $\{210\}_\beta$ texture is typically produced in deformed metastable β Ti alloys contrarily to $\{110\}_\beta$ texture developed in stable ones [18]. The operation of both, twinning and slip is deemed to be responsible for this. Although the orientation changes caused by $\{112\}\langle 111\rangle$ twinning are similar to those caused by $\{110\}\langle 111\rangle$ dislocation slip resulting in a $\langle 110\rangle_\beta$ fibre texture [296], $\{332\}\langle 113\rangle$ twinning leads to strong $\langle 100\rangle_\beta$ and $\langle 111\rangle_\beta$ textures, and a combination of both twinning types produces a $\langle 210\rangle_\beta$ texture. It was also reported that formation of α′′ martensite initially occurs in $\{110\}_\beta$ family, whereas the deformation of $\{310\}_\beta$ families at higher stress levels takes place via a combination of martensite formation and slip [297]. According to the ORs for β→α′′ transformation, $[1\bar{1}0]_\beta \rightarrow [100]_{\alpha''}$, $[110]_\beta \rightarrow [010]_{\alpha''}$ and $[001]_\beta \rightarrow [001]_{\alpha''}$. Thus, $(010)[001]_{\alpha''}$ originated from $(001)[0\bar{1}0]_\beta$, whereas $(011)[3\bar{2}2]_{\alpha''}$ formed from $(011)[0\bar{1}1]_\beta$ (Fig. 4.14d). Other weaker martensite orientations could be related to its formation within β twins.

4.6 Conclusions

Based on the application of combined characterisation techniques to gain insight into both AB and deformed microstructures, the following conclusions are reached:

1. The microstructure after LMD consisted of coarse columnar grains elongated in the build direction with a preferential <100> orientation, common for β phase microstructures of AM

Ti alloys. The occurrence of sparsely distributed equiaxed grains in certain layers of the deposited coupon (Table 4.1) confirms an inhomogeneity in AB grain structure and thus the need for post fabrication processing to homogenise grain structure. Athermal ω formed in the β matrix during heating/cooling cycles of LMD.

2. Three distinct zones were visible in each deposited layer, e.g., FZ, RZ and HAZ. Correspondingly, the non-uniform distribution of Mo was recorded with a significant enrichment of FZ, followed by a lower concentration of homogeneously distributed Mo in RZ, and Mo-rich and Mo-lean layers in cellular-dendritic structure of HAZ.
3. These distinct zones created by varying β-stability across the AB microstructure has been the reason for non-homogeneous forming of deformation products. There is therefore the need for post-fabrication processing to homogenise Mo and achieve isotropic mechanical properties.
4. The accommodation of plastic deformation took place by $\{332\}\langle 113\rangle$ primary twinning, primary and secondary α″ martensite formation, secondary $\{112\}\langle 111\rangle$ twinning within $\{332\}\langle 113\rangle$ twins, deformation-induced ω_D formation in β matrix and slip. The formation of the deformation texture was consistent with the operation of the above mechanisms. Comparison of tEL to those of conventionally manufactured versions of the same alloy suggests that twinning induced plasticity and transformation induced plasticity was not present in the current work confirming that both deformation mechanisms were activated successively and not simultaneously.
5. The achieved tensile strength was higher than that previously reported for both wrought and SLM Ti-15Mo alloys. However, this came with a reduction in ductility (~0.9 vs 0.14-0.3 total strain). For further improvement in mechanical properties, the refinement of the LMD microstructure is required. This can be achieved either at the fabrication stage through ultrasound, or by post-fabrication processing. The later option is explored in this thesis.

5 Effect of heat treatment on mechanical properties of LMDed Ti-15Mo-0.25O

The primary aim of this chapter is to homogenise molybdenum distribution and refine AB columnar β-grain. As reported in Section 4.2, the heterogeneous microstructure of as-LMDed Ti-15Mo comprises of predominant coarse columnar grains, a relatively small fraction of equiaxed grains and sparsely distributed pores. Uniformly distributed nano-sized ω_{ath} was also reported in Section 4.3.3 in the as-LMDed microstructure. This heterogeneity in grain structure causes anisotropy in mechanical properties of AM Ti-alloys [298, 299] and in other AM metals [300-302].

The alloy under investigation is subject to heat treatment at different temperatures. The emerging microstructures are then compared to the AB state for possible outcomes of homogenisation of composition and grain structure as well as possible grain refinement. Since a homogenised microstructure paves the way for uniformity in deformation products, isotropic mechanical properties could be achieved depending on the outcome of heat treatment.

The β-stability of Ti-alloys which is described by its MoE factor determines the kind of deformation products and density of product formed during tensile deformation [45, 192]. As reported in Section 4.3.2.2, segregation in Mo in the microstructure created small surface fraction differences (i.e., 0.3 – 3%) in deformation products between the RZ and HAZ of the alloy. The HAZ consistently featured relatively higher surface fraction of products. Solute segregation reported in Refs. [303, 304], also had a direct correlation with products formed during deformation and resulted in anisotropic mechanical properties.

5.1 Pre-heat treatment analysis

5.1.1 Differential Scanning Calorimetry

DSC was conducted to gain a first indication of temperature ranges in which inflections occur in the specific heat flux profile. The purpose for conducting three DSC tests was to ensure repeatability of results and to understand the effect of stored energy on inflection extent and inflection temperature range of AB and DS samples. Two tests were conducted on the same DS sample to better understand

the possible loss of all stored energy after the first test. The presence of inflections in DS-2nd tests (Fig. 5.1c) could imply that complete homogenisation may not have been attained at 1200°C for 6 hours as some stored energy remains after 1st test.

Inflections could be a hint at a possible grain recrystallisation and phase transformation, as stored energy is released in this process [305]. Fig. 5.1a, 5.1b and 5.1c show the thermogravimetric (TG/%) (i.e., green curve) and specific heat flux profiles (i.e., blue curve) of samples in the AB, DS-1st run and DS-2nd run states of the alloy under investigation. The TG profile proves that there is negligible mass gain throughout the DSC experiment implying an insignificant level of oxidation established by argon, used as shielding gas throughout the experiment. The small rise in mass at the beginning stages of experiment (red ellipse of Fig. 5.1a) is due to buoyancy effect. Fig. 5.1a shows an endotherm in the AB alloy occurring at an approximate start and finish temperatures of 500°C and 600°C, respectively. These temperatures compare very closely to those of the observed inflections in the DS curves (i.e., Fig. 2.1b and 2.1c). The exotherm of Figure 2.1b has a finish temperature of approximately 650°C. The DS-2nd test includes only heating and isothermal segment with the cooling segment excluded. This profile shows an area of endothermal trough immediately followed by an exothermal peak. Approximate temperatures are from 550°C to 570°C for endotherm and 570°C to 635°C for exotherm.

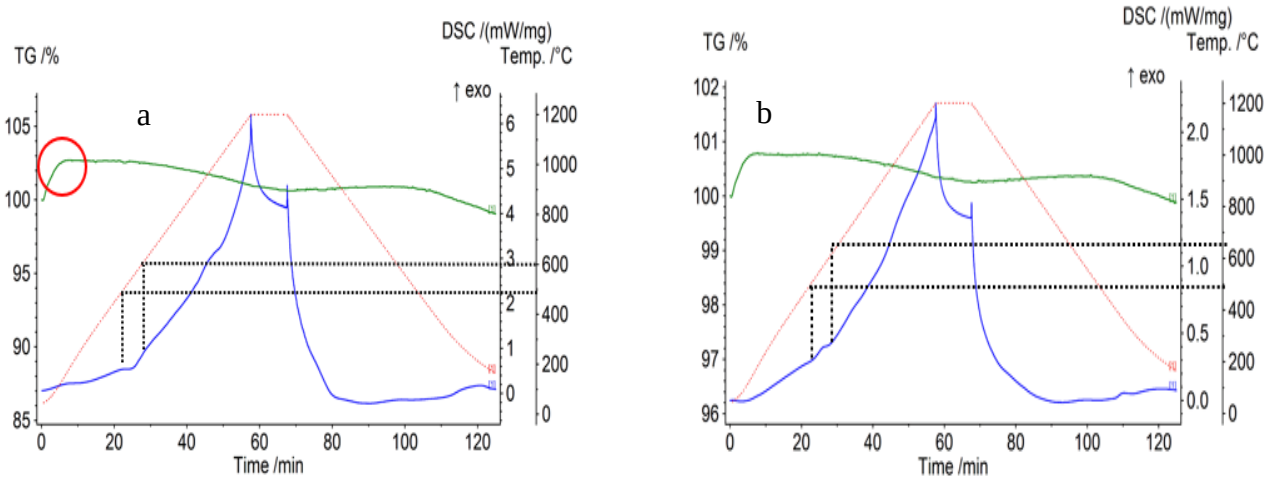

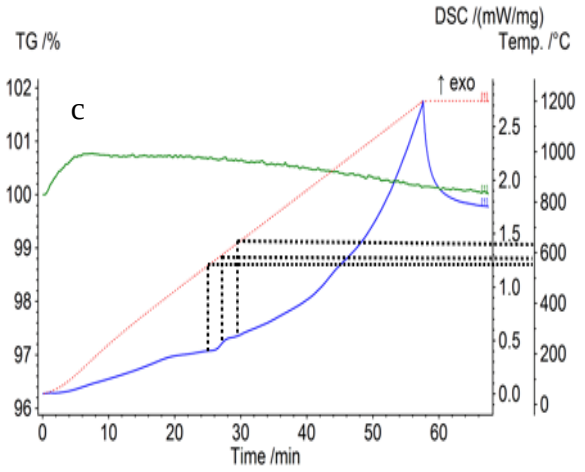

Figure 5.1. Thermogravimetric (green) and specific heat flux (blue) profiles recorded on Ti-15Mo-0.25O by Differential Scanning Calorimetry at a heating and cooling rate of 50°C/min for (a) As-Built alloy; (b) Deformed alloy; (c) 2nd test of deformed alloy used in (b).

5.1.2 Literary basis

In Ref. [34], homogenization heat treatment (HHT) was conducted on Ti-15Mo at 1473K (~1205.9°C) for 3h followed by air cooling. 100mm x 50mm x 15mm plate of Ti-15Mo was homogenized at 1473K for 6h in Ref. [33]. In Ref. [35], the same alloy was homogenized at 1373K (~1100°C) for 6h and water quenched and yielded fully equiaxed microstructure. It should be noted that while the claim on grain structure homogenization was substantiated in the cited references above, there was no EDS analysis conducted to confirm solute homogenization (i.e., single phase homogenization).

In Ref. [306], β-grain refinement was achieved in Ti-6Al-4V by epitaxial recrystallisation enabled by rapid heat treatment (RHT). Heating was conducted at a rate of 10°C/s to a target temperature of 1030°C with a dwell time of 1s before air cooling. β grain size after RHT was not reported in the cited work, however lower E-Mod and higher tEl were obtained in comparison to the AB sample. In Ref [36], RHTs were conducted on the same alloy at rates of 10°C/s and 50°C/s to a target temperature of 995°C and held for 5s before quenching to room temperature. Ultra-fine β-grain of 40µm and 8µm were achieved, respectively even though grain size before heat treatment was not reported. Also, in

Ref. [36] the target temperatures were both in the single β-phase field and a short holding time was used as will be used in the current work to reduce tendency for grain growth.

5.1.3 Diffusivity

In Equation 2.1, t = diffusion time, x = diffusion distance and D = diffusivity of Mo in Ti.

$t \approx x^2/2D$ [275] Equation 5.1

Ref. [307] gave the diffusivity of Mo in Ti as 370 x 10^{-14} m^2/s at 1479K and an atomic concentration of 90 at.% (~82 wt.%) for titanium. Time required for diffusion of Mo across 2 layers (0.4mm of deposited coupon shown in Fig. 3.4) is calculated as follows:

$$t \approx \left[\left(\frac{0.4}{1000}\right)^2 m^2\right]/(2 \times 370 \times 10^{-14})\ m^2/s = 21621.6 \text{ sec}$$

21621.6 sec / (60 x 60) = 6 hours.

The obtained diffusion time compares closely to those reported in Section 5.1.2. Hence, this should be ample time for Mo to diffuse between 2 adjacent layers to establish the required state of solute equilibrium among all 25 layers. Ref. [308] gave the diffusivity of Mo in Ti-Zr system as 5.04 x $10^{-13} \pm 1.24$ m^2/s with 4.85 at.% of Zr. Applying Equation 2.1 yields a diffusion time of 44 hours across 2 layers. The influence of Zr in this alloy causes a wide disparity in this result from the 6 hours obtained in a Ti-Mo binary system.

Based on DSC results and data obtained from literature, several heat treatment experiments were conducted in the temperature range from 650°C to 850°C with the aim to achieve β grain refinement by either recrystallisation or grain fragmentation. Even though inflections of Fig. 5.1 have a start temperature of 500°C, recrystallisation experiments were conducted above this temperature to avoid the lower domains of the $\alpha + \beta$ phase field to allow sufficient β-domain size for possible formation of deformation products during subsequent tensile test [45, 278]. An attempt at grain/compositional homogenisation was conducted for 6 hours at 1200°C which lies in the single β-phase field.

5.2 Heat treatment

The specimens used for heat treatment were selected based on limited material availability. β-phase field heat treatment experiments were conducted at a rate of 20°C/s to a target temperature of 1200°C and held for 21600s (6h) before quenching to RT as shown in Fig. 5.2 (blue). Two samples including AB-1200 and pre-deformed (PDS-1200) were subject to this experiment aimed at microstructural homogenisation. The pre-deformed sample underwent uniaxial tensile test to failure before heat treatment at 1200°C. This experiment was conducted to understand what happens to deformation products when subject to heat treatment at 1200°C for 6 hours.

Sub-1200°C heat treatment experiments were conducted according to the schedule represented in Fig. 5.2 (black) at 650°C, 700°C, 730°C, 750°C and 850°C at a rate of 20°C/s and held for 600s (0.17h) before quenching in water to RT. Hold time of 600s was used to allow for soaking at that temperature while preventing possibility of grain growth at extended hold times. These samples will hereafter be referred to as AB-650, AB-700, AB-730, AB-750 and AB-850, respectively. Multiple sub-1200°C experiments were conducted to determine sample with the smallest grain size after heat treatment.

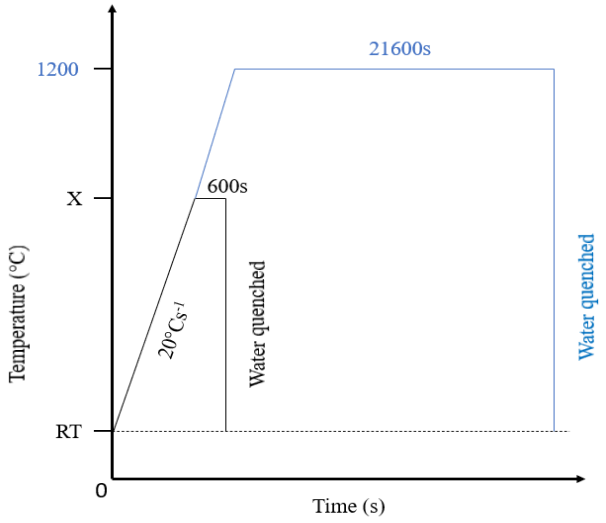

Figure 5.2. A schematic diagram of the heat treatment schedule used in this study for 1200°C (blue) and sub-1200°C (black) experiments.

5.3 XRD pattern analysis

The XRD patterns of the AB-1200 (green) and PDS-1200 (blue) samples subject to heat treatment at 1200°C are presented in Fig. 5.3a. The non-heat-treated AB sample (red) is also included in this figure for comparison. As seen in the decreased $(110)_{\beta}$ and $(211)_{\beta}$ peak intensities of the green and blue patterns, the predominant β microstructure reported in Chapter 4 of this work in the AB alloy, is replaced by a microstructure with significantly reduced β-domain size and newly formed α-phase. This confirms that phase transformation did occur, as predicted by DSC specific heat flux inflections (Figs. 5.1a-c). Also, in Fig. 5.3a the $(100)_{\omega_{ath}}$ and $(200)_{\omega_{ath}}$ peaks are only present in the AB-1200 pattern and non-existent in the PDS-1200 and AB samples (Also see red and green patterns of Fig. 4.1).

Fig. 5.3b shows the pattern for AB-700 sample (red) subject to heat treatment at 700°C and the 700-DS sample subject to uniaxial tensile deformation after heat treatment at 700°C (green). AB-700 pattern shows peaks for α, β and ω while the 700-DS also shows α_D'' in addition to α, β and ω. There is a decrease in $(041)_{\alpha''}$ martensite peak intensity from 665 counts in the DS sample (i.e., blue pattern of Fig. 4.1) to 460 counts in the 700-DS sample (i.e., blue pattern of Fig. 5.3b). $(110)_{\beta}$ and $(002)_{\alpha}$ peaks occur at an interface between both phases with β being the primary and shoulder peak in the AB-700 and 700-DS samples, respectively. The (100) omega peak is the athermal type as it also appears in the AB-700 sample. The (110) and (200) omega peaks are of the deformation induced type as they only appear in the 700-DS sample.

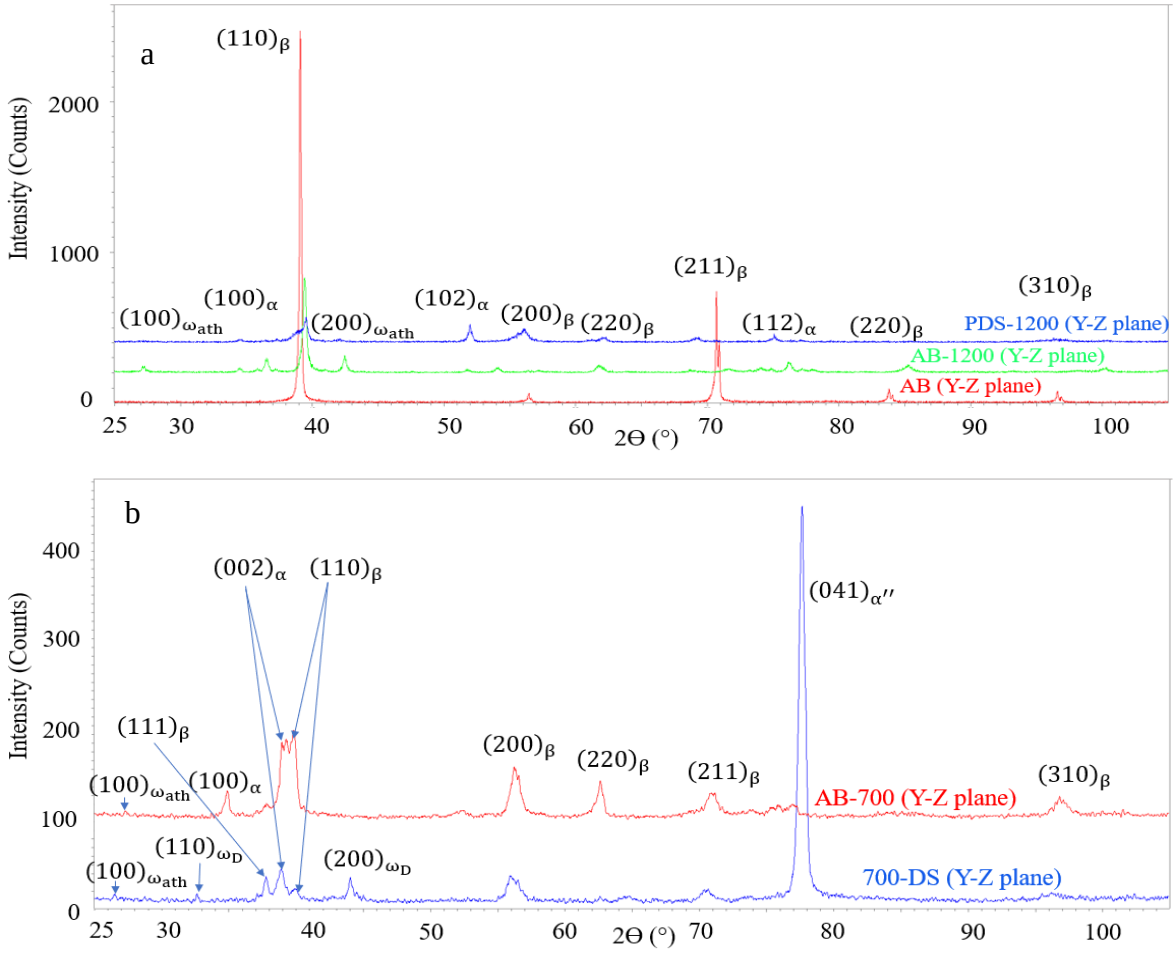

Figure 5.3 XRD patterns of (a) As-Built sample (red), As-Built sample subject to homogenisation (green), deformed sample subject to homogenisation (blue); (b) sample heat treated at 700°C (red) and deformed sample after heat treatment (green).

5.4 Microstructural characterisation of heat-treated samples

5.4.1 SEM analysis

All images in Fig. 5.4 were acquired at 250x magnification except for images of Fig. 5.4e and 5.4f which were taken at 1000x and 5000x, respectively to show specific microstructural features. Grain refinement was analysed in comparison to the initial AB condition (Figs. 5.4a and 5.4b).

The AB-650 (Fig. 5.4c) and AB-850 (Fig. 5.4i) samples were obtained from the Y-Z plane, same as the AB sample of Fig. 5.4a. These samples show grain refinement as reported in Fig. 5.5 howbeit still of predominantly columnar structure. The AB-700 (Figs. 5.4d, 5.4e and 5.4f), AB-730 (Fig. 5.4g) and AB-750 (Fig. 5.4h) samples were extracted from the X-Y plane and these have predominantly equiaxed grains which got refined in comparison to the equiaxed grains of the AB sample (Fig. 5.4b).

As shown in Fig. 5.5 the AB-700 X-Y plane sample was the most refined of the three X-Y plane samples heat treated at sub-1200°C temperatures. Also, this sample had the highest number of grains bearing equiaxed morphology.

Based on the inhomogeneity of the AB coupon, there was the need to further investigate the influence of sample orientation on observed X-Y plane grain refinement. A sample having orientation in the Y-Z plane was subject to HT at 700°C (Fig. 5.4e) and grain refinement (Fig. 5.5) was also determined in comparison to the AB Y-Z sample (Fig. 5.4b). Partially recrystallised grains of heterogeneous structure were determined. Green and red arrows of Fig. 5.4e indicate recrystallised β-grains growing epitaxially and non-epitaxially, respectively. There was also more convincing evidence of recrystallised grain boundaries in the AB-700 sample than those observed in the AB-730 and AB-750 samples. Therefore, recrystallisation of smaller grains within prior-columnar grains is confirmed in the AB-700 sample, regardless of specimen orientation.

Fig. 5.4f is a 5000x magnification of the red rectangle in Fig. 5.4e. It shows precipitates which bear a needle-like structure forming at right angles to each other with a dense distribution in all areas of the microstructure except for the FZ. These precipitates were identified as α-phase by XRD (red pattern of Fig. 5.3) and they occupy about 53% surface fraction in the AB-700 microstructure. The green ellipse shows a precipitate free zone while the red ellipse shows an area of sparse precipitate distribution which is also part of the FZ.

Fig. 5.4g shows short inter-dendritic cells of segregated Mo in the X-Y plane, and this appear as interlayers of thin long lamellae in the Y-Z plane (Figure 2.3c).

The relatively dense pore distribution (black spots) of Fig. 5.4h is another evidence of the inhomogeneous state of the AB coupon.

Fig. 5.4j is the AB-1200 sample. It shows lath-like precipitates forming within columnar grains at different distribution densities as well as at grain boundaries (yellow arrows) which in some instances extend into adjacent β grains. Figure 2.3k shows the PDS-1200 sample, and it shows the same features in Figure 2.3j howbeit with an overall sparser distribution. Images of PDS-1200 sample bear no

representation of deformation bands, implying a possible reversal of β-twins back to β. EBSD of this sample which goes beyond the financial scope of this work, is required to determine if athermal and deformation induced α″ martensite is present in the AB-1200 and PDS-1200 samples, respectively as these phases were not detected by XRD patterns of Fig. 5.3a.

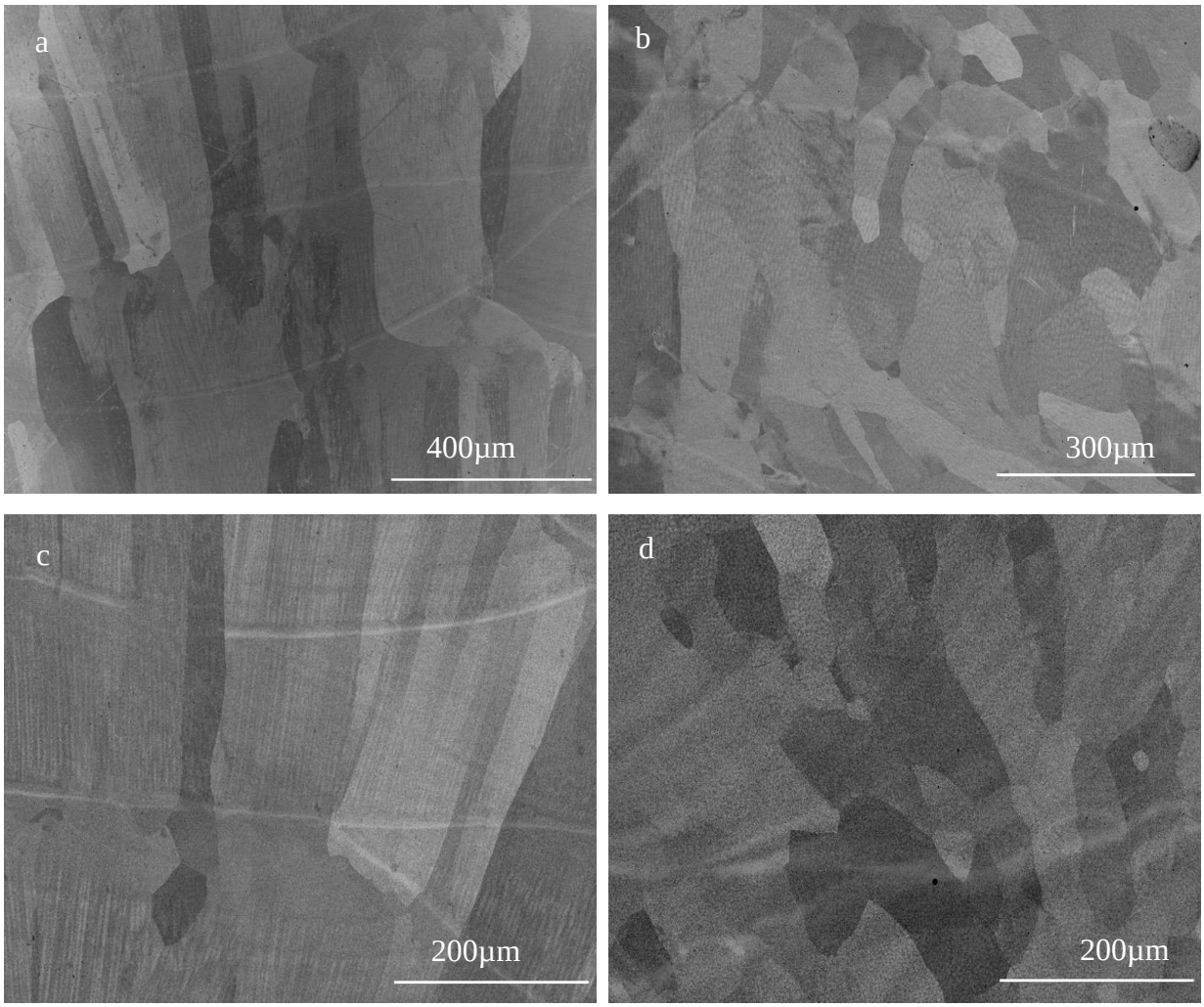

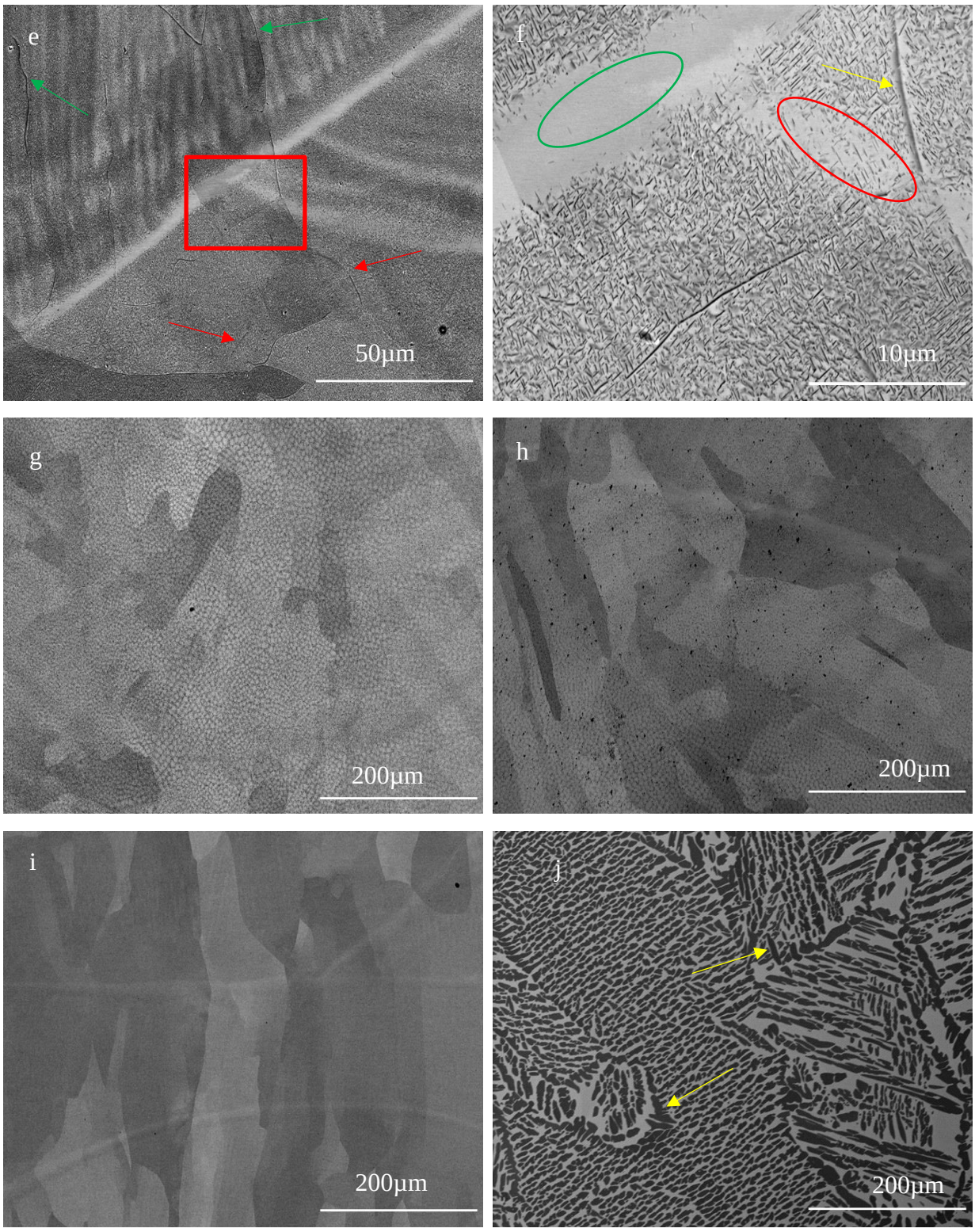
e
50µm
f
10µm
g
200µm
h
200µm
i
200µm
j
200µm

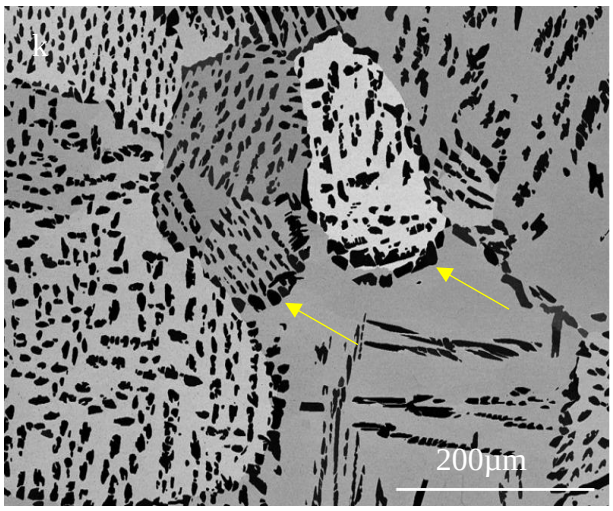

Figure 5.4. SEM images of (a) AB (Y-Z plane); (b) AB (X-Y plane); (c) AB-650 (Y-Z plane); (d) AB-700 (X-Y plane); (e) AB-700 (Y-Z plane); (f) Magnified view of red rectangle of "e"; (g) AB-730 (X-Y plane); (h) AB-750 (X-Y plane); (i) AB-850 (Y-Z plane); (j) AB-1200 (Y-Z plane); (k) PDS-1200 (Y-Z plane).

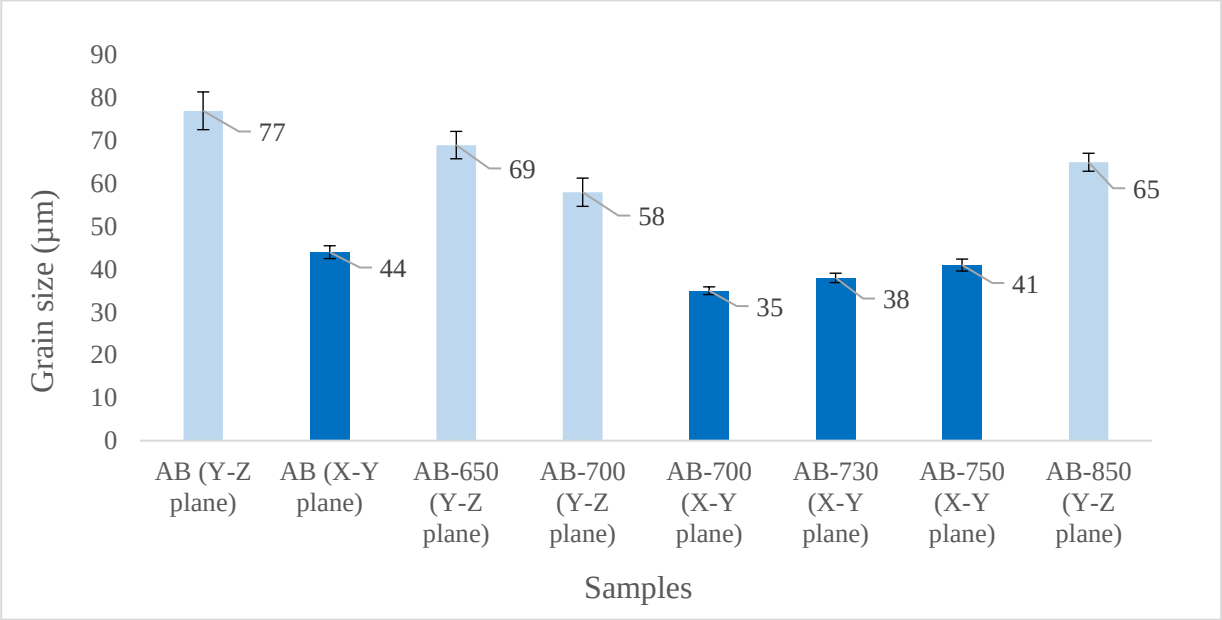

Figure 5.5. Mean grain sizes of AB and sub-1200°C heat treated samples.

Based on results from HT, mechanical testing was conducted on AB-700 sample and reported in Section 5.6.

5.4.2 EDS points analysis

Mo distribution maps are shown for AB sample (Fig. 5.6a), AB-700 sample (Fig. 5.6b) and AB-1200 sample (Fig. 5.6c). The FZ, RZ and interlayers of HAZ are present in samples subject to heat treatment below 1200°C (Fig. 5.6b). However, these distinct microstructural zones are not found in the sample subject to heat treatment at 1200°C for 6 hours (Fig. 5.6c).

As shown in Fig. 5.7a, the FZ and interlayers of HAZ of AB and AB-700 samples show small differences in Mo concentration. However, the RZ of the AB-700 sample attained a higher degree of homogenisation compared to the AB sample, as indicated by the lower standard deviation. Spectrum 97 and 101 of Fig. 5.6b show enhanced β-stability with Mo concentrations of 18.4 and 23.0 Wt. %, respectively while spectrum 99 bears 0 Wt. % of Mo, indicative of pure α-Ti. Similar dendritic lamellas of enhanced and depleted β were also found in the AB sample.

As shown in Fig. 5.7c, microstructure after heat treatment at 1200°C for 6 hours featured super-rich β-matrix and extremely depleted α-laths with Mo Wt.% of 30.1±0.5 and 0.7±0.1, respectively. A single β microstructure was therefore not achieved after heat treatment in the β- phase field. In the phase calculations of Appendix A of Ref. [309], a single β phase is predicted at this temperature. Results of Fig 5.7c does not conform to the cited phase diagram prediction possibly due to entrance of more oxygen into the alloy during the 6-hr holding time inspite of the use of Ar as shielding gas.

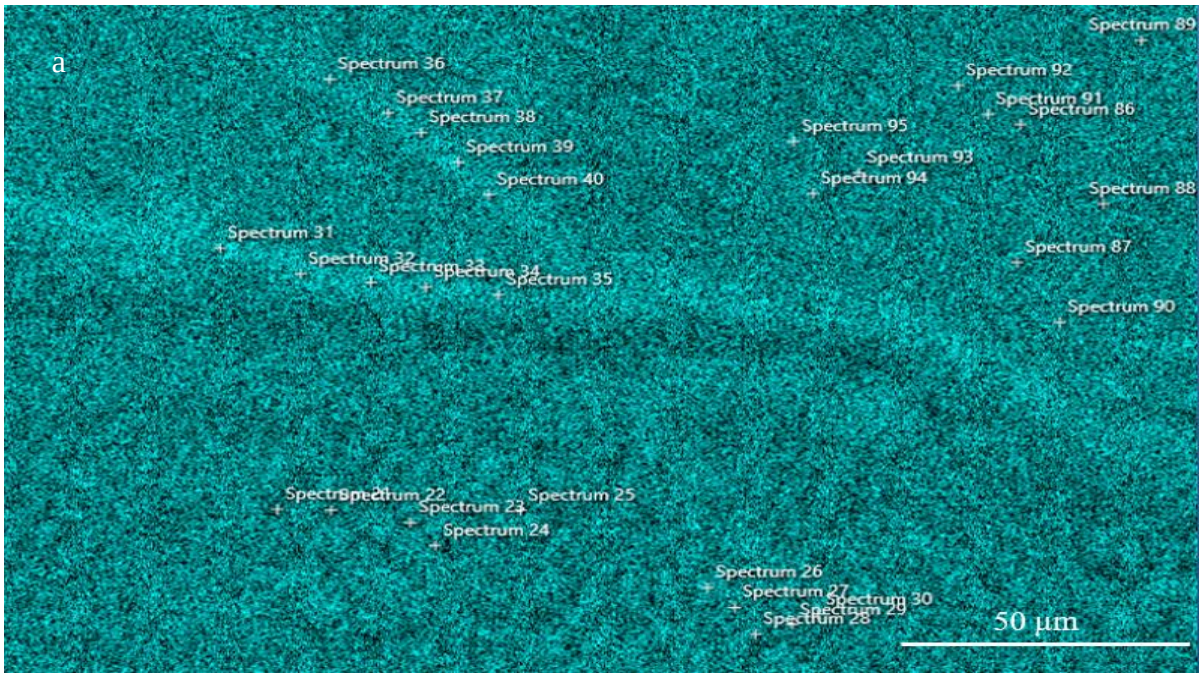

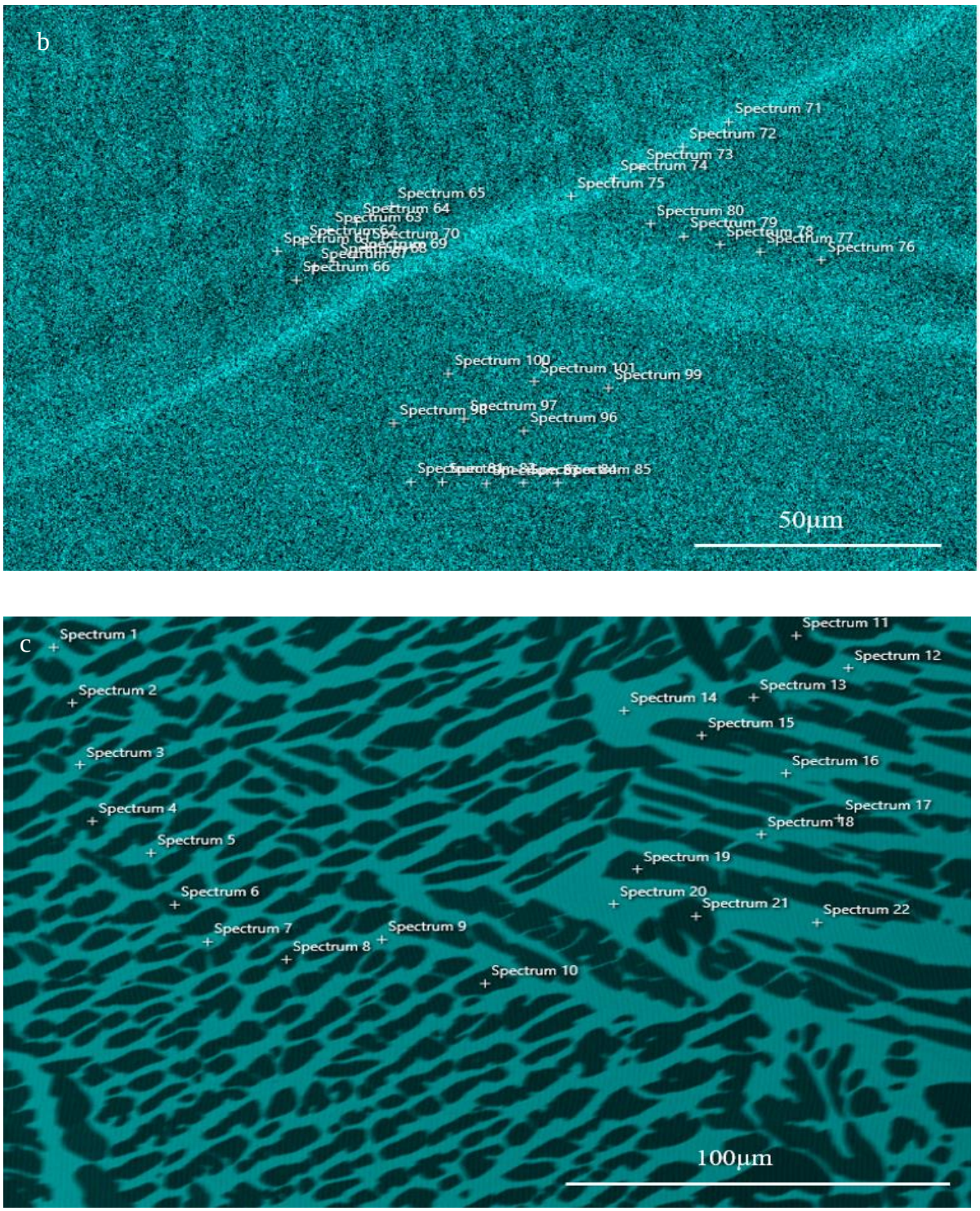

Figure 5.6. Point spectrum locations for (a) AB; (b) AB-700 and (c) AB-1200 samples.

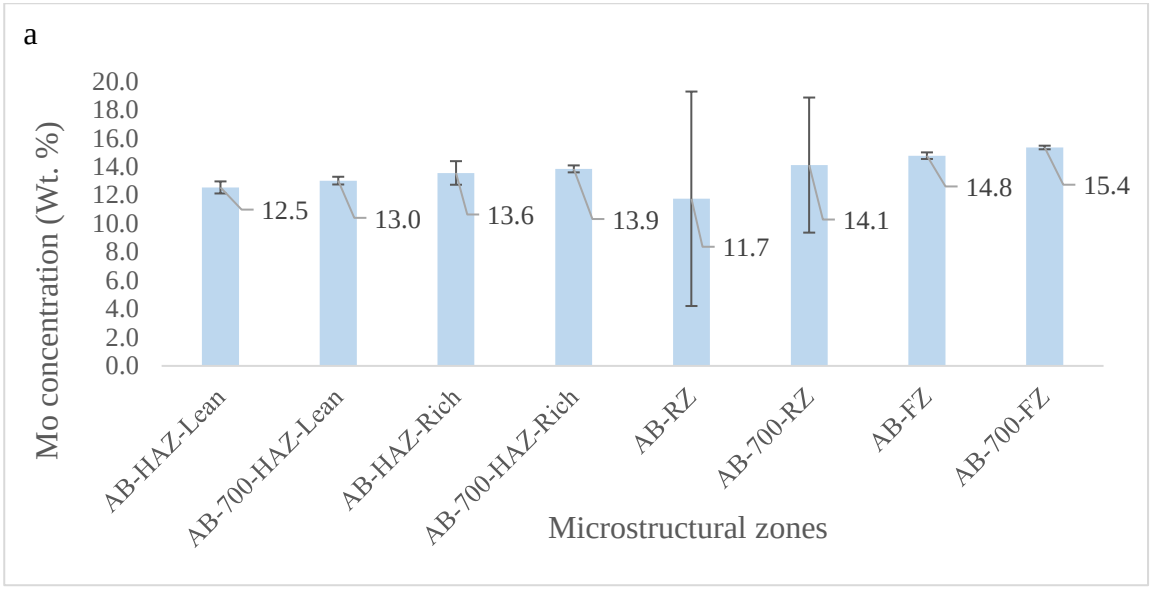

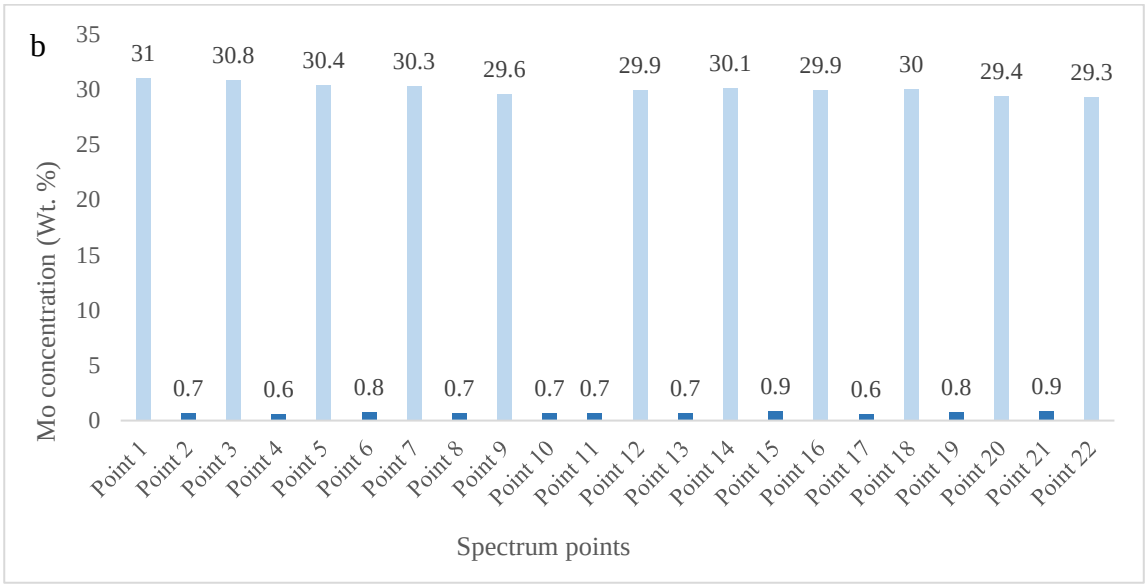

Figure 5.7. Statistical Mo concentration of points in (a) Fig. 5.6a and 5.6b; (b) Fig. 5.6c.

5.5 Characterisation of deformed microstructure

5.5.1 SEM analysis

All images of Fig. 5.8 were taken from the uniform elongation zones (i.e., area of gauge length of tensile specimen not including the visibly necked region). Fig. 5.8a and 5.8e show deformed microstructures of AB alloy from X-Y and X-Z planes from Chapter 4, respectively featuring deformation bands and martensite plates forming primarily on β matrix and within the bands. The deformed microstructures of 700-DS sample (Fig. 5.8b-d (X-Y plane) and 5.8f-h (X-Z plane)) bear no strong representation of deformation bands. 700-DS images were taken from different planes and different areas of the sample at magnifications of 250x, 500x and 1000x to confirm the absence of deformation bands after tensile failure. Lighter and darker regions (depending on β-grain orientation) appearing in these images mainly represent untransformed β. However, these regions could also bear non-banded deformation products. Further investigation by EBSD is presented in Section 5.5.2. Substructures which are indicated by the red arrows of Fig. 5.8c formed during heat treatment. The substructures appear to be growing across prior β-grain (white arrow of Fig. 5.8c). Yellow ellipse of Fig. 5.8d shows short dendritic cells representing the segregated state of Mo. These cells appear as thin long lamellae in Fig. 5.8f. Within the yellow rectangle of Fig. 5.8h, there is a pattern of alternating dark and light, diagonally oriented elongated rectangles forming across prior columnar β-GBs. This occurrence seems to indicate the very nascent stages of β-twinning where light areas in-between could be un-reoriented β. Segregated Mo lamellas (white arrows of Fig. 5.8h) also occur in these grains at steeper angles than reported earlier and they intersect the alternating diagonal rectangles.

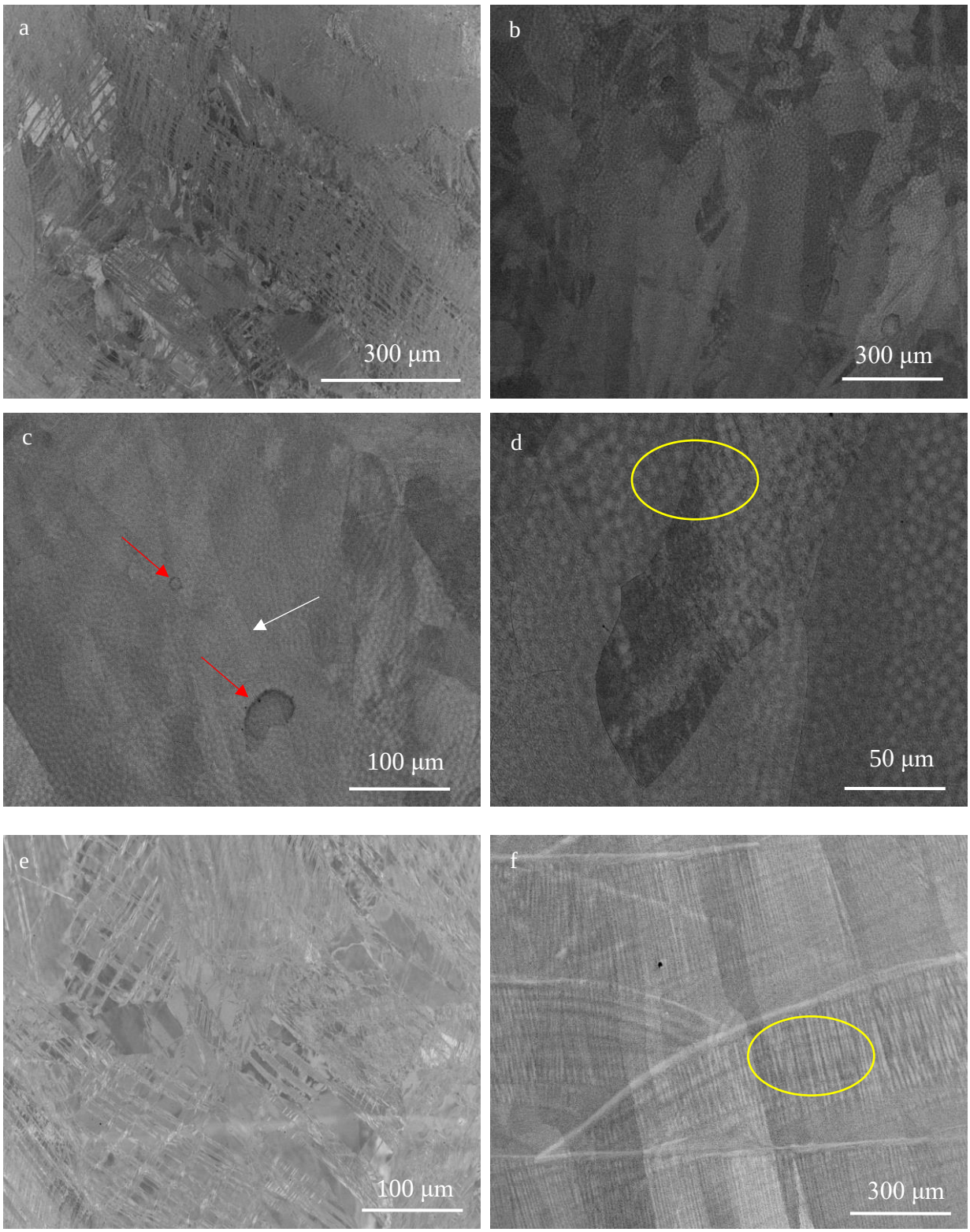
a
300 µm
b
300 µm
c
100 µm
d
50 µm
e
100 µm
f
300 µm

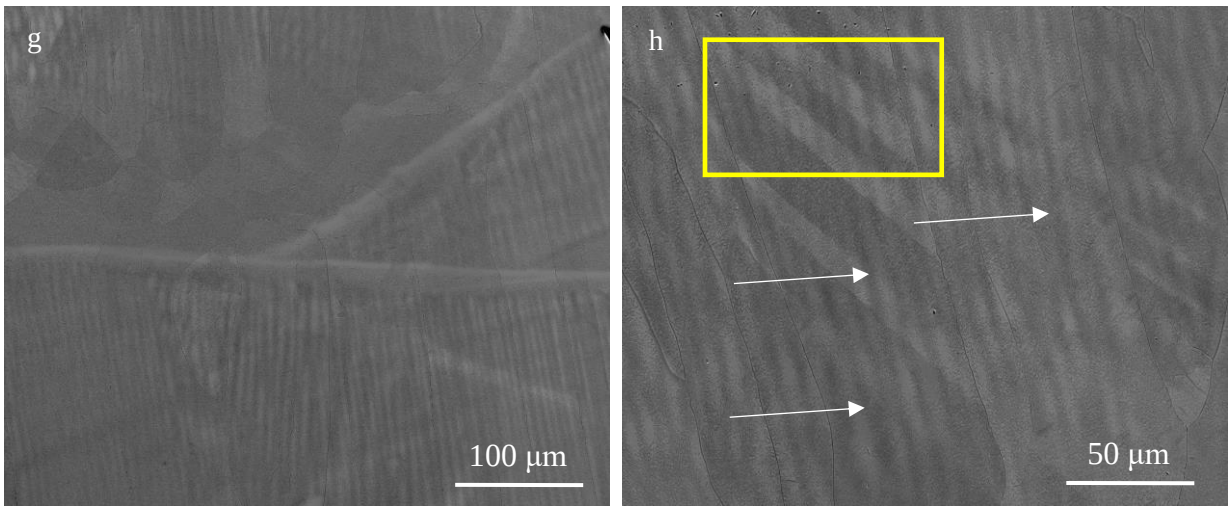

Figure 5.8. Deformed microstructures taken from X-Y plane for (a) AB; (b) 700-DS-250x; (c) 700-DS-500x; (d) 700-DS-1000x samples; Deformed microstructures taken from X-Z plane for (e) AB; (f) 700-DS-250x; (g) 700-DS-500x; (h) 700-DS-1000x samples.

5.5.2 EBSD analysis

Fig. 5.9a, 5.9b and 5.9c show the IPF, BC with overlayed α″ martensite and twin boundary and GB maps of the 700-DS sample, respectively. These maps come from area within the yellow rectangle of Fig. 5.8h. IPFs were generated with respect to the X-axis of LMD sample which is the tensile direction and axis of most relevance. Comparison of Fig. 5.9a and 5.9b provides convincing evidence that regardless of grain size/orientation, there is the complete absence of β-twins in the deformed 700°C heat treated alloy. From Fig. 5.9c, the seeming beginning stages of twinning reported in Section 5.5.1 are confirmed to be LAGB grains extending across adjacent columnar grains.

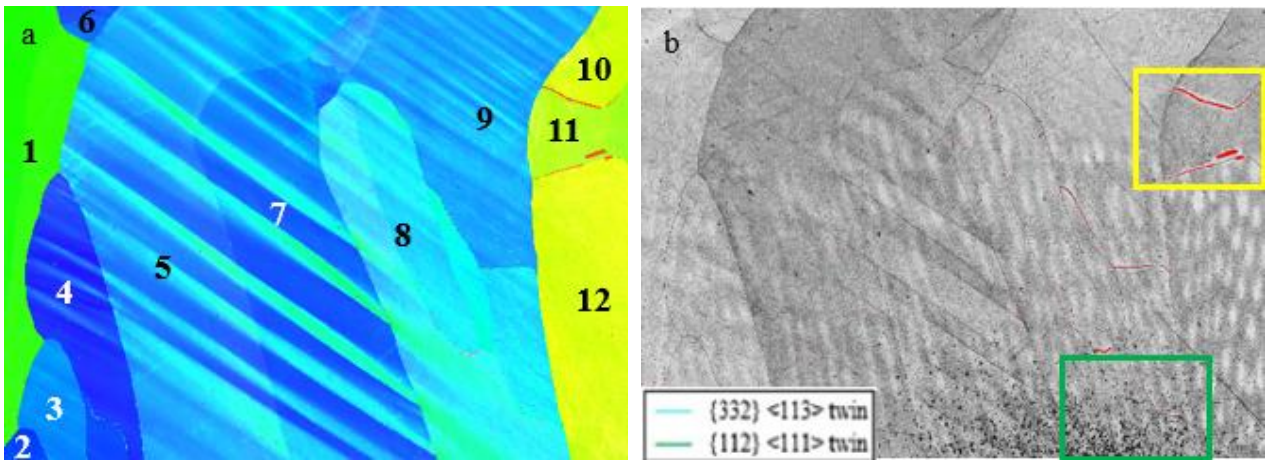

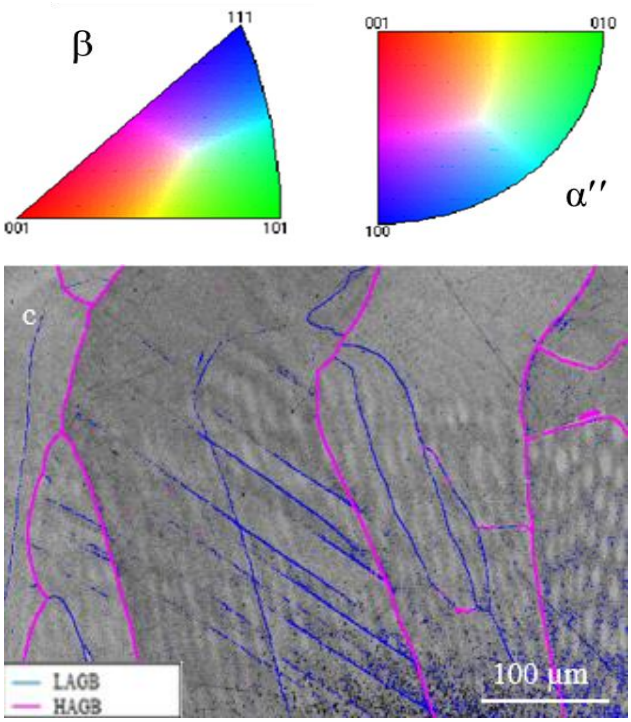

Figure 5.9(a). IPF; (b) BC with overlayed α'' martensite and twin boundary and (c) GB maps of X-Z plane of 700-DS sample obtained from area within yellow rectangle of Fig. 5.8h. Red in (b) is an overlay for α'' martensite. The twin boundary function in (b) is included to confirm absence of twinning in the deformed HT sample. Z is vertical and the horizontal axis corresponds to X, which is the tensile loading direction.

Maps of Fig. 5.10 (a, c, e, and g) and Fig. 5.10 (b, d, f, h) are magnified views of the area within the yellow and green rectangles of Fig. 5.9b, respectively. Fig. 5.10a and 5.10b show the formation of continuous and broken GB-α′′ martensite. From Fig. 5.10e and 5.10f it is seen that the continuous GB-α′′ form on HAGB while those of the broken type mainly form on LAGB, respectively. Fig. 5.10b also shows α′′ martensite forming within β-grains (white arrows). The dark particles of Fig. 5.10b are non-indexed features which remailed after ridding map of features below 2° of misorientation in map cleaning process. These could represent the α-phase retained from heat treatment before deformation. The KAM maps (Figs. 5.10c and 5.10d) show a non-uniform distribution of strain in the deformed matrix. Untransformed β, predominantly accommodates intermediate strain (green colour in maps) and also accommodates a significantly smaller fraction of low strains (blue colour in maps). Higher strain areas (yellow and red in maps) are mostly related to LAGBs and HAGBs where broken and continuous martensite are featured, respectively. Martensite

which formed within β-grain accommodates high strains appearing as red particles in the midst of a surrounding blue and green colour (white ellipse of Fig. 5.10b and 5.10d). Intermediate strains (green colour) are accommodated in martensite free portions of LAGB and HAGB with seldom accommodation of higher strains. Fig. 5.10g and 5.10h prove the absence of the {332}⟨113⟩ and {112}⟨111⟩ twin systems. This map was also investigated for other β-twins and α″-twins and no data were obtained. Hence a twin free microstructure was obtained after deformation of the 700°C heat treated alloy.

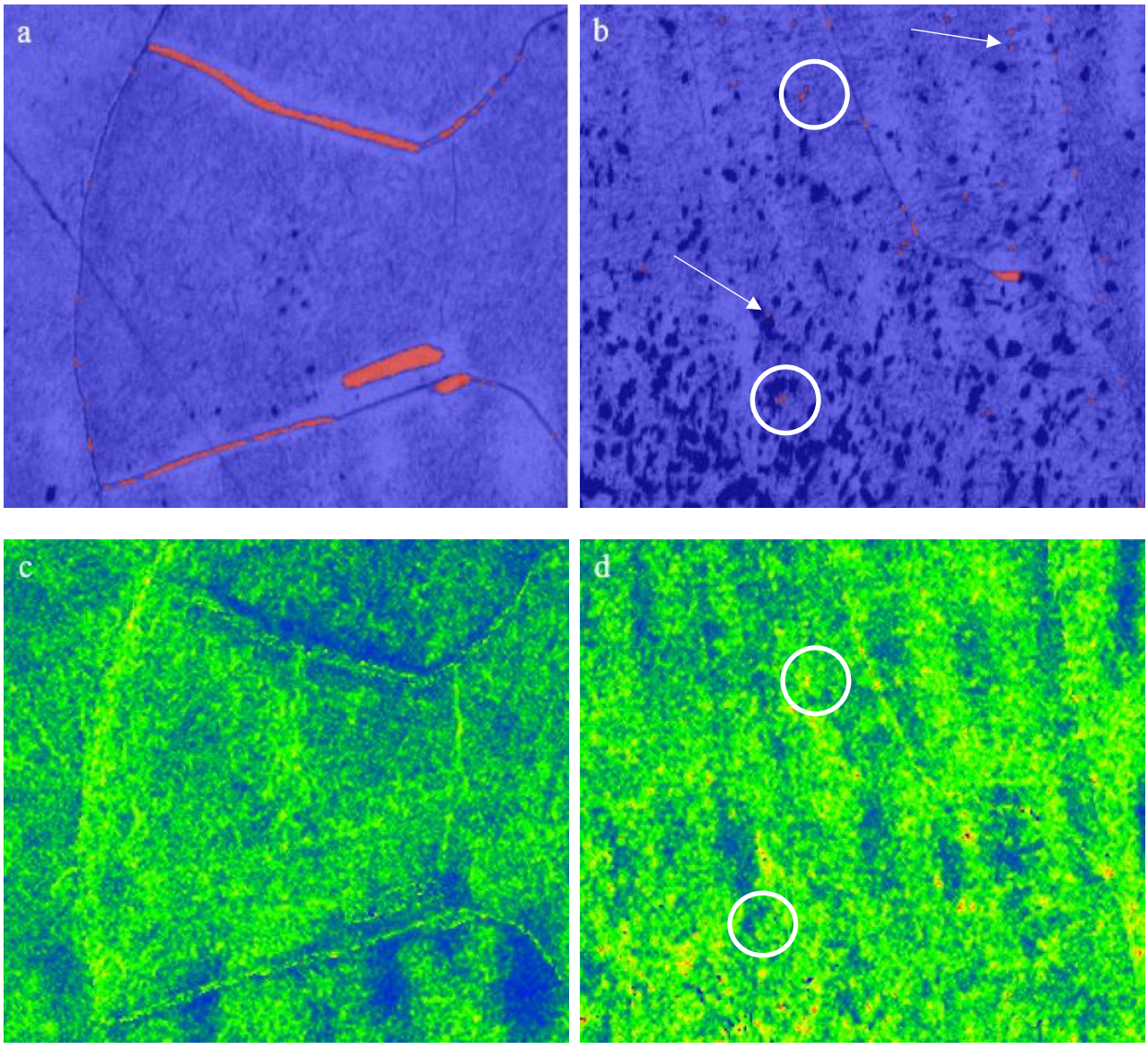

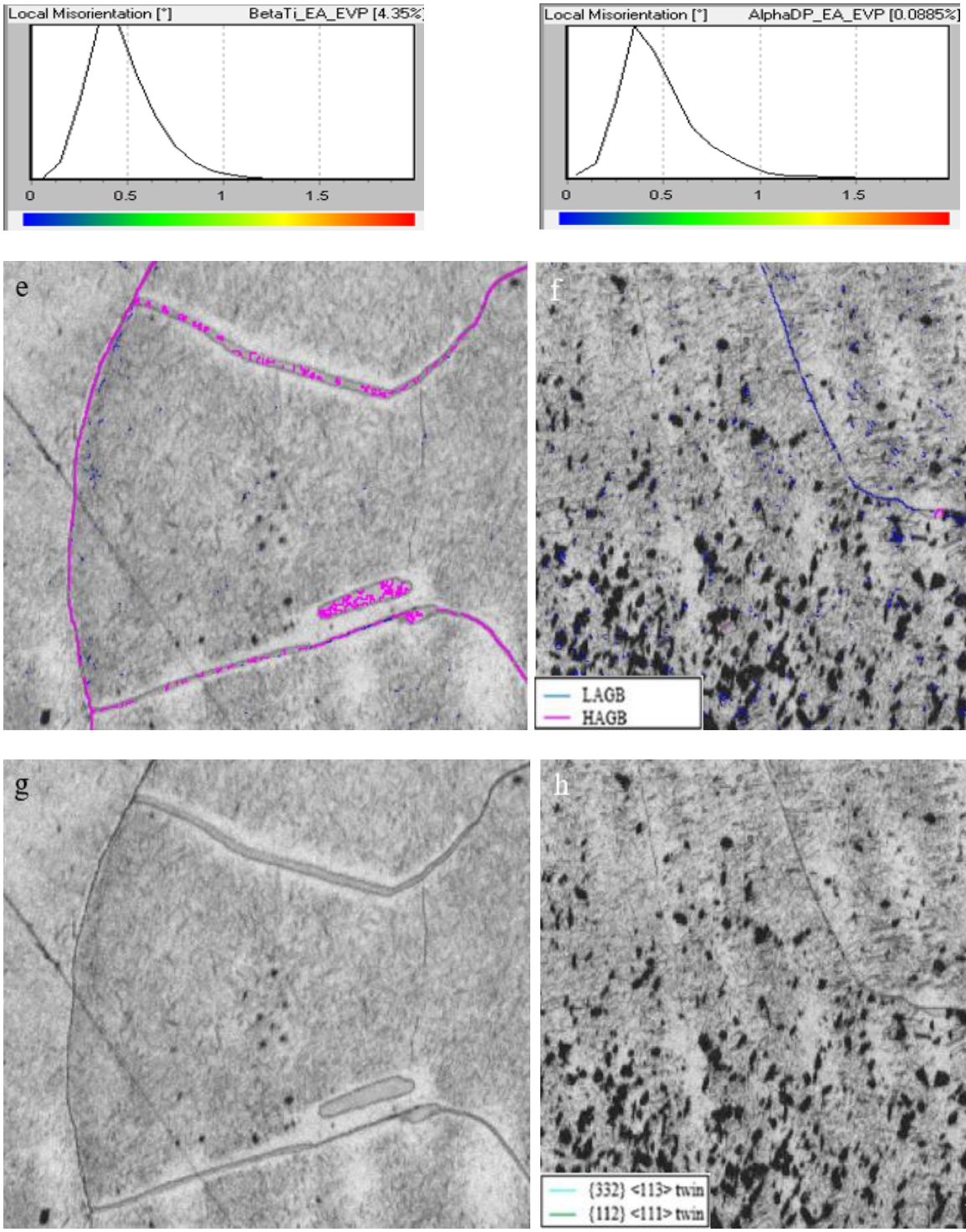

Figure 5.10 (a, b). Phase map with blue and red colours representing β and α″ martensite, respectively, (c, d) kernel average misorientation map, (e, f) grain boundary map and (g, h) twin boundary map for the regions outlined by yellow rectangle (a, c, e, g) and green rectangle (b, d, f, h) in Fig. 5.9b. The twin boundary key was included as confirmation that twinning did not occur on deformed heat-treated sample. The horizontal is X axis (tensile loading direction) and vertical is Z axis.

5.5.3 Texture analysis

Figure 5.11a and 5.11b show β and α″ orientation textures after deformation of Sample AB-700 to understand the combined effect of heat-treatment and deformation on textures. The multiple orientation textures reported for β in the AB sample (Figure 5.11c) and deformed AB sample in Figure 4.14c were not reported after sub-β-solvus heat treatment as shown in Figure 5.11a. This could be due to a decrease in particular orientation preference of β grains after heat treatment. The $(441)[2\bar{2}1]$ β orientation determined in the ϕ_2 = 45° orientation distribution function (ODF) happens to be the only significant orientation texture. As ODF sections were not acquired in the as-heat-treated state before deformation, it is difficult to tell if this orientation texture evolved as a sole impact of heat treatment or a combined contribution from both heat treatment and subsequent deformation of heat-treated sample. ODF sections for α″ martensite (Figure 5.11b), yields no significant orientation texture

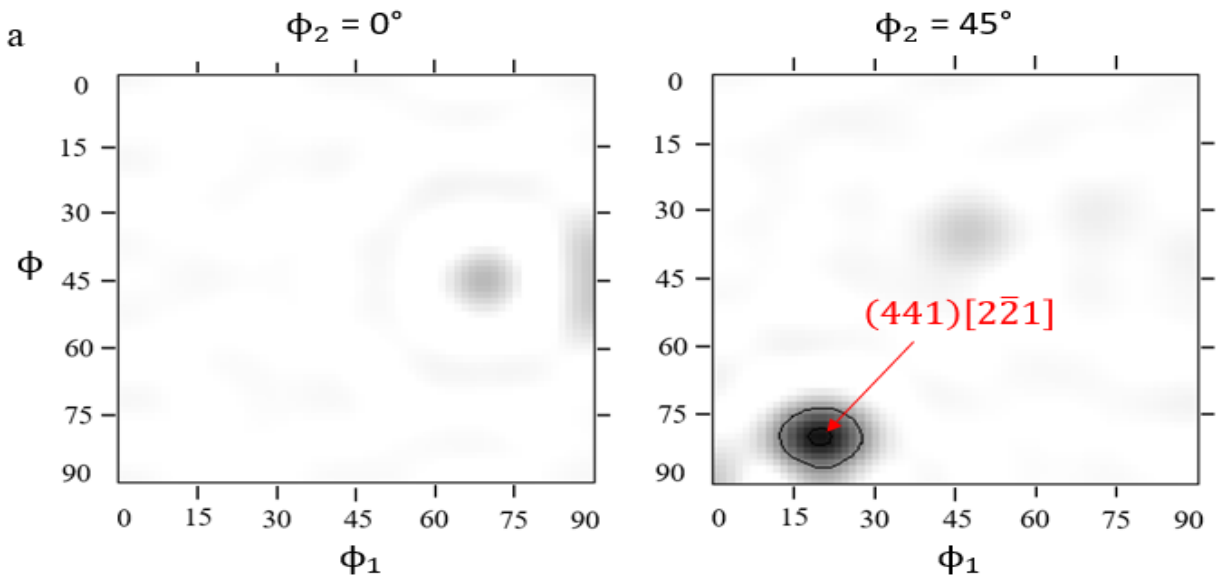

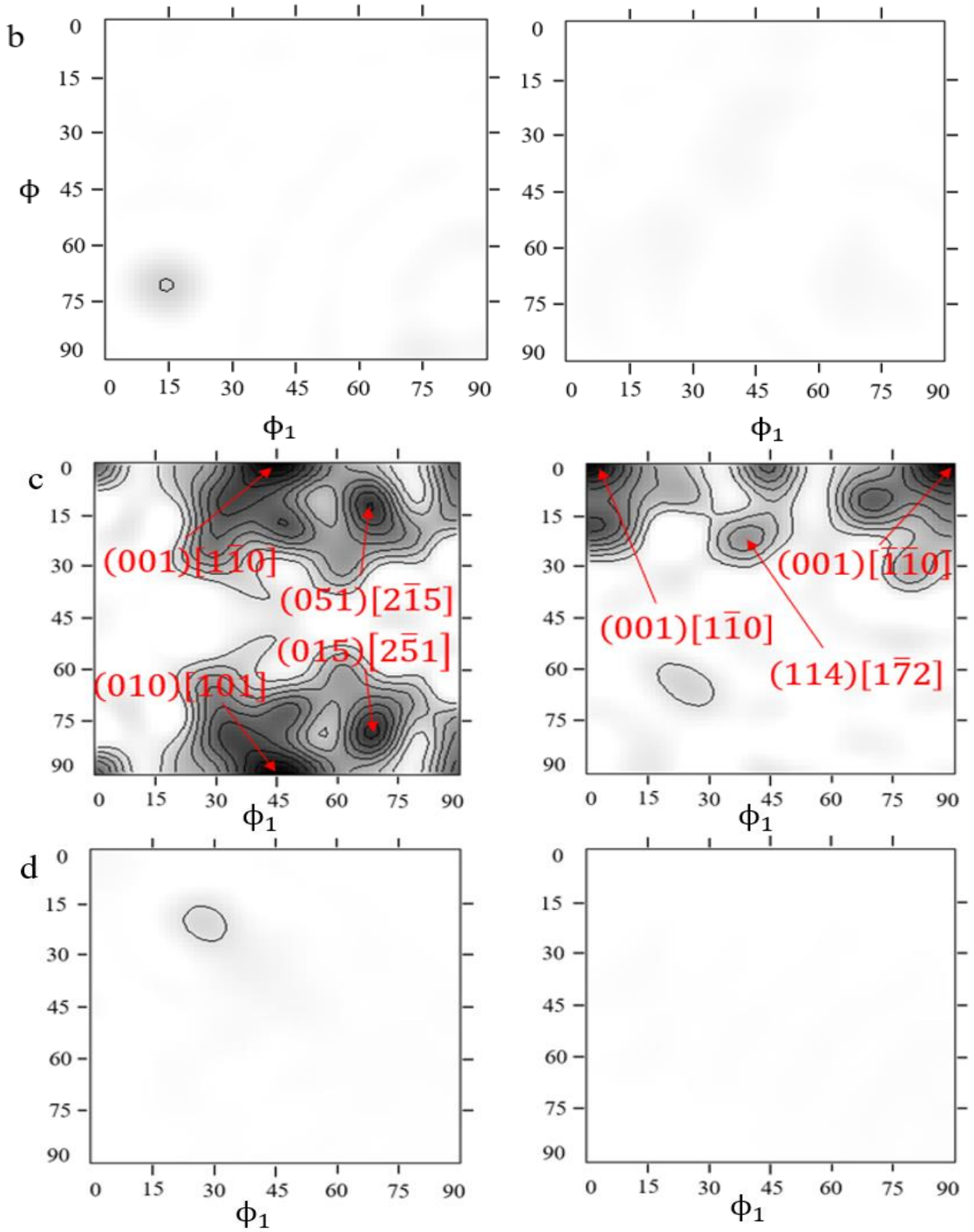

Figure 5.11. Orientation Distribution Function ϕ_2 sections for (a) β-phase and (b) α″ martensite taken from X-Y plane of 700-DS sample. Intensity levels for β phase are x5.53 whereas for α″ martensite x14.2. AB ODF ϕ_2 sections for (c) β-phase and (d) α″ martensite taken from X-Y plane. Intensity levels for β phase are x1.67 and x2.46 for α″ martensite. X-axis is the horizontal direction and Z-axis is vertical/build direction.

5.6 Tensile properties

As shown in Fig. 5.12 and listed in Table 5.1, the 700-DS sample is stronger but exhibits less tEL in comparison to the AB one. A higher elastic strain is obtained per stress input after heat treatment, as confirmed by the lower E-Mod value. The region of non-uniform deformation just before failure in the AB specimen (purple ellipse), is absent from the 700-DS one. This implies that the necked region in 700-DS sample was less obvious than in the AB one, as a consequence of continued increase in strain hardening up to the point of failure in the heat-treated sample.

Mechanical properties derived in the current study were compared to those of other heat-treated AM metastable and near β Ti alloys (Table 5.1). The microstructural features of heat-treated Ti-alloys reported by other authors are listed in Column 4 of Table 5.1. Similar phases/features were reported in the AB-700 sample of the current study. MoE factor which is representative of β-stability were determined from Eq. 2.1 and listed in the second column of Table 5.1. YS of the 700-DS alloy was inferior to those reported in the other alloys, UTS was superior to those in Refs [13, 133] and tEL was superior to those in Refs. [37, 310]. E-Mod value compared very closely to that of Ref. [133].

Vickers hardness was measured at 300g load and the AB-1200 sample of this study presents superior hardness to the sub-1200°C samples of the current study and also to those listed by other authors (Fig. 5.13 and Table 5.1). The hardness of the heat-treated samples at any given temperature was superior to the AB ones. Hardness of the AB-700 sample was the highest among the sub-1200°C samples and this is a direct consequence of its smallest grain size reported in Fig. 5.5, since a more closely packed network of grain boundaries could present more resistance to near-surface deformation.

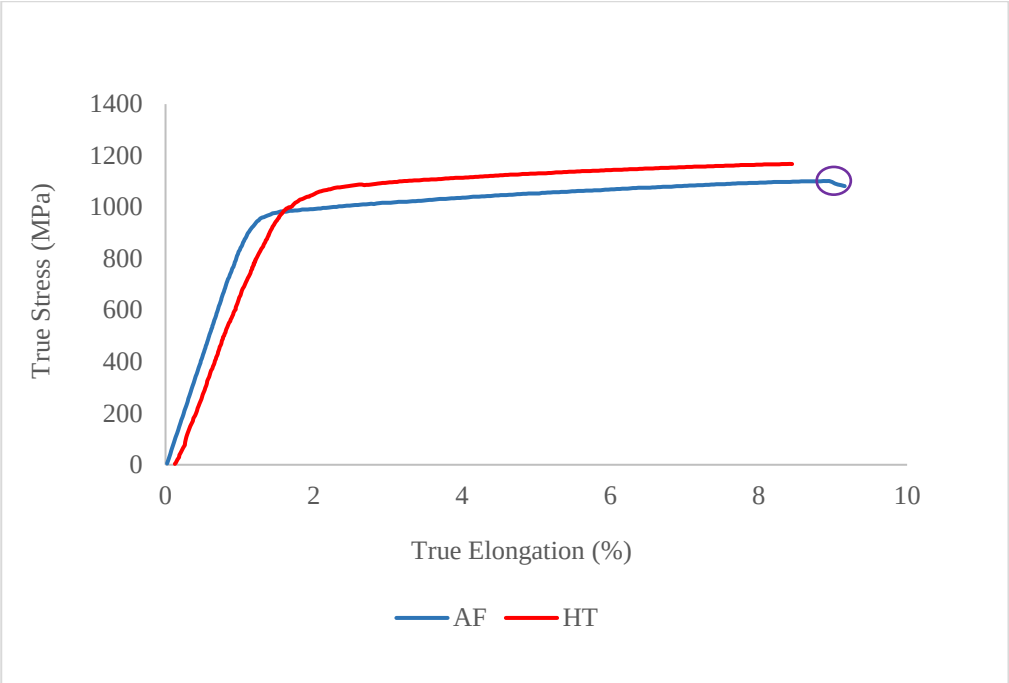

Figure 5.12. Stress-Strain curve of AB (blue) and 700-DS (red) samples.

Table 5.1. Tensile properties of additively manufactured AB and heat treated metastable and near-β Ti alloys.

The term MoE is the molybdenum equivalence which defines β stability.

Alloy	MoE	Processing	Microstructure	True YS (MPa)	True UTS (MPa)	E-Mod (GPa)	True uEl (%)	True tEl (%)	H_V
Ti-15Mo-0.25O [Present]	15	LMD	Columnar β	850± 1.43	1099± 2.3	86.9±0.5	8.91±0.004	9.2±0.004	296±7
			Equiaxed β						300±6.5
Ti-15Mo-0.25O [Present]	15	LMD + HT at 700°C/0.17h	Equiaxed, sparse columnar β, recryst β and needle like α	920± 0.98	1168± 1.12	72.8±0.65	8.45±0.002	8.45±0.002	329±6.2
Ti-15Mo-0.25O [Present]	15	LMD + HHT at 1200°C/6h	Columnar and equiaxed β	-	-	-	-	-	449±5
			Lath-like and GB α						564±3
Ti-5Mo-5V-8Cr-3Al [13]	18.2	LMD + HT at 800°C/0.5h + 500°C/8h + 620°C/0.5h	Equiaxed β, lath-like, pyramidal and GB α	1076±15	1136±14	-	9.8±0.2	-	394.6±12.7
Ti-12Mo-6Zr-2Fe [133]	18.5	LPBF + HT at 1000°C/1h	Equiaxed, recryst β and needle-shaped α″	943±8	988±14	70.9±0.1	-	12.0±0.3	326±4
Ti-15Mo-3Nb-3Al-0.2Si [310]	12.8	LPBF + HT at 850°C/0.5h + 538°C/8h	Columnar β and α-plates	1281	1348	-	-	6.5	380±13
Ti-5Al-5Mo-5V-3Cr-1Zr [37]	8.26	LMD + 880°C/1h + 600°C/4h	Transformed β matrix with secondary and GB α	1360±12.1	1371±18.6	-	-	6.4±0.51	449.5±8.8
Ti-5Al-2Sn-2Zr-4Mo-4Cr [311]	5.6	LAM + 840°C/1h +800°C/4h + 630°C/8h	Transformed β matrix with primary, secondary and GB α	1093±11	1138±13	-	-	11.4±1.0	-

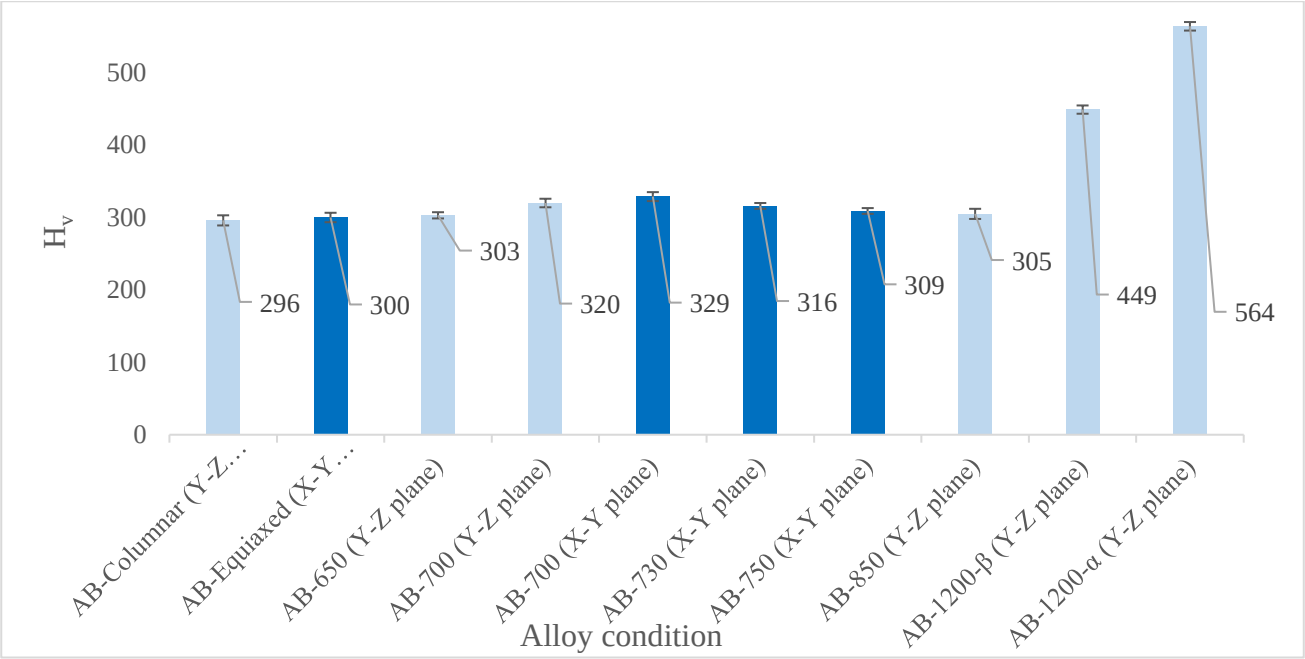

Figure 5.13. Hardness of AB and heat-treated Ti-15Mo-0.25O.

5.6.1 Fracture analysis

Analysis and comparison of fracture surfaces of AB sample (Fig. 5.14a) and 700-DS sample (Fig. 5.14b) was conducted. Large area fracture surface in Fig. 5.14b features dimples, smooth cleavages, tear ridges (yellow arrows of Fig. 5.14c), pores and protruded fragments (white arrows of Fig. 5.14d) as also reported in the fracture surface of AB sample (Section 4.4.1). A significant difference in dimple depth was absent between the two fracture surfaces. However, a slightly smaller average dimple diameter of 12.33±4.01μm was determined in the 700-DS sample. A higher surface fraction of smooth cleavages was determined after heat treatment, suggesting less plasticity before tensile failure. An interpore spacing of 265±88μm for the 700-DS sample confirms less dense pore distribution after heat treatment.

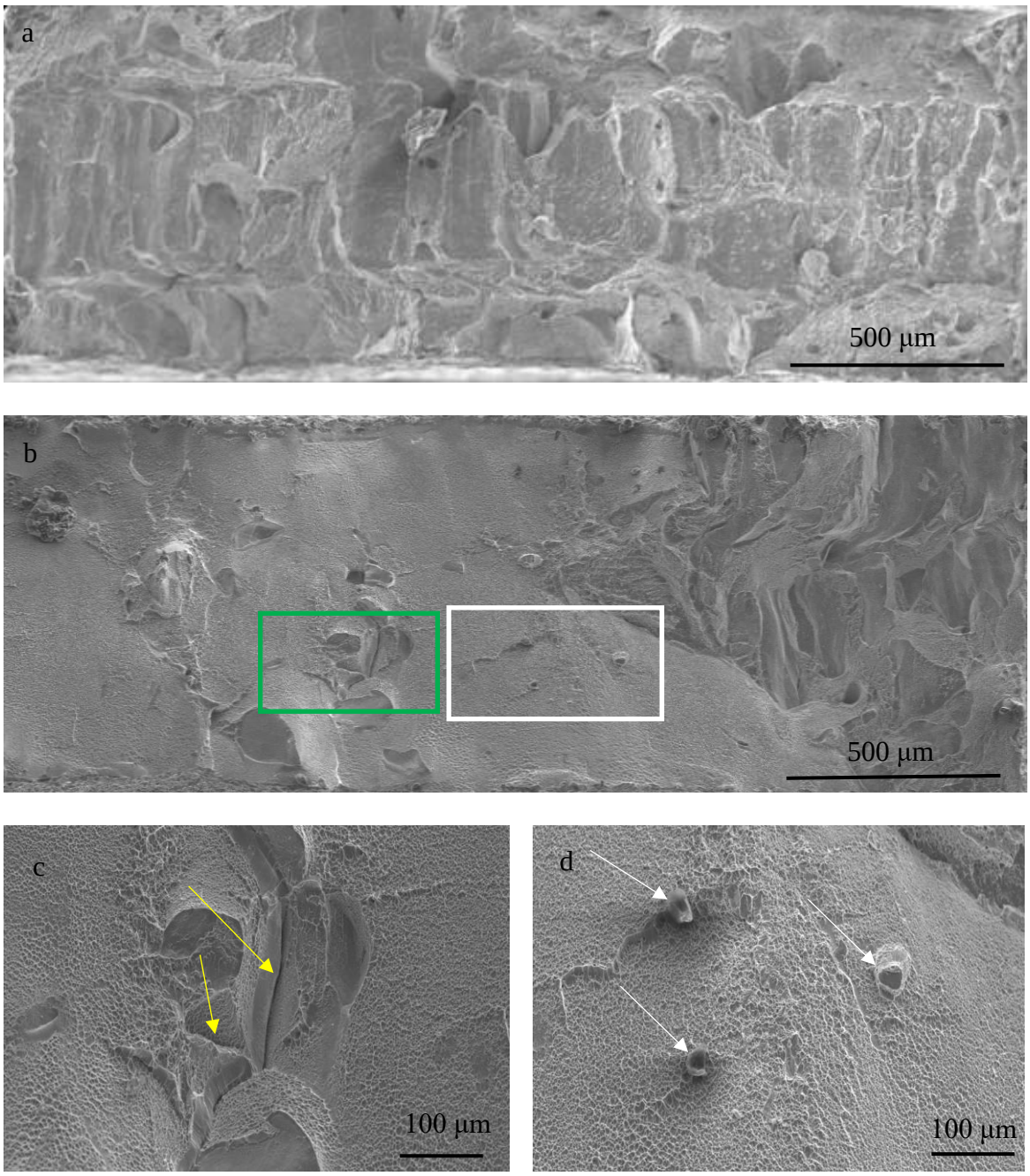

Figure 5.14. Large area fracture surface of (a) deformed AB sample; (b) deformed HT sample; Magnified view of area within the (c) white rectangle and (d) green rectangle.

5.7 Discussion

α-phase was reported in the pre-deformed state (i.e., AB-700 sample) by XRD (i.e., red pattern of Fig. 5.3b), confirmed by EDS quantitative analysis (i.e., Spectrum 99 of Fig. 5.6b) as extremely depleted microstructural points and SEM as a phase which bears a needle-like morphology occupying 53% of AB-700 microstructure (i.e., Fig. 5.4f). In general, at the α+β phase-field temperatures between 420°C and 650°C α-phase forms in metastable β-Ti alloys in a displacive-diffusional mechanism [51, 54, 67, 126]. The 700°C heat treatment temperature used in the current study is very close to the upper temperature limit determined in literature. The influence of oxygen has also contributed to the formation of α [312] in this sample, where oxygen has functioned as an α-phase stabiliser, promoting the exit of Mo from precipitated α by diffusion into adjacent β matrix. This claim was corroborated in Appendix A of Ref. [309] where phase analysis for Ti-15Mo-0.15O and Ti-15Mo-0.35O both featured the HCP α-phase at temperatures ranging from 650°C to 700 °C as a consequence of oxygen present in the alloy. Thus, this phase is to be expected in the alloy under study which contains 0.25 Wt. % O. These needle-like precipitate intersect each other at right angles and occur intragranularlly. Continuous GB-α is indicated by yellow arrow of Fig. 5.4f and appear to have formed on recrystallised β-grain. The α-free areas and areas of sparse α distribution mainly occur in the FZ which is the most β-stabilised zone in the microstructure (Fig. 5.4f). It is interesting that the FZ which is the most solute-rich zone in the AB sample, remains so even after heat treatment. Hence a positive net-diffusion into this zone was maintained during heat treatment.

The absence of $\langle 110 \rangle_\beta$ fiber texture in Figure 5.11a confirms the non-activation of $\{112\}\langle 111 \rangle_\beta$ twin in the 700-DS sample. This twin system has been reported to cause orientation changes similar to those caused by $\{110\}\langle 111 \rangle$ dislocation slip resulting in a $\langle 110 \rangle_\beta$ fibre texture [313]. $\{332\}\langle 113 \rangle_\beta$ twinning leads to strong $\langle 100 \rangle_\beta$ and $\langle 111 \rangle_\beta$ textures, and a combination of both twinning systems produces a $\langle 210 \rangle_\beta$ texture [313]. The absence of $\langle 100 \rangle_\beta$, $\langle 111 \rangle_\beta$ and $\langle 210 \rangle_\beta$ orientation textures from ODF of Figure 5.11a is proof that $\{332\}\langle 113 \rangle$ twin system was not activated as indicated by EBSD maps of Figure 5.9b and Figure 5.10g-h. Also, in Ref. [41] it was reported in AB Ti-15Mo

that β-twins occur within the bounds of a given columnar grain and do not extend beyond grain boundaries. The diagonal rectangular features are proven by EBSD maps of Figure 5.9c to extend past a given columnar grain boundary. This observation supports the claim that the diagonally oriented rectangular sub-grain features of Figure 5.9c are neither fully developed nor nascent twins [24, 132, 206], but LAGB sub-grains occurring within columnar grains. Further analysis revealed the non-occurrence of other β- and α′′ martensite- twin systems associated with Ti-alloys [207, 314-319]. It was reported in Refs. [46, 47] that β-twin was not detected in β-Ti alloys, as there was not sufficient β-domain size to allow the formation of twins. The 47% surface fraction of β in the AB-700 sample may have confirmed this claim in the current study.

One of the two deformation induced α′′ martensite variants reported in the AB sample [41] also formed in the 700-DS sample and this was the primary variant. This variant formed in parent β as chunks assuming multiple sizes in units of micron range and multiple amorphous morphologies. They also formed on β-GBs as lenticular continuous primary products or short fragmented ones (Figure 5.10a and 5.10b). XRD analysis of the $(041)_{\alpha''}$ martensite peak intensity, suggests a decrease in phase fraction from the deformed AB (665 counts) [41] sample to the 700-DS (460 counts) sample. This claim was corroborated by EBSD phase analysis which reported a 0.0022 phase fraction for martensite which falls below the lower limit for AB alloy which is from 0.007 to 0.02 [41]. ODF results of Figure 5.11b which showed no significant martensite orientation texture also proves that martensite surface fraction was significantly reduced in the 700-DS sample as the AB ODF of Figure 5.12b of Ref. [41] did feature significant martensite orientations. The decreased martensite surface fraction in the 700-DS sample must be principally due to the presence of about 53% surface fraction of α-phase [46, 47]. In the cited work, it was determined that an α surface fraction of 50% or more inhibits the formation of α′′ martensite. However, in the current study a complete inhibition of α′′ martensite was not reported. Athermal martensite which is not present in the AB-700 microstructure has a start and finish temperature during heating/cooling to/from single β-phase field and is not dependent on temperature after cooling/quenching to room temperature. However, deformation

induced martensite depends primarily on three factors namely, β grain/domain size, β stability donated by molybdenum equivalence factor of the alloy and individual β-grain pre-deformation orientation. This orientation may or may not favour the formation of any of the six lattice correspondent martensite variants [134]. Thus, heat treatment conducted at 700°C created a combination of these three factors which favours formation of α″ martensite howbeit with a smaller surface fraction than the martensite phase formed during deformation of AB sample [41]. This is to be expected as there existed a smaller β-domain size after heat treatment to and holding at 700°C created by precipitation of HCP α-phase. Smaller β-domain size therefore allows the formation of less martensite surface fraction than that of the AB sample deformed at room temperature with a predominantly β microstructure. Decreased parent β-grain domain size confines the number of available nucleation sites for α″ martensite [45].

The marginally higher surface fraction of α″ martensite in the HAZ than the RZ determined in the AB sample [41] was preserved after heat treatment. It was determined by comparing Figure 5.10a-b to Figure 5.10e-f that a higher surface fraction of martensite forms primarily as continuous HAGB product in the HAZ of the next layer. In the same vein, a lower surface fraction of martensite forms in the RZ of the previous layer as a primary LAGB product, bearing a segmented/discontinuous appearance. The operation of high free Gibb's energy in the HAZ-GBs must have contributed to the forming of continuous α″ martensite.

A marginal improvement in ultimate tensile strength as well as a borderline deration of total elongation at fracture is observed in the 700-DS sample when compared to the deformed AB one [41]. Improvement in ultimate tensile strength can be ascribed to the increase in the number of β/α interfaces after heat treatment, which serves as a barrier to dislocation movement. The absence of β-twins has impacted the total strain hardening achieved and this is seen in the decreased plasticity of the 700-DS sample. Reduction in ductility is also due to increased strain localisations accommodated by GB-α which serve as nucleation sites for crack and subsequent propagation from thence [320, 321]. The high yield stress difference between adjacent α-phase and β matrix also limits β elongation

as reported in Ref. [322]. Adjacent phases are illustrated by the interfacial $(110)_{\beta}/(002)_{\alpha}$ XRD peaks of Figure 5.3b. The pre-existence of $(100)_{\omega_{ath}}$ and formation of $(110)_{\omega_D}$ and $(200)_{\omega_D}$ peaks shown in XRD pattern of Figure 5.3b have also contributed to the decreased total elongation of the 700-DS sample. Hexagonal closed pack ω_{ath}/ω_D have been reported to embrittle Ti-alloys thereby causing a decrease in plasticity before failure [323-325].

5.8 Conclusion

Based on the application of combined characterisation techniques to gain insight into both heat-treated and deformed microstructures, the following conclusions were reached:

1. After heat treatment of Ti-15Mo in the dual α+β phase field, the distinct microstructural zones of the AB sample (i.e., FZ, RZ and HAZ) were preserved. These zones followed a descending order of Mo-concentration from FZ to RZ to HAZ as also reported in the AB sample [41]. Thus, anisotropic mechanical properties are expected over the microstructure after sub-β-solvus heat treatment.
2. Heat treatment of Ti-15Mo in the dual α+β phase field permits the formation of needle-like α both intragranularlly and at the GBs. These α-phase combined with recrystallised grains and sub-structures established fragmentation of β-grains. These occurrences had an enhancing effect on ultimate tensile strength.
3. Solute homogenisation of Ti-15Mo was not achieved at the single β-phase field of 1200°C after 6hrs. However, distinct FZ, RZ and HAZ were erased and replaced with a microstructure composed of extremely lean and super-rich in Mo zones. Air-tight encapsulation which goes beyond experimental capabilities at UOW coupled with longer than 6hrs holding time could homogenise Mo and create the expected single β microstructure and isotropic mechanical properties. Significantly higher ultimate tensile strength than that achieved in AB sample is expected in the AB-1200-A sample due to the presence of α, should a uniaxial tensile test be

conducted. This is suggested by the high hardness achieved in the sample reported in Figure 13.

4. β-twins were not activated during plastic deformation of 700-DS sample. EBSD twin analysis provided no evidence to prove the operation of β-twins. The absence of $\langle 110 \rangle_{\beta}$ and a combined absence of $\langle 100 \rangle_{\beta}$, $\langle 111 \rangle_{\beta}$ and $\langle 210 \rangle_{\beta}$ textures from β ODF of Figure 5.11 is proof that the $\{112\}\langle 111 \rangle$ and $\{332\}\langle 113 \rangle$, were respectively not activated during plastic deformation of 700-DS sample. This could have contributed to the marginal decrease in total elongation in comparison to AB alloy, stemming from a decreased work hardening.
5. Only a marginal improvement in ultimate tensile strength and a borderline deration of total elongation was achieved in the 700-DS sample.
    a. Small increase in ultimate tensile strength was as a result of β-grain fragmentation by α and recrystallised sub-grains within columnar β.
6. The elastic modulus of about 73GPa obtained in the 700-DS sample is lower than that of the deformed AB alloy [41] and conventionally manufactured Ti alloys [79]. It comes closer to requirement of about 25-30GPa for biomaterials applications [326] and also for aerospace applications where a low elastic modulus is required.
7. AB-1200-A sample displayed a hardness of 564 H_V which is a significant improvement from that determined in the AB and AB-700 samples which were 300 H_V and 329 H_V, respectively as shown in Figure 5.13. This is a pointer to significantly improved ultimate tensile strength should the AB-1200-A sample be subject to uniaxial tensile deformation.
8. The absence of multiple significant orientation texture for β in the 700-DS sample and the total dis-appearance of martensite orientation texture, is a pointer to a more isotropic state of mechanical properties. This comes from a comparison to the AB sample which had multiple significant orientations for both phases. Thus, similar mechanical properties may be obtained in different directions of the microstructure after heat treatment, even though the microstructural zones from AB sample were retained in the 700-DS sample.

6 Effect of thermo-mechanical processing on compressive mechanical properties of LMDed Ti-15Mo-0.25O

The primary aim of this chapter is to refine AB columnar β-grain. It was determined in Chapter 5 of this thesis, that recrystallisation/grain refinement occurred at 700°C solely from heat treatment. In the current chapter, AB cylindrical samples were first subject to RT compression for reference purposes and subsequently, thermomechanical controlled processing (TMCP) at 650°C to observe possible dynamic effect on microstructure. TMCP followed the schedule of Fig. 6.1 and were conducted to two strains (20% and 40%) at different strain rates ($0.00055S^{-1}$, $0.0011S^{-1}$, $1S^{-1}$ and $4S^{-1}$). Compressed samples include Sample I (RT-20%-$0.0011S^{-1}$), Sample II (RT-40%-$0.0011S^{-1}$), Sample III (650°C-20%-$0.00055S^{-1}$), Sample IV (650°C-20%-$0.0011S^{-1}$), Sample V (650°C-40%-$0.0011S^{-1}$), Sample VI (650°C-40%-$1S^{-1}$) and Sample VII (650°C-40%-$4S^{-1}$). The influence of strain and strain rate on microstructure and compressive mechanical properties were investigated using XRD, EDS, SEM and EBSD. Investigation outcomes in this chapter sets expectations for a recommended future study in uni-axial deformation of pre-TMCPed Ti-15Mo, manufactured by LMD or other AM techniques with similar AB microstructure.

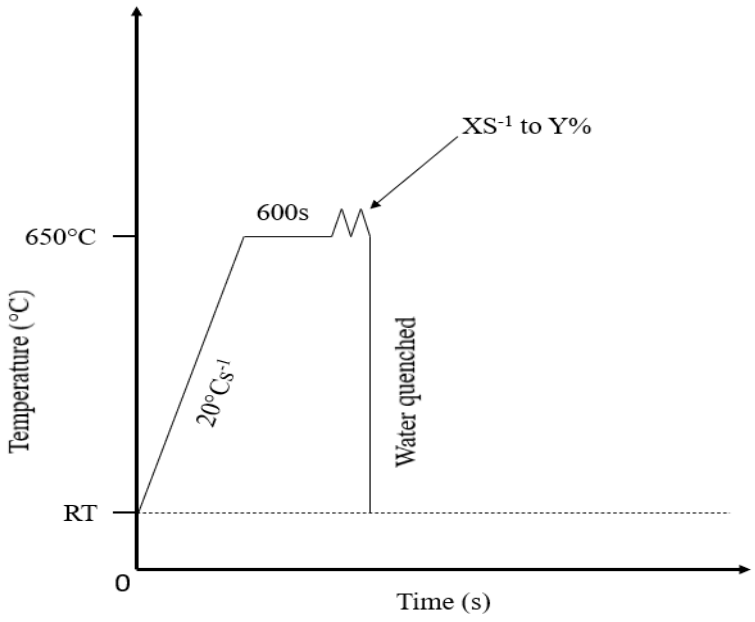

Figure 6.1. A schematic diagram of the thermo-mechanical processing used in this study

6.1 XRD pattern analysis

The XRD patterns of Fig. 6.2 were acquired from RT compressed and TMCP samples and they primarily consist of β and α_D'' peaks. The $(041)_{\alpha''}$ peak has seen a drastic decrease in intensity compared to the deformed AB and 700-DS intensities of Fig. 4.1 and 5.3, respectively. This points to the reduced surface fraction of α'' martensite formed during RT compression, compared to that formed during RT tensile tests of AB and AB-700 samples. Also, it indicates decreased martensite formation during elevated temperature deformation. The presence of $(114)_{\alpha}$ peak in the RT samples (i.e., Sample I and II), could imply that α pre-existed in very small surface fraction in the AB condition. The lower $(114)_{\alpha}$ peak intensity of Sample II is an indication that more of α precipitated during elevated temperature compression. The $(100)_{\omega_{ath}}$ peak occurs at approximately the same 2Θ position as previously reported in Chapter 4 and 5. The same applies to the $(110)_{\omega_D}$ peak.

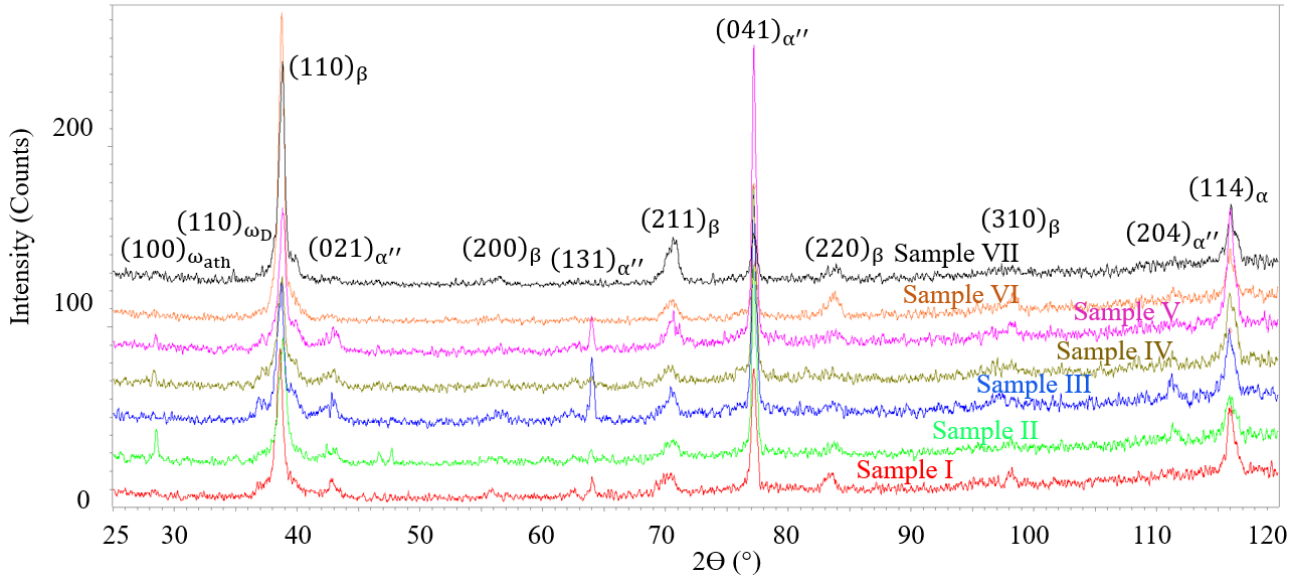

Figure 6.2. XRD patterns of RT compressed and TMCP samples.

6.2 Compression tests

The effect of friction on flow stress during elevated temperature compression of metals have been reported in Refs. [327-329]. This friction exists at the interface between the platens and flat surface of cylindrical specimens. Ebrahimi et al. [49] developed mathematical correlations (Eq. 6.1, 6.2 and 6.3) for correcting experimentally measured flow stress. This accounts for the friction factor based

on the physical measurement of the barrelled shape of the cylinder in its post deformation state in comparison to it pre-deformation shape. Hence, this method has the advantage of not requiring mechanical properties of the material and forming loads. It also was stated in Ref. [49] that R could be approximated as R_T which is the top radius of the cylindrical specimen in its compressed state.

$$b = 4\frac{\Delta R}{R}\frac{H}{\Delta H}\ [49] \qquad \text{Equation 6.1}$$

$$m = \frac{(R/H)b}{(4/\sqrt{3})-(2b/3\sqrt{3})}\ [49] \qquad \text{Equation 6.2}$$

$$\frac{\sigma_e}{\sigma_c} = 8b\frac{R}{H}\left\{\left[\frac{1}{12}+\left(\frac{H}{R}\right)^2\frac{1}{b^2}\right]^{3/2}-\left(\frac{H}{R}\right)^3\frac{1}{b^3}-\frac{m}{24\sqrt{3}}\frac{e^{-b/2}}{e^{-b/2}-1}\right\}\ [49] \qquad \text{Equation 6.3}$$

In Eq. 6.1:

b = Bulge factor after deformation.

R = Average radius of cylinder after deformation.

ΔR = Difference between the maximum and the top radius after deformation

H = Height of the cylinder after deformation.

ΔH = Difference between the original cylinder height and height after deformation.

In Eq. 6.2:

m = friction factor

In Eq. 6.3:

σ_e = Experimental stress.

σ_c = Corrected stress/Actual flow stress of material.

6.2.1 Barrelling effect

The large area images of Fig. 6.3 were all taken at 29x magnification after deformation. Images are presented at varying sizes on purpose, to reflect the post deformation aspect ratio denoted by $H_N/2R_M$ listed in Table 6.1. H_N and R_M represent height and maximum radius after deformation, respectively.

Also in Table 6.1, the quantities b, m and correction factor were calculated using Eq. 6.1, 6.2 and 3.3, respectively. The dimensionless $H_N/2R_M$ parameter fell below zero for all samples compressed to 0.4 strain. H_N at a given strain was consistently lower for samples deformed at 650°C in comparison to the RT compressed samples, as a consequence of thermal softening. As shown in Table 6.1, a correction factor of unity is obtained using Eq. 3.3 for samples compressed at RT. Sample I and II proves this result to be independent on strain, implying that there is negligible or no barrelling effect at RT and low strain rate as also reported in Ref [330]. At a given temperature, correction factor did not differ for same strain rate even when strain differed, as seen between Sample I and II and between Sample IV and V. Also, at a given temperature correction factor differs for different strain rates even when strain is the same as seen between Sample III and IV and among sample V, VI and VII. Hence, barrelling effect is mainly controlled by strain rate which determines level of frictional shear force generated between flat end of cylinder and platens during compressive test. However, there isn't a linear correlation between bulge factor and strain rate as bulge factor increased from sample III to IV where strain rate increased but decreased from sample V to VI where strain rate increased. The observed non-linearity was also reported in Ref [329].

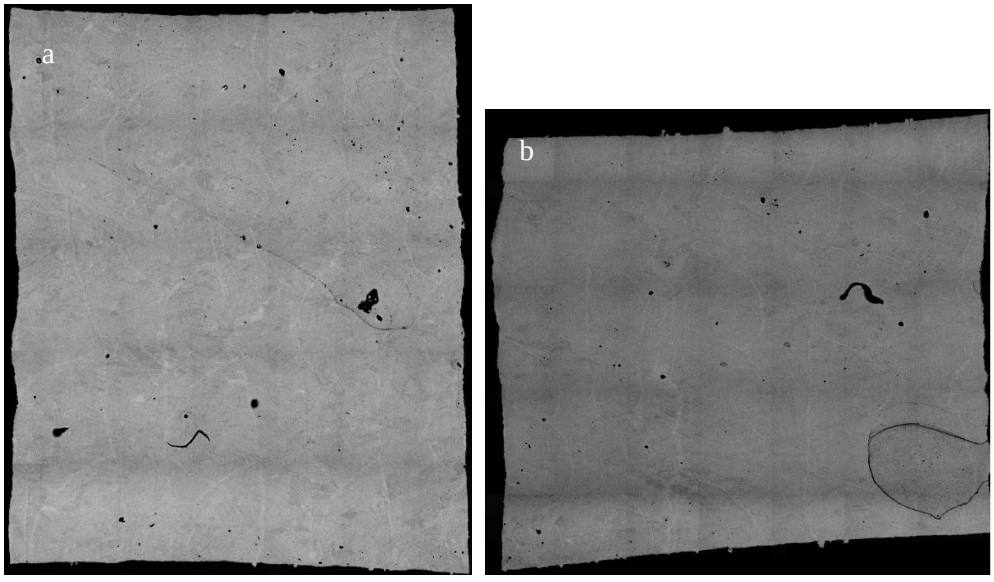

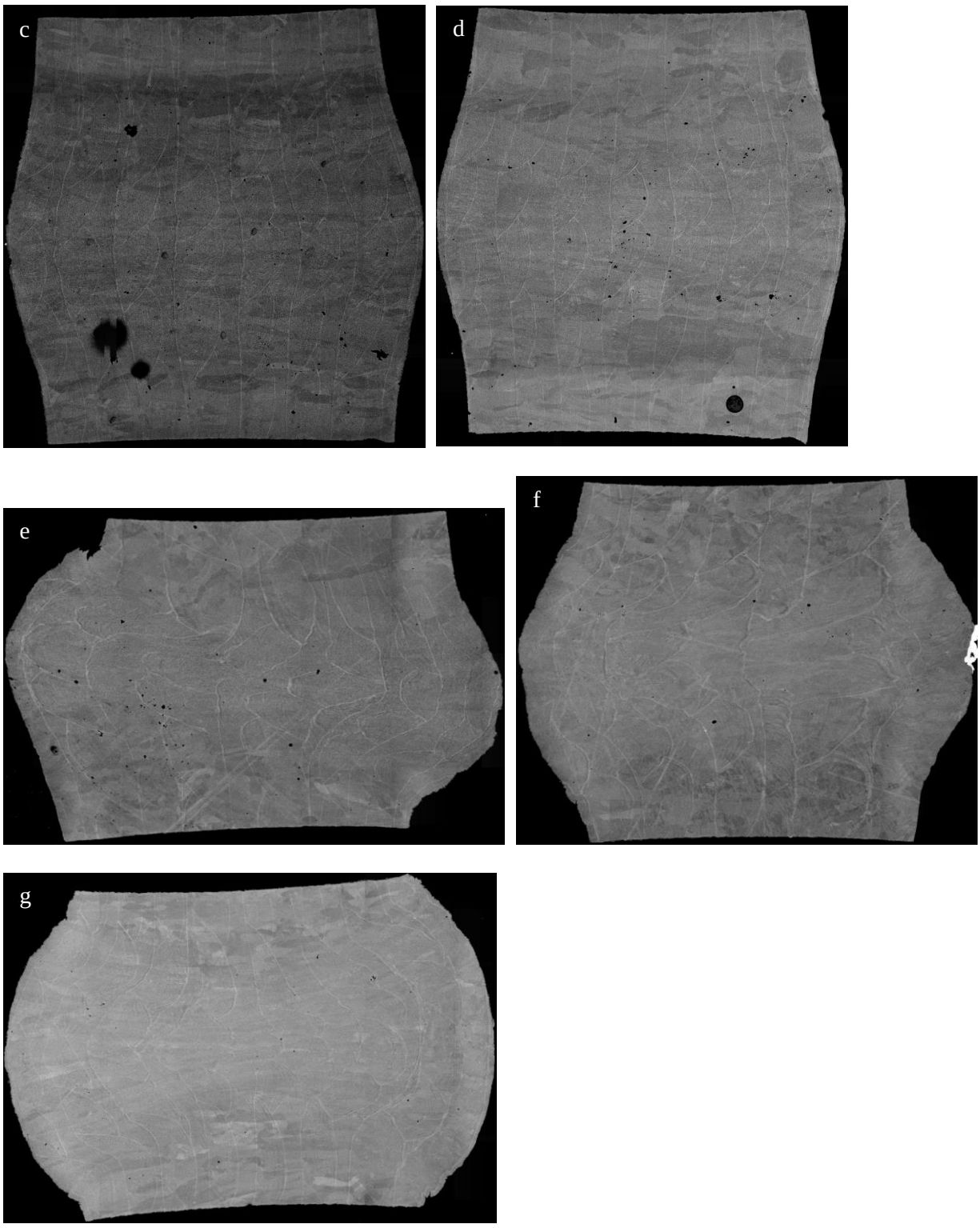

Figure 6.3. Post-deformation large area SEM images of (a) Sample I; (b) Sample II; (c) Sample III; (d) Sample IV; (e) Sample V; (f) Sample VI; (g) Sample VII

Table 6.1. Sample parameters measured after compression test.

	H_N (mm)	R_T (mm)	R_M (mm)	R	$2R_M$	$H_N/2R_M$	b	m	Correction factor
Sample I	5.20	2.13	2.14	2.13	4.27	1.22	0.12	0.02	1
Sample II	4.24	2.29	2.30	2.29	4.59	0.92	0.04	0.01	1
Sample III	5.05	2.05	2.42	2.23	4.83	1.05	3.84	1.87	1.15
Sample IV	5.02	1.93	2.35	2.14	4.69	1.07	4.46	2.89	1.17
Sample V	3.83	2.02	2.87	2.45	5.74	0.67	2.97	1.34	1.17
Sample VI	4.20	2.04	2.63	2.33	5.26	0.80	2.7	1.03	1.13
Sample VII	3.99	1.93	2.80	2.36	5.59	0.71	3.58	1.86	1.18

6.3 Microstructure after TMCP

6.3.1 SEM analysis

SEM images of Fig. 6.4 were taken at the center of the images of Fig. 6.3 at 1000x magnification except for Fig. 6.4e, f and h which were taken at 5000x. Red ellipse of Fig. 6.4a shows a representative area of short dark and light interdendritic cells representing the solute segregation reported in Chapter 4 and 5. In the RT compressed samples of Fig. 6.4a and 6.4b, β-grains feature intragranular deformation bands which form a grid structure similar to those reported for tensile deformed samples in Chapter 4 of this thesis. These bands feature black amorphous packets within (i.e., yellow arrows of Fig. 6.4b). These packet products also occur primarily on parent β grains (i.e., white arrows of Fig. 6.4b). Deformation products are of a higher density in Sample II (Fig. 6.4b) than Sample I (Fig. 6.4a) due to the greater 0.4 compressive strain in Sample II. In the TMCP samples of Fig. 6.4c and 6.4d, deformation bands do appear to be thinner than those of the RT compressed samples. The bands of the TMCP samples appear not to have well defined band-boundaries. There are also, in-between band areas which are product free (blue arrows of Fig. 6.4d). Fig. 6.4e and 6.4f are the magnified views of the red and white rectangles of Fig. 6.4d, respectively. Within the bands are acicular/needle-like products forming at right angles to each other bearing varying sizes in units of microns. At the β/band interfaces (yellow arrows of Fig. 6.4e), there exists very sparsely distributed black products of varying morphology. The yellow ellipses of Fig. 6.4f show the intersection of bands at approximately 90° as there appears to be a cluster of secondary acicular products not following the predominant parallel arrangement. This may not be very visible as the band-boundaries are not well defined in the TMCP

microstructure compared to the RT compressed ones. As band-boundaries appear predominantly vague/washed out, the subtle difference in acicular product orientation/arrangement can be an indication of transition between two adjacent bands with a common boundary. In the microstructure of Sample V (Fig. 6.4g) no evidence of parallel deformation bands is apparent. Primary precipitates which resemble the precipitates of Fig. 5.4f predominates the microstructure of Sample V. The precipitate free portion of Sample V (i.e., area within the red rectangle of Fig. 6.4g) occurs mainly within the FZ. This is similar to the occurrence of PFZ reported in the AB-700 sample of Fig. 5.4f. This is therefore a confirmation that neither precipitates nor deformation products form in the FZ regardless of processing. This is because the FZ represents the region of highest β-stability in the microstructure at the AB, sub-1200°C-HT and sub-1200°C-TMCP conditions. The black products of Fig. 6.4e also appear in Sample V (Fig. 6.4h) with a higher frequency of occurrence at β-GBs. The representative coupon areas of Sample VI (Fig. 6.4i) and VII (Fig. 6.4j) show the same primary acicular products intersecting each other at approximately 90° as reported earlier, howbeit with finer sizes. Dynamically recrystallised β-grains (red and green arrows of Fig. 6.4i and 6.4j) are also identified in Sample III (red arrows of Fig. 6.4c).

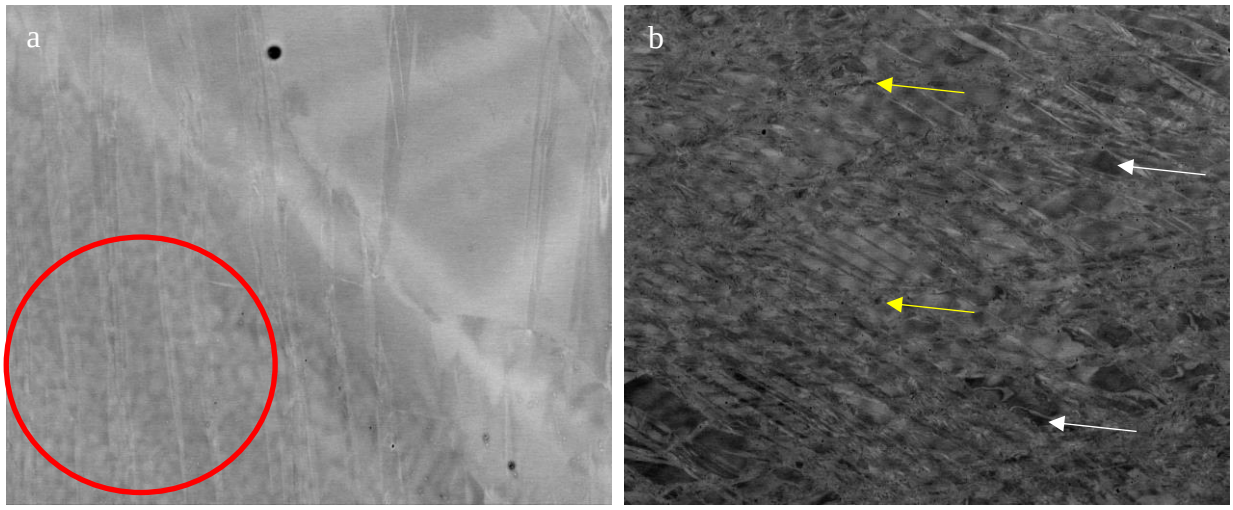

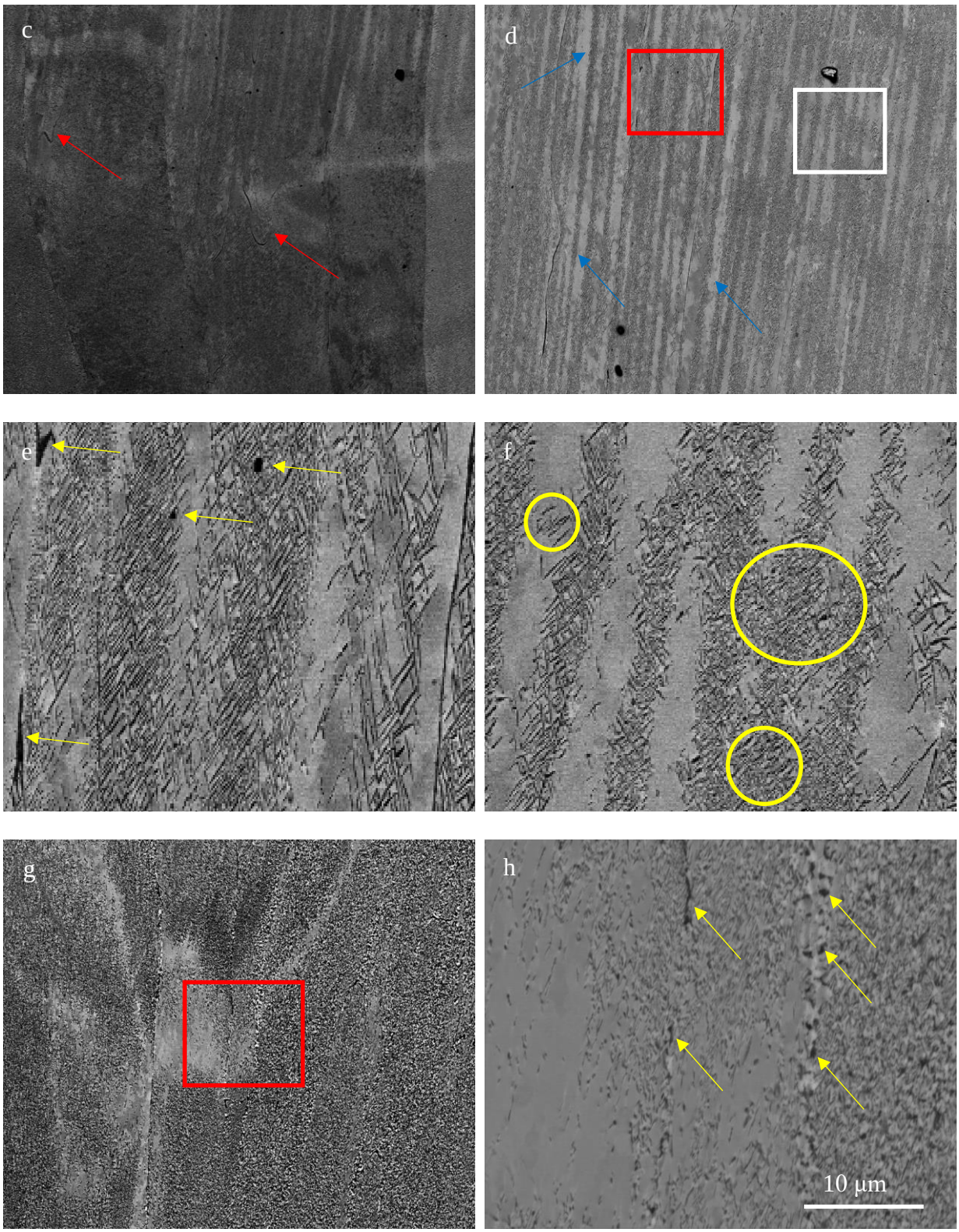
c
d
e
f
g
h
10 µm

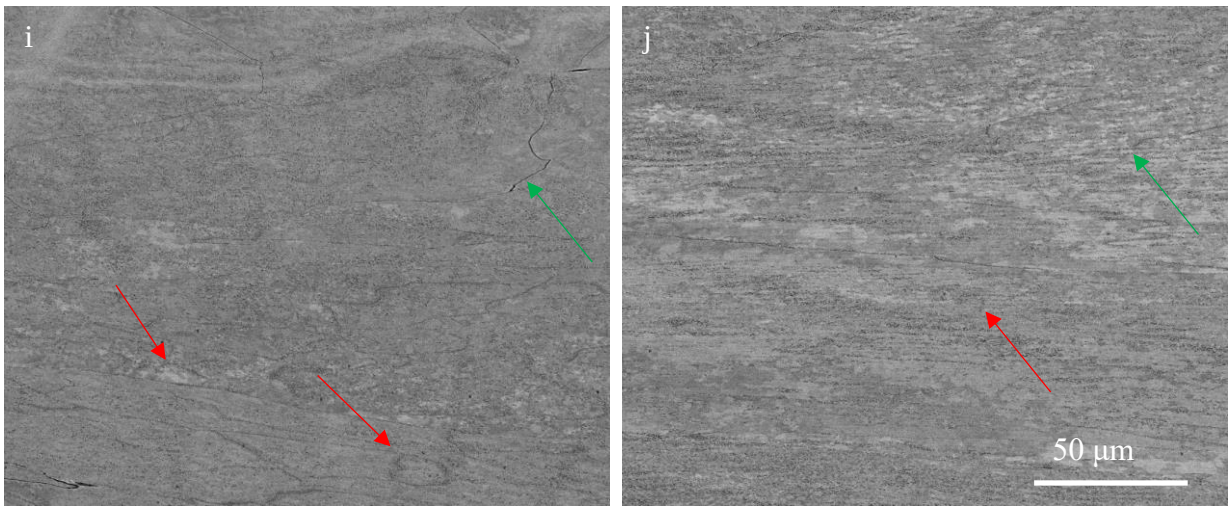

Figure 6.4. SEM images of (a) Sample I; (b) Sample II; (c) Sample III; (d) Sample IV; (e) Magnification of red rectangle of "d"; (f) Magnification of white rectangle of "d"; (g) Sample V; (h) Magnification of red rectangle of "g"; (i) Sample VI; (j) Sample VII.

6.3.2 EDS points analysis

Sample IV and V (Fig. 6.5a and 6.5b) were used for EDS point analysis and compared to the AB sample (Fig. 4.4) to understand the effect of strain on alloy composition at a given temperature and low strain rate of $0.0011S^{-1}$. In Sample V, the FZ is retained (yellow arrow of Fig. 6.5b) however there is no evidence of prior thin long inter-lamellas in the HAZ. This suggests a fragmentation of this structure at 40% strain. The evolving structure are segregated dark and bright spots/particles like those observed in the RZ of AB sample (Fig. 4.3). Thus, there was a lamella structural refinement during low strain rate TMCP between 20% and 40% strain as the prior thin long lamellas are retained in Sample IV which underwent 20% strain. Composition of these broken-down lamellas of the HAZ zone are identical to those of the RZ in Sample V (i.e., 12.5 Wt. % for HAZ-lean, HAZ-rich and RZ of Sample V), howbeit with a smaller standard deviation (Fig. 6.6). The lowest Mo concentration obtained from the RZ between both samples is 5.5 Wt. % (spectrum 114 of Sample V). There are super-enriched zones with solute concentrations of 22.3 Wt. % and 21.1 Wt. % obtained from Spectrum 102 of Sample IV and Spectrum 111 of Sample V, respectively.

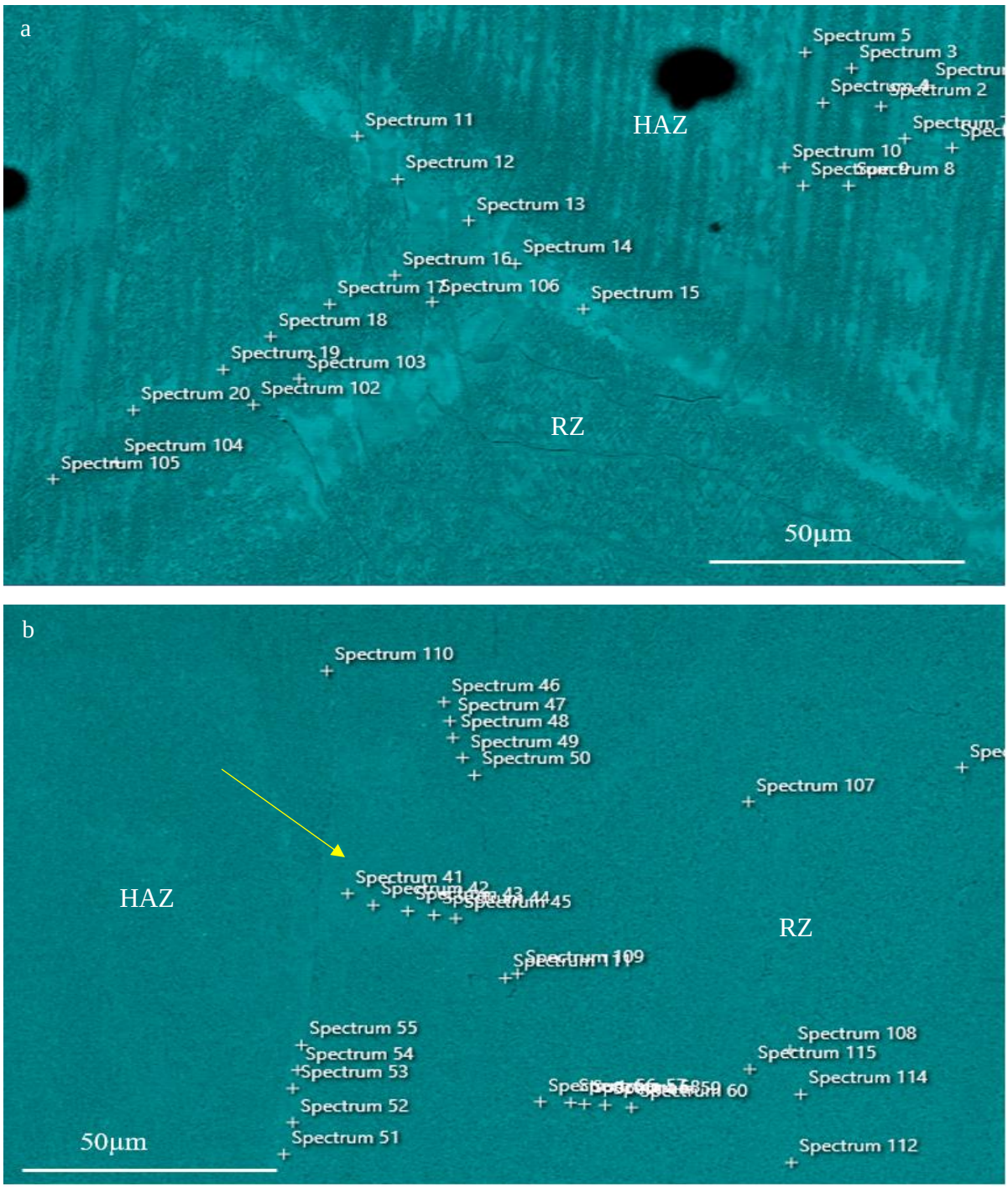

Figure 6.5. Mo distribution map for (a) sample IV and (b) sample V.

The differential in Mo concentration between Sample IV and V shown in Fig. 6.6 is as a result of the additional diffusion which occurs from 20% to 40% strain at the same temperature and strain rate. This sees the depletion and enrichment of the RZ and FZ of Sample V, respectively. As expected, the standard deviation in the RZ of Sample IV and V are both smaller than the AB alloy, confirming a higher degree of homogenisation after TMCP.

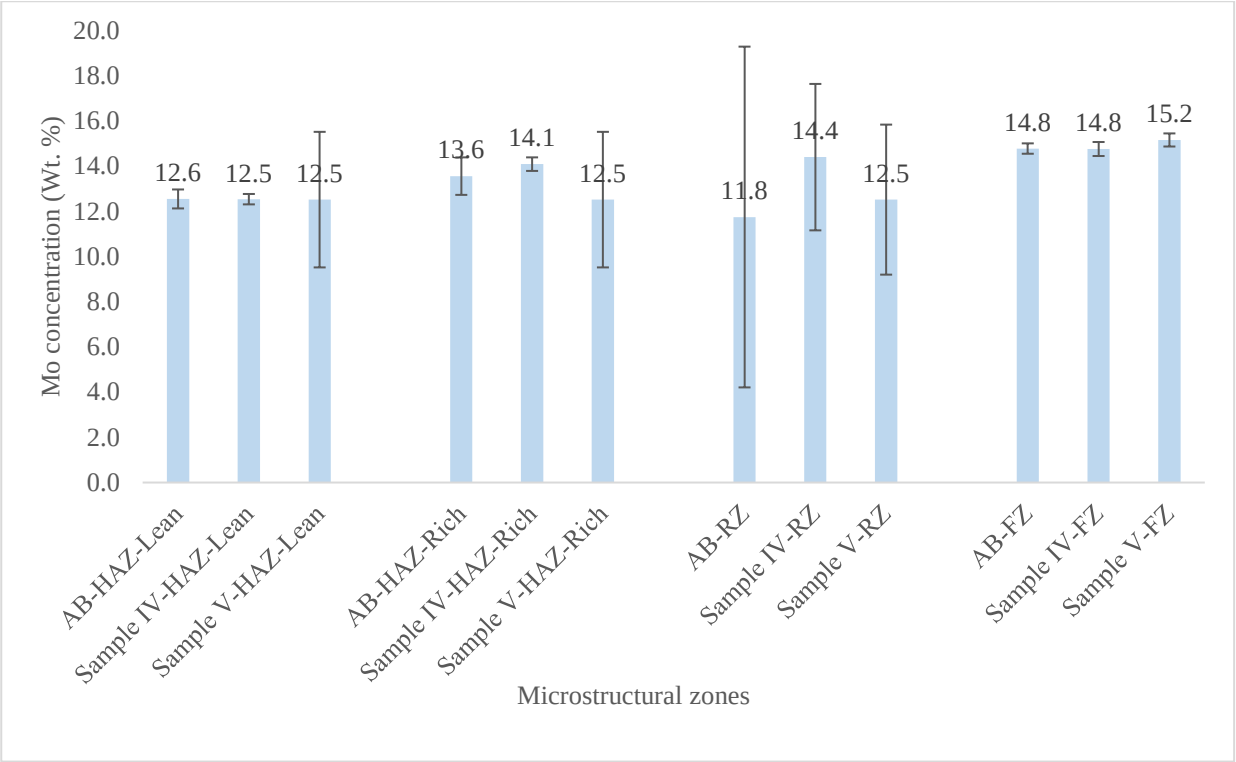

Figure 6.6. Mo concentration of zones in AB sample, Sample IV, and Sample V.

6.3.3 EBSD analysis

The EBSD maps of Fig. 6.7 were acquired from the area within the red rectangle of Fig. 6.4d. IPF map shown in Fig. 6.7a reveals a predominant $[111]_{\beta}$ and $[001]_{\beta}$ of columnar β-grains after TMCP. Fig. 6.7b shows a band contrast map with overlayed α″ martensite. α″ phase fraction was determined to be 1.66% after noise reduction and this is close to the 2% upper limit determined for the deformed AB sample reported in Section 4.3.2. The reduced martensite fraction reported in Section 6.1 is therefore confirmed by EBSD.

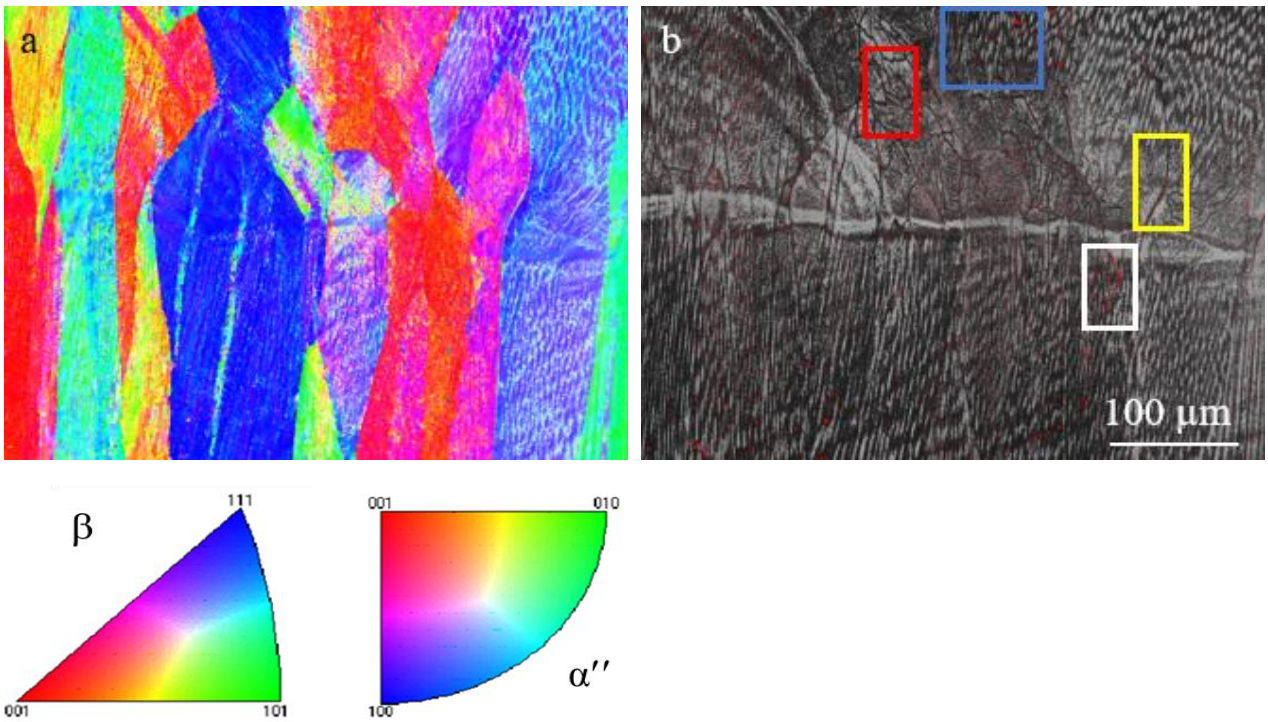

Figure 6.7(a). IPF and (b) BC with overlayed α'' martensite obtained from area within the red rectangle of Fig. 6.4d. Red particles/chunks in (b) is the overlay for α'' martensite. Compression axis is along the map horizontal X-axis.

Figs. 6.8a, 6.8b and 6.8c are the magnified phase maps of the white, yellow, and blue rectangles of Fig. 6.7b, respectively. Fig. 6.8a and 6.8b show continuous and discontinuous grain boundary α'', respectively. Both grain boundary α'' were also reported in the 700-DS sample (see Section 5.5.2). However, this was not observed in the deformed AB sample. Fig 6.8c shows α'' which formed within parent β, surrounded by un-indexed dark phases which could be the α-phase identified by XRD analysis of Section 6.1. Fig. 6.8d, 6.8e and 6.8f are the magnified KAM, GB, and TB maps of the red rectangle of Fig. 6.7b. Fig. 6.8d shows the strain accommodations of untransformed β and deformation induced products. The observed occurrences agree with those of the deformed AB sample (see Section 4.3.2) and the 700-DS sample (see Section 5.5.2). Fig. 6.8f confirms the deformation bands reported in Section 6.3.1 to be the $\{332\}\langle 113\rangle_{\beta}$ and $\{112\}\langle 111\rangle_{\beta}$ twin-systems with some un-indexed bands in the area. The $\{112\}\langle 111\rangle_{\beta}$ twin system had the dominance and the prevalence of secondary α'' which formed within β-twins in the deformed AB sample (see Section 4.3.2) was also observed after TMCP, howbeit as a seldom occurrence (i.e., white ellipse of Fig. 6.8f).

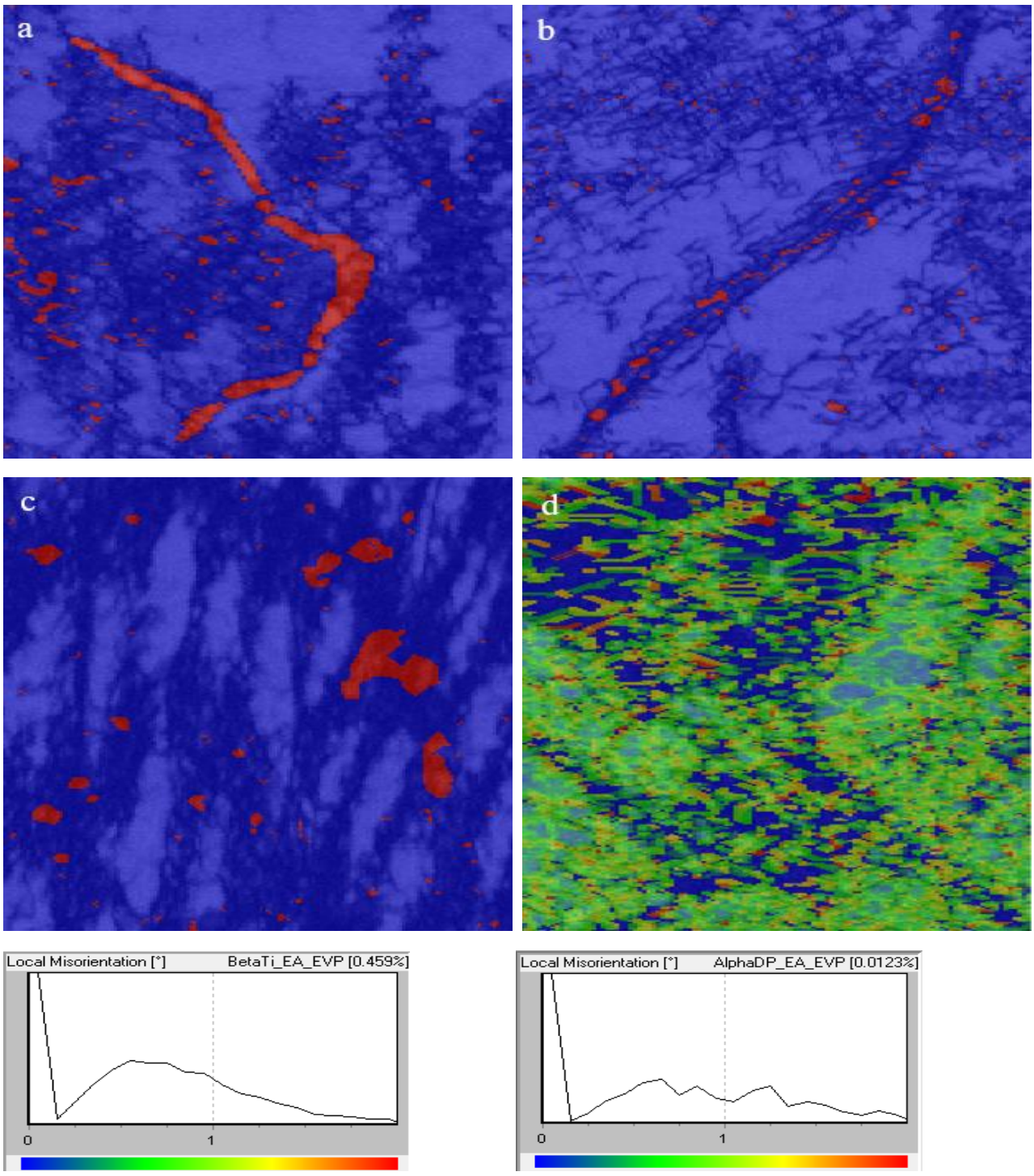
a
b
c
d
Local Misorientation [°]
BetaTi_EA_EVP [0.459%]
0
1
Local Misorientation [°]
AlphaDP_EA_EVP [0.0123%]
0
1

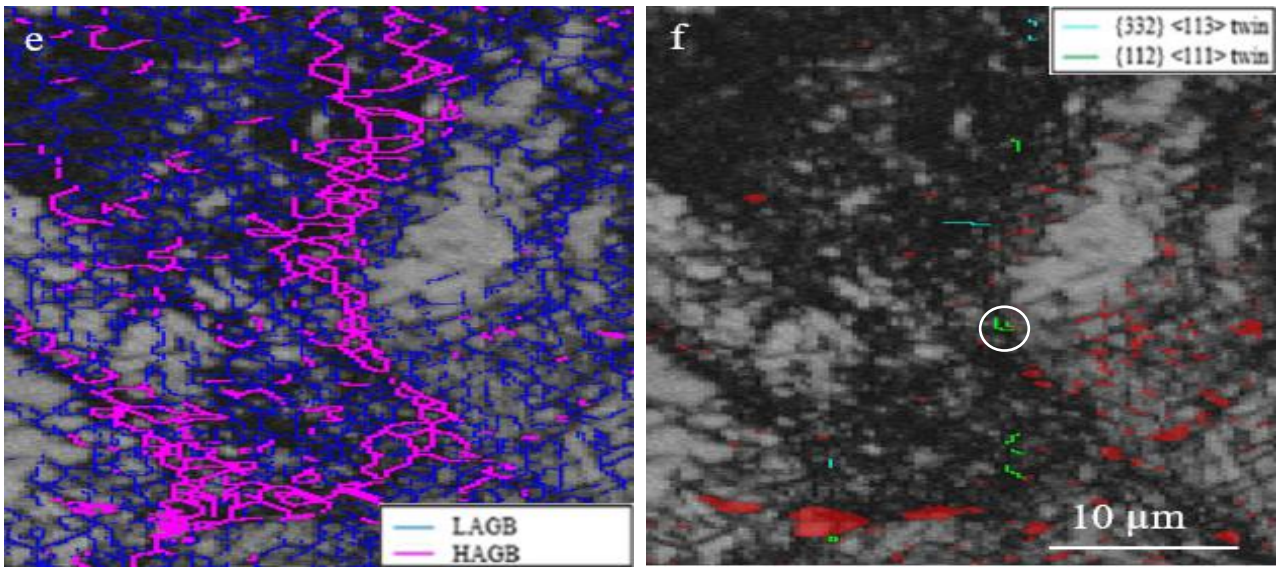

Figure 6.8(a-c). Phase map of area within the white, yellow, and blue rectangles of Fig. 6.7b, respectively. Blue represents β-phase and red represent α'' martensite; (d) KAM map; (e) Grain boundary map and (f) Band Contrast map with overlayed β-twins and α'' martensite, obtained from area within the red rectangle of Fig. 6.7b.

6.3.4 Texture analysis

As shown in Fig. 6.9a, the $\Phi_2 = 0°$ section of β bears no significant orientation texture. However, the $\Phi_2 = 45°$ section (Fig. 6.9b) shows the $(331)[2\bar{2}1]$ orientation which is the same (i.e., a planar multiple) as the $(441)[2\bar{2}1]$ orientation reported for the 700-DS sample (i.e., Fig. 5.11a). The appearance of this orientation texture in Sample IV, is a confirmation that it is certainly not a fabrication one as suggested by its absence from the AB microstructure (i.e., Fig. 4.14a). This orientation is also absent from the DS sample (i.e., Fig. 4.14c). It is therefore, both a recrystallisation and dynamic-recrystallisation texture. Also, it is independent on deformation mode and temperature of deformation as it appears in both RT tensile deformed (i.e., 700-DS sample) and elevated temperature TMCP (i.e., Sample IV) samples of Chapter 5 and 6, respectively howbeit with a stronger intensity in the heat treated-RT tensile deformed sample (i.e., 700-DS sample). The $(113)[0\bar{3}1]$ orientation of Fig. 6.9a also formed in the DS microstructure (i.e., Fig. 4.14c) and did not pre-exist in the AB microstructure. As discussed in Section 4.5, this orientation has been associated with the operation of $\{332\}[113]$ and $\{112\}[111]$ β-twin systems confirmed by Fig. 6.8f. The $(112)[\bar{2}\bar{5}3]$

orientation of Fig. 6.9a is unique to the TMCPed sample microstructure and may have a connection with the operation of {112}[111] β-twinning.

The ODF sections of Fig. 6.9b bear no significant orientations for α″ martensite.

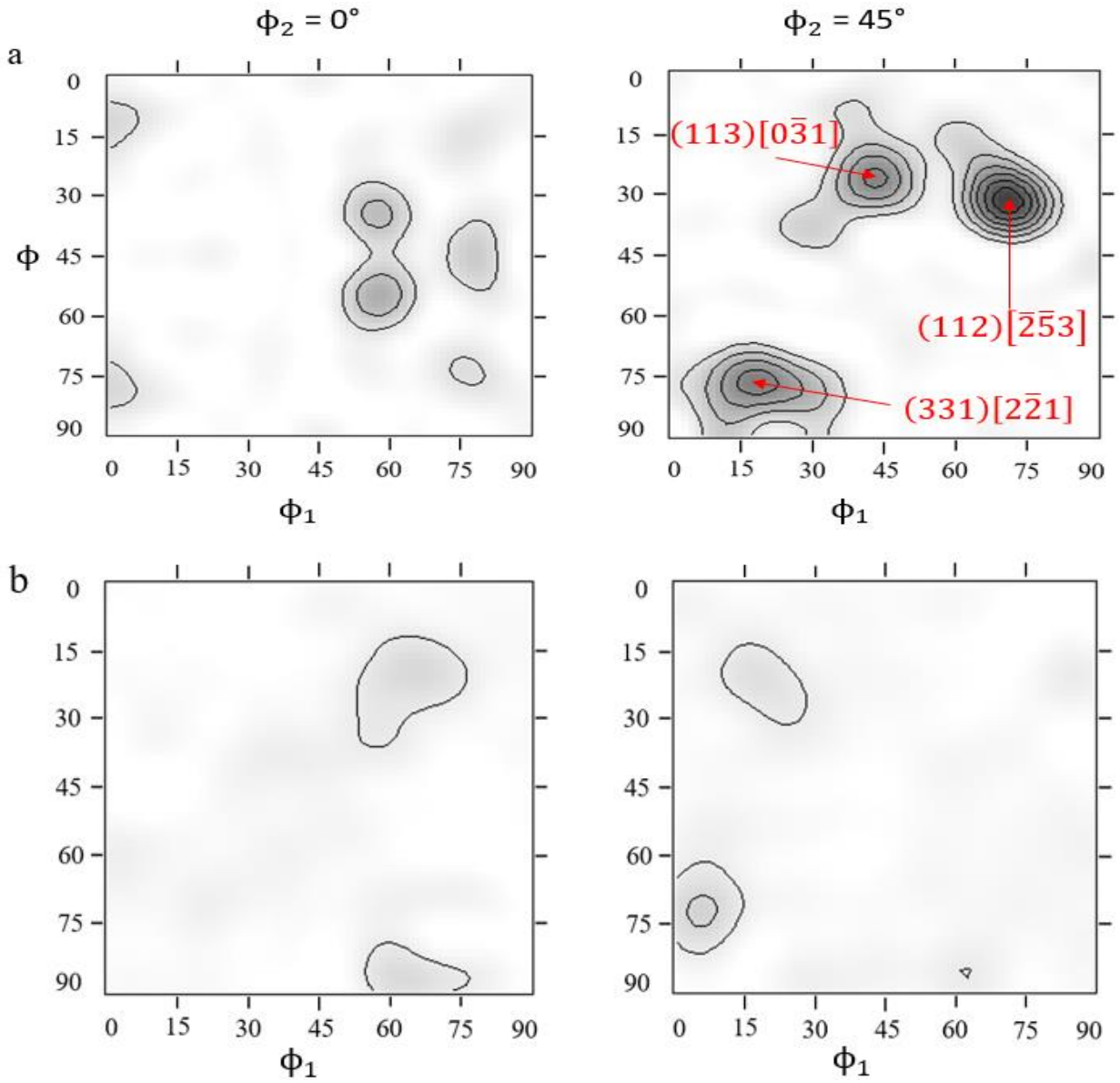

Figure 6.9. Orientation Distribution Function ϕ_2 sections for (a) β-phase and (b) α″ martensite taken from X-Y plane of Sample IV. Intensity levels for β phase are x1.67 and x2.46 for α″ martensite.

6.4 Compressive properties

Fig. 6.10a shows evidence of double yielding (red arrows) in Sample II which was compressed to 40% at RT. The stress plateau indicated by the lower red arrow was also reported in metastable Ti alloys investigated in Refs [43, 331]. In Ref. [43], all samples were compressed at RT and thermal

softening of flow stress occurred by adiabatic temperature rise with the exception of the sample compressed at a low strain rate of 10^{-3} S^{-1}. Sample II in the current study was compressed at RT and at a similar strain rate of 0.0011 S^{-1} and also exhibited continuous work hardening up to 0.4 strain. A serrated stress flow reported in Refs. [332, 333] is also observed in Sample II between the strains of 0.14 and 0.4.

Samples which underwent TMCP at 650°C all displayed thermal softening (Fig. 6.10f) with Sample V (Fig. 6.10b) being the softest due to its lowest strain rate which created more time for thermal effect. Correspondingly, the yield strength increased with strain rate and the second yield point (green arrows of Fig. 6.10b, 6.10c and 6.10d) occurred before flow softening. Unlike the double yielding of the RT compressed sample (Fig. 6.10a), the TMCP samples exhibited no stress plateau but a noticeable change in gradient before thermal softening occurred. Also, the softening trend showed a decrease in steepness after a strain of 0.27 for Sample VII. This also occurred in Sample V and VI after a strain of 0.31 and 0.29, respectively. It is the usual response of β titanium alloys deformed below β transus temperature to display continuous flow softening after rapid increase up to a maximum stress of 150±0.4MPa or higher [334-337]. Only Sample V in the current study conformed to this claim, as Samples VI and VII displayed noticeable softening at higher stress levels.

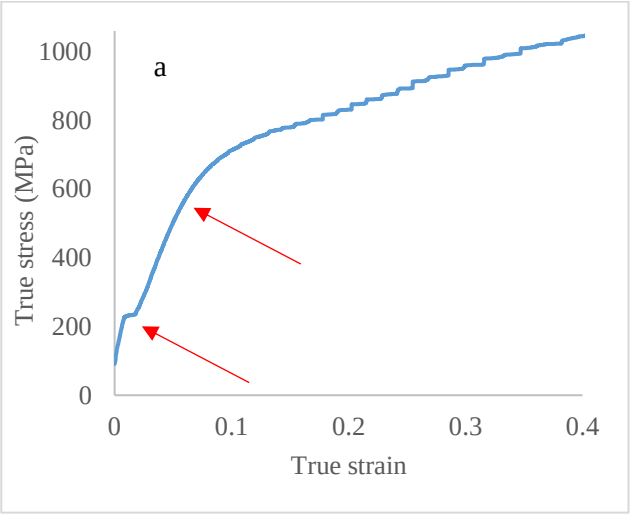

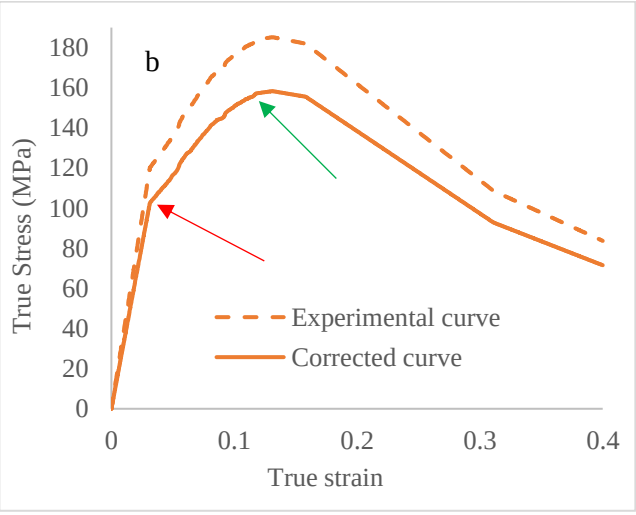

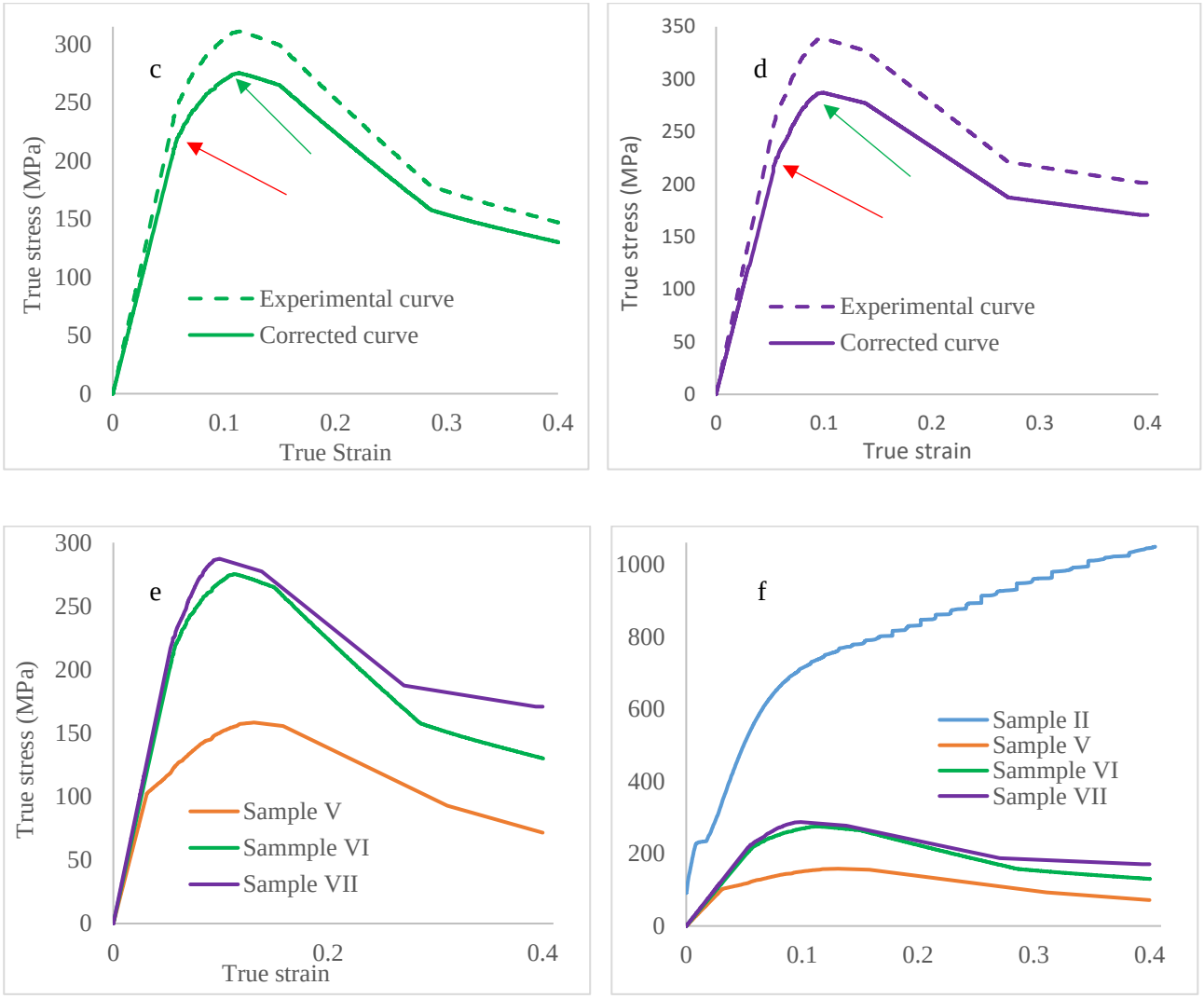

Figure 6.10 Compressive stress-strain curves of (a) Sample II; (b) Sample V; (c) Sample VI; (d) Sample VII; (e) combined TMCP samples; (f) combined RT and TMCP samples.

6.4.1.1 Hardness

All hardness data presented in Fig. 6.11 were determined at room temperature. TMCP samples are harder than the RT ones and Sample VII is the hardest of all TMCP samples. Also, samples strained to 40% are harder than those of 20% at both temperatures. Hardness property of TMCP samples cannot be correlated with compressive mechanical properties of Fig. 6.10 as the former was determined at RT while the later was obtained at 650°C.

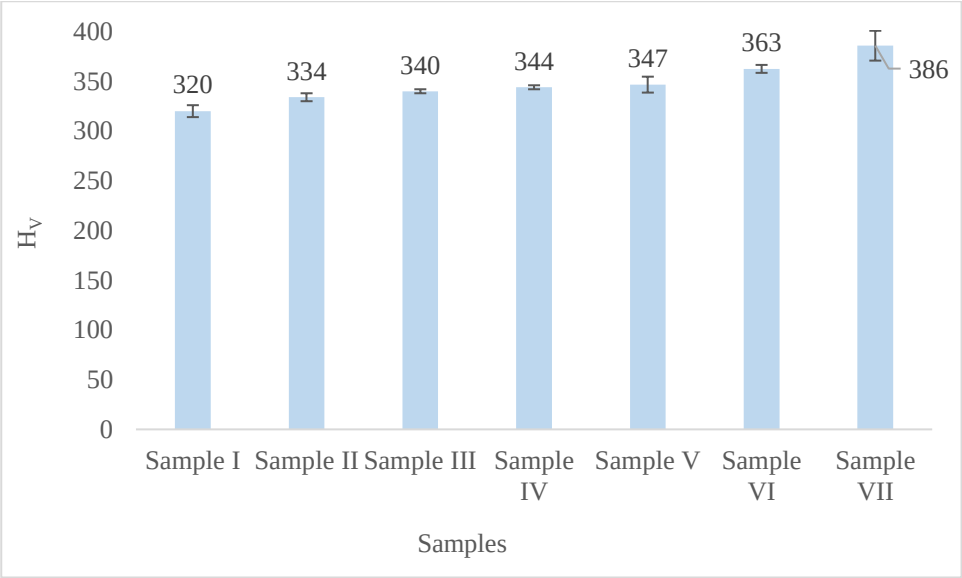

Figure 6.11. Hardness of RT compressed and TMCP samples.

6.5 Discussion

Deformation bands with grid-like configuration which formed in Sample I and II bear the same morphology as those identified by EBSD and TEM as {332}⟨113⟩ and {112}⟨111⟩ β-twins for the AB sample [41]. The black amorphous packets forming both primarily on parent β and secondarily within β-twins in the same samples were also confirmed to be deformation induced α″ martensite.

The observed phases and deformation products in TMCP samples were not consistent in distribution density/arrangement over the microstructure. Due to the inhomogeneous state of AB coupon, existing pre-compression phases either permit or inhibit the formation of deformation products depending on zone in which a specific cylinder was extracted (Figure 3.5). Samples III (Figure 6.4c) and IV (i.e., Figure 6.4d) feature a representative area where deformation products confirmed to be β-twins formed. The distribution density of twins increased with less product free area in sample IV compared to Sample III which featured a larger non-banded area of predominantly α-phase (entire area below red arrows of Figure 6.4c). This implies a higher surface fraction of twins which is expected at higher strains rates [338], regardless of the inhibiting effect of reduced β domain size caused by the varying α-phase fraction among the TMCP samples. In Ref. [338] it was determined that in BCC metals, higher strain rate generates higher density and faster movement of dislocations leading to more twin

nucleation events so long as the critical resolved shear stress for twinning is independent on strain rate. In Ref. [339], it was reported for Ti-6Al-4V that higher density of mobile dislocations decreases the activation energy required for the nucleation of twins. The observed intersection of deformation bands shown by yellow ellipse of Figure 6.4f is a hint at the activation of multiple twin systems in metastable Ti–10V–3Fe–3Al–0.27O [43] which is confirmed in Figure 6.8f in the current study. Sample V features an area in the alloy where there exist primary α-dominance which completely inhibits the formation of β-twins. In Samples VI and VII where compression proceeded at higher strain rates than in Sample V, the α phase underwent further refinement resulting in a much finer morphology. Also, the dominance of α in Samples VI and VII completely inhibited twin formation during compression.

The deformation-band free grains/areas in all compressed samples may occur due to three primary reasons. Firstly, due to super-stabilised β-zones/areas reported by EDS analysis of Section 3.3.2. The molybdenum equivalence factor distribution within a specific β-grain is non-uniform. Some areas were super solute enriched and such areas commonly occurred on the immediate adjacent side of a super depleted area. This gives rise to product free areas surrounded by product dense areas. Secondly, Bertrand et al [205] reported that the absence of deformation products in different β-grains is dependent on their crystallographic orientation with respect to the direction of applied stress. It was further explained that grains with a minimum SF of 0.38 show the activation of twinning. Hence the grains with no twins in the current study must have less than 0.38 SF. Thirdly, it was reported in Ref. [279] that a steep shear modulus gradient existing at neighbouring β/ω phases can cause the inhibition of deformation products in certain β grains. Even though a TEM analysis of ω phase was not conducted in the current study, the claimed occurrence of steep shear modulus gradient can still stand-in as a plausible cause. This is because TMCP temperature of 650°C includes temperature range of 350-400°C required for formation of ω_{ath} in β Ti-alloys [86, 340]. Such event would only add to the already existing ω_{ath} phase fraction from LMD process. This would increase the number of β/ω

interfaces, which in turn increases the number of sites where such shear modulus chasm exists thereby validating the claim.

Within the deformation bands of Sample III and IV are secondary needle-like products predominantly criss-crossing each other at approximately 90°. These secondary products were confirmed to be α'' martensite by EBSD analysis (Figure 6.8a-c) to have a true packet morphology after map cleaning. These secondary α'' forming within β_{twin} seemed to have a sparse occurrence (Figure 6.8f) in the microstructure due to map cleaning process which set critical misorientation angle at 2°. This resulted in the sparse remnant distribution of secondary α'' after TMCP. In Ref. [43], it was reported in metastable Ti-10V-3Fe-3Al-0.27O that at 10^{1} S^{-1} or higher strain rates, the dominant deformation mechanism is twinning while stress induced martensite dominated at low strain rates of 10^{-3} S^{-1} and 10^{-1} S^{-1}. Contrarily, in the current study the surface fraction of secondary martensite increased correspondingly to the increase in twin surface fraction, within which martensite form. This is a conclusion reached by comparing Sample III (Figure 6.4c) to Sample IV (Figure 6.4d). The dependence of primary GB martensite on strain and strain rate would require EBSD map acquisitions for Samples III, VI and VII and the very evolution of it would require an in-situ compression observation which exceeds the scope of the current study.

The stress plateau of Sample II (Figure 6.10a) starts and terminates at stress/strain of approximately 203 MPa/0.006 and 233 MPa/0.014, respectively. The stress required to initiate the operation of twins and α'' martensite, occurring within the stress plateau is regarded as the triggering stress. This stress plateau demarcates the two yield points of Sample II and double yielding occurs as a result of the triggering stress for twins/α''_D being lower than the material yield strength of the alloy [341]. Triggering stress is therefore defined as the intersection of the elastic modulus tangent and the tangential extension of the slope of slowly rising stress region [331]. As observed in Sample V-VII (Figure 6.10e), triggering stress is strain rate dependent at elevated temperature deformation as substantiated by the higher first yield point at higher strain rates. The observed dependence was also reported for RT compressed metastable Ti alloys in Refs. [42, 43], implying that this dependence

holds true regardless of temperature of deformation. Comparing Sample II (Figure 6.10a) to the sample strained at a similar strain rate of $10^{-3}S^{-1}$ in Ref. [43], the triggering stress of 190 MPa falls below the lower plateau limit of 203 MPa of the current work. It is worth noting that although both alloys are of the metastable Ti class, the one in the current study represents a higher β-stability denoted by a molybdenum equivalence factor of 15 compared to 12.4 for the cited work. Thus, a higher triggering stress is rightfully confirmed at higher β stability. Also, the presence of α-phase in the alloy of the cited work reduces the β-domain size which also contributes to its lower triggering stress. A similar increase in triggering stress with β-stability was also reported in Ref. [45]. In the cited work, RT compression proceeded on Ti-10V-3Fe-3Al at a strain rate of $10^{-3}S^{-1}$ after a well-designed heat treatment to precipitate varying surface fractions of α. Samples which had α surface fractions of 14±2% and 21±3%, exhibited triggering stresses of 203±5 MPa and 228±4 MPa, respectively. These values are closely comparable to the lower and upper limit obtained in the current study. Thus, the diffusion of β-stabilising element from α-phase made the cited alloy more β-stable thereby increasing its triggering stress inspite of the lower β-domain size. In Ref. [42], the Ti-10V-2Fe-3Al metastable sample compressed at a strain rate of $10^{-4}S^{-1}$ exhibited a triggering stress of 203MPa which equals the lower plateau limit of Sample II of the present study. However, in the cited study the sample compressed at a strain rate of $10^{-3}S^{-1}$ exhibited a triggering stress of 263MPa. This is unexpected as a lower β-stability of 9.50 MoE factor should only allow a lower than 203MPa triggering stress. Also, the influence of diffusion of β stabilising elements from α was not reported in the cited study. The reason for this occurrence is unclear. The serrated section observed in the plastic domain of Sample II (Figure 6.10a) is associated with formation of more deformation products beyond the triggering stress region. This is seen in SEM image which shows the product distribution of Sample II (Figure 6.4b) which is apparently denser than that of Sample I (Figure 6.4a). Since this serration occurs in the plastic domain, it is therefore indicative that majority of deformation products formed are structurally irreversible beyond the second yield point. Serrations has also been linked to flow localisation/alloy cracking in Ti40 [342].

The TMCP samples (Figure 6.10e) do not exhibit a stress plateau but do show evidence of double yielding at all strain rates (red arrows of Figure 6.10b-d). The first yield point increases from 105 MPa in Sample V to 230MPa in sample VII. The second yield point increases from 157MPa in Sample V to 282MPa in Sample VII. The first yield point indicates the triggering stress for β-twins which are all lower in comparison to the RT sample as expected. Though ex-situ SEM images show lower surface fractions of β-twins in the TMCP samples (Figure 6.4c and 6.4d) than the RT compressed ones (Figure 6.4a and 6.4b), the double yielding occurrence only serves as an indication that deformation products may have been activated at lower strains in the TMCP samples. The observed yield point and flow stress increase with strain rate during elevated temperature compression was also reported in Refs. [329, 332]. As seen in Figure 6.10e, the dynamic softening effect and flow stress plateauing occurred earlier (i.e., at lower strains) at higher strain rates. This could be attributed to the increased dislocation densities at higher strain rates which could promote the earlier completion of product formation just before initiation of softening, where the softening zone denotes a region where products may not be forming. The speculation of no product formed in the softening zones of TMCP samples after second yield point is hinted by the absence of serrated flow (Figure 6.10e). This serrated flow was very evident in Sample II (Figure 6.10a).

Dynamic softening can be an indication of dynamic recovery or dynamic recrystallisation [332]. Dynamic recrystallisation can occur by four mechanisms namely strain induced boundary migration [343], particle stimulated nucleation [344], at triple junctions [345] and intragranularlly [345]. The intragranular mechanism is identified in the present work and growth of sub-grains takes place epitaxially (green arrows of Figure 6.4i and 6.4j) and non-epitaxially (red arrows of Figure 6.4i and 6.4j). The recrystallised grains forming intragranularlly within columnar grains have been reported to bear large misorientations from deformed β-matrix [345].

6.6 Conclusions

1. After elevated temperature TMCP, columnar β-grains were refined by a combined contribution from precipitated α, β-twins and α″ martensite. However, grain structure homogenisation was not achieved as these precipitates and deformation induced products were inconsistently/in-homogeneously distributed over the microstructure. Thus, improved but anisotropic mechanical properties should be expected after uniaxial tensile deformation of a pre-TMCPed alloy.
    a. As a result of increased fragmentation of prior columnar β-grains, ultimate tensile strength of tensile deformed pre-TMCPed alloy could be higher than that of AB alloy.
2. The compositional inhomogeneity of the initial AB sample is the direct basis for the occurrence of α-precipitate dominance in Sample V-VII, a near-equal split-share between α and β-twin in Sample III and a β-twin dominance in Sample IV.
    a. There is therefore a partitioning of alloy microstructure after elevated temperature TMCP. This is caused by a competition between α-precipitates and β-twins. This partitioning occurred as a direct consequence of the non-uniform precipitation of α during TMCP. Argon did not provide absolute shielding of samples against oxygen which contributed to α precipitation in addition to the fact that the 650°C TMCP condition is in the α+β phase field [309]. Thus, anisotropy in mechanical properties would imply a high ultimate tensile strength in α dominated zones, more ductility in zones with predominantly β-twins and intermediate properties in the near-even split zones.
3. True martensite morphology was determined after map cleaning by EBSD analysis, to be amorphous packets as also reported for the AB alloy [41]. This martensite phase formed at chunkier sizes than those reported in the AB alloy. Also, the fact that this phase formed as continuous products on columnar and sub-columnar β-grain boundaries serves as a strengthening effect for potential enhancement of yield and ultimate tensile strength.

4. Dynamic recrystallisation primarily occurred within prior columnar β-grains following both an epitaxial and non-epitaxial growth mechanism.
5. It was determined in the current work that a triggering stress within the range from 203MPa to 233MPa is required to initiate twins/α_D'' during uniaxial compression at RT, and this compared very closely to data reported by other authors. Double yielding is also evident in TMCP samples howbeit without the occurrence of a stress plateau. The understanding of triggering stress is a valuable input to designing a uniaxial test on pre-TMCPed sample. This would follow an engineering analysis which establishes correlations/conversion factors between mechanical data from a compressive test and that of a tensile test.
6. In TMCP samples, higher strain rate resulted in higher compressive yield strength, higher flow stress and earlier start (i.e., at lower strains) of dynamic softening. As a result, higher than $10^{-3}s^{-1}$ strain rate applications are recommended in order to obtain maximum mechanical performance from the alloy when loaded in compression. Suitable conversions would be required to know the implication of this in a tensile application.

7 Conclusions and recommendations

This chapter presents a comprehensive summary of all the main findings of the current study by establishing similarities and differences among the conclusions of each results chapter viewed in comparison with revelations gained from literature review. The microstructure of As-LMDed Ti-15Mo was first characterised and then subject to uniaxial tensile test after which the deformed microstructure was analysed, and its mechanical properties compared to its counterparts reported by other authors. Subsequently, several AB samples were heat-treated and thermo-mechanically processed with the aim of refining prior columnar β-grains.

Themes are also proffered on possible areas for further investigation with regards to the fabrication stage of LMDed Ti-15Mo, its characterisation and post-fabrication processing.

7.1 Comprehensive summary

1. Parent β and ω_{ath} were the only two phases determined in the AB microstructure. The heat-treated and thermomechanical processed microstructures featured α precipitates in addition. XRD peaks revealed a higher surface fraction of ω_{ath} in the post-fabrication-processed microstructure than the AB one.
2. The three distinct zones including the FZ, RZ and HAZ as well as the inter-dendritic lamellas of the HAZ found in the AB microstructure were retained after sub-β-solvus heat treatment and thermo-mechanical processing. The FZ maintained the highest Mo concentration and the RZ attained a higher degree of homogenisation after sub-β-solvus post-fabrication-processing. However, these distinct zones were completely erased from the microstructure of the super-β-solvus heat-treated sample which featured super-Mo-rich and super-Mo-lean phases. Thus, heat treatment at 1200°C for 6 hours did not yield solute homogenisation as erroneously reported in literature where these authors have lacked convincing substantiation of this claim in form of EDS analysis.

3. The predominant columnar grains present in the AB microstructure were refined after heat treatment and thermomechanical processing. Refinement occurred both by epitaxial/non-epitaxial recrystallisation/dynamic recrystallisation and by the fragmentation of columnar grains by precipitated α-phase. The average grain size of the AB sample saw a reduction from 44μm to 35μm with a smaller standard deviation after heat treatment, implying a more homogenised grain structure.
4. In the microstructures of the AB and TMCP samples, accommodation of plastic deformation took place by $\{332\}\langle 113\rangle$ primary twinning, $\{112\}\langle 111\rangle$ primary and secondary twinning within $\{332\}\langle 113\rangle$ twins, primary and secondary stress-induced α'' martensite formation and stress-induced ω_D formation in β matrix and slip. $\{332\}\langle 113\rangle$ β-twin was present in a much higher surface fraction than the $\{112\}\langle 111\rangle$ ones in the deformed AB microstructure. However, the reverse was true in the TMCP sample microstructure. In the 700-DS sample, plastic deformation was accommodated by all of the above with the exception of β-twins.
5. In the AB microstructure, stress-induced martensite nucleated preferentially at β/β-twin interfaces and intragranularlly as primary products or within β-twins as secondary products. In the deformed microstructure of the heat-treated sample, martensite did not form as secondary products due to the absence of advanced stages of β-twinning. However, they formed as primary products intragranularlly as well as in β-grain boundaries both as continuous and discontinuous products. The samples subjected to compression at RT comprised of intragranular and grain boundary martensite as well as fully developed β-twins which accommodated secondary martensite. Elevated temperature TMCP samples featured β-twins with poorly defined twin boundaries. Martensite formed in these samples intragranularlly as well as in grain boundaries as continuous and discontinuous products, howbeit with a larger representative chunk/packet size than the AB and heat-treated ones.
6. There were differences in distribution density of twins and martensite in the AB microstructure between the RZ and HAZ where the HAZ consistently featured a higher

density of deformation products. The FZ featured very insignificant and in some cases no deformation products at all due to it being the zone of highest β-stability in microstructure. These occurrences were also evident in the microstructure of the heat-treated samples for martensite and in addition precipitated α was distributed rather sparsely or did not form at all in the FZ of the heat treated and TMCP samples creating precipitate free zones.

7. Texture analysis revealed the presence of multiple strong β-orientations in AB, heat-treated and TMCP samples howbeit with less intensities in the post-processed microstructures. However, there were fewer martensite orientations in the TMCP sample and none in the heat-treated sample. This hints at a possible decrease in an-isotropy of mechanical properties after post-fabrication processing.
8. The achieved tensile strength in the AB sample was higher than that previously reported for both wrought and SLM Ti-15Mo alloys. However, this came with a reduction in ductility (~0.9 vs 0.14-0.3 total strain). After heat treatment, the UTS and YS increased marginally, and this was accompanied by a slight deration in total elongation. The slight increase in UTS has been associated with the increased surface fraction of β/α interfaces which contributed to the fragmentation of β-grains along-side the contributions from recrystallised grains forming within β-grains.
9. The Vickers hardness of the sample heat-treated at 1200°C for 6 hours (i.e., 564 HV) was determined to be the hardest of all samples including the AB, the sub-β-solvus heat-treated and TMCP ones.
10. The emerging microstructure after TMCP which is highly fragmented, hints at a possible improvement of UTS if a pre-TMCPed sample were to be subject to uniaxial tensile deformation. However, much cannot be said about what could transpire with the total elongation as the average grain size did not differ significantly from the AB microstructure.

7.2 Recommendations for future study

The compositional variations in Mo across the microstructure of AB, sub-β-solvus heat-treated and TMCP samples, had a direct consequence in the unique formation patterns of deformation products during uniaxial tensile tests. These differences were mainly determined between the RZ and HAZ of each of the deposited layers. The columnar grains of the AB microstructure in combination with non-uniform Mo distribution are the reasons for an-isotropy in mechanical properties. Hence, a wide range of temperatures from 650°-850°C were deployed for heat treatment and thermomechanical processing and an optimal temperature of 700°C was determined to yield the highest degree of columnar grain refinement/fragmentation. However, there still exists a lot of possibilities which are worth exploring with regards to grain structure and compositional homogenisation of LMDed Ti-15Mo. Below are some ideas proffered for further understanding of microstructure-property relationship, attainment of a greater degree of mechanical isotropy and overall acceptance of as-LMDed Ti-15Mo in industry.

1. Incorporation of ultrasound step into LMD fabrication process for possible refinement of columnar grains and attainment of predominantly equiaxed grains in the AB alloy.
2. Heat treatment at 1200°C with a holding time of 12 hours or more to investigate for the possible emergence of a single β-phase microstructure.
3. Insitu observation of uniaxial tensile deformation to determine how martensite triggering stress compares to the prediction of Eq. 2.9 and other models in literature. This will also provide information on triggering stress of multiple β-twinning systems.
4. Multiple strain rate uniaxial tensile deformation of AB and heat-treated samples. Recommended strain rates include lower than $0.0011S^{-1}$ and higher than $10S^{-1}$. Deformation at low strain rates will provide more understanding on β-twinning operations in the heat-treated sample and high strain rate will display variance in deformation product morphology and distribution density from the outcomes of $0.001S^{-1}$ strain rate. Multiple strain rate experiments were not conducted in the current study due to limited availability of samples.

5. Uniaxial tensile deformation of AB-1200 sample, which displayed hardness of 564 H_V.
6. Tensile test on dog-bone extract from pre-TMCPed cylinder to observe effect of grain refinement/fragmentation on tensile properties.
7. Use of Hopkinson's bar apparatus for impact experiment at pre-defined high strain rates. This will enable, understanding of alloy's response and show its applicability in airplane wings which are exposed to shock loads from objects/birds.
8. Multiscale (i.e., macro, micro and nano) determination of residual stress in AB alloy to understand its influence on mechanical properties and also investigate how residual stress changes after heat-treatment and TMCP.

References

1. Sing, S.L., et al., Laser and electron-beam powder-bed additive manufacturing of metallic implants: A review on processes, materials and designs. Journal of Orthopaedic Research, 2016. **34**(3): p. 369-385.
2. Węglowski, M.S., S. Błacha, and A. Phillips, Electron beam welding–techniques and trends–review. Vacuum, 2016. **130**: p. 72-92.
3. Cho, J., Characterization of the α′-Martensite Phase and Its Decomposition in Ti-6Al-4V Additively Manufactured by Selective Laser Melting. RMIT University, 2018.
4. Graf, B., A. Gumenyuk, and M. Rethmeier, Laser metal deposition as repair technology for stainless steel and titanium alloys. Physics Procedia, 2012. **39**: p. 376-381.
5. Wang, M., X. Lin, and W. Huang, Laser additive manufacture of titanium alloys. Materials Technology, 2016. **31**(2): p. 90-97.
6. Zhong, C., et al., Laser metal deposition of Ti6Al4V—a brief review. Applied Sciences, 2020. **10**(3): p. 764.
7. Dinda, G., L. Song, and J. Mazumder, Fabrication of Ti-6Al-4V scaffolds by direct metal deposition. Metallurgical and Materials Transactions A, 2008. **39**: p. 2914-2922.
8. Mahamood, R.M. and E.T. Akinlabi, Scanning speed and powder flow rate influence on the properties of laser metal deposition of titanium alloy. The International Journal of Advanced Manufacturing Technology, 2017. **91**: p. 2419-2426.
9. Song, T., et al., Simulation-informed laser metal powder deposition of Ti-6Al-4V with ultrafine α-β lamellar structures for desired tensile properties. Additive Manufacturing, 2021: p. 102139.
10. Bhardwaj, T., et al., Direct energy deposition-laser additive manufacturing of titanium-molybdenum alloy: Parametric studies, microstructure and mechanical properties. Journal of Alloys and Compounds, 2019. **787**: p. 1238-1248.

11. Nag, S. and R. Banerjee, Laser deposition and deformation behavior of Ti–Nb–Zr–Ta alloys for orthopedic implants. Journal of the Mechanical Behavior of Biomedical Materials, 2012. **16**: p. 21-28.
12. Collins, P., et al., Laser deposition of compositionally graded titanium–vanadium and titanium–molybdenum alloys. Materials Science and Engineering: A, 2003. **352**(1-2): p. 118-128.
13. Pang, X., et al., Strength and ductility optimization of laser additive manufactured metastable β titanium alloy by tuning α phase by post heat treatment. Materials Science and Engineering: A, 2022. **831**: p. 142265.
14. Sharma, D., et al., The ageing response of direct laser deposited metastable β-Ti alloy, Ti–5Al–5Mo–5V–3Cr. Additive Manufacturing, 2021. **48**: p. 102384.
15. Thijs, L., et al., A study of the microstructural evolution during selective laser melting of Ti–6Al–4V. Acta materialia, 2010. **58**(9): p. 3303-3312.
16. Schwab, H., et al., Microstructure and mechanical properties of the near-beta titanium alloy Ti-5553 processed by selective laser melting. Materials & Design, 2016. **105**: p. 75-80.
17. Vrancken, B., et al., Microstructure and mechanical properties of a novel β titanium metallic composite by selective laser melting. Acta Materialia, 2014. **68**: p. 150-158.
18. Cai, S., et al., Discovery of a 〈210〉-fiber texture in medical-grade metastable beta titanium wire. Acta Materialia, 2015. **87**: p. 390-398.
19. Cardoso, F.F., et al., Ti–Mo alloys employed as biomaterials: effects of composition and aging heat treatment on microstructure and mechanical behavior. journal of the mechanical behavior of biomedical materials, 2014. **32**: p. 31-38.
20. Furuhara, T., et al., Morphology and crystallography of α precipitates in β Ti–Mo binary alloys. Materials Transactions, JIM, 1998. **39**(1): p. 31-39.
21. Qian, B., et al., On the transformation pathways in TRIP/TWIP Ti–12Mo alloy. Materials Science and Engineering: A, 2021. **822**: p. 141672.

22. Oka, M. and Y. Taniguchi, Stress-Induced Products in Metastable Beta Ti--Mo and Ti--V Alloys. Journal of the Japan Institute of Metals, 1978. **42**(8): p. 814-820.
23. Qian, B., et al., In-situ observations of a hierarchical twinning–detwinning process in stress-induced α ″-martensite of Ti-12Mo alloy. Materials Research Letters, 2022. **10**(2): p. 45-51.
24. Sun, F., et al., Investigation of early stage deformation mechanisms in a metastable β titanium alloy showing combined twinning-induced plasticity and transformation-induced plasticity effects. Acta Materialia, 2013. **61**(17): p. 6406-6417.
25. Marteleur, M., et al., On the design of new β-metastable titanium alloys with improved work hardening rate thanks to simultaneous TRIP and TWIP effects. Scripta Materialia, 2012. **66**(10): p. 749-752.
26. Min, X., et al., Mechanism of twinning-induced plasticity in β-type Ti–15Mo alloy. Scripta Materialia, 2013. **69**(5): p. 393-396.
27. Hanada, S., T. Yoshio, and O. Izumi, Effect of Plastic Deformation Modes on Tensile Properties of Beta Titanium Alloys. Transactions of the Japan Institute of Metals, 1986. **27**(7): p. 496-503.
28. Mantri, S., et al., Suppression and reactivation of transformation and twinning induced plasticity in laser powder bed fusion additively manufactured Ti-10V-2Fe-3Al. Additive Manufacturing, 2021. **48**: p. 102406.
29. Liu, Y., Y. Zhang, and L. Zhang, Transformation-induced plasticity and high strength in beta titanium alloy manufactured by selective laser melting. Materialia, 2019. **6**: p. 100299.
30. Qiu, C. and Q. Liu, Multi-scale microstructural development and mechanical properties of a selectively laser melted beta titanium alloy. Additive Manufacturing, 2019. **30**: p. 100893.
31. Qiu, C., Q. Liu, and R. Ding, Significant enhancement in yield strength for a metastable beta titanium alloy by selective laser melting. Materials Science and Engineering: A, 2021. **816**: p. 141291.

32. Xu, H., et al., Study of superior strength in Ti15Mo alloy manufactured using selective laser melting. Journal of Alloys and Compounds, 2021. **885**: p. 161186.

33. Im, Y.-D., et al., Effect of Deformation Twinning in Metastable β-Type Ti-15Mo Alloys. JOM, 2018. **70**(11): p. 2582-2589.

34. Min, X., et al., Deformation microstructural evolution and strain hardening of differently oriented grains in twinning-induced plasticity β titanium alloy. Materials Science and Engineering: A, 2016. **659**: p. 1-11.

35. Zhao, X., et al., Beta type Ti–Mo alloys with changeable Young's modulus for spinal fixation applications. Acta biomaterialia, 2012. **8**(5): p. 1990-1997.

36. Chong, Y., et al., Mechanical properties of fully martensite microstructure in Ti-6Al-4V alloy transformed from refined beta grains obtained by rapid heat treatment (RHT). Scripta Materialia, 2017. **138**: p. 66-70.

37. Deng, H., et al., Microstructure and mechanical properties of as-deposited and heat treated Ti–5Al–5Mo–5V–3Cr–1Zr (Ti-55531) alloy fabricated by laser melting deposition. Journal of Alloys and Compounds, 2019. **810**: p. 151792.

38. Wain, N., et al., The influence of carbon on precipitation of α in Ti–5Al–5Mo–5V–3Cr. Materials Science and Engineering: A, 2010. **527**(29): p. 7673-7683.

39. Contrepois, Q., C. Marc, and J. Lecomte-Beckers, Characterization of the β phase decomposition in Ti-5Al-5Mo-5V-3Cr at slow heating rates. Open Journal of Metal, 2011. **1**.

40. Settefrati, A., et al., Precipitation sequences in beta metastable phase of Ti-5553 alloy during ageing. Ti-2011. Science Press Beijing, Beijing, 2011: p. 468-472.

41. Awannegbe, E., et al., Microstructural characterisation and mechanical evaluation of Ti-15Mo manufactured by laser metal deposition. Journal of Alloys and Compounds, 2023. **947**: p. 169553.

42. Ma, X., et al., Stress-induced martensitic transformation in a β-solution treated Ti–10V–2Fe–3Al alloy during compressive deformation. Materials Science and Engineering: A, 2021. **801**: p. 140404.

43. Ahmed, M., et al., Strain rate dependence of deformation-induced transformation and twinning in a metastable titanium alloy. Acta Materialia, 2016. **104**: p. 190-200.

44. Samiee, A., et al., Formation of deformation-induced products in a metastable-β titanium alloy during high temperature compression. Metals, 2018. **8**(2): p. 100.

45. Ahmed, M., et al., The influence of β phase stability on deformation mode and compressive mechanical properties of Ti–10V–3Fe–3Al alloy. Acta Materialia, 2015. **84**: p. 124-135.

46. Li, C., et al., Effect of strain rate on stress-induced martensitic formation and the compressive properties of Ti–V–(Cr,Fe)–Al alloys. Materials Science and Engineering: A, 2013. **573**: p. 111-118.

47. Li, C., et al., Tuning the stress induced martensitic formation in titanium alloys by alloy design. Journal of Materials Science, 2012. **47**(9): p. 4093-4100.

48. Naseri, R., et al., Effect of strain on microstructural development during uniaxial compression of metastable beta Ti–10V–2Fe–3Al alloy. Materials Science and Engineering: A, 2021. **804**.

49. Ebrahimi, R. and A. Najafizadeh, A new method for evaluation of friction in bulk metal forming. Journal of Materials Processing Technology, 2004. **152**(2): p. 136-143.

50. Kolli, R.P. and A. Devaraj, A review of metastable beta titanium alloys. Metals (Basel), 2018. **8**(7): p. 506.

51. Polmear, I., et al., Light Alloys : Metallurgy of the Light Metals. Light Alloys: Metallurgy of the Light Metals, ed. L.A.M.o.t.L. Metals. 2017, Oxford, UNITED KINGDOM: Elsevier Science & Technology.

52. Dieter, G.E. and D.J. Bacon, Mechanical metallurgy. SI metric ed. / adapted by David Bacon. ed. McGraw-Hill series in materials science and engineering. 1988, London ;: McGraw-Hill.

53. G. Lutjering *, J.C.W.a.A.G., MICROSTRUCTURE AND MECHANICAL PROPERTIES OF TITANIUM ALLOYS. 1988.

54. Barriobero-Vila, P., et al., Phase transformation kinetics during continuous heating of a β-quenched Ti–10V–2Fe–3Al alloy. Journal of Materials Science, 2015. **50**(3): p. 1412-1426.

55. Burgers, W., On the process of transition of the cubic-body-centered modification into the hexagonal-close-packed modification of zirconium. Physica, 1934. **1**(7-12): p. 561-586.

56. Yumak, N. and K. Aslantaş, A review on heat treatment efficiency in metastable β titanium alloys: the role of treatment process and parameters. Journal of Materials Research and Technology, 2020.

57. Xu, W., et al., Mechanical properties, in vitro corrosion resistance and biocompatibility of metal injection molded Ti-12Mo alloy for dental applications. Journal of the mechanical behavior of biomedical materials, 2018. **88**: p. 534-547.

58. Ho, W.-F., A comparison of tensile properties and corrosion behavior of cast Ti–7.5 Mo with cp Ti, Ti–15Mo and Ti–6Al–4V alloys. Journal of Alloys and Compounds, 2008. **464**(1-2): p. 580-583.

59. Zhang, L., et al., Manufacture by selective laser melting and mechanical behavior of a biomedical Ti–24Nb–4Zr–8Sn alloy. Scripta Materialia, 2011. **65**(1): p. 21-24.

60. Yadroitsev, I., P. Krakhmalev, and I. Yadroitsava, Titanium Alloys Manufactured by In Situ Alloying During Laser Powder Bed Fusion. JOM (1989), 2017. **69**(12): p. 2725-2730.

61. Bhardwaj, T., et al., Direct Energy Deposition - Laser Additive Manufacturing of Titanium-Molybdenum alloy: Parametric studies, microstructure and mechanical properties. Journal of Alloys and Compounds, 2019. **787**: p. 1238-1248.

62. Donachie, M.J., Titanium: a technical guide. 2000: ASM international.

63. Ankem, S. and C.A. Greene, Recent developments in microstructure/property relationships of beta titanium alloys. Materials Science and Engineering: A, 1999. **263**(2): p. 127-131.

64. Bania, P.J., Beta Titan. Alloys Role Titan. Ind., 1993: p. 3-14.

65. Hansen, M., Institute of metals division-systems titanium–molybdenum and titanium–columbium. Trans. AIME, 1951. **191**: p. 882-889.

66. Welsch, G., R. Boyer, and E. Collings, Materials properties handbook: titanium alloys. 1993: ASM international.

67. Ankem, S. and S. Seagle, Heat Treatment of Metastable Beta Titanium Alloys. Beta Titanium Alloys in the 1980's, 1983: p. 107-126.

68. Devaraj, A., Phase separation and second phase precipitation in beta titanium alloys. 2011.

69. Banerjee, S., R. Tewari, and G. Dey, Omega phase transformation–morphologies and mechanisms: dedicated to Professor Dr. Knut Urban on the occasion of his 65th birthday. Zeitschrift für Metallkunde, 2006. **97**(7): p. 963-977.

70. De Fontaine, D., N. Paton, and J. Williams, The omega phase transformation in titanium alloys as an example of displacement controlled reactions. Acta Metallurgica, 1971. **19**(11): p. 1153-1162.

71. Lyasotskaya, V.S. and S.I. Knyazeva, Metastable phases in titanium alloys and conditions of their formation. Metal science and heat treatment, 2008. **50**(7): p. 373-377.

72. Nag, S., et al., Novel mixed-mode phase transition involving a composition-dependent displacive component. Physical review letters, 2011. **106**(24): p. 245701.

73. Devaraj, A., et al., Experimental evidence of concurrent compositional and structural instabilities leading to ω precipitation in titanium–molybdenum alloys. Acta Materialia, 2012. **60**(2): p. 596-609.

74. Devaraj, A., et al., Three-dimensional morphology and composition of omega precipitates in a binary titanium–molybdenum alloy. Scripta Materialia, 2009. **61**(7): p. 701-704.

75. Wang, C.H., et al., Martensitic microstructures and mechanical properties of as-quenched metastable β-type Ti–Mo alloys. Journal of materials science, 2016. **51**(14): p. 6886-6896.

76. Ho, W.F., C.P. Ju, and J.H. Chern Lin, Structure and properties of cast binary Ti–Mo alloys. Biomaterials, 1999. **20**(22): p. 2115-2122.

77. Sun, F., et al., β phase transformation kinetics in Ti60 alloy during continuous cooling. Journal of alloys and compounds, 2013. **576**: p. 108-113.

78. Fellah, M., et al., Effect of Molybdenum content on structural, mechanical, and tribological properties of hot isostatically pressed β-type titanium alloys for orthopedic applications. Journal of Materials Engineering and Performance, 2019. **28**(10): p. 5988-5999.

79. Zhang, W.-d., et al., Elastic modulus of phases in Ti–Mo alloys. Materials Characterization, 2015. **106**: p. 302-307.

80. Sabeena, M., et al., Microstructural characterization of transformation products of bcc β in Ti-15 Mo alloy. Journal of Alloys and Compounds, 2016. **658**: p. 301-315.

81. D'yakonova, N., I. Lyasotskii, and Y.L. Rodionov, Orthorhombic martensite and the ω phase in quenched and deformed titanium alloys with 20–24 at% Nb. Russian Metallurgy (Metally), 2007. **2007**(1): p. 51-58.

82. Ji, X., et al., Effect of oxygen addition on microstructures and mechanical properties of Ti-7.5Mo alloy. Journal of alloys and compounds, 2018. **737**: p. 221-229.

83. Sakaguchi, N., et al., Relationships between tensile deformation behavior and microstructure in Ti–Nb–Ta–Zr system alloys. Materials Science and Engineering: C, 2005. **25**(3): p. 363-369.

84. Geetha, M., et al., Effect of thermomechanical processing on evolution of various phases in Ti–Nb–Zr alloys. Journal of Alloys and Compounds, 2004. **384**(1): p. 131-144.

85. Dubinskiy, S., et al., In situ X-ray diffraction study of athermal and isothermal omega-phase crystal lattice in Ti-Nb-based shape memory alloys. Materials Letters, 2016. **168**: p. 155-157.

86. Sauer, C. and G. Luetjering, Thermo-mechanical processing of high strength β-titanium alloys and effects on microstructure and properties. Journal of materials processing technology, 2001. **117**(3): p. 311-317.

87. Weiss, I. and S. Semiatin, Thermomechanical processing of beta titanium alloys—an overview. Materials Science and Engineering: A, 1998. **243**(1-2): p. 46-65.

88. Fang, Z.Z., et al., Powder metallurgy of titanium–past, present, and future. International Materials Reviews, 2018. **63**(7): p. 407-459.

89. Ahmed, M., Effect of Thermo-mechanical Processing, Ageing and Compression on Microstructure and Mechanical Properties of near β Ti Alloys Made from Powder. School of Mechanical, Materials and Mechatronic Engineering.

90. Banerjee, D. and J.C. Williams, Perspectives on Titanium Science and Technology. Acta Materialia, 2013. **61**(3): p. 844-879.

91. Williams, R.E.A., Development and Application of Advanced Electron Microscopy Characterization Techniques to Binary Titanium–Molybedenum Alloys. 2010, The Ohio State University.

92. Cheng, G., et al., Deformation-induced ω phase in nanocrystalline Mo. Scripta Materialia, 2013. **68**(2): p. 130-133.

93. Hsiung, L. and D. Lassila, Shock-induced deformation twinning and omega transformation in tantalum and tantalum–tungsten alloys. Acta materialia, 2000. **48**(20): p. 4851-4865.

94. Lai, M.J., et al., Origin of shear induced β to ω transition in Ti–Nb-based alloys. Acta Materialia, 2015. **92**: p. 55-63.

95. Williams, J., B. Hickman, and H. Marcus, The effect of omega phase on the mechanical properties of titanium alloys. Metallurgical transactions, 1971. **2**(7): p. 1913-1919.

96. Horiuchi, T., et al., In-situ High Resolution Electron Microscope Observation of ω-Phase Precipitation in β-Type Titanium Alloys. Materials transactions. JIM, 1995. **36**(12): p. 1455-1462.

97. Sikka, S.K., Y.K. Vohra, and R. Chidambaram, Omega phase in materials. Progress in Materials Science, 1982. **27**(3): p. 245-310.

98. Wang, X.L., et al., Role of oxygen in stress-induced ω phase transformation and {3 3 2}〈1 1 3〉 mechanical twinning in βTi–20V alloy. Scripta Materialia, 2015. **96**: p. 37-40.

99. Silcock, J., An X-ray examination of the to phase in TiV, TiMo and TiCr alloys. Acta Metallurgica, 1958. **6**(7): p. 481-493.

100. Qazi, J., et al., Phase transformations in Ti–35Nb–7Zr–5Ta–(0.06–0.68) O alloys. Materials Science and Engineering: C, 2005. **25**(3): p. 389-397.

101. MIN, X., et al., Effect of {332} Twins Combined with Isothermal ω-Phase on Mechanical Properties in Ti-15Mo Alloy with Different Oxygen Contents. Acta Metall Sin, 2018. **54**(9): p. 1262-1272.

102. Samiee, A., et al., The effect of continuous heating on microstructure development in thermo-mechanically processed Ti-10V-3Fe-3Al alloy produced by powder metallurgy. Materials Characterization, 2020. **161**: p. 110172.

103. Jackson, M., et al., Effect of initial microstructure on plastic flow behaviour during isothermal forging of Ti–10V–2Fe–3Al. Materials Science and Engineering: A, 2009. **501**(1-2): p. 248-254.

104. Giannuzzi, L., et al., Focused ion beam milling and micromanipulation lift-out for site specific cross-section TEM specimen preparation. MRS Online Proceedings Library (OPL), 1997. **480**.

105. Blackburn, M. and J. Williams, PHASE TRANSFORMATIONS IN Ti--Mo AND Ti--V ALLOYS. 1968, Boeing Scientific Research Labs., Seattle.

106. Hanada, S. and O. Izumi, Transmission electron microscopic observations of mechanical twinning in metastable beta titanium alloys. Metallurgical Transactions A, 1986. **17**(8): p. 1409-1420.

107. Hanada, S. and O. Izumi, Correlation of tensile properties, deformation modes, and phase stability in commercial β-phase titanium alloys. Metallurgical and Materials Transactions A, 1987. **18**(2): p. 265-271.

108. Santhosh, R., M. Geetha, and M.N. Rao, Recent developments in heat treatment of beta titanium alloys for aerospace applications. Transactions of the Indian Institute of Metals, 2017. **70**(7): p. 1681-1688.

109. Ahmed, M., et al., The effect of cooling rates on the microstructure and mechanical properties of thermo-mechanically processed Ti–Al–Mo–V–Cr–Fe alloys. Materials Science and Engineering: A, 2013. **576**: p. 167-177.

110. Nag, S., et al., ω-Assisted nucleation and growth of α precipitates in the Ti–5Al–5Mo–5V–3Cr–0.5 Fe β titanium alloy. Acta Materialia, 2009. **57**(7): p. 2136-2147.

111. Ohmori, Y., et al., Effects of ω-phase precipitation on β→ α, α″ transformations in a metastable β titanium alloy. Materials Science and Engineering: A, 2001. **312**(1-2): p. 182-188.

112. Li, T., et al., The role of ω in the precipitation of α in near-β Ti alloys. Scripta Materialia, 2016. **117**: p. 92-95.

113. Zheng, Y., et al., Role of ω phase in the formation of extremely refined intragranular α precipitates in metastable β-titanium alloys. Acta Materialia, 2016. **103**: p. 850-858.

114. Zhang, X., et al., Evolution of the secondary α phase morphologies during isothermal heat treatment in Ti-7333 alloy. Journal of alloys and compounds, 2013. **577**: p. 516-522.

115. Boyer, R. and G. Kuhlman, Processing properties relationships of Ti-10V-2Fe-3Al. Metallurgical Transactions A, 1987. **18**(12): p. 2095-2103.

116. Furuhara, T. and T. Maki, Variant selection in heterogeneous nucleation on defects in diffusional phase transformation and precipitation. Materials Science and Engineering: A, 2001. **312**(1-2): p. 145-154.

117. Furuhara, T., et al., Crystallography of grain boundary α precipitates in a β titanium alloy. Metallurgical and Materials Transactions A, 1996. **27**(6): p. 1635-1646.

118. Devaraj, A., Phase separation and second phase precipitation in beta titanium alloys. 2011: University of North Texas.

119. Costa, F.H.d., et al., Alpha phase precipitation in Ti-30Nb-1Fe alloys – phase transformations in continuous heating and aging heat treatments. Materials Science and Engineering A, Structural Materials: Properties, Microstructure and Processing, 2016: p. 222-229.

120. Li, T., et al., The mechanism of ω-assisted α phase formation in near β-Ti alloys. Scripta Materialia, 2015. **104**: p. 75-78.

121. Ivasishin, O., et al., Precipitation and recrystallization behavior of beta titanium alloys during continuous heat treatment. Metallurgical and Materials Transactions A, 2003. **34**(1): p. 147-158.

122. Zheng, Y., et al., Role of ω phase in the formation of extremely refined intragranular α precipitates in metastable β-titanium alloys. Acta Materialia, 2016. **103**: p. 850-858.

123. Ahmed, M., et al., The evolution of microstructure and mechanical properties of Ti–5Al–5Mo–5V–2Cr–1Fe during ageing. Journal of Alloys and Compounds, 2015. **629**: p. 260-273.

124. Prima, F., et al., Evidence of α-nanophase heterogeneous nucleation from ω particles in a β-metastable Ti-based alloy by high-resolution electron microscopy. Scripta materialia, 2006. **54**(4): p. 645-648.

125. Azimzadeh, S. and H. Rack, Phase transformations in Ti-6.8 Mo-4.5 Fe-1.5 Al. Metallurgical and materials transactions A, 1998. **29**(10): p. 2455-2467.

126. Salib, M., et al., Influence of transformation temperature on microtexture formation associated with α precipitation at β grain boundaries in a β metastable titanium alloy. Acta materialia, 2013. **61**(10): p. 3758-3768.

127. Xu, J., et al., Analysis of crystallographic orientation and morphology of microstructure during hot working for an alpha/beta titanium alloy. Journal of Materials Science & Technology, 2020. **59**: p. 1-13.

128. G. Lutjering *, J.C.W.a.A.G. MICROSTRUCTURE AND MECHANICAL PROPERTIES OF TITANIUM ALLOYS. 1988.

129. Ren, Y., et al., Mechanical response and effects of β-to-α" phase transformation on the strengthening of Ti–10 V–2 Fe–3 Al during one-dimensional shock loading. Materials Science and Engineering: A, 2013. **562**: p. 137-143.

130. Du, Z., et al., Effect of heat treatment on microstructure and mechanical properties of a new β high strength titanium alloy. Materials & Design, 2014. **55**: p. 183-190.

131. Karasevskaya, O., et al., Deformation behavior of beta-titanium alloys. Materials Science and Engineering: A, 2003. **354**(1-2): p. 121-132.

132. Mantri, S.A., et al., Deformation Induced Hierarchical Twinning Coupled with Omega Transformation in a Metastable beta-Ti Alloy. Sci Rep, 2019. **9**(1): p. 1334.

133. Duan, R., et al., A high strength and low modulus metastable β Ti-12Mo-6Zr-2Fe alloy fabricated by laser powder bed fusion in-situ alloying. Additive Manufacturing, 2021. **37**: p. 101708.

134. Chai, Y., et al., Self-accommodation in Ti–Nb shape memory alloys. Acta Materialia, 2009. **57**(14): p. 4054-4064.

135. Herrera, C., D. Ponge, and D. Raabe, Design of a novel Mn-based 1GPa duplex stainless TRIP steel with 60% ductility by a reduction of austenite stability. Acta Materialia, 2011. **59**(11): p. 4653-4664.

136. Davis, R., H. Flower, and D. West, Martensitic transformations in Ti-Mo alloys. Journal of Materials Science, 1979. **14**(3): p. 712-722.

137. Bania, P.J., Beta titanium alloys and their role in the titanium industry. Beta Titanium Alloys in the 1990's, 1998: p. 3-14.

138. Bagariatskii, I.A., G. Nosova, and T. Tagunova. Factors in the formation of metastable phases in titanium-base alloys. in Soviet Physics Doklady. 1958.
139. Yannetta, C.J., Additive Manufacturing of Metastable Beta Titanium Alloys. 2017. p. 4.
140. Kruth, J.-P., et al., Lasers and materials in selective laser sintering. Assembly Automation, 2003.
141. Vandenbroucke, B. and J.-P. Kruth, Selective laser melting of biocompatible metals for rapid manufacturing of medical parts. Rapid Prototyping Journal, 2007. **13**: p. 196-203.
142. Sarker, A., Development of Additively Manufactured Titanium Based (Ti6Al4V) Implants with Different Inclination Angle and its Implications on Bio-interface for Orthopaedic Applications. 2019, RMIT University Melbourne, Australia.
143. Peters, M., et al., Structure and properties of titanium and titanium alloys. Titanium and titanium alloys: fundamentals and applications, 2003: p. 1-36.
144. Gibson, I., et al., Additive manufacturing technologies. Vol. 17. 2014: Springer.
145. Zhang, D., et al., Grain Refinement of Alloys in Fusion-Based Additive Manufacturing Processes. Metallurgical and Materials Transactions A, 2020. **51**(9): p. 4341-4359.
146. Mahamood, R.M., Laser metal deposition process of metals, alloys, and composite materials. 2018: Springer.
147. Xu, W., et al., Additive manufacturing of strong and ductile Ti–6Al–4V by selective laser melting via in situ martensite decomposition. Acta Materialia, 2015. **85**: p. 74-84.
148. Todaro, C.J., et al., Grain structure control during metal 3D printing by high-intensity ultrasound. Nature Communications, 2020. **11**(1): p. 142.
149. Murr, L.E., et al., Microstructure and mechanical behavior of Ti-6Al-4V produced by rapid-layer manufacturing, for biomedical applications. J Mech Behav Biomed Mater, 2009. **2**(1): p. 20-32.

150. Liu, Y.J., et al., Microstructure, defects and mechanical behavior of beta-type titanium porous structures manufactured by electron beam melting and selective laser melting. Acta Materialia, 2016. **113**: p. 56-67.

151. Gu, D.D., et al., Laser additive manufacturing of metallic components: materials, processes and mechanisms. International Materials Reviews, 2012. **57**(3): p. 133-164.

152. Mines, R., Additive Manufacturing Processes and Materials for Metallic Microlattice Structures Using Selective Laser Melting, Electron Beam Melting and Binder Jetting, in Metallic Microlattice Structures. 2019, Springer. p. 17-31.

153. Li, Y. and D. Gu, Thermal behavior during selective laser melting of commercially pure titanium powder: Numerical simulation and experimental study. Additive Manufacturing, 2014. **1**: p. 99-109.

154. Gupta, N., C. Weber, and S. Newsome, Additive manufacturing: status and opportunities. Science and Technology Policy Institute, Washington, 2012.

155. Mahamood, R.M., et al., Functionally graded material: an overview. 2012.

156. Hofmeister, W., et al., Investigating solidification with the laser-engineered net shaping (LENSTM) process. Jom, 1999. **51**(7): p. 1-6.

157. Kelly, S. and S. Kampe, Microstructural evolution in laser-deposited multilayer Ti-6Al-4V builds: Part I. Microstructural characterization. Metallurgical and Materials Transactions A, 2004. **35**: p. 1861-1867.

158. Choi, J. and J. Mazumder. Rapid manufacturing by laser aided direct metal deposition process: issues and examples. in International Design Engineering Technical Conferences and Computers and Information in Engineering Conference. 2001. American Society of Mechanical Engineers.

159. Tang, L., et al., Variable powder flow rate control in laser metal deposition processes. Journal of manufacturing science and engineering, 2008. **130**(4).

160. Li, S., et al., Influence of cell shape on mechanical properties of Ti–6Al–4V meshes fabricated by electron beam melting method. Acta biomaterialia, 2014. **10**(10): p. 4537-4547.

161. Knapp, G.L., et al., Experiments and simulations on solidification microstructure for Inconel 718 in powder bed fusion electron beam additive manufacturing. Additive Manufacturing, 2019. **25**: p. 511-521.

162. Zhang, L.C., et al., Additive manufacturing of titanium alloys by electron beam melting: a review. Advanced Engineering Materials, 2018. **20**(5): p. 1700842.

163. Gaytan, S.M., et al., Advanced metal powder based manufacturing of complex components by electron beam melting. Materials Technology, 2009. **24**(3): p. 180-190.

164. Liu, Y., et al., Investigation into spatter behavior during selective laser melting of AISI 316L stainless steel powder. Materials & Design, 2015. **87**: p. 797-806.

165. Liu, Y.J., et al., Processing and properties of topologically optimised biomedical Ti–24Nb–4Zr–8Sn scaffolds manufactured by selective laser melting. Materials Science and Engineering: A, 2015. **642**: p. 268-278.

166. Taheri Andani, M., et al., Spatter formation in selective laser melting process using multi-laser technology. Materials & Design, 2017. **131**: p. 460-469.

167. Sing, S.L., W.Y. Yeong, and F.E. Wiria, Selective laser melting of titanium alloy with 50 wt% tantalum: Microstructure and mechanical properties. Journal of Alloys and Compounds, 2016. **660**: p. 461-470.

168. Kempen, K., et al. Process optimization and microstructural analysis for selective laser melting of AlSi10Mg. in Solid Freeform Fabrication Symposium. 2011.

169. Simonelli, M., Y.Y. Tse, and C. Tuck, On the Texture Formation of Selective Laser Melted Ti-6Al-4V. Metallurgical and Materials Transactions A, 2014. **45**(6): p. 2863-2872.

170. Sing, S.L., F.E. Wiria, and W.Y. Yeong, Selective laser melting of titanium alloy with 50 wt% tantalum: Effect of laser process parameters on part quality. International Journal of Refractory Metals and Hard Materials, 2018. **77**: p. 120-127.

171. Sidambe, A.T., Biocompatibility of advanced manufactured titanium implants—A review. Materials, 2014. **7**(12): p. 8168-8188.

172. Asgharzadeh, H. and A. Simchi, Effect of sintering atmosphere and carbon content on the densification and microstructure of laser-sintered M2 high-speed steel powder. Materials Science and Engineering: A, 2005. **403**(1-2): p. 290-298.

173. Santos, E.C., et al., Rapid manufacturing of metal components by laser forming. International Journal of Machine Tools and Manufacture, 2006. **46**(12-13): p. 1459-1468.

174. Ren, Y., et al., Microstructure and deformation behavior of Ti-6Al-4V alloy by high-power laser solid forming. Acta Materialia, 2017. **132**: p. 82-95.

175. Gäumann, M., et al., Single-crystal laser deposition of superalloys: processing–microstructure maps. Acta Materialia, 2001. **49**(6): p. 1051-1062.

176. Porter, D.A. and K.E. Easterling, Phase transformations in metals and alloys (revised reprint). 2009: CRC press.

177. Ahmed, T. and H.J. Rack, Phase transformations during cooling in α+β titanium alloys. Materials Science and Engineering: A, 1998. **243**(1): p. 206-211.

178. Kobryn, P.A. and S.L. Semiatin, Microstructure and texture evolution during solidification processing of Ti–6Al–4V. Journal of Materials Processing Technology, 2003. **135**(2): p. 330-339.

179. Mebed, A.M. and T. Miyazaki, Computer simulation and experimental investigation of the spinodal decomposition in the β Ti-Cr binary alloy system. Metallurgical and materials transactions. A, Physical metallurgy and materials science, 1998. **29**(3): p. 739-749.

180. Nag, S., et al., Non-classical homogeneous precipitation mediated by compositional fluctuations in titanium alloys. Acta Materialia, 2012. **60**(18): p. 6247-6256.

181. Boyne, A., et al., Pseudospinodal mechanism for fine α/β microstructures in β-Ti alloys. Acta materialia, 2014. **64**: p. 188-197.

182. Davis, R., H. Flower, and D. West, The decomposition of Ti-Mo alloy martensites by nucleation and growth and spinodal mechanisms. Acta Metallurgica, 1979. **27**(6): p. 1041-1052.

183. Chen, Y.-C., J.-H.C. Lin, and C.-P. Ju, Effects of post-aging cooling condition on structure and tensile properties of aged Ti–7.5Mo alloy. Materials & Design (1980-2015), 2014. **54**: p. 515-519.

184. Chung, C.-C., et al., Effect of cold rolling on structure and tensile properties of cast Ti–7.5Mo alloy. Materials Science and Engineering: A, 2015. **631**: p. 52-66.

185. Kang, N., et al., Microstructure and tensile properties of Ti-Mo alloys manufactured via using laser powder bed fusion. Journal of alloys and compounds, 2019. **771**: p. 877-884.

186. Collings, E., The metal physics of titanium alloys. Titanium'80, Science and Technology, 1980. **1**: p. 77-132.

187. Long, M. and H.J. Rack, Titanium alloys in total joint replacement—a materials science perspective. Biomaterials, 1998. **19**(18): p. 1621-1639.

188. Geetha, M., et al., Ti based biomaterials, the ultimate choice for orthopaedic implants – A review. Progress in Materials Science, 2009. **54**(3): p. 397-425.

189. Niinomi, M., Mechanical properties of biomedical titanium alloys. Materials Science and Engineering: A, 1998. **243**(1): p. 231-236.

190. Abdel-Hady, M., K. Hinoshita, and M. Morinaga, General approach to phase stability and elastic properties of β-type Ti-alloys using electronic parameters. Scripta materialia, 2006. **55**(5): p. 477-480.

191. Tane, M., et al., Elastic-modulus enhancement during room-temperature aging and its suppression in metastable Ti–Nb-Based alloys with low body-centered cubic phase stability. Acta Materialia, 2016. **102**: p. 373-384.

192. Kolli, R.P., W.J. Joost, and S. Ankem, Phase stability and stress-induced transformations in beta titanium alloys. Jom, 2015. **67**(6): p. 1273-1280.

193. Grosdidier, T. and M.-J. Philippe, Deformation induced martensite and superelasticity in a β-metastable titanium alloy. Materials Science and Engineering: A, 2000. **291**(1-2): p. 218-223.

194. Min, X., et al., Heterogeneous twin formation and its effect on tensile properties in Ti–Mo based β titanium alloys. Materials Science and Engineering: A, 2012. **554**: p. 53-60.

195. Schmid, E. and W. Boas, Kristallelastizität, in Kristallplastizität. 1935, Springer. p. 15-24.

196. Li, C., et al., Influence of α morphology and volume fraction on the stress-induced martensitic transformation in Ti–10V–2Fe–3Al. Materials Science and Engineering: A, 2011. **528**(18): p. 5854-5860.

197. Wang, X.L., et al., Dependence of stress-induced omega transition and mechanical twinning on phase stability in metastable β Ti–V alloys. Materials Characterization, 2015. **107**: p. 149-155.

198. Furuta, T., et al., Elastic deformation behavior of multi-functional Ti–Nb–Ta–Zr–O alloys. Materials transactions, 2005. **46**(12): p. 3001-3007.

199. Blackburn, M.J. and J.A. Feeney, Stress-induced transformations in Ti-Mo alloys. 1970, BOEING CO RENTON WA COMMERCIAL AIRPLANE GROUP.

200. Min, X., et al., Effect of oxygen content on deformation mode and corrosion behavior in β-type Ti-Mo alloy. Materials Science and Engineering: A, 2017. **684**: p. 534-541.

201. Rusakov, G., A. Litvinov, and V. Litvinov, Deformation twinning of titanium β-alloys of transition class. Metal science and heat treatment, 2006. **48**(5): p. 244-251.

202. Kawabata, T., S. Kawasaki, and O. Izumi, Mechanical properties of TiNbTa single crystals at cryogenic temperatures. Acta materialia, 1998. **46**(8): p. 2705-2715.

203. Crocker, A., Twinned martensite. Acta Metallurgica, 1962. **10**(2): p. 113-122.

204. Tobe, H., et al., Origin of {3 3 2} twinning in metastable β-Ti alloys. Acta materialia, 2014. **64**: p. 345-355.

205. Bertrand, E., et al., Twinning system selection in a metastable β-titanium alloy by Schmid factor analysis. Scripta Materialia, 2011. **64**(12): p. 1110-1113.

206. Furuhara, T., K. Kishimoto, and T. Maki, Transmission Electron Microscopy of {332}⟨ 113⟩ Deformation Twin in Ti–15V–3Cr–3Sn–3Al Alloy. Materials Transactions, JIM, 1994. **35**(12): p. 843-850.

207. Castany, P., et al., Reversion of a Parent {130}⟨ 310⟩ α″ Martensitic Twinning System at the Origin of {332}⟨ 113⟩ β Twins Observed in Metastable β Titanium Alloys. Physical review letters, 2016. **117**(24): p. 245501.

208. Dini, G., et al., Flow stress analysis of TWIP steel via the XRD measurement of dislocation density. Materials Science and Engineering: A, 2010. **527**(10): p. 2759-2763.

209. Allain, S., J.P. Chateau, and O. Bouaziz, A physical model of the twinning-induced plasticity effect in a high manganese austenitic steel. Materials Science and Engineering: A, 2004. **387-389**: p. 143-147.

210. Ojima, M., et al., Work hardening mechanism in high nitrogen austenitic steel studied by in situ neutron diffraction and in situ electron backscattering diffraction. Materials Science and Engineering: A, 2009. **527**(1): p. 16-24.

211. Min, X.H., et al., {332}〈113〉 Twinning system selection in a β-type Ti–15Mo–5Zr polycrystalline alloy. Materials Science and Engineering: A, 2013. **579**: p. 164-169.

212. Naseri, R., et al., The effect of β-phase condition on the tensile behaviour in a near-β Ti alloy produced by blended elemental powder metallurgy. Materials Science and Engineering: A, 2019. **747**: p. 232-243.

213. Mantri, S.A., et al., Change in the deformation mode resulting from beta-omega compositional partitioning in a Ti[sbnd]Mo alloy: Room versus elevated temperature. Scripta materialia, 2017. **130**: p. 69-73.

214. Ahmed, T. and H. Rack, Martensitic transformations in Ti-(16–26 at%) Nb alloys. Journal of materials science, 1996. **31**(16): p. 4267-4276.

215. Jeong, H., et al., Elastic softening behavior of Ti–Nb single crystal near martensitic transformation temperature. Journal of Applied Physics, 2010. **108**(6): p. 063515.

216. Niessen, F., E.V. Pereloma, and A.A. Saleh, Predicting the available work from deformation-induced α″ martensite formation in metastable β Ti alloys. Journal of Applied Crystallography, 2020. **53**(4).

217. Min, X., et al., Transition of multi-deformation modes in Ti–10Mo alloy with oxygen addition. Materials Science and Engineering: A, 2014. **590**: p. 88-96.

218. Martins, J.J.R.S., et al., Influence of Oxygen Content and Microstructure on the Mechanical Properties and Biocompatibility of Ti-15 wt%Mo Alloy Used for Biomedical Applications. Materials, 2014. **7**(1): p. 232-243.

219. Júnior, J.R.S.M., et al., Diffusion of oxygen and nitrogen in the Ti-15Mo alloy used for biomedical applications. Defect and Diffusion Forum, 2012. **326-328**: p. 696-701.

220. Severino Martins Jr, J.R. and C.R. Grandini, Structural characterization of Ti-15Mo alloy used as biomaterial by Rietveld method. Journal of Applied Physics, 2012. **111**(8): p. 083535.

221. Martins Júnior, J.R.S., et al., Preparation and characterization of Ti-15Mo alloy used as biomaterial. Materials Research, 2011. **14**(1): p. 107-112.

222. Williams, J., D. De Fontaine, and N. Paton, The ω-phase as an example of an unusual shear transformation. Metallurgical Transactions, 1973. **4**(12): p. 2701-2708.

223. Liu, H., et al., Mechanical properties and cytocompatibility of oxygen-modified β-type Ti–Cr alloys for spinal fixation devices. Acta biomaterialia, 2015. **12**: p. 352-361.

224. Niu, J., et al., Suppression effect of oxygen on the β to ω transformation in a β-type Ti alloy: insights from first-principles. Modelling and Simulation in Materials Science and Engineering, 2013. **22**(1): p. 015007.

225. Geng, F., M. Niinomi, and M. Nakai, Observation of yielding and strain hardening in a titanium alloy having high oxygen content. Materials Science and Engineering: A, 2011. **528**(16-17): p. 5435-5445.

226. Kim, J.I., et al., Shape memory behavior of Ti–22Nb–(0.5–2.0) O (at%) biomedical alloys. Materials transactions, 2005. **46**(4): p. 852-857.

227. Tahara, M., et al., Lattice modulation and superelasticity in oxygen-added β-Ti alloys. Acta materialia, 2011. **59**(16): p. 6208-6218.

228. Nii, Y., et al., Effect of randomness on ferroelastic transitions: Disorder-induced hysteresis loop rounding in Ti-Nb-O martensitic alloy. Physical Review B, 2010. **82**(21): p. 214104.

229. Duan, H.-p., et al., Effect of oxygen on the microstructure and mechanical properties of Ti-23Nb-0.7 Ta-2Zr alloy. International Journal of Minerals, Metallurgy, and Materials, 2012. **19**(12): p. 1128-1133.

230. Zhang, L.C., et al., Nucleation of stress-induced martensites in a Ti/Mo-based alloy. Journal of Materials Science, 2005. **40**(11): p. 2833-2836.

231. Paladugu, M., et al., Strengthening of cast Ti–25Nb–3Mo–3Zr–2Sn alloy through precipitation of α in two discrete crystallographic orientations. Materials Science and Engineering: A, 2010. **527**(24): p. 6601-6606.

232. Nishiyama, Z., Martensitic transformation. 2012: Elsevier.

233. Min, X.H., et al., Enhancement of uniform elongation in high strength Ti–Mo based alloys by combination of deformation modes. Materials Science and Engineering: A, 2011. **528**(13): p. 4569-4578.

234. Min, X.H., et al., Microstructure, tensile deformation mode and crevice corrosion resistance in Ti–10Mo–xFe alloys. Materials Science and Engineering: A, 2010. **527**(21): p. 5499-5506.

235. Wang, C., et al., Martensitic microstructures and mechanical properties of as-quenched metastable β-type Ti–Mo alloys. Journal of Materials Science, 2016. **51**(14): p. 6886-6896.

236. Mantani, Y., et al., Phase transformation of α ″martensite structure by aging in Ti-8 mass% Mo Alloy. Materials Transactions, 2004. **45**(5): p. 1629-1634.

237. Takemoto, Y., et al., Tensile behavior and cold workability of Ti-Mo alloys. Materials transactions, 2004. **45**(5): p. 1571-1576.

238. Chai, Y.W., et al., Interfacial defects in Ti–Nb shape memory alloys. Acta Materialia, 2008. **56**(13): p. 3088-3097.

239. Kim, H.Y. and S. Miyazaki, Martensitic transformation and superelastic properties of Ti-Nb base alloys. Materials Transactions, 2015. **56**(5): p. 625-634.

240. Bywater, K.A. and J.W. Christian, Martensitic transformations in titanium-tantalum alloys. The Philosophical Magazine: A Journal of Theoretical Experimental and Applied Physics, 1972. **25**(6): p. 1249-1273.

241. Yan, J.-Y. and G.B. Olson, Computational thermodynamics and kinetics of displacive transformations in titanium-based alloys. Journal of Alloys and Compounds, 2016. **673**: p. 441-454.

242. Ghosh, G. and G.B. Olson, Kinetics of F.C.C. → B.C.C. heterogeneous martensitic nucleation—I. The critical driving force for athermal nucleation. Acta Metallurgica et Materialia, 1994. **42**(10): p. 3361-3370.

243. Ghosh, G. and G.B. Olson, Kinetics of F.c.c. → b.c.c. heterogeneous martensitic nucleation—II. Thermal activation. Acta Metallurgica et Materialia, 1994. **42**(10): p. 3371-3379.

244. Murakami, Y. and D. Shindo, Lattice modulation preceding to the R-phase transformation in a Ti50Ni48Fe2 alloy studied by TEM with energy-filtering. Materials Transactions, JIM, 1999. **40**(10): p. 1092-1097.

245. Wang, D., et al., Strain glass in Fe-doped Ti–Ni. Acta materialia, 2010. **58**(18): p. 6206-6215.

246. Zhang, Z., et al., Phase diagram of Ti 50− x Ni 50+ x: Crossover from martensite to strain glass. Physical Review B, 2010. **81**(22): p. 224102.

247. Obbard, E., et al., The effect of oxygen on α ″martensite and superelasticity in Ti–24Nb–4Zr–8Sn. Acta Materialia, 2011. **59**(1): p. 112-125.

248. Sakamoto, H., Distinction between Thermal and Stress-Induced Martensitic Transformations and Inhomogeneity in Internal Stress. MATERIALS TRANSACTIONS, 2002. **43**(9): p. 2249-2255.

249. Kim, H.Y., et al., Martensitic transformation, shape memory effect and superelasticity of Ti–Nb binary alloys. Acta Materialia, 2006. **54**(9): p. 2419-2429.

250. Demakov, S., I. Semkina, and A. Yurovskikh, Parameters Evolution of Orthorhombic Martensite Lattice Ti-Mo-Al Alloys Studied by in Situ T-XRD. IOP conference series. Materials Science and Engineering, 2018. **301**(1): p. 12003.

251. Gil, F.J., C. Aparicio, and J.A. Planell, Effect of oxygen content on grain growth kinetics of titanium. J. Mater., 2003. **10**: p. 10-13.

252. Bolzoni, L., E.M. Ruiz-Navas, and E. Gordo, Influence of vacuum hot-pressing temperature on the microstructure and mechanical properties of Ti–3Al–2.5V alloy obtained by blended elemental and master alloy addition powders. Materials Chemistry and Physics, 2012. **137**(2): p. 608-616.

253. ASTM. Standard Test Methods for Tension Testing of Metallic Materials. 1996-2022 [cited 2022 30/11]; Available from: https://www.astm.org/e0008_e0008m-22.html.

254. Struers. Struers Citopress-20. 2022 [cited 2022 30/11]; Available from: https://www.struers.com/en/Products/Mounting/Mounting-equipment/CitoPress.

255. M., G.K.F.D.K.W.-U.R.u.c., Metallographic and Materialographic Specimen Preparation Light Microscopy Image Analysis and Hardness Testing. Online-ausg ed. West Conshohocken Pa: ASTM International, 2007.

256. Struers. Struers Tegramin-21 2022 [cited 2022 30/11]; Available from: https://www.struers.com/en/Products/Grinding-and-Polishing/Grinding-and-polishing-equipment/Tegramin#.

257. Scientific, T. FEI Helios NanoLab G3 CX. 2022 [cited 2022 30/11]; Available from: https://www.thermofisher.com/au/en/home/electron-microscopy/products/dualbeam-fib-sem-microscopes/helios-5-dualbeam.html.

258. Niessen, F., crystalAligner: a computer program to align crystal directions in a scanning electron microscope by global optimization. Journal of Applied Crystallography, 2020. **53**(1): p. 282-293.

259. GBC. GBC MMA X ray diffractometer. 2022 [cited 2022 30/11]; Available from: https://gbcsci.com/xrd/.

260. Warren, B.E., X-ray Diffraction. 1990: Courier Corporation.

261. Australia, M. XRD basics. 2022 [cited 2022 1/12]; Available from: https://myscope.training/#/XRDlevel_2_1.

262. JEOL. JEOL. 2022 [cited 2022 30/11]; Available from: https://www.jeol.com/products/scientific/sem/.

263. Schneider, C.A., W.S. Rasband, and K.W. Eliceiri, NIH Image to ImageJ: 25 years of image analysis. Nature Methods, 2012. **9**(7): p. 671-675.

264. ISO 643:2019, S.-. Micrographic determination of the apparent grain size, 2019.

265. Australia, M. SEM Basics. 2022 [cited 2022 1/12]; Available from: https://myscope.training/#/SEMlevel_3_1.

266. Australia, M. EDS Theory. 2022 [cited 2022 1/12]; Available from: https://myscope.training/#/EDSlevel_2_1.

267. Wisniewski, W. and C. Rüssel, An experimental viewpoint on the information depth of EBSD. Scanning, 2016. **38**(2): p. 164-171.

268. International, A., Standard Terminology for Additive Manufacturing—General Principles—Terminology. 2015, ASTM International West Conshohocken, PA, USA.

269. Day, A. and P. TRIMBY, Channel 5 User Manual, HKL Technology A/S. 2001, Hobro, Denmark.

270. Beausir, J. and J. Fundenberger, Analysis Tools for Electron and X-ray Diffraction, ATEX—Software 2007. Université de Lorraine-Metz, 2017.

271. Williams, D.B. and C.B. Carter, The transmission electron microscope, in Transmission electron microscopy. 1996, Springer. p. 3-17.

272. Cezairliyan, A., K. Maglic, and V. Peletsky, Compendium of Thermophysical Property Measurement Methods: Volume 2 Recommended Measurement Techniques and Practices. 2012: Springer Science & Business Media.

273. Instron. MATERIALS TESTING SYSTEMS. 2022 [cited 2022 30/11]; Available from: https://www.instron.com/en/products/testing-systems.

274. Sobriety. Mercury®RT video extensometer. 2011 - 2017 [cited 2022 30/11]; Available from: http://www.dynrot.eu/t_optical_systems_en.htm.

275. Callister, W.D., et al., Materials science and engineering: an introduction. 2021: wiley.

276. Matsuzawa. Automatic micro hardness tester. 2010 [cited 2022 30/11]; Available from: http://www.matsuzawa-ht.com/us/index.htm.

277. Gleeble. Gleeble 3500-GTC thermo-mechanical processing sytem. 2022 [cited 2022 30/11]; Available from: https://www.gleeble.com/products/gleeble-systems/gleeble-3500.html#:~:text=With%20the%20introduction%20of%20the,thermal%20and%20mechanical%20testing%20system.

278. Ducreux, C.I.P., et al., An in-situ neutron diffraction investigation of martensitic transformation in a metastable β Ti-10V-2Fe-3Al alloy during uniaxial tension. Journal of Alloys and Compounds, 2021. **869**: p. 159301.

279. Lai, M.J., T. Li, and D. Raabe, ω phase acts as a switch between dislocation channeling and joint twinning- and transformation-induced plasticity in a metastable β titanium alloy. Acta Materialia, 2018. **151**: p. 67-77.

280. Zhu, W., et al., Tensile brittleness and ductility improvement in a novel metastable β titanium alloy with lamella structure. Journal of Alloys and Compounds, 2020. **827**: p. 154311.

281. Ruzic, J., et al., Mo segregation and distribution in Ti–Mo alloy investigated using nanoindentation. Materials Science and Engineering: A, 2018. **718**: p. 48-55.

282. Sasano H., S.T., Crystal structure of martensites in Ti-Mo-Al alloys, in Titanium '80, science and technology: proceedings of the Fourth International Conference on Titanium, O.I. Hirozo Kimura, Editor. 1980, Metallurgical Society of AIME, 1980: Kyoto, Japan. p. 717-724.

283. Niessen, F., et al., In-situ observation of nucleation, growth and interaction of deformation-induced α″ martensite in metastable Ti–10V–2Fe–3Al. Materials Science and Engineering: A, 2021. **802**: p. 140237.

284. Duerig, T.W., et al., Formation and reversion of stress induced martensite in Ti-10V-2Fe-3Al. Acta Metallurgica, 1982. **30**(12): p. 2161-2172.

285. Mantri, S.A., et al., Suppression and reactivation of transformation and twinning induced plasticity in laser powder bed fusion additively manufactured Ti-10V-2Fe-3Al. Additive Manufacturing, 2021. **48**: p. 102406.

286. Chen, W., et al., Controlling the microstructure and mechanical properties of a metastable β titanium alloy by selective laser melting. Materials Science and Engineering: A, 2018. **726**: p. 240-250.

287. Qiu, C. and Q. Liu, Multi-scale microstructural development and mechanical properties of a selectively laser melted beta titanium alloy, Addit. Manuf. 30 (2019) 100893. 2019.

288. Weinberg, F. and B. Chalmers, FURTHER OBSERVATIONS ON DENDRITIC GROWTH IN METALS. Canadian Journal of Physics, 1952. **30**(5): p. 488-502.

289. Lee, D.N., et al., Factors determining crystal orientation of dendritic growth during solidification. Materials Chemistry and Physics, 1997. **47**(2): p. 154-158.

290. Vrancken, B., et al., Microstructure and mechanical properties of a novel β titanium metallic composite by selective laser melting. Acta Materialia, 2014. **68**: p. 150-158.

291. Mantri, S.A. and R. Banerjee, Microstructure and micro-texture evolution of additively manufactured β-Ti alloys. Additive Manufacturing, 2018. **23**: p. 86-98.

292. Xu, H., et al., Selective laser melting of biomedical Ti15Mo alloy: A proper combination of strength and ductility under the effects of multiple mechanisms. Journal of Alloys and Compounds, 2021. **873**: p. 159686.

293. Qian, B., et al., On the transformation pathways in TRIP / TWIP Ti – 12Mo alloy. Materials Science & Engineering A, 2021. **822**.

294. Lai, M., C.C. Tasan, and D. Raabe, On the mechanism of {332} twinning in metastable β titanium alloys. Acta Materialia, 2016. **111**: p. 173-186.

295. Niessen, F., et al., In-situ observation of nucleation, growth and interaction of deformation-induced α ″martensite in metastable Ti–10V–2Fe–3Al. Materials Science and Engineering: A, 2021. **802**: p. 140237.

296. Ling, F.W., E.A. Starke, and B.G. Lefevre, Deformation behavior and texture development in beta Ti-V alloys. Metallurgical Transactions, 1974. **5**(1): p. 179-187.

297. Cai, S., J.E. Schaffer, and Y. Ren, Stress-induced phase transformation and room temperature aging in Ti-Nb-Fe alloys. Materials Science and Engineering: A, 2017. **680**: p. 13-20.

298. Kang, N., et al., Selective laser melting of low modulus Ti-Mo alloy: α/β heterogeneous conchoidal structure. Materials Letters, 2020. **267**: p. 127544.

299. Zhou, L., et al., Anisotropic mechanical behavior of biomedical Ti-13Nb-13Zr alloy manufactured by selective laser melting. Journal of Alloys and Compounds, 2018. **762**: p. 289-300.

300. Jeon, J.M., et al., Effects of microstructure and internal defects on mechanical anisotropy and asymmetry of selective laser-melted 316L austenitic stainless steel. Materials Science and Engineering: A, 2019. **763**: p. 138152.

301. Kok, Y., et al., Anisotropy and heterogeneity of microstructure and mechanical properties in metal additive manufacturing: A critical review. Materials & Design, 2018. **139**: p. 565-586.

302. Ben, D.D., et al., Heterogeneous microstructure and voids dependence of tensile deformation in a selective laser melted AlSi10Mg alloy. Materials Science and Engineering: A, 2020. **798**: p. 140109.

303. Chen, C. and R.R. Boyer, Practical considerations for manufacturing high-strength Ti-10V-2Fe-3A1 Alloy Forgings. JOM, 1979. **31**(7): p. 33-39.

304. Liang, L. and O.B.M. Hardouin Duparc, First-principles study of four mechanical twins and their deformation along the c-axis in pure α-titanium and in titanium in presence of oxygen and hydrogen. Acta Materialia, 2016. **110**: p. 258-267.

305. Fejes, G.R., V. Gonda, and K. Széll, Analysis of Recrystallization Peak Occuring During DSC Measurement. Acta Materialia Transylvanica, 2018. **1**(2): p. 73-76.

306. Zou, Z., et al., Refinement of the grain structure of additive manufactured titanium alloys via epitaxial recrystallization enabled by rapid heat treatment. Scripta Materialia, 2020. **180**: p. 66-70.

307. Kale, G.B. and R.V. Patil, Chemical Diffusion in Titanium-Molybdenum System. Materials Transactions, JIM, 1994. **35**(7): p. 439-444.

308. Bai, W., et al., Diffusivities and Atomic Mobilities in bcc Ti-Mo-Zr Alloys. Materials, 2018. **11**(10): p. 1909.

309. Boeckels, H., Phase Transformation in Ti-Mo-O. 2012.

310. Macias-Sifuentes, M.A., et al., Microstructure and mechanical properties of β-21S Ti alloy fabricated through laser powder bed fusion. Progress in Additive Manufacturing, 2021. **6**(3): p. 417-430.

311. Zhu, Y.-y., et al., Influence of heat treatments on microstructure and mechanical properties of laser additive manufacturing Ti-5Al-2Sn-2Zr-4Mo-4Cr titanium alloy. Transactions of Nonferrous Metals Society of China, 2018. **28**(1): p. 36-46.

312. Conradie, F., N. Treurnicht, and N. Sacks. Alpha case characterization of hot rolled titanium. in Advanced Materials Research. 2014. Trans Tech Publ.

313. Ling, F.-W., E.A. Starke, and B.G. Lefevre, Deformation behavior and texture development in beta Ti-V alloys. Metallurgical transactions, 1974. **5**(1): p. 179-187.

314. Yang, Y., et al., Plastic deformation via hierarchical nano-sized martensitic twinning in the metastable β Ti-24Nb-4Zr-8Sn alloy. Acta Materialia, 2020. **194**: p. 27-39.

315. Chen, B. and W. Sun, Transitional structure of {332}< 113> β twin boundary in a deformed metastable β-type Ti-Nb-based alloy, revealed by atomic resolution electron microscopy. Scripta Materialia, 2018. **150**: p. 115-119.

316. Bertrand, E., et al., Deformation twinning in the full-α ″martensitic Ti–25Ta–20Nb shape memory alloy. Acta Materialia, 2016. **105**: p. 94-103.

317. Tobe, H., et al., Effect of Nb content on deformation behavior and shape memory properties of Ti–Nb alloys. Journal of Alloys and Compounds, 2013. **577**: p. S435-S438.

318. Ping, D., et al., Stress-induced α ″martensitic (110) twinning in β-Ti alloys. Applied Physics Letters, 2008. **93**(15): p. 151911.

319. Zhang, X., W. Wang, and J. Sun, Formation of {332}< 113> β twins from parent {130}< 310> α ″plastic twins in a full α ″Ti-Nb alloy by annealing. Materials Characterization, 2018. **145**: p. 724-729.

320. Clément, N., A. Lenain, and P. Jacques, Mechanical property optimization via microstructural control of new metastable beta titanium alloys. Jom, 2007. **59**(1): p. 50-53.

321. Chesnutt, J. and F. Froes, Effect of. cap alpha.-phase morphology and distribution on the tensile ductility of a metastable beta titanium alloy. Metall. Trans., A;(United States), 1977. **8**(6).

322. Terlinde, G., T. Duerig, and J. Williams, Microstructure, tensile deformation, and fracture in aged ti 10V-2Fe-3Al. Metallurgical Transactions A, 1983. **14**(10): p. 2101-2115.

323. Bowen, A., Omega phase embrittlement in aged Ti-15% Mo. Scripta Metallurgica, 1971. **5**(8): p. 709-715.

324. Koul, M. and J. Breedis, OMEGA PHASE EMBRITTLEMENT IN AGED Ti--V. 1970, Massachusetts Inst. of Tech., Cambridge.

325. Chen, W., et al., New insights into ω-embrittlement in high misfit metastable β-titanium alloys: Mechanically-driven ω-mediated amorphization. Materials & Design, 2021. **205**: p. 109724.

326. Niinomi, M., et al., Biomedical titanium alloys with Young's moduli close to that of cortical bone. Regenerative biomaterials, 2016. **3**(3): p. 173-185.

327. Li, Y., E. Onodera, and A. Chiba, Friction Coefficient in Hot Compression of Cylindrical Sample. MATERIALS TRANSACTIONS, 2010. **51**(7): p. 1210-1215.

328. Chen, F.K. and C.J. Chen, On the nonuniform deformation of the cylinder compression test. Journal of Engineering Materials and Technology, Transactions of the ASME, 2000. **122**(2): p. 192-197.

329. Wang, X., et al., Inverse finite element modeling of the barreling effect on experimental stress-strain curve for high temperature steel compression test. Journal of Materials Processing Technology, 2017. **243**: p. 465-473.

330. Martínez, H.V., D. Coupard, and F. Girot, Constitutive model of the alloy 2117-T4 at low strain rates and temperatures. Journal of Materials Processing Technology, 2006. **173**(3): p. 252-259.

331. Duerig, T., et al., Formation and reversion of stress induced martensite in Ti-10V-2Fe-3Al. Acta Metallurgica, 1982. **30**(12): p. 2161-2172.

332. Han, Y., et al., The influence of thermomechanical processing on microstructural evolution of Ti600 titanium alloy. Materials Science and Engineering: A, 2011. **528**(29-30): p. 8410-8416.

333. Ahmed, M. and E.V. Pereloma, Observation of simultaneous operation of deformation twins in both α and β phases in metastable β titanium alloy. Journal of Alloys and Compounds, 2022. **910**: p. 164794.

334. Balasubrahmanyam, V. and Y. Prasad, Deformation behaviour of beta titanium alloy Ti–10V–4.5 Fe–1.5 Al in hot upset forging. Materials Science and Engineering: A, 2002. **336**(1-2): p. 150-158.

335. WANG, Z.-j., et al., Constitutive model for a new kind of metastable β titanium alloy during hot deformation. Transactions of Nonferrous Metals Society of China, 2012. **22**(3): p. 634-641.

336. Lei, L., et al., Effect of hot compressive deformation on the martensite transformation of Ti–10V–2Fe–3Al titanium alloy. Materials Science and Engineering: A, 2011. **530**: p. 591-601.

337. Fan, J., et al., Characterization of hot deformation behavior of a new near beta titanium alloy: Ti-7333. Materials & Design, 2013. **49**: p. 945-952.

338. Meyers, M.A., O. Vöhringer, and V.A. Lubarda, The onset of twinning in metals: a constitutive description. Acta Materialia, 2001. **49**(19): p. 4025-4039.

339. Manero, J.M., F.J. Gil, and J.A. Planell, Deformation mechanisms of Ti–6Al–4V alloy with a martensitic microstructure subjected to oligocyclic fatigue. Acta Materialia, 2000. **48**(13): p. 3353-3359.

340. Nag, S., et al., ω-Assisted nucleation and growth of α precipitates in the Ti–5Al–5Mo–5V–3Cr–0.5Fe β titanium alloy. Acta Materialia, 2009. **57**(7): p. 2136-2147.

341. Maghsoudlou, A., et al., The room temperature tensile deformation behavior of thermomechanically processed β-metastable Ti-Nb-Ta-Zr bio-alloy: the role of deformation-induced martensite. Materials Science and Engineering: A, 2018. **738**: p. 15-23.

342. Sun, Y., et al., Modeling constitutive relationship of Ti40 alloy using artificial neural network. Materials & Design, 2011. **32**(3): p. 1537-1541.

343. Suwas, S. and R.K. Ray, Crystallographic Texture of Materials. Crystallographic Texture of Materials, 2014.

344. Imandoust, A., et al., Nucleation and preferential growth mechanism of recrystallization texture in high purity binary magnesium-rare earth alloys. Acta Materialia, 2017. **138**: p. 27-41.

345. Li, J., et al., Texture evolution and the recrystallization behavior in a near β titanium alloy Ti-7333 during the hot-rolling process. Materials Characterization, 2020. **159**: p. 109999.